

SPINTERFACE WITH FULLERENE

By

SRIJANI MALLIK

Enrolment No. PHYS11201204017

National Institute of Science Education and Research (NISER)

Bhubaneswar

A thesis submitted to the

Board of Studies in Physical Sciences

In partial fulfilment of requirements

for the Degree of

DOCTOR OF PHILOSOPHY

of

HOMI BHABHA NATIONAL INSTITUTE

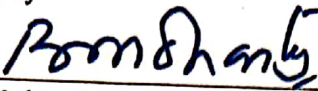
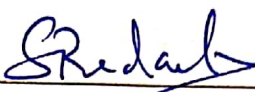
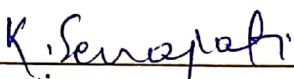
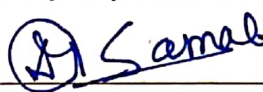


March, 2019

Homi Bhabha National Institute

Recommendations of the Viva Voce Committee

As members of the Viva Voce Committee, we certify that we have read the dissertation prepared by Srijani Mallik entitled "Spinterface with Fullerene" and recommend that it may be accepted as fulfilling the thesis requirement for the award of Degree of Doctor of Philosophy.

	<u>27/3/2019</u>
Chairman - Prof. Bedangadas Mohanty	Date:
	<u>S. Bedanta</u>
Guide / Convener - Dr. Subhankar Bedanta	Date: <u>27/03/19</u>
	<u>27-3-2019</u>
Examiner - Dr. Pranaba Kishor Muduli	Date:
	<u>27/03/2019</u>
Member 1- Dr. Kartikeswar Senapati	Date:
	<u>27/03/2019</u>
Member 2- Dr. Joydeep Bhattacharjee	Date:
	<u>27/03/19</u>
Member 3- Dr. Debakanta Samal	Date:

Final approval and acceptance of this thesis is contingent upon the candidate's submission of the final copies of the thesis to HBNI.

I/We hereby certify that I/we have read this thesis prepared under my/our direction and recommend that it may be accepted as fulfilling the thesis requirement.

Date: 27/03/2019

Place: SPS, NISER, Jatni


27/03/2019
Guide

Dr. Subhankar Bedanta

STATEMENT BY AUTHOR

This dissertation has been submitted in partial fulfilment of requirements for an advanced degree at Homi Bhabha National Institute (HBNI) and is deposited in the Library to be made available to borrowers under rules of the HBNI.

Brief quotations from this dissertation are allowable without special permission, provided that accurate acknowledgement of source is made. Requests for permission for extended quotation from or reproduction of this manuscript in whole or in part may be granted by the Competent Authority of HBNI when in his or her judgment the proposed use of the material is in the interests of scholarship. In all other instances, however, permission must be obtained from the author.

Srijani Malik
(Srijani Mallik)

DECLARATION

I, hereby declare that the investigation presented in the thesis has been carried out by me. The work is original and has not been submitted earlier as a whole or in part for a degree / diploma at this or any other Institution / University.

Srijani Mallik
(Srijani Mallik)

List of Publications arising from the thesis

Journal

1. *Interplay of uniaxial and cubic anisotropy in epitaxial Fe thin films on MgO (001) substrate, **S. Mallik**, N. Chowdhury, and S. Bedanta, *AIP Advances*, **2014**, 4, 097118-1 – 097118-6.
2. *Effect of the growth conditions on the anisotropy, domain structures and the relaxation in Co thin films, **S. Mallik**, S. Mallick and S. Bedanta, *J. Magn. Magn. Mater.* **2017**, 428, 50 – 58.
3. *Study of anisotropy, magnetization reversal and damping in ultrathin Co films on MgO (001) substrate, **S. Mallik** and S. Bedanta, *J. Magn. Magn. Mater.* **2018**, 446, 270 – 275.
4. *Effect of magnetic fullerene on magnetization reversal created at the Fe/C₆₀ interface, **S. Mallik**, S. Mattauch, M. K. Dalai, T. Brückel and S. Bedanta, *Scientific Reports*, **2018**, 8, 5515-1 – 5515-9.

Manuscript in preparation

1. *Tuning spinterface properties in Iron/Fullerene thin films, **S. Mallik**, A. S. Mohd., A. Koutsoubas, S. Mattauch, B. Satpati, T. Brückel, and S. Bedanta (Under review).
2. *Magnetic C₆₀ driven magnetization reversal and anisotropy in Co/C₆₀ bilayer thin film, **S. Mallik**, B. Sahoo, P. Sharangi, S. Mattauch, T. Brückel, and S. Bedanta (Under review).
3. *Spinterface induced enhancement of anisotropy in FM/ OSC bilayers, **S. Mallik et al.** (Manuscript under preparation).
4. *Study of magnetization reversal and anisotropy in ultrathin Fe thin film on MgO (001) substrate, **S. Mallik et al.** (Manuscript under preparation).

Others

1. Spacer layer and temperature driven magnetic properties in multilayer structured FeTaC thin films, A. K. Singh, **S. Mallik**, S. Bedanta and A. Perumal, *J. Phys. D: Appl. Phys.* **2013**, 46, 445005-1 – 445005-11.
2. Effect of Postannealing and Multilayer Structure on Soft Magnetic Properties of FeTaC Thin Film, A. K. Singh, **S. Mallik**, S. Bedanta and A. Perumal, *IEEE Trans. Magn.* **2014**, 50, 1, 2000804-1 – 2000804-4.
3. Effect of substrate rotation on domain structure and magnetic relaxation in magnetic antidot lattice arrays, S. Mallick, **S. Mallik** and S. Bedanta, *J. Appl. Phys.* **2015**, 118, 083904-1 – 083904-6.
4. Study of Magnetization Relaxation in Co Thin Films Prepared by Oblique Deposition and Substrate Rotation, N. Chowdhury, S. Mallick, **S. Mallik** and S. Bedanta, *Thin Solid Films*, **2016**, 616, 328 – 334.
5. Effects of composition, thickness and temperature on the magnetic properties of amorphous CoFeB thin films, A. Gayen, G. K. Prasad, **S. Mallik**, S. Bedanta and A. Perumal, *J. Alloys Compnds.* **2017**, 694, 823 – 832.

6. Tuning the anisotropy and domain structure of Co films by variable growth conditions and seed layers, S. Mallick, S. Mallik, B. B. Singh, N. Chowdhury, R. Gieniusz, A. Maziewski and S. Bedanta, *J. Phys. D: Appl. Phys.* **2018**, *51*, 275003-1 – 275003-8.

Srijani Mallik

(Srijani Mallik)

List of conferences attended:

1. Presented a **contributory oral** in International Conference on Magnetic Materials and Applications (ICMAGMA) in 2017, in DMRL Hyderabad, India
2. Presented a **poster** in 'Current Trends in Materials Science and Engineering (CTMSE)' in 2018, in SNBNCBS, Kolkata, India
3. Presented a **poster** in 'International Conference on Magnetism (INTERMAG)' in 2017, in Dublin, Ireland
4. Presented a **poster** in 'DAE Solid State Physics Symposium (SSPS)' in 2016, in KIIT Bhubaneswar, India
5. Presented a **poster** in 'Conference on Emerging Materials (CEMAT)' in 2016, in IISc Bangalore, India.
6. Presented a **poster** in 'International Symposium on Metallic Multilayers (MML)' in 2016, in Uppsala University, Uppsala, Sweden
7. Presented a **poster** in 'Emerging Trends in Advanced Functional Materials (ETA FM)' in 2016, in IOP Bhubaneswar, India
8. Presented a **poster** in 'International Conference on Magnetic Materials and Applications (ICMAGMA)' in 2015, in VIT Vellore, Vellore, India
9. Presented a **poster** in 'Indo-Japan Workshop on Magnetism at Nanoscale (IJWMN)' in 2015, in NISER, Bhubaneswar, India
10. Presented a **poster** in 'Current Trends in Condensed Matter Physics (CTCMP)' in 2015, in NISER Bhubaneswar, India
11. Presented a **poster** in 'International Conference on Physics at Surfaces and Interfaces (PSI)' in 2014, in IOP Bhubaneswar, India
12. Presented a **poster** in 'International Conference on Magnetic Materials and Applications (ICMAGMA)' in 2013, in IIT Guwahati, Guwahati, India

List of schools/workshops attended:

Attended a school on 'Basics of Magnetism and Investigations of Magnetic Properties of Materials' using Synchrotron Radiation in RRCAT Indore, India

Srijani Mallik
(Srijani Mallik)

Dedicated to my Parents

ACKNOWLEDGEMENTS

The success and final outcome of this thesis work required a lot of guidance and assistance from many people. To begin with, I would like to express my sincere gratitude to my supervisor Dr. Subhankar Bedanta for his continuous guidance, support, patience and motivation throughout my PhD tenure. I am extremely thankful as he took keen interest on my thesis work and guided me all along, till the completion of my PhD by providing all the necessary supports to grow as a researcher. I will always be in debt to him for giving me the opportunity to work with an interesting topic, for the fruitful discussions and for his help in understanding the work.

Besides my advisor, I would like to thank the chairman of my thesis monitoring committee (TMC) as well as the chairperson of school of physical sciences (SPS), NISER, Prof. Bedangadas Mohanty for his continuous support and valuable suggestions regarding my work. I would also like to thank the rest of my TMC members Dr. Kartikeswar Senapati, Dr. Joydeep Bhattacharjee, and Dr. Debakanta Samal for their constant evaluation, insightful comments and encouragement which helped me to widen my knowledge from various perspectives.

I sincerely acknowledge NISER and DAE, Govt. of India for providing the research funding to carry out my thesis work. I am also thankful to DST-SERB project EMR/2016/007725 for the financial support during the last few months of my PhD.

I would like to thank Dr. Braj Bhusan Singh, Inspire faculty, SPS, NISER for the fruitful discussions, suggestions regarding FMR measurements and for his help to carry out one PNR beamtime. I thank my fellow lab mates Niru di, Sovakara bhैया, Purbasha, Bikash, Swapna, Esita, Brindaban, Aroop, Thiru, Koustuv, Pushpendra, Gajanan, Biswajit, Sukanta, Sagarika, Mona, Abhilash for the stimulating discussions, for the sleepless nights we worked to fix equipment, and for all the fun we have had in the past years. My special thanks towards my senior Dr. Niru Chowdhury for her valuable suggestions to make me learn the minute details of the instruments. I would like to thank Dr. Thiruvengadam Vijayabaskaran for his

help in SQUID measurements. I heartily thank Purbasha and Esita for their technical helps in my need. My special thanks to Dr. Palash K. Manna for his help in proof reading the thesis.

I express my warm regards to Prof. Thomas Brückel, Forschungszentrum Jülich, Germany for giving me the opportunity to work in neutron facilities. I am grateful to Dr. Stefan Mattauch, Dr. Alexandrous Koutsioubas, Dr. Amir Syed Mohd., and Dr. Yury Khaydakov, MLZ, Garching, Germany for their help in the neutron experiments. Without their precious support it would not be possible to perform PNR measurements. I specially thank Dr. Amir Syed Mohd. for his suggestions regarding the PNR data analysis. I also thank the Department of Science and Technology, India (SR/NM/Z-07/2015) for the financial support for performing the neutron experiments and Jawaharlal Nehru Centre for Advanced Scientific Research (JNCASR) for managing the project.

I would express my gratitude to our collaborator Dr. Manas K. Dalai, NPL, New Delhi for his help in carrying out the SIMS measurements and data analysis.

I am thankful to and fortunate enough to get constant encouragement, support, and cooperation from my best friend, lab mate and husband Mr. Sougata Mallick. You were always the first person to share not only my achievements but also all the frustrations I went through during the PhD tenure. Our prolonged discussions on various scientific topics and the constructive partnership in work helped me to grow as a better personality. Without your presence it was not possible to complete the journey of PhD.

I thank all my family members and friends Rita, Sony, Anima, Abhisek, and Arup for their support in completing the degree.

Finally, I take this opportunity to express my gratitude and love to my parents for their constant support, faith, immense patience and encouragement to live my dream. They always stood like banyan tree over my head to protect me from all kind of problems. We walked together through the path of PhD to achieve the degree. I cannot forget to mention about the immense love I have received from my ever-charming grandmother. I am grateful to my late grandfather who always encouraged me in pursuing higher studies. I believe, it was your blessings which helped me in achieving the degree.

CONTENTS

Content Details	Page No.
SYNOPSIS	i-ix
LIST OF ABBREVIATIONS	x-xi
LIST OF FIGURES	xii-xxix
LIST OF TABLES	xxx
CHAPTER 1: Introduction and Fundamentals	1-32
1.1: Introduction	1
1.2: Fundamentals	6
1.2.1: Ferromagnetic metals	6
1.2.2: Spin-orbit interaction	7
1.2.3: Hyperfine interaction	9
1.2.4: Magnetic anisotropy	10
1.2.4.1: Magnetocrystalline anisotropy	11
1.2.4.1.1: Uniaxial anisotropy	12
1.2.4.1.2: Cubic anisotropy	13
1.2.5: Induced magnetic anisotropy	14
1.2.6: Magnetic domains	15
1.2.7: Magnetization reversal	19
1.2.7.1: Domain wall motion	21
1.2.7.2: Coherent rotation	22
1.2.8: Magnetization dynamics	24
1.2.9: Inverted thin films	26
1.2.10: Organic semiconductors	27
1.2.10.1: sp^3 hybridization	27
1.2.10.2: sp^2 hybridization	27
1.2.10.3: sp hybridization	28
1.2.11: Ferromagnet/Organic semiconductor interface: SPINTERFACE	30
1.2.12: State of art of spinterfaces	31
CHAPTER 2: Experimental Techniques	33-74
2.1: Physical vapor deposition	33
2.1.1: Sputtering	34
2.1.2: Thermal evaporation	37
2.1.3: Sample details	41
2.2: Atomic force microscopy	42
2.3: X-ray diffraction and reflectivity	46
2.3.1: X-ray diffraction	46
2.3.2: X-ray reflectivity	48
2.4: Secondary ion mass spectroscopy	51

2.5: Superconducting quantum interference device magnetometry	53
2.6: Kerr microscopy	55
2.7: Polarized neutron reflectivity	65
2.8: Ferromagnetic resonance	72
CHAPTER 3: Study of magnetic properties in ultrathin Fe and Co films on MgO (001) substrates	75-94
3.1: Study of magnetization reversal in Fe (3 nm) thin film on MgO (001) substrate	77
3.2: Study of anisotropy, magnetization reversal and damping properties in Co (3 nm) thin films on MgO (001) substrate	86
CHAPTER 4: Thickness dependence of spinterfaces in polycrystalline Fe/C₆₀ films	95-117
4.1: Study of magnetization reversal and anisotropy symmetry in single layer Fe thin films with variable thickness	96
4.2: Study of Fe/C ₆₀ spinterface induced magnetic properties in polycrystalline Fe/C ₆₀ bilayer thin films with variable thickness	101
4.3: Effect of two spinterfaces on the thickness, induced moment and magnetization reversal of tri-layer Fe/C ₆₀ system	113
CHAPTER 5: Spinterface in epitaxial Fe and C₆₀ systems	118-144
5.1: Study of magnetization reversal, domain structure and anisotropy in single layer epitaxial Fe thin film	119
5.2: Effect of magnetic C ₆₀ on the magnetic properties of Fe thin film (bilayer of epitaxial Fe/C ₆₀)	131
CHAPTER 6: Spinterface in polycrystalline Co and C₆₀ systems	145-159
6.1: Study of magnetic properties in Co thin film on Si (100) substrate	146
6.2: Study of spinterface induced magnetic properties in Co/C ₆₀ bilayer thin films on Si (100) substrate	150
CHAPTER 7: Spinterface in textured Co and C₆₀ systems	160-184
7.1: Effect of the growth conditions on the anisotropy, domain structures and the relaxation in Co thin films on MgO (001) substrate	161
7.2: Effect of magnetic C ₆₀ on the textured Co/C ₆₀ bilayer thin film on MgO (001) substrate	177
CHAPTER 8: Summary and Outlook	185-189
Annexure	190-192
REFERENCES	193-199

SYNOPSIS

The constant aspiration of faster as well smaller and non-volatile electronic devices has led to saturation of conventional semiconductor industry due to high power dissipation, quantum limits and other factors. The fundamental spintronic devices consist of two ferromagnetic (FM) layers separated by a non-magnetic metallic or insulating layer. However, due to the presence of high spin orbit coupling, the spin dephasing length of the spacer material becomes less which further limits the spin transportation length between two FM electrodes. Organic spintronics help in overcoming the aforementioned issue by replacing the spacer layer with an organic semiconductor (OSC) [1,2]. The advantages of OSCs are their low production cost, low weight, chemically interactive nature and most importantly their long spin relaxation time [3,4]. OSCs consist of low Z (atomic number) materials like Carbon, Hydrogen, Oxygen where both the spin orbit coupling and the hyperfine interaction are less. As a consequence, the spin of a carrier interacts weakly in organic environment and spin information is sustained for a long time. Along with the importance from the application point of view there exists a significant role of organic spintronics in understanding the fundamental physics associated to the hybridization of the FM and OSC atomic orbitals at the interface. The span of the interface where spin polarized charge transfer occurs from the FM layer to the OSC is known as ‘Spinterface’ [5]. Among many available OSCs, Buckminsterfullerene (C_{60}) is a potential candidate for such spin polarized charge transfer due to the absence of hydrogen atoms and associated hyperfine field [6-9]. In this work, we have created spinterfaces of Fe/ C_{60} and Co/ C_{60} to study the change in the magnetic properties (viz. magnetization reversal, domain structures, anisotropy symmetry etc.) as compared to the parent FM (Fe or Co) thin films. In this context the magnetic properties of the respective single layer FM thin films have been studied in the beginning. The thesis work focuses on magnetic systems having three types of crystalline structures *e.g.* polycrystalline, textured

and epitaxial. The results are divided into four sections depending on the material and the crystalline quality of the FM layer.

(i) First the magnetic properties of *polycrystalline* Fe single layer and Fe/C₆₀ bilayers on Si (100) substrates are discussed.

(ii) Afterward, results from similar studies on *epitaxial* Fe single layer and Fe/C₆₀ bilayer systems prepared on MgO (001) substrates have been presented.

Then we have studied similar effects with spinterface having another FM material Co.

(iii) The study of Co/C₆₀ spinterface for *polycrystalline* Co grown on Si (100) substrate is discussed.

(iv) It has been possible to grow *textured* Co thin films on MgO (001) substrates with specific growth conditions. The magnetic properties of such textured Co films as well as Co/C₆₀ bilayers were explored in the last section.

(i) Spinterface with Fe/C₆₀ on Si (100) substrate:

Single layer Fe samples with different thicknesses ($t_{\text{Fe}} = 18 \text{ nm}, 7.5 \text{ nm}, 3.5 \text{ nm}$) have been prepared on Si (100) substrate with native oxide layer. Due to the geometry of our deposition chamber the FM layers (both Fe and Co) are deposited with an oblique angle of 30° with respect to (w.r.t.) the substrate normal. A uniaxial anisotropy is induced in the system as the grains of the FM material become elongated towards the perpendicular to the projection of the plume direction [10,11]. Therefore, all the samples discussed in this thesis possess growth-induced uniaxial anisotropy. Large stripe domains are observed in these samples. Stripe domains are often observed in the films having dispersed uniaxial anisotropy due to strain [12]. In our samples, the polycrystalline growth of Fe may add dispersion in the oblique angle deposition induced uniaxial anisotropy direction. To study the effect of non-magnetic C₆₀ on the aforementioned magnetic properties of the Fe films, Fe/C₆₀ bilayers have been prepared on Si (100) substrates with similar thicknesses and deposition parameters of Fe

layers. Polarized neutron reflectivity (PNR) measurement indicates formation of spinterface in all the bilayer samples due to the π - d hybridization between C and Fe atoms. The induced moment in C_{60} is highest for the thicker ($t_{Fe} = 18$ nm) sample. About 1.8 nm thick spinterface is created in this sample with an induced moment of $1.9 \mu_B/\text{cage}$ of C_{60} . Other two samples ($t_{Fe} = 7.5$ and 3.5 nm) exhibit 1.5 and 1.1 nm of spinterface with an induced moment of 1.52 and $1.37 \mu_B/\text{cage}$ of C_{60} , respectively. Due to large lattice mismatch between Fe (0.278 nm) and SiO_2 ($a = 0.491$ nm; $c = 0.54$ nm), the growth of Fe is polycrystalline in nature. Because of this lattice mismatch the Fe atoms next to the SiO_2 layer experience strain during its growth. With increase in thickness the Fe atoms get relaxed, as with the growth of each monolayer of Fe the strain associated at the SiO_2/Fe interface should decrease [13]. Therefore, both the moment and thickness of the spinterface increases with increase in the Fe layer thickness. The domain size decreases in case of the bilayer samples in comparison to their respective reference (single layer) samples. The variation in the coercivity between the easy and hard axis decreases in case of the bilayer samples, which indicates that the formation of spinterface leads to a decrease in uniaxial anisotropy in comparison to their reference samples. In the case of the samples having thicker Fe layer ($t_{Fe} = 18$ nm), the anisotropy strength reduces to its $\sim 50\%$ w.r.t. the reference single layer sample [14]. We have also prepared tri-layers of Fe/ C_{60} samples to study the effect of spinterface in both side of the C_{60} . The induced moment in C_{60} for tri-layer samples are higher in comparison to their respective bilayers. This indicates that the amount of induced moment in C_{60} depends on either the number of Fe/ C_{60} interfaces or the total thickness of the Fe layer. The tri-layer samples exhibit isotropic nature by following the trend of decreasing anisotropy due to the presence of Fe/ C_{60} interface.

(ii) Spinterface with Fe/C₆₀ on MgO (001) substrate:

It is known that most of the physical properties are improved in a system when prepared with better crystalline structure. To improve the crystalline quality of the Fe, it has been deposited on MgO (001) substrate instead of Si (100). Urano *et al.* first reported the epitaxial growth of bcc Fe on MgO (001). The epitaxy between Fe ($a = 0.2866$ nm) and MgO ($a = 0.4213$ nm) follows the relation Fe(001)[110] || MgO(001)[100] [15]. Ultrathin films are always desired for the spintronic devices. 3 nm Fe has been prepared using dc magnetron sputtering with substrate pre-annealing and without rotating the substrate during deposition. However, the growth of 3 nm Fe is not found to be epitaxial as discussed in the literature. Therefore, instead of the cubic anisotropy, oblique angular deposition induced uniaxial anisotropy dominates in the sample. Both one and two steps hysteresis loops are observed in this sample for the angle between the easy axis and applied field, $\phi \leq 50^\circ$ and $\phi \geq 90^\circ$, respectively. A peculiar cross over of magnetic switching has been observed in the hysteresis loop along $\phi = 90^\circ$ as the first reversal occurs before the switching of the magnetic field direction. For the two stepped loops, two types of domains are observed during the reversal. Magnetization reversal before the switching of the field direction is observed along $\phi = 90^\circ$ which indicates presence of anti-parallel spin alignment in the sample. Polarized neutron reflectivity (PNR) measurement has been performed on this sample to confirm such possibilities. The preliminary fits from the PNR data indicate that due to high temperature growth of Fe in ultrathin limit, an intermixing layer of Fe and Ta (capping layer) gets formed on top of the pure Fe layer. Depending on the reversal field of these two layers two step loops arise near the hard axis of the sample [16]. Further, we have prepared thicker Fe thin films ($t_{\text{Fe}} = 25$ and 15 nm) on annealed MgO (001) substrates which led to formation of epitaxial Fe films. Along with the oblique growth-induced uniaxial anisotropy, another four-fold cubic anisotropy is superimposed in the system due the epitaxial growth of Fe. A detailed study of

in-plane magnetic hysteresis with simultaneous domain imaging has been performed by state-of-art magneto optic Kerr effect (MOKE) based microscopy. Both the thicker samples exhibit similar magnetization reversal mechanism however, the hysteresis loops and the domain images get modified substantially w.r.t. the ultrathin (3 nm) sample. Single step and double step loops are also observed depending on the angle between the applied field and easy axis. Unlike the ultrathin sample, 90° domain wall motion is observed in the thicker samples. Two simultaneous and successive 90° domain wall nucleation and motion are observed along the cubic easy cum uniaxial easy axes and cubic easy cum uniaxial hard axes, respectively. However, along cubic hard axis two separate 180° domain wall motions with a distinct plateau region dominate the magnetization reversal process. Therefore, in spite of having four-fold anisotropy it is essential to explain magnetization reversal mechanism in $0^\circ < \phi < 90^\circ$ span as uniaxial anisotropy plays a major role in this system [17]. We have prepared similar Fe (15 nm) sample with C_{60} (40 nm) to study and compare the results with the single layer Fe film of similar thickness. It is observed that the Fe moment gets reduced by $\sim 27\%$ and a thin layer of about 2 nm of C_{60} close to the Fe interface exhibits magnetic moment of $\sim 2.95 \mu_B/\text{cage}$ (according to the best fit of the PNR measurement). This is the highest reported induced moment in C_{60} so far. Future theoretical calculation may elucidate if induction of such high magnetic moment in C_{60} is possible only via direct charge transfer or any secondary processes are also involved. From the PNR measurements it has also been found that the magnetic C_{60} layer prefers to be aligned anti-parallel with the Fe layer at the remanent state. The magnetic C_{60} has substantial effect on the magnetization reversal and the domain microstructure of the Fe layer when compared to that of the parent single layer Fe film. The effect is profound near the cubic hard axis of the sample. The hysteresis loop shape as well as the domain structure gets strongly modified at the cubic hard axis. From the energy configuration it is known that the cubic hard axis is energetically unstable. Therefore, a small

perturbation may lead to strong change in the spin structure. We believe that the interaction between the magnetic C₆₀ and Fe layers causes such perturbation, which leads to a clear change in hysteresis loop shape. Magnetization reversal before the switching of the field direction indicated anti-parallel alignment of two ferromagnetic layers, which has been confirmed by the result obtained from the PNR data fitting [9]. In this case, the uniaxial anisotropy of the bilayer sample increases by an order in comparison to its single layer reference sample. It is believed that the $\pi - d$ hybridization between the C and Fe atoms may elongate the shape of the orbitals in a specific direction [18], which leads to the increase in the uniaxial anisotropy [19]. Therefore, the crystallinity of the Fe layer plays a major role in determining the spinterface induced magnetic properties.

(iii) Spinterface with Co/C₆₀ on Si (100) substrate:

Similar to the Fe/C₆₀ spinterface, we have studied the effect of Co/C₆₀ spinterface on the magnetic properties of the Co thin film. We have prepared 10 nm Co thin film on oxidised Si (100) substrate with a buffer layer of Ta to minimize the strain in Co growth due to lattice mismatch. Angle dependent hysteresis loops and corresponding domain images indicate a local dispersion in the growth-induced uniaxial anisotropy. This may occur due to the polycrystalline growth of Co. Large stripe domains are observed in this film. The domain size gets decreased while going away from the easy axis up to 40° and starts increasing in the range of 45° < ϕ < 60°. Afterwards the reversal happens through coherent rotation for field applied at angles close to the hard axis of the sample. The sudden increase in domain size within a specific range of ϕ suggests presence of dispersion in the anisotropy. To study the Co/C₆₀ spinterface induced properties, bilayer of Co (10 nm)/C₆₀ (12 nm) has been prepared on Si (100) substrate with Ta seed layer. The coercivity increases for the bilayer sample, which indicates increase in exchange coupling in the sample possibly due to the Co/C₆₀ hybridized interface. In this sample also the domain size increases for specific range of ϕ

similar to the single layer one. However, the proportion of increment in domain size is higher in the bilayer sample in comparison to the single layer reference sample. This signifies increase in dispersion in the anisotropy of the system. By comparing the anisotropy symmetry of both the samples, it is found that the bilayer sample shows combination of uniaxial and another anisotropy. The enhancement in the contribution of the other anisotropy may arise from the Co/C₆₀ spinterface. PNR measurement of the bilayer sample indicates that 0.8 μ_B /cage of moment is induced in C₆₀ cage at the interface up to 2 nm. Co moment decreases by 6% in case of the bilayer sample in comparison to the single layer sample. Anisotropy evaluation using FMR measurement shows that the anisotropy gets enhanced by ~2 times in bilayer Co/C₆₀ sample in comparison to the single layer Co sample [20]. A possible reason for such enhancement in anisotropy is the $\pi - d$ hybridization between C and Co atoms. The increase in anisotropy in bilayer samples signifies that better growth of the bottom FM layer promotes enhancement in anisotropy when FM/C₆₀ spinterface is present in the sample.

(iv) Spinterface with Co/C₆₀ on MgO (001) substrate:

To improve the crystallinity of Co, we have prepared Co ultrathin (3 nm) films with or without pre-annealing the MgO (001) substrate. An additional uniaxial anisotropy is observed in the substrate pre-annealed sample along with the oblique angular deposition induced uniaxial anisotropy. 180° domain wall motion is observed for both the samples. Ferromagnetic resonance (FMR) measurement confirms the existence of two uniaxial anisotropies in the pre-annealed sample. The misalignment between these two anisotropy directions is evaluated by fitting the angle dependent FMR data [21]. However, cubic anisotropy has not been observed in these samples may be due to improper growth in ultrathin limit. To achieve better crystalline structure of Co, thicker Co (25 nm) thin films have been prepared on MgO (001) substrates by varying the growth conditions. Nukaga *et al.*

have reported that it is possible to prepare epitaxial Co films on MgO (001) substrates with some specific preparation condition where the Co and MgO follows the following relation $\text{Co}(11\bar{2}0)[0001]//\text{MgO}(100)[001]$ and $\text{Co}(11\bar{2}0)[1\bar{1}00]//\text{MgO}(100)[001]$ [22]. However, Co thin film on MgO substrate is usually not expected to grow epitaxially due to the large misfit between MgO and hcp Co lattices ($\sim 16\%$) [23,24]. This may lead to the formation of textured or polycrystalline Co films. We have prepared four samples by varying the combination of substrate pre-annealing and substrate rotation ($R_{\text{sub}} = 0$ and 10 rpm) during deposition. XRD measurement reveals that textured Co thin films are obtained due to the effect of substrate annealing prior to deposition whereas absence of substrate pre-annealing led to the formation of polycrystalline Co thin films. From the grain analysis by atomic force microscopy (AFM), it has been observed that the pre-annealing and rotation of substrate during deposition led to most dense packing of Co grains. This indicates the possibility of highest exchange coupling in this sample among all four samples. It has been observed that the anisotropy symmetry varies significantly with different growth conditions. Depending on the deposition parameters, the samples exhibit the presence of either both the cubic and uniaxial or only uniaxial anisotropies. The domain images measured by Kerr microscopy reveal the characteristic domain structure (ripple domains) for inverted Co thin films. Magnetic relaxation has been performed in all the samples to observe the evolution of domains under the thermal excitation by keeping the Zeeman energy fixed. Fastest relaxation is observed for the sample prepared with substrate pre-annealing and $R_{\text{sub}} = 10$ rpm due to the densest packing of grains (highest exchange coupling) among all the samples [25]. To study the effect of spinterface grown on textured Co sample, bilayer of Co (25 nm)/ C_{60} (15 nm) has been prepared on pre-annealed MgO (001) substrate without substrate rotation ($R_{\text{sub}} = 0$ rpm). PNR measurement indicates the formation of spinterface with higher induced moment than the polycrystalline Co/ C_{60} spinterface. However, for both the polycrystalline and textured

samples the induced moment in C_{60} is lower in comparison to the similar spinterface created with Fe. In the case of the bilayer sample, stripe domains are observed along the easy axis whereas branch domains are observed in case of the single layer Co sample prepared with similar deposition conditions. However, ripple domains are observed in both the samples away from the easy axis. The domain size as well as the coercivity decreases in case of the bilayer sample. The anisotropy symmetry obtained from the angle dependent hysteresis measurement indicates increase in the uniaxial anisotropy for the bilayer sample. In case of the textured Co/ C_{60} sample, the uniaxial anisotropy dominates over the cubic anisotropy unlike the parent single layer Co film [20].

In summary, our present work shows that it is possible to create a few layers of magnetic C_{60} out of non-magnetic C_{60} through formation of FM/OSC spinterface. The induced moment and the thickness of magnetic C_{60} strongly depends on the crystalline quality, thickness and the material of the FM layer. Non-negligible magnetic moment in the Fe/ C_{60} and Co/ C_{60} spinterfaces have profound effect on the magnetic properties viz. magnetization reversal mechanism, domain structures, anisotropy symmetry etc. as compared to the parent FM thin films. We believe that work has significant impact on understanding the fundamental interfacial properties of FM/OSC bilayers which may be useful for the future spintronics applications.

List of Abbreviation:

AFM: Atomic force microscopy
CMA: Cubic magnetic anisotropy
CPW: Coplanar waveguide
DC: Direct current
DED: Double exponential decay
DOS: Density of states
DFT: Density functional theory
DW: Domain wall
EA: Easy axis / axes
FM: Ferromagnet
FMR: Ferromagnetic resonance
FWHM: Full width at half maxima
GUI: Graphical User Interface
GMR: Giant magnetoresistance
HFI: Hyperfine interaction
 H : External magnetic field
HA: Hard axis / axes
 H_c : Coercive field
 H_{eff} : Effective field
 H_K : Anisotropy field
 H_M : Reverse magnetic field for relaxation measurements
 H_N : Nucleation field
HOMO: Highest occupied molecular orbital
 H_R : Resonance field
 H_S : Saturation field
 K_2 : Uniaxial / two-fold anisotropy constant
 K_4 : Cubic / four-fold anisotropy constant
 K_B : Boltzmann constant
 K_{in} : In-plane anisotropy constant
 K_U : Perpendicular uniaxial anisotropy constant
LLG: Landau-Lifshitz-Gilbert
LUMO: Lowest unoccupied molecular orbital
 M_{eff} : Effective magnetization
MOKE: Magneto optic Kerr effect

MR: Magnetoresistance
 M_R : Remanent magnetization
 M_S : Saturation magnetization
NM: Non-magnet
NSF: Non-spin flip
OSC: Organic semiconductor
PNR: Polarized neutron reflectivity
PVD: Physical vapor deposition
QCM: Quartz crystal monitor
 R^{++} : Neutron up-up scattering cross section
 R^{--} : Neutron down-down scattering cross section
 R^{+-} : Neutron up-down scattering cross section
 R^{-+} : Neutron down-up scattering cross section
RF: Radio frequency
 R_{sub} : Substrate rotation
RT: Room temperature
SED: Single exponential decay
SIMS: Secondary ion mass spectroscopy
SLD: Scattering length density
SO: Spin-orbit
SOC: Spin-orbit coupling
SQUID: Superconducting quantum interference device
TAMR: tunneling anisotropic magnetoresistance
TOF: Time-of-flight
TMR: Tunneling magnetoresistance
UMA: Uniaxial magnetic anisotropy
XMCD: X-ray magnetic circular dichroism
XRD: X-ray diffraction
XRR: X-ray reflectivity

** A-B: Interdiffusion layer between element A and element B. In this thesis we have used this notation to describe the intermixing layers in the multilayer samples.

List of Figures:

- 1.1 Schematic showing the density of the states of s and d band electrons in (a) non-magnetic and (b) ferromagnetic metals.
- 1.2 Schematic to show different components of the spin orbit interaction where the orbital angular momentum arises from a current carrying loop.
- 1.3 Coordinate system showing the direction cosines of the magnetization vector.
- 1.4 (a) Schematic representation of the deposition geometry of our sputtering chamber. (b) Schematic illustration of the self-shadowing process taken from the ref [10] where the plume direction is at 60° and the red arrow corresponds to the easy axis.
- 1.5 (a) to (c) show schematic representation of reduction of the magnetic stray field energy by formation of domains. Different domains are represented in different colors. The flux closure domain known as the Landau pattern is shown in (c) which commonly represents the domain pattern in systems with cubic anisotropy.
- 1.6 Schematic representation of (a) Bloch wall and (b) Néel wall showing the out-of-plane and in-plane spin rotations, respectively.
- 1.7 Schematic diagram for (a) 180° , (b) 90° , and (c) 360° DWs.
- 1.8 Hysteresis loop showing the typical magnetization (M) behavior as a function of the applied field (H) in a ferromagnet.
- 1.9 Schematic representation of the magnetization reversal process via (a) DW motion along EA and (b) coherent rotation along HA.
- 1.10 Schematic of the coordinate system to understand the coherent rotation process known as Stoner Wohlfarth model.
- 1.11 Schematic representation of the precessional motion of magnetization (\mathbf{M}) along with a damping factor around the applied field (\mathbf{H}) direction.

- 1.12 (a) Schematic for the energy diagram of carbon ground state and sp^3 hybridized state.
(b) A cartoon showing the sp^3 hybridized carbon in Methane structure [110].
- 1.13 (a) Schematic for the energy diagram of carbon ground state and sp^2 hybridized state.
(b) A cartoon showing the sp^2 hybridized carbon in Ethene structure [110].
- 1.14 (a) Schematic for the energy diagram of carbon ground state and sp hybridized state.
(b) A cartoon showing the sp hybridized carbon in Ethyne structure [110].
- 1.15 Schematic diagram to show the effect of orbital hybridization on the density of states (DOS) of the organic molecules. (a) DOS for the ferromagnet and organic semiconductor when they are separated from each other. (b) and (c) show the DOS for the same when they are brought close enough to participate in the orbital hybridization. This figure has been taken from the ref [5].
- 2.1 A schematic representation of the sputtering process where the vacuum components required for this process are also depicted. The light violet solid cone inside the vacuum chamber represents the plasma. Different atoms involved in this process are shown with different colored balls and labelled in the image. A few extra facilities available in our deposition chamber viz. substrate heating, rotation, thickness monitor (QCM), pressure controlling throttle valve etc. are also shown in the image.
- 2.2 A schematic representation of the thermal evaporation process where the vacuum components required for this process are also depicted. The atoms involved in this process are shown with different colored balls and labeled in the image. The design of the chamber has been kept the same as the sputtering process as both the techniques are present inside the same chamber in our deposition unit.
- 2.3 Image of QPrep multi-deposition unit present in our lab. The inset shows the inside top view of the chamber. The numbers correspond to different sources available in the chamber. 1 to 3 are dc sputtering sources, 4 is the MAT60 (for creating atomic plasma out

of the molecular gases like O₂) source, 5 to 6 are rf sputtering sources, 7 is the e-beam evaporation source, 8 is the nanogen supply and 9 is the thermal evaporation source (having two boats). Except the thermal evaporation source all other sources are distributed at 45° angle with respect to each other in the horizontal plane. These sources are at 30° angle with respect to the substrate plane (vertical plane).

2.4 Schematic diagram showing the working principle of atomic force microscopy.

2.5 Different modes of operation of AFM techniques i.e. contact mode, non-contact mode, tapping mode are shown in (a) to (c), respectively. (d) The force diagram of AFM is shown in the plot. Different force regions for different modes of operation of AFM are marked in the graph. The concept of the image has been taken from ref [133].

2.6 Schematic representation of x-ray diffraction phenomena in specular geometry on a crystallographic plane where the separation between the planes are denoted by d . The incoming rays fall on the planes in θ angle and diffraction is measured at 2θ angle. The wavelength of x-ray is denoted by λ . The path difference between two consecutive beams of x-rays is shown by the yellow colored lines.

2.7 Schematic representation of X-ray reflection phenomena in specular geometry on a multilayer thin film. The incident and reflected wave vectors are denoted by k_i and k_f , respectively. The angle of incidence θ_i and reflection θ_f are equal and defined with respect to the surface plane. The momentum transfer vector Q_z is measured along the surface normal.

2.8 Schematic diagram showing the working principle of secondary ions mass spectroscopy. The concept of the image has been taken from ref [147].

2.9 Schematic diagram showing the pick-up-coil geometry and a demo plot for the response signal while centering the sample in MPMS SQUID magnetometer [100].

- 2.10 Schematic diagram showing the elementary magneto optical interaction for the longitudinal Kerr effect. This image has been taken from ref [156]. Due to the interaction between incident light wave and the magnetic dipoles of the samples, the incident plane polarized light becomes elliptically polarized light along with a rotation after getting reflected from the sample. The phase shift can be corrected using a compensator and the rotation of the light is measured which is proportional to the magnetization of the sample.
- 2.11 Schematic diagram of magneto optic Kerr effect setup showing all the optical and electrical components. The concept of the image has been taken from ref [100].
- 2.12 Different geometries of MOKE measurements are depicted with respect to the magnetization of the sample and plane of incidence of the light. (a), (b) and (c) show the longitudinal, transverse and polar geometries, respectively.
- 2.13 (a) Schematic diagram showing the principle of domain formation in Kerr microscope. (b) The essential components and ray paths for perpendicular light incidence and (c) image-forming path. Images shown in (b) and (c) are taken from the ref [156].
- 2.14 Schematic diagram of the scattering geometry for polarized neutron reflectivity in specular reflection mode. The Y-axis is the quantization axis for the neutrons known as the non-spin flip (NSF) axis and the X-direction is the spin flip (SF) axis. The resultant Q_z vector points towards the perpendicular to the surface along z-axis.
- 2.15 Schematic layout of the reflectometers (a) MARIA [176] and (b) NREX [177] at MLZ, Garching Germany. The image has been taken from the respective websites. In both the facilities spin polarized neutrons interact with the sample and the reflected state (+ or -) of the neutron is measured using the ^3He detector. Spin flipper helps in measuring the non-spin flip and spin flip reflectivity.
- 2.16 (a) Zeeman splitting of the energy levels of a ferromagnetic sample on application of uniform external magnetic field. (b) A typical FMR spectrum showing the resonance

phenomenon occurred due to transitions between the energy levels shown in (a). (c) Schematic overview of the CPW FMR set-up used in our lab [180].

3.1 (a) Hysteresis loop measured along the easy axis ($\phi = 0^\circ$) for sample 3S_A in longitudinal mode at RT using MOKE microscope. (b) – (e) show the domain states corresponding to the field points marked by points 1 – 4, respectively in the hysteresis loop (a). The applied field direction is shown with the red arrow. The scale bar shown in (b) is same for all the images.

3.2 (a) Hysteresis loop measured along $\phi = 65^\circ$ for sample 3S_A in longitudinal mode at RT using MOKE microscope. (b) to (e) show the domain states corresponding to the field points marked by points 1 – 4, respectively in the hysteresis loop (a). The applied field direction is shown with the red arrow. The scale bar shown in (b) is same for all the images.

3.3 (a) Hysteresis loop measured along $\phi = 90^\circ$ for sample 3S_A in longitudinal mode at RT using MOKE microscope. (b) to (e) show the domain states corresponding to the field points marked in the hysteresis loop (a). The applied field direction is shown with the red arrow. The scale bar shown in (b) is same for all the images.

3.4 (a) Polarized neutron reflectivity data measured at the saturation state along $\phi = 0^\circ$ at RT and its corresponding fits for sample 3S_A. The red and blue open circles represent the data measured for the R^{++} , and R^{--} channels, respectively. The solid lines correspond to their respective fits. (b) A schematic representation of the sample structure obtained by fitting the PNR data shown in (a). The numbers written in brackets correspond to the fitted thickness of the respective layer. (c) and (e) show the PNR data and fits near the remanence and coercivity, respectively. Similar to R^{++} , and R^{--} channels, pink and green open circles represent the data measured for the R^{+-} and R^{-+} channels, respectively. (d) and (f) show the schematic representation of the ferromagnetic layers.

The arrows shown in (b), (d) and (f) correspond to the net magnetization direction of the respective layer. The red arrow shows the direction of the applied field for (a) – (c).

3.5 Structural and magnetic scattering length density (SLD) vs thickness for sample 3S_A

3.6 Polarized neutron reflectivity data and its corresponding fits for sample 3S_A along $\phi = 65^\circ$ at (a) remanence and (c) coercivity state. The red, blue, pink and green open circles represent the data measured for the R^{++} , R^{--} , R^{+-} and R^{-+} channels, respectively. The solid lines correspond to their respective fits. (b) and (d) show the schematic representation of the ferromagnetic layers where the arrows correspond to the net magnetization direction of the respective layer. The red arrow shows the direction of the applied field.

3.7 Polarized neutron reflectivity data and its corresponding fits for sample 3S_A along $\phi = 90^\circ$ at (a) remanence and (c) coercivity state. The red, blue, pink and green open circles represent the data measured for the R^{++} , R^{--} , R^{+-} and R^{-+} channels, respectively. The solid lines correspond to their respective fits. (b) and (d) show the schematic representation of the ferromagnetic layers where the arrows correspond to the net magnetization direction of the respective layer. The red arrow shows the direction of the applied field.

3.8 Hysteresis loops measured using longitudinal MOKE microscopy for (a) sample 3S_B, and (b) sample 3S_C along $\phi = 0^\circ$ (EA), 30° , 60° and 90° . The legends to represent different angles for both the samples are shown in (a). Both the graphs are plotted in same scale for better comparison.

3.9 M_r/M_s vs ϕ plot for samples 3S_B (blue colored squares) and 3S_C (orange colored circles) measured using MOKE microscopy showing the anisotropy behavior.

3.10 Domain images measured using longitudinal MOKE microscopy at coercivity for sample 3S_B (a) – (d) and sample 3S_C (e) – (h) along 0° (EA), 30° , 60° and 90° . The

arrow shown in (a) represents the applied field direction for all the measurements. The scale bars in (a) and (e) are same for all other images for samples 3S_B and 3S_C, respectively.

3.11 Schematic of the direction of the magnetization, applied field, easy axis with respect to the sample orientation considered for the analysis of the FMR data.

3.12 Anisotropy symmetry plot and the fits for sample 3S_B measured using FMR keeping the frequency fixed at 6.5 GHz.

3.13 Hysteresis loops measured by SQUID for sample 3S_B when the field is applied along (a) in-plane and (b) out-of-plane direction.

4.1 Angle dependent hysteresis loops (a) – (c) for samples 4S_A, 4S_B and 4S_C, respectively. The measurements have been performed using MOKE microscopy in longitudinal mode at RT. The loops have been plotted in the same scale for better comparison of the coercivity w.r.t. the thickness of the Fe layer.

4.2 The hysteresis loops ((a), (f), (k)) and the corresponding domain images ((b) – (e), (g) – (j), (l) – (o)) measured along the easy axis for samples 4S_A, 4S_B and 4S_C, respectively. The images shown in (b) – (e) correspond to the domain states observed in sample 4S_A at the field points 1 – 4, respectively marked in (a). Similarly, the images shown in (g) – (j) and (l) – (o) correspond to the domain states observed in samples 4S_B and 4S_C at the field points 5 – 8 and 9 – 12 as marked in (f) and (k), respectively. All the domain images are in same length scale shown in (b), (g) and (l). The arrows shown in image (b), (g) and (l) represent the direction of the applied field.

4.3 (a) FMR signal vs applied field measured at various angles for sample 4S_C. (b) Anisotropy symmetry plot and its fit for sample 4S_C measured using ferromagnetic resonance (FMR) technique by keeping the frequency fixed at 12 GHz. The blue colored

solid circles and the red line correspond to the measured data and the fit to equation 4.2, respectively.

4.4 (a) – (c) M–H loops measured at RT using superconducting quantum interference device (SQUID) for samples 4S_A, 4S_B and 4S_C, respectively. The insets of the figures show the zoomed in version of the loops near the coercivity.

4.5 Depth profile of sample 4B_C measured by secondary ion mass spectroscopy.

4.6 (a) Polarized neutron reflectivity data measured at the saturation state at RT and its corresponding fits for sample 4B_A. The red and blue open circles represent the data measured for the R^{++} and R^{--} channels, respectively. The solid lines correspond to their respective fits. (b) A schematic representation of the sample structure obtained by fitting the PNR data shown in (a). The numbers written in brackets beside each layer correspond to the thickness of various layers obtained from the best fit. (c) and (d) show the PNR data and corresponding fits for the near remanence and coercivity measurement for sample 4B_A, respectively.

4.7 (a) Polarized neutron reflectivity data measured at the saturation state at RT and its corresponding fits for sample 4B_B. The red and blue open circles represent the data measured for the R^{++} and R^{--} channels, respectively. The solid lines correspond to their respective fits. (b) A schematic representation of the sample structure obtained by fitting the PNR data shown in (a). The numbers written in brackets beside each layer correspond to the thickness of various layers obtained from the best fit. (c) and (d) show the PNR data and corresponding fits for the near remanence and coercivity measurement for sample 4B_B, respectively.

4.8 (a) Polarized neutron reflectivity data measured at the saturation state at RT and its corresponding fits for sample 4B_C. The red and blue open circles represent the data measured for the R^{++} and R^{--} channels, respectively. The solid lines correspond to their

respective fits. (b) A schematic representation of the sample structure obtained by fitting the PNR data shown in (a). The numbers written in brackets beside each layer correspond to the thickness of various layers obtained from the best fit. (c) and (d) show the PNR data and corresponding fits for the near remanence and coercivity measurement for sample 4B_C, respectively.

4.9 (a) Polarized neutron reflectivity data measured at the saturation state at RT and its corresponding fits for sample 4B_D. The red and blue open circles represent the data measured for the R^{++} and R^{--} channels, respectively. The solid lines correspond to their respective fits. (b) A schematic representation of the sample structure obtained by fitting the PNR data shown in (a). The numbers written in brackets beside each layer correspond to the thickness of various layers obtained from the best fit.

4.10 Angle dependent hysteresis loops (a) – (c) for samples 4B_A ($t_{Fe} = 3.5$ nm), 4B_B ($t_{Fe} = 7.5$ nm) and 4B_C ($t_{Fe} = 18$ nm), respectively. The measurements have been performed using MOKE microscopy in longitudinal mode at RT. The loops have been plotted in the same scale for better comparison of the coercivity w.r.t. the thickness of the Fe layer.

4.11 The hysteresis loops ((a), (f), (k)) and the corresponding domain images ((b) – (e), (g) – (j), (l) – (o)) measured along the easy axis for samples 4B_A, 4B_B and 4B_C, respectively. The images shown in (b) – (e) correspond to the domain states observed in sample 4B_A at the field points 1 – 4, respectively. Similarly, the images shown in (g) – (j) and (l) – (o) correspond to the domain states observed in samples 4B_B and 4B_C at the field points 5 – 8 and 9 – 12, respectively. All the domain images are in same length scale shown in (b), (g) and (l). The arrows shown in image (b), (g) and (l) represent the direction of the applied field.

- 4.12 (a) FMR signal vs applied field measured at various angles for sample 4B_C. (b) Anisotropy symmetry plot and its fit for sample 4B_C measured using ferromagnetic resonance (FMR) technique by keeping the frequency fixed at 12 GHz. The blue colored solid circles and the red line correspond to the measured data and the fit to equation 4.2, respectively.
- 4.13 (a) Polarized neutron reflectivity data measured at the saturation state at RT and its corresponding fits for sample 4T_A. The red and blue open circles represent the data measured for the R^{++} and R^{--} channels, respectively. The solid lines correspond to their respective fits. (b) A schematic representation of the sample structure obtained by fitting the PNR data shown in (a). The numbers written in brackets beside each layer correspond to the fitted thickness of the respective layer.
- 4.14 (a) Polarized neutron reflectivity data measured at the saturation state at RT and its corresponding fits for sample 4T_B. The red and blue open circles represent the data measured for the R^{++} and R^{--} channels, respectively. The solid lines correspond to their respective fits. (b) A schematic representation of the sample structure obtained by fitting the PNR data shown in (a). The numbers written in brackets beside each layer correspond to the fitted thickness of the respective layer.
- 4.15 Hysteresis loops measured using MOKE microscopy in longitudinal mode by varying the angle (ϕ) between the applied field and the easy axis at RT for samples (a) 4T_A and (f) 4T_B, respectively. The images shown in ((b) – (e)) and ((g) – (j)) correspond to the domain states observed in samples 4T_A and 4T_B along the easy axis (red curve with solid circles) at the field points 1 – 4 and 5 – 8, respectively. All the domain images are in same length scale shown in (b) and (g). The arrows shown in images (b) and (g) represent the direction of the applied field.

- 5.1 Coordinate system used to describe the anisotropy configuration of epitaxial Fe thin film on MgO (001) substrate having both cubic and uniaxial anisotropies.
- 5.2 Coercivity (H_C) vs. angle (ϕ) plot for (a) sample 5S_A and (b) sample 5S_B. H_{C1} and H_{C2} values are extracted from hysteresis loops measured by longitudinal MOKE.
- 5.3 Hysteresis loops measured at RT by longitudinal (a – c) and transverse (d – f) MOKE for different ϕ (0° , 45° and 90°) for sample 5S_A.
- 5.4 Hysteresis loop (a) and its corresponding domain images (b – e) measured by longitudinal Kerr microscope along $\phi = 0^\circ$ for sample 5S_A. The images shown in (b) – (d) correspond to the domain states in the hysteresis loop for the numbers 1 – 4, respectively. The red arrows in the images represent the net magnetization of that particular area of the sample. The green arrow in (b) shows the direction of applied magnetic field (H). All the images are in same length scale as shown in (b).
- 5.5 High Resolution Domain image along $\phi = 0^\circ$ for sample 5S_A captured by Kerr microscope. The area encircled shows two 90° DWs.
- 5.6 Hysteresis loop (a) and its corresponding domain images (b – e) measured by longitudinal Kerr microscope along $\phi = 45^\circ$ for sample 5S_A. The images shown in (b) – (d) correspond to the domain states in the hysteresis loop for the numbers 1 – 4, respectively. The red arrows in the images represent the net magnetization of that particular area of the sample. The green arrow in (b) shows the direction of applied magnetic field (H). All the images are in same length scale as shown in (b).
- 5.7 Hysteresis loop (a) and its corresponding domain images (b – e) measured by longitudinal Kerr microscope along $\phi = 50^\circ$ for sample 5S_A. The images shown in (b) – (d) correspond to the domain states in the hysteresis loop for the numbers 1 – 4, respectively. The red arrows in the images represent the net magnetization of that particular area of the

sample. The green arrow in (b) shows the direction of applied magnetic field (H). All the images are in same length scale as shown in (b).

5.8 Hysteresis loop (a) and its corresponding domain images (b – e) measured by longitudinal Kerr microscope along $\phi = 90^\circ$ for sample 5S_A. The images shown in (b) – (d) correspond to the domain states in the hysteresis loop for the numbers 1 – 4, respectively. The red arrows in the images represent the net magnetization of that particular area of the sample. The green arrow in (b) shows the direction of applied magnetic field (H). All the images are in same length scale as shown in (b).

5.9 (a) Frequency dependent FMR signal for sample 5S_A. (b) ΔH vs ω and (c) ω vs H_R plots for sample 5S_A to calculate the damping constant and anisotropy field, respectively.

5.10 Anisotropy symmetry plot and its fit for sample 5S_A measured using ferromagnetic resonance (FMR) technique by keeping the frequency fixed at 10 GHz. The blue colored solid circles and the red line correspond to the measured data for $0^\circ < \phi < 360^\circ$ in 10° interval and the fit to equation 5.3, respectively.

5.11 (a) Schematic layer structure of sample 5B_A. (b) Depth profile of sample 5B_A measured using secondary ion mass spectroscopy (SIMS) technique.

5.12 Polarized neutron reflectivity (PNR) data for sample 5B_A measured at RT at (a) saturation ($\mu_0 H = 100$ mT), (b) near remanence ($\mu_0 H = 2.1$ mT) for magnetic field applied along $\phi = 45^\circ$ and (c) saturation ($\mu_0 H = 100$ mT) for magnetic field applied along $\phi = 90^\circ$. The PNR data (open circles) and their corresponding fits (solid lines) for R^{++} and R^{--} channels are shown by red and blue color, respectively. (d) The model layer structure for sample 5B_A where the thicknesses for each layer have been obtained by fitting the PNR data.

5.13 Figure of merit (FOM) versus different values of induced magnetic moment of C_{60} to show the best fitted value of the induced moment.

- 5.14 Schematic of one C₆₀ cage sitting on top of the Fe layer to calculate the area of contact between C₆₀ and Fe surface.
- 5.15 Hysteresis loop (a) and its corresponding domain images (b – e) measured by longitudinal Kerr microscope along $\phi = 0^\circ$ for sample 5B_A. The images shown in (b) – (d) correspond to the domain states in the hysteresis loop for the numbers 1 – 4, respectively. The red arrows in the images represent the net magnetization of that particular area of the sample. The green arrow in (b) shows the direction of applied magnetic field (H). All the images are in same length scale as shown in (b).
- 5.16 Hysteresis loop (a) and its corresponding domain images (b – e) measured by longitudinal Kerr microscope along $\phi = 45^\circ$ for sample 5B_A. The images shown in (b) – (d) correspond to the domain states in the hysteresis loop for the numbers 1 – 4, respectively. The red arrows in the images represent the net magnetization of that particular area of the sample. The green arrow in (b) shows the direction of applied magnetic field (H). All the images are in same length scale as shown in (b).
- 5.17 Hysteresis loop (a) and its corresponding domain images (b – g) measured by longitudinal Kerr microscope along $\phi = 50^\circ$ for sample 5B_A. (b) – (g) correspond to the domain images in the hysteresis loop for the numbers 1 – 6, respectively. The red and cyan arrows in the images represent the net magnetization of that particular area of the Fe and C₆₀ layers, respectively. The green arrow in (b) shows the direction of applied magnetic field (H). All the images are in same length scale as shown in (b).
- 5.18 Hysteresis loop (a) and its corresponding domain images (b – e) measured by longitudinal Kerr microscope along $\phi = 90^\circ$ for sample 5B_A. The images shown in (b) – (d) correspond to the domain states in the hysteresis loop for the numbers 1 – 4, respectively. The red arrows in the images represent the net magnetization of that

particular area of the sample. The green arrow in (b) shows the direction of applied magnetic field (H). All the images are in same length scale as shown in (b).

5.19 (a) Frequency dependent FMR signal for sample 5B_A. (b) ΔH vs frequency ω plot to calculate the damping constant and (c) frequency ω vs $\mu_0 H_R$ plot for sample 5B_A.

5.20 Anisotropy symmetry plot and its fit for sample 5B_A measured using ferromagnetic resonance (FMR) technique by keeping the frequency fixed at 10 GHz. The blue colored solid circles and the red line correspond to the measured data and the fit to equation 5.3, respectively.

6.1 (a) Hysteresis loops measured using MOKE based microscopy at RT in longitudinal mode by varying the angle (ϕ) between the easy axis and the applied field direction for sample 6S_A. The inset of the figure shows the zoomed in view of the hysteresis loops near the coercivity for better visibility.

6.2 (a) Hysteresis loop measured along the easy axis ($= \phi 0^\circ$) at RT in longitudinal mode for sample 6S_A. (b) - (e) show the domain images correspond to the field points 1 – 4 in the hysteresis loop, respectively. All the domain images are in the same scale shown in (b).

6.3 Angle (ϕ) dependent domain images near the coercivity for sample 6S_A are shown in (a) - (e). The domain images are measured using MOKE based microscopy at RT in longitudinal mode. The scale bars of the images are shown in image (a). The applied field direction shown in image (a) has been kept constant during all the measurements and the sample was rotated accordingly. (f) Plot for the angle dependent average domain width.

6.4 (a) Plot for frequency dependent linewidth and corresponding fit for sample 6S_A. (b) Angle dependent resonance field (H_R) plot for sample 6S_A to evaluate the anisotropy constants of the system.

6.5 X-ray reflectivity (XRR) data and its corresponding fit for sample 6B_A.

- 6.6 (a) Hysteresis loops measured using MOKE based microscopy at RT in longitudinal mode by varying the angle (ϕ) between the easy axis and the applied field direction for sample 6B_A. The inset of figure (a) shows the zoomed version of the hysteresis loops near the coercivity for better visibility. (b) Angle dependent coercivity plot for sample 6B_A.
- 6.7 (a) Hysteresis loop measured along the easy axis ($\phi = 0^\circ$) at RT in longitudinal mode for sample 6B_A. (b) – (e) show the domain images correspond to the field points 1 – 4 in the hysteresis loop, respectively. All the domain images are in the same scale shown in (b).
- 6.8 Angle (ϕ) dependent domain images near the coercivity for sample 6B_A are shown in (a) - (e). The domain images are measured using MOKE based microscopy at RT in longitudinal mode. The scale bars of the images are shown in image (a). The applied field direction shown in image (a) has been kept constant during all the measurements and the sample was rotated accordingly. (f) Plot for the angle dependent average domain width.
- 6.9 (a) Polarized neutron reflectivity (PNR) data and the corresponding fits for sample 6B_A. The red and blue open circles represent the data measured for the R^{++} and R^{--} channels, respectively. The solid lines correspond to their respective fits. The measurement was performed at the saturation state at RT. (b) A schematic representation of the sample structure obtained by fitting the PNR data is shown in (a). The numbers written in brackets correspond to the fitted thickness of the respective layer. (c) shows the PNR data and the corresponding fits for sample 6B_A near the coercive field (H_C) at RT. (d) A schematic representation of the magnetic states of the layers with respect to the saturation state.

- 6.10 Hysteresis loops measured by superconducting quantum interference device (SQUID) to quantify and compare the net magnetization in the samples. Presence of Co/C₆₀ interface decreases the magnetization of Co significantly in sample 6B_A.
- 6.11 (a) Plot for frequency dependent linewidth plot and corresponding fit for sample 6B_A. (b) Angle dependent resonance field (H_R) plot for sample 6B_A to evaluate the anisotropy constants of the system.
- 7.1 (a) – (d) Plots showing intensity vs. 2θ measured using XRD for samples 7S_A, 7S_B, 7S_C, and 7S_D, respectively. The insets of (a), (b) and (c) depict the zoomed plot for a specific range of 2θ for samples 7S_A, 7S_B, and 7S_C, respectively.
- 7.2 Plots showing intensity vs. 2θ measured around Co (10 $\bar{1}$ 0) and Co (10 $\bar{1}$ 1) peaks using XRD for samples 7S_A (a, b) and 7S_C (c, d), respectively.
- 7.3 (a) – (d) Surface topography imaged using atomic force microscopy (AFM) technique for samples 7S_A, 7S_B, 7S_C, and 7S_D, respectively. All the images are in same length scale as shown in (a).
- 7.4 (a) – (d) Surface topography imaged by AFM for the samples 7S_A*, 7S_B*, 7S_C*, and 7S_D*, respectively, prepared without the capping (AlO_x) layer.
- 7.5 (a) – (d) Hysteresis loops measured along easy, intermediate and hard axes by longitudinal MOKE at RT for samples 7S_A, 7S_B, 7S_C and 7S_D, respectively.
- 7.6 (a) Comparison of the coercivity vs. ϕ plots are shown in polar symmetry for samples 7S_A (red solid squares), 7S_B (blue solid circles), 7S_C (green solid stars) and 7S_D (pink solid triangles). (b) Polar plot for difference in coercivity between samples 7S_A and 7S_B vs. ϕ .
- 7.7 (a) Hysteresis loop measured by longitudinal Kerr microscope for sample 7S_A along the EA ($\phi = 0^\circ$). (b) – (e) are the domain images corresponding to the field points 1 to 4

marked in (a) respectively. The arrow in (b) represents the direction of applied magnetic field. The scale bar shown in (b) is same for all the images.

7.8 Domain images measured at the coercive field for all the sample are shown here. First to third row of the domain images are measured along EA, IA and HA, respectively. The HA was different for different samples and therefore the values of ϕ are written in the domain images in (i) – (l). Four columns of the figure correspond to four different samples 7S_A, 7S_B, 7S_C, and 7S_D. The inset of figure (h) in red square box corresponds to the zoomed image of the red circled area. The direction of the applied field (H) for all the images is shown in (a). All the images are in same length scale shown in (a).

7.9 (a) – (d) Relaxation measurement along easy axis performed at $H_M/H_C \sim 0.99$ by longitudinal Kerr Microscope for samples 7S_A, 7S_B, 7S_C, and 7S_D, respectively. Open circles and solid lines represent the experimental data and the fits, respectively.

7.10 (a) Hysteresis loops measured by varying ϕ in longitudinal mode using MOKE microscopy at RT for sample 7B_A. (b) Polar plot showing the variation of coercivity with respect to ϕ which reflects the anisotropy symmetry of sample 7B_A.

7.11 (a) Hysteresis loop measured by longitudinal Kerr microscope for sample 7B_A along the EA ($\phi = 0^\circ$). (b) – (e) are the domain images corresponding to the field points 1 to 4 marked in (a) respectively. The arrow in (b) shows the direction of applied magnetic field. The scale bar shown in (b) is same for rest of the images (c) – (e).

7.12 (a) Hysteresis loop measured by longitudinal Kerr microscope for sample 7B_A along IA ($\phi = 30^\circ$). (b) – (e) are the domain images corresponding to the field points 1 to 4 marked in (a) respectively. The arrow in (b) represents the direction of applied magnetic field. The scale bar shown in (b) is same for rest of the images.

- 7.13 (a) Polarized neutron reflectivity (PNR) data and the corresponding fits for sample 7B_A. The red and blue open circles represent the data measured for the R^{++} and R^{--} channels, respectively. The solid lines correspond to their respective fits. The measurement has been performed at the saturation state at RT. (b) A schematic representation of the sample structure obtained by fitting the PNR data is shown in (a). The numbers written in brackets in each layer correspond to the fitted thickness of the respective layer.
- 7.14 Angle dependent resonance field (H_R) plot and corresponding fits for the samples (a) 7S_A and (b) 7B_A measured using ferromagnetic resonance (FMR) technique at a fixed frequency of 8 GHz.

List of Tables:

- 4.1 Details of single layer polycrystalline Fe samples prepared on Si (100) substrate
- 4.2 Details of bilayer polycrystalline Fe/C₆₀ samples prepared on Si (100) substrate
- 4.3 Details of tri-layer polycrystalline Fe/C₆₀ samples prepared on Si (100) substrate
- 5.1 Details of the epitaxial single layer Fe samples
- 7.1 Details of prepared Co samples on MgO (001) substrate
- 7.2 Average Roughness and grain size for the samples calculated from AFM images
- 7.3 Fitting parameters of relaxation data measured at $H_M/H_C \sim 0.99$

Chapter 1: Introduction and Fundamentals

1.1. Introduction

‘Spinterface’ is the gateway between two layers through which polarized spins can be transferred. It is a special type of interface having properties which are significantly different from their constituent layers [5,26-28]. Study of such spinterfaces is fascinating from both fundamental as well as application point of view. The surging demand for the smaller, faster, and non-volatile electronic devices has led the conventional semiconductor industry to its limit of miniaturization due to high power dissipation, quantum limits, etc. To overcome such difficulties nanoscale spin-based electronic devices have emerged as the potential alternatives. Extensive research has been performed to control the conventional spin valve devices having two ferromagnets (FM) separated by a non-magnetic (NM) spacer layer [29-32]. The spacer layer plays a major role in determining the spin injection, transport, and detection in a device structure. The advantages of incorporating the organic semiconductors (OSC) in spintronics as a spacer layer are their low production cost, low weight, chemically interactive nature, etc. [33-35]. Further, the major advantage of OSCs over the conventional inorganic materials is their longer spin relaxation time. OSCs consist of low Z (atomic number) materials like Carbon, Hydrogen, Oxygen, etc. where the spin-orbit coupling and hyperfine interaction are less than the heavy metals or insulators used as conventional spacer layers. As a consequence, the spin of a carrier weakly interacts in organic environment and spin information is sustained for a longer time [3,36,37]. In the early time of evolution of organic spintronics, 8-hydroxy-quinoline aluminium (Alq_3) was the mostly used OSC after the observation of 40% giant magnetoresistance (GMR) at 11K for 130 nm thick Alq_3 spacer layer [38]. However, for real life applicable devices it is necessary to observe such effects at room temperature (RT). Zero-bias magnetoresistance (MR) of $12.5 \pm 0.3\%$ was observed at RT for an exchange-biased tunnel junction with Alq_3 as spacer layer [39]. It is observed that

the electrons preserve most of their spin polarization as they pass into and out of the OSC layers. This result shows that achieving electrical spin injection and detection with an OSC is easier than that with Si or GaAs [39]. Dediu *et al.* improved the spin injection properties of both the spin polarized electrode/Alq₃ interfaces and achieved RT inverse spin valve operation [40]. After a few years, they showed that the carrier mobility is 5 orders more in Rubrene than that in Alq₃ [4]. In addition, the spin-orbit coupling is one order less for Rubrene in comparison to Alq₃ [41]. A relatively larger MR ratio of 6% was observed at RT in vertical spin valve device with Fe₃O₄/Rubrene/Co structure [42]. The MR ratio of C₆₀ based spin valve of similar structure varies between 3 – 5% at RT but shows large spin transport length of 110 nm [2,43]. Recently, tunneling anisotropic magnetoresistance (TAMR) has been observed in a spin valve structure having only one ferromagnet (Co) as bottom electrode and C₆₀ as the spacer layer [44,45]. Further, the studies of MR, GMR, TAMR, etc. by changing the FM electrodes and using different OSC as a spacer layer have become one of the most exciting research topics of the last decade [3,4,46-51]. The highest reported MR in OSC based spin valves is 300% at 2K in which Alq₃ was used as the spacer layer between LSMO and Co electrodes [52]. However, so far only ~ 9% MR has been observed at RT for Co/AlO_x/C₆₀/Ni₈₀Fe₂₀ vertical spin valve [53].

Organic spintronics is not only interesting to mediate or control a spin polarized signal between two FM layers but also to understand the physics of spin polarized charge transfer at the interface. Buckminsterfullerene (C₆₀) is a potential candidate for such spin polarized charge transfer due to the absence of hydrogen atoms and associated hyperfine field [6-9,54]. As the formula suggests, C₆₀ is composed of carbon atoms only. The C atoms present in C₆₀ may undergo *sp* hybridization to attain stabilization by lowering the total energy of the system. Thus, it is prone to hybridize with metallic materials having unfilled *d* orbitals by sharing the electrons. Theoretical calculation predicts that the density of states (DOS) of C₆₀

change significantly when brought in contact with a FM layer by either broadening or shifting of the DOS [5,55]. An induced moment of $1.2 \mu_B$ per cage of C_{60} has been observed by suppression of 21% ferromagnetic moment in Co for Co/ C_{60} multilayers [6]. Polarized neutron reflectivity (PNR) and x-ray magnetic circular dichroism (XMCD) measurements have revealed the presence of an antiferromagnetic (AFM) coupling at the interface between Co and C_{60} . Next to the AFM coupled interface, a few nm of C_{60} layers exhibit weak ferromagnetism [6]. However, the exact thickness of the spinterface where moment has been induced in C_{60} layers is not reported in literature. Similarly, C_{60} monolayers on Fe (001) reveal magnetic polarization of C_{60} due to hybridization of C_{60} and Fe orbitals [7]. The hybrid interface between Fe and C_{60} leads to magnetic moments $\mu_S = -0.21$ and $-0.27 \mu_B$ per C atom for C_{60} layers on Fe(001) and Fe/W(001), respectively [8]. The strength of hybridization strongly depends on the adsorption geometry of C_{60} w.r.t. the crystallographic orientation of the FM film [56-58]. Theoretical models show that a large spin polarization in the C_{60} can be achieved if the molecule is adsorbed with a pentagonal ring on a bcc (001) FM surface [56]. Therefore, the 4 atom hole reconstruction where one of the pentagons of C_{60} sinks in bcc Fe, is the most stable structure to produce high spin polarization in C_{60} [58]. The experimental results can be explained by considering the aforementioned theoretical model. Theory also predicts that Hund-rule magnetism could be achieved in fullerene resulting in C_{60}^{n+} ions [59]. However, the thickness of the hybridized C_{60} that possesses the magnetic moment is not quantified in the literature. Moreover, the effect of spinterfaces on the magnetization reversal mechanism and the domain structure has not been explored so far. Further, a thin film can grow in different crystalline structures (epitaxial, textured, polycrystalline, amorphous) depending on the growth parameters as well as the substrate and the thin film material lattice mismatch. The dependence of the hybridized spinterfacial properties on such growth parameters is still unknown. It has been reported that due to the non-planar structure of C_{60} ,

spin-orbit coupling (SOC) is non-negligible which leads to a reduction in the hybridization strength [54]. However, the spin-polarized interface states close to the Fermi level are maintained [54]. It should be noted that the presence of oxygen atoms between the Fe and C₆₀ interface is non-desirable as it reduces the probability of hybridization [60]. As the hybridization between the FM and OSC molecules directly involve the orbitals, it is expected that the anisotropy of such systems may get modified. The presence of a C₆₀ layer on Co (5.5 ML) ultrathin film can control the anisotropy symmetry of the system through an inverse spin reorientation transition from in-plane to out-of-plane by the local hybridization between C₆₀ p_z and Co d_{z^2} orbitals [18,61]. However, the effect of hybridization on the global anisotropy symmetry of in-plane magnetized systems is not explored so far in literature.

Recently, Ma'Mari *et al.* demonstrated that it is possible to alter the electronic state of non-ferromagnetic materials (Sc, Mn, Cu, Pt etc.) and create ferromagnetism at RT when in contact with organic materials [62-64]. It has been observed that charge transfer of 3 electrons per molecule is possible from Cu to the C₆₀ layer in a C₆₀/Cu bilayer thin film [65]. Theoretically, it has also been shown that hybridization of molecular orbital is possible at C₆₀/metal interface [66,67]. Tseng *et al.* have shown the electron transfer at the interface between a metal surface and the organic electron acceptor tetracyano-pquinodimethane by both experimental and theoretical analysis. It leads to substantial structural rearrangements on both the organic and metallic sides of the interface [68].

The magnetic properties of FM/OSC spinterfaces have been studied in this thesis where Fe and Co have been considered as the FM and C₆₀ has been taken as the OSC. The following open questions are addressed in this thesis:

- The induced moment as well as thickness of the Fe/C₆₀ and Co/C₆₀ spinterfaces are quantified experimentally by PNR measurements. The dependence of these properties on

the thickness of the FM layer (Fe or Co) and the number of spinterfaces have also been studied.

- The effect of crystallinity of the FM layers (Fe or Co) on the spinterfaces is also studied.
- The magnetization reversal mechanism and domain structures of such hybridized heterostructures have been studied extensively which was lacking in the literature so far.
- The possibility of tuning the anisotropy of the FM/C₆₀ spinterfaces has been explored by changing the growth conditions of the spinterface.

The thesis is arranged in the following manner: in **chapter 1** the state of the science and the motivation behind the work presented in this thesis have been detailed. Further, some basic concepts related to ferromagnetism which are relevant to understand the results have been discussed. **Chapter 2** describes the working principle and details of the experimental techniques used to prepare and characterize the samples discussed in this thesis. The magnetic properties of ultrathin (3 nm) Fe and Co single layer thin films prepared on MgO (001) substrate have been presented in **chapter 3**. In **chapter 4**, the thickness dependent magnetic properties of polycrystalline Fe films on Si (100) substrate have been discussed. Further, bilayer and tri-layer of Fe/C₆₀ films have been studied to observe the effect of Fe/C₆₀ spinterface on the magnetization reversal mechanism and anisotropy of the system. The effect of Fe thickness on the spinterfacial properties has also been discussed here. To observe the effect of crystallinity of the Fe layer on such spinterfaces, the magnetization reversal mechanism and anisotropy symmetry for epitaxial Fe single layer as well as Fe/C₆₀ bilayer on MgO (001) substrate have been studied in **chapter 5**. Similar studies have been performed in **chapter 6** on polycrystalline Co single layer and bilayer thin films to observe the effect of Co/C₆₀ spinterface. In **chapter 7**, the effect of different growth conditions on the magnetic properties has been studied for Co thin films on MgO (001) substrate. Further, the effect of textured Co/C₆₀ spinterface on the magnetic properties has been discussed here. Finally, all the results have been summarized and the future prospects of this work have been presented in **chapter 8**.

1.2. Fundamentals:

1.2.1. Ferromagnetic metals:

In the periodic table, the $3d$ transition metals i.e. Fe, Co and Ni are popularly known as the ferromagnetic (FM) metals. The Curie temperature (T_C) i.e. the critical temperature beyond which the FM properties get lost are quite higher than the RT for these $3d$ FM metals. The T_C for Fe, Co and Ni are 1043°C , 1388°C , and 627°C , respectively. The origin of ferromagnetism in these metals lies in the band structures of the $3d$ electrons [69].

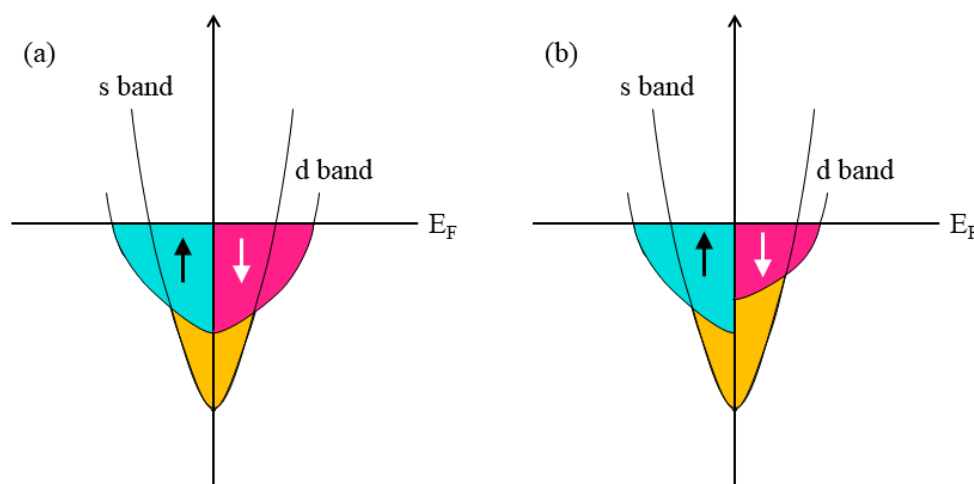


Figure 1.1: Schematic showing the density of the states of s and d band electrons in (a) non-magnetic and (b) ferromagnetic metals.

The $3d$ and $4s$ atomic energy levels for the free atoms of Fe, Co or Ni are the hosts of the valence electrons. In the metallic state these $3d$ and $4s$ levels are broadened into energy bands. The $4s$ orbitals try to overlap with $4s$ orbitals of the neighboring atom and ends up in band spreading over a wide energy range of $15 - 20$ eV. In contrary, the $3d$ orbitals are less extended in space and associated energy range is narrower ($4 - 7$ eV). In reality, the $3d$ and $4s$ orbitals are indistinguishable due to the strong s - d coupling at the Fermi level [70]. Therefore, both the bands are shown in figure 1.1 where only $3d$ electrons are considered to be metallic. However, in practice the mobility of $4s$ electrons are higher than that of the $3d$ electrons. According to the Pauli exclusion principle, a particular state can be occupied by

only one electron. However, each state can host two opposite spin electrons as they are degenerate with respect to the spins. The spins start filling up from the lowest energy state and the highest occupied energy level is known as the Fermi level denoted by E_F . The electron polarization due to the imbalance of electron density of spin-up (\uparrow) and spin-down (\downarrow) electrons at the Fermi level can be defined as:

$$P = \frac{D_{\uparrow}(E_F) - D_{\downarrow}(E_F)}{D_{\uparrow}(E_F) + D_{\downarrow}(E_F)} \quad \dots \dots \dots \quad (1.1)$$

where, $D_{\uparrow}(E_F)$ and $D_{\downarrow}(E_F)$ are the density of states (DOS) of spin up and down electrons at the Fermi level, respectively [71]. It can be observed from figure 1.1(a) that the number of spin-up and down electrons at the Fermi level for non-magnetic metals are equal. Therefore, they show spin-polarization P to be zero. However, for the FM metals, the DOS for spin-up and down electrons are not same at the Fermi Level (figure 1.1(b)). Consequently, the spin polarization for the FM materials is non-zero ($P \neq 0$). The vertical displacement between the DOS of the spin-up and down shown in figure 1.1(b) is caused by the exchange energy between spin up and down energy bands. Typically, the value of P for the 3d transition FM metals are 40%, 35%, and 23% for Fe, Co, and Ni, respectively. In addition, another type of FM material exists called “half-metal” where only one spin direction electrons are present at the Fermi level. These materials show $\sim 100\%$ spin polarization at the Fermi level [72]. However, the T_C of these materials are generally less than that of the 3d transition FM metals and lies very close to the RT. An example of half-metal is Lanthanum strontium manganite (LSMO) with composition $\text{La}_{0.7}\text{Sr}_{0.3}\text{MnO}_3$ which exhibits $T_C \sim 77^\circ\text{C}$ [72].

1.2.2. Spin-orbit interaction:

The spin-orbit (SO) interaction is the coupling between the spin angular momentum \mathbf{S} and the orbital angular momentum \mathbf{L} , where the total angular momentum is defined as $\mathbf{J} = \mathbf{L} + \mathbf{S}$. The SO interaction plays a crucial role in determining the spin relaxation time and the

anisotropy of a magnetic system. Therefore, it is necessary to understand it well to control the spintronic properties. Figure 1.2 shows a schematic diagram for orbital angular momentum arising from a current carrying loop. A magnetic field (\mathbf{H}_{orb}) is generated at the centre of the loop due to the motion of the electron. The magnetostatic energy associated to such a condition can be written as [73]:

$$E = -\boldsymbol{\mu}_s \cdot \mathbf{H}_{orb} = -\mu_s H_{orb} \cos\theta \quad (1.2)$$

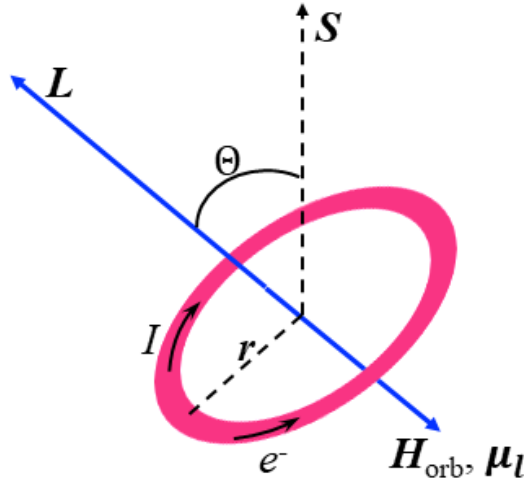


Figure 1.2: Schematic to show different components of the spin orbit interaction where the orbital angular momentum arises from a current carrying loop.

The orbital magnetic field can be expressed as (considering mass of electron as m_e and Z as the atomic number):

$$\mathbf{H}_{orb} = \frac{\boldsymbol{\mu}_l}{2\pi\mu_0 r^3} = -\frac{Ze\mathbf{L}}{4\pi m_e r^3} \quad (1.3)$$

The SO energy can be calculated by substituting \mathbf{H}_{orb} from equation 1.3 in equation 1.2 and putting $\mu_0 = \frac{1}{\epsilon_0 c^2}$,

$$\langle E \rangle = -\boldsymbol{\mu}_s \cdot \langle \mathbf{H}_{orb} \rangle = -\frac{Ze^2}{4\pi\epsilon_0 m_e^2 c^2} \langle \frac{1}{r^3} \rangle \mathbf{L} \cdot \mathbf{S} \quad (1.4)$$

where, $\langle \frac{1}{r^3} \rangle$ is proportional to Z^3 . Therefore, the SO splitting is directly proportional to Z^4 .

As the OSCs comprise of low weight materials like Carbon, Hydrogen etc. the strength of

SO is low. It should be noted that the strength of SO is inversely proportional to the spin relaxation time (τ_S) [74].

$$\mathcal{L}^2 \approx \frac{\hbar \Delta^2}{2\Gamma} \frac{1}{\tau_S} \quad \dots (1.5)$$

Here, $\mathcal{L}, \Delta, \Gamma$ are the strength of SO, band gap and quasi spin-scattering rate, respectively. As a result, spin relaxation time is larger in OSCs in comparison to inorganic materials [52]. Further, the energy of the system depends on the angle between \mathbf{L} and \mathbf{S} according to equation 1.4. If the spin \mathbf{S} becomes parallel to \mathbf{L} , the system stays in the minimum energy state (favoured configuration). Similarly, if \mathbf{S} becomes perpendicular to \mathbf{L} , the energy maximizes. Therefore, if the direction of \mathbf{L} is preferred along a particular crystallographic axis in a material then the energy will be the difference between the favored (\mathbf{S} parallel to \mathbf{L}) and unfavored (\mathbf{S} perpendicular to \mathbf{L}) orientations. This leads to formation of magnetocrystalline anisotropy in the ferromagnetic system.

1.2.3. Hyperfine interaction:

The hyperfine interaction (HFI) is an interaction between the electron cloud with the nuclear spins in an atom. HFI arises due to the following reasons: (i) interaction between the energy of the nuclear magnetic dipole moment and the magnetic field generated by the electrons, (ii) the energy of the nuclear electric quadrupole moment in the electric field gradient due to the distribution of charge within the atom. In reality, the electrons can interact with more than one nucleus during the transport. Therefore, the Hamiltonian associated to the HFI can be written as:

$$H_{HFI} = \sum_i^N A_i \mathbf{I}_i \cdot \mathbf{S} \quad (1.6)$$

where, A_i is the coupling constant, \mathbf{I}_i and \mathbf{S} are the nuclear and electron spin operators, respectively. The effective HFI strength for the interaction of an electron with N nuclear spins can be expressed as $H_{HFI} = a\mathbf{I} \cdot \mathbf{S}$ with the effective coupling constant $a \sim \frac{A}{\sqrt{N}}$ [75]. In

general, the HFI becomes weaker with more nuclei - electron interactions, and/or with more delocalization of the electron wavefunction. Therefore, the HFI is much stronger for hydrogen in comparison to other elements.

It should be noted that the spin relaxation time of a material strongly depends on the HFI. The electron-nuclear spin interaction and fluctuation in nuclear spins lead to spin flipping and spin dephasing, respectively [3]. As a result, the spin relaxation time decreases with increase in HFI. However, the organic elements without hydrogen atom e.g. Fullerene (C_{60} or C_{70}) shows negligible HFI which in turn suggests increase in spin relaxation time [3,6].

1.2.4. Magnetic anisotropy:

If the energy of a ferromagnet depends on the spatial direction of the magnetic spins, then the system can be considered as magnetically anisotropic. It is known that, the Heisenberg interaction for the magnetic system is isotropic in nature [76]. Hence, in the absence of any other energy term, the magnetization of a ferromagnetic material would vanish without the presence of an applied field. However, in reality, ferromagnetic materials are not isotropic. Further, it should be noted that the magnetic moments inside a material cannot be rotated by any infinitesimal energy. Therefore, the additional energy which is responsible for ferromagnetism at finite temperature arises due to the anisotropy energy. Magnetic anisotropy is the measure of the preferential alignment of spontaneous magnetization in a ferromagnetic material. Hence, along certain specific directions, it is easier to magnetize the material which are known as easy axes (EA). Similarly, the hard axes (HA) represent the directions along which it is harder to magnetize the material due to the requirement of higher energy. It should be noted that the strength of the magnetic anisotropy is usually less in comparison to the exchange energy. However, exchange interaction tries to align the magnetic moments parallel irrespective of its directions. Hence, the orientation of

magnetization in a magnetic material is solely determined by the magnetic anisotropy of the system. Magnetic anisotropy can be divided into four major parts [76]:

- Magnetocrystalline anisotropy: Here, the magnetization orientation is along a specific crystallographic direction. The SO interaction is responsible for this anisotropy contribution.
- Shape anisotropy: In this case, the orientation of magnetization is determined by the shape of the material. The magnetostatic interaction is the origin of this anisotropy.
- Surface anisotropy: For ultrathin ferromagnetic films, the surface contribution of anisotropy dominates over the volume anisotropy as the surface and/or interface exhibits different magnetic properties in comparison to the bulk ones.
- Strain anisotropy: In a few specific cases the magnetization leads to spontaneous deformation and vice-versa, leading to the occurrence of stress induced anisotropy or magnetostriction. Similar to magnetocrystalline anisotropy, the SO interaction is responsible for strain anisotropy.

However, for the work presented in this thesis, magnetocrystalline anisotropy govern the overall anisotropy nature of the systems. Hence, in the following, we have discussed the origin and different components of magnetocrystalline anisotropy in detail.

1.2.4.1. Magnetocrystalline anisotropy:

Magnetocrystalline anisotropy arises due to the SO interaction of the electrons in a magnetic material. Each of the electron orbitals corresponds to a specific crystallographic direction. Hence, due to the interaction between the electron orbitals and the magnetic spins, the spins get aligned to certain crystallographic directions. The direction of magnetization $\mathbf{m} = \frac{\mathbf{M}}{|\mathbf{M}|}$ can be expressed in terms of the direction cosines a_i since $\mathbf{m} = (a_1, a_2, a_3)$ as shown in figure

1.3. Hence,

$$a_1 = \sin\theta\cos\phi, a_2 = \sin\theta\sin\phi, a_3 = \cos\theta \quad (1.7)$$

which fulfils the normalization condition, i.e. $a_1^2 + a_2^2 + a_3^2 = 1$.

The magnetocrystalline anisotropy energy per unit volume can be expressed as a power series expansion of the components of magnetization [76]:

$$E_{crystal} = E_0 + \sum_i b_i a_i + \sum_{ij} b_{ij} a_i a_j + \sum_{ijk} b_{ijk} a_i a_j a_k + \sum_{ijkl} b_{ijkl} a_i a_j a_k a_l + T(a^5) \quad (1.8)$$

where b is the coefficient of the anisotropy energy, and $T(a^5)$ are fifth or higher order in a terms and can be neglected. The energy terms associated with the oppositely magnetized states are equal in magnitude and $E(a_i) = E(-a_i)$. Hence, all odd terms of a_i in equation (1.8) will cancel out leading to:

$$E_{crystal} = E_0 + \sum_{ij} b_{ij} a_i a_j + \sum_{ijkl} b_{ijkl} a_i a_j a_k a_l \quad (1.9)$$

Magnetocrystalline anisotropy in a ferromagnetic system can be broadly subdivided into several parts depending on the crystallographic orientation viz. uniaxial anisotropy, cubic anisotropy, six-fold anisotropy (hexagonal system), etc. However, the major types of anisotropies considered in this thesis are uniaxial and cubic in nature.

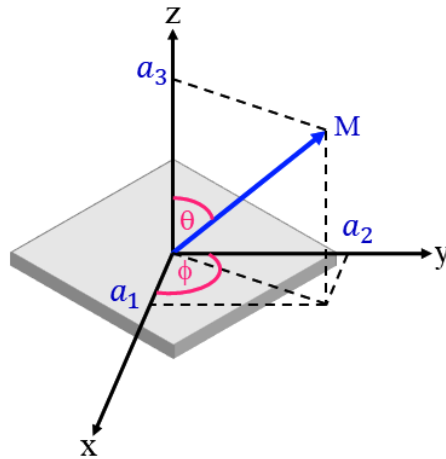


Figure 1.3: Coordinate system showing the direction cosines of the magnetization vector.

1.2.4.1.1. Uniaxial anisotropy: A system governed by uniaxial magnetic anisotropy (UMA) consists of only one specific orientation of EA over 180° interval. Since $E(a_i) = E(-a_i)$, all the cross terms of $a_i a_j$ will cancel out each other, i.e. $b_{ij} = 0$ for $i \neq j$. If the EA is aligned

along the z axis for a system with uniaxial symmetry, the anisotropy energy associated can be expressed as:

$$E_{crystal} = K_a + b_{xx}a_x^2 + b_{yy}a_y^2 = K_a + b_{xx}(a_x^2 + a_y^2), \text{ since } b_{xx} = b_{yy} \quad (1.10)$$

Hence, for uniaxial anisotropy, the energy per unit volume can be represented as $E_{crystal} = b_{xx}\sin^2\theta$, where K_a is the zeroth coefficient and b_{xx} is the uniaxial/two-fold anisotropy constant. The strength of the uniaxial anisotropy (constant) has been denoted by K_2 in this thesis due to its two-fold symmetry over whole 360° .

1.2.4.1.2. Cubic anisotropy: For a system with cubic anisotropy symmetry there are two EA mutually perpendicular to each other over 180° interval. In such situation, the indices $i = 1, 2, 3$, are indistinguishable, hence $b_{xx} = b_{yy} = b_{zz}$. The second term of equation 1.9 can be expressed as: $\sum_{ij} b_{ij}a_i a_j = b_{xx}(a_x^2 + a_y^2 + a_z^2) = b_{xx}$. Similarly, the third term can be expressed as [76]:

$$\sum_{ijkl} b_{ijkl}a_i a_j a_k a_l = b_{xxxx}(a_x^4 + a_y^4 + a_z^4) + 6b_{xxyy}(a_x^2 a_y^2 + a_x^2 a_z^2 + a_y^2 a_z^2) \quad (1.11)$$

Equation 1.9 can be rewritten as (by considering terms up to sixth order): [76]

$$\begin{aligned} E_{crystal}^{cubic} &= E_a + b_{xx} + b_{xxxx}(a_x^4 + a_y^4 + a_z^4) + 6b_{xxyy}(a_x^2 a_y^2 + a_x^2 a_z^2 + a_y^2 a_z^2) + \\ &b_{xxxxxx}(a_x^6 + a_y^6 + a_z^6) + 90b_{xxyyzz}a_x^2 a_y^2 a_z^2 + 15b_{xxxxyy}(a_x^2 a_y^4 + a_x^4 a_y^2 + a_x^2 a_z^4 + a_x^4 a_z^2 + \\ &a_y^2 a_z^4 + a_y^4 a_z^2) \\ \Rightarrow E_{crystal}^{cubic} &= K'_a + K_b(a_x^2 a_y^2 + a_x^2 a_z^2 + a_y^2 a_z^2) + K_c a_x^2 a_y^2 a_z^2 + \dots \end{aligned} \quad (1.12)$$

Where, K'_a , K_b and K_c are the functions of the coefficients b.

Energy associated to [100] ($a_x = 1, a_y = a_z = 0$) is given by: $E_{100} = K'_a$

Energy associated to [110] ($a_x = a_y = \frac{1}{\sqrt{2}}, a_z = 0$) is given by: $E_{110} = K'_a + \frac{1}{4}K_b$.

Energy associated to [111] ($a_x = a_y = a_z = \frac{1}{\sqrt{3}}$) is given by: $E_{111} = K'_a + \frac{1}{3}K_b + \frac{1}{27}K_c$.

Now assuming, $K_b, K_c > 0$, [100] is the easy direction whereas [111] is the hard direction. If the anisotropy is distributed purely over in-plane (xy-plane) so that there is no component of

magnetization along the z-axis, then [100] is the easy direction whereas [110] is the hard direction. Similarly, [010] will also lead to another easy direction since $E_{100} = E_{010}$. The strength of the cubic anisotropy has been denoted as K_4 in this thesis due to its four-fold symmetry over 360° .

1.2.5. Induced magnetic anisotropy:

Except the anisotropy contribution arising from the inherent nature of a system, the anisotropy can also be induced externally by means of different techniques viz. self-shadowing effect due to oblique angle of deposition [77-82], preparation under a magnetic field [83], post-annealing under a field [84], interface effect arising from the bonding between the magnetic film and the substrate [85,86] etc. The aforesaid processes define a specific growth direction in the sample and promotes the induction of uniaxial anisotropy.

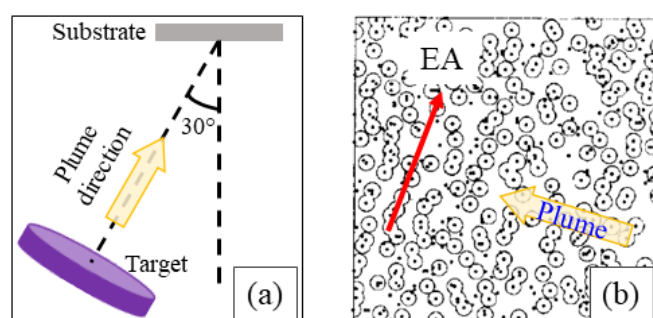


Figure 1.4: (a) Schematic representation of the deposition geometry of our sputtering chamber. (b) Schematic illustration of the self-shadowing process taken from the ref [10] where the plume direction is at 60° and the red arrow corresponds to the easy axis.

Due to the geometry of our deposition chamber all the targets are distributed in such a way that the produced plume points at 30° angle with respect to the substrate normal. Figure 1.4(a) shows the schematic of the deposition geometry. Therefore, uniaxial anisotropy has been induced in all the samples discussed in this thesis due to deposition under oblique incidence. The origin of such oblique deposition induced uniaxial anisotropy is the following: long range dipolar interaction between the grains promotes the induction of the uniaxial

anisotropy. The grains become elongated along the perpendicular to the projection of the in-plane flux direction which defines the preferential direction of the induced anisotropy. Figure 1.4(b) shows a schematic representation of formation of chain like structures due to oblique angular deposition where the incident beam has been 60° from the right-hand side of the image [10]. The magnetization prefers to align along the length of the elongated chains due to the shape anisotropy [10]. Further, due to such columnar growth the grains become tilted towards the deposition direction [87]. Hence, strain anisotropy also contributes to the induced uniaxial anisotropy [78].

1.2.6. Magnetic domains:

The magnetic domains, introduced by P. Weiss [88], are small regions inside a material where all the spins are aligned along a particular direction. However, the direction of the magnetization for the domains need not necessarily be aligned along the EA of the material. In reality, in the absence of any external magnetic field, the spontaneous magnetization of the domains aligns themselves randomly to yield the lowest energy configuration i.e. zero magnetization state. This is the reason why a piece of ferromagnet can appear as non-magnetic at RT in absence of any external field. The region separating two different domains should have a finite width of several hundred of lattice constants since the Heisenberg exchange interaction between the spins forbids an abrupt transition. These finite boundaries separating different domains are namely known as the domain walls (DWs) [89]. Under the influence of anisotropy and exchange energy, all the spins inside the materials should align themselves towards the EA forming a single domain state, since the exchange energy is minimum when the spins are either parallel or anti-parallel to each other. However, the demagnetizing energy associated with a uniformly magnetized single crystal can be larger in comparison to the anisotropy energy. Hence, multiple domains are formed to minimize the demagnetizing as well as the total energy of the system.

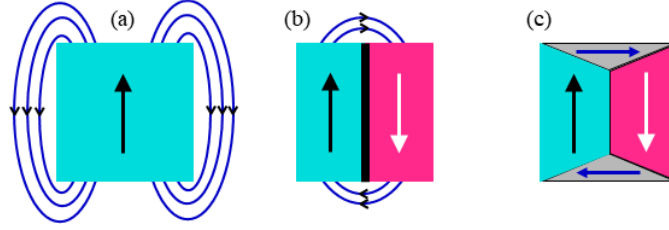


Figure 1.5: (a) to (c) show schematic representation of reduction of the magnetic stray field energy by formation of domains. Different domains are represented in different colors. The flux closure domain known as the Landau pattern is shown in (c) which commonly represents the domain pattern in systems with cubic anisotropy.

It should be further noted that the formation of DWs require a finite energy. Hence, a competition between the stray field and DW formation energy determines the ground state magnetic microstructure of the system. Landau and Lifshitz suggested that the stray field energy of a system can be reduced to zero by flux-closure type domain [90]. Due to Heisenberg exchange interaction, the direction of the magnetic spins inside a DW change continuously to maintain the energy minimization. The exchange energy between two neighboring moments (at an angle ϵ with respect to each other) is given by:

$$E_{exch} = -2JS_1 \cdot S_2 = -2JS^2 \cos\epsilon \quad (1.13)$$

Therefore, the energy required to flip one spin in between two oppositely saturated magnetic states ($\epsilon = \pi$) is $2JS^2$. Now for an ensemble of spins, the total exchange energy distributed among each pair of spins over N lattice spacing is given by:

$$\Delta E_{exch}^{total} = E_{exch} - E_{exch}^{\epsilon=0} = -N \cdot JS^2 \left(\cos \frac{\epsilon}{N} - 1 \right) = -N \cdot JS^2 \left(1 - \frac{\epsilon^2}{N^2} - 1 \right) = \frac{JS^2 \pi^2}{N} \quad (1.14)$$

The higher order terms of $\frac{\epsilon}{N}$ can be neglected due to large value of N . If the lattice constant for the magnetic material is a , then the number of spin rotation inside a DW for bulk is $1/a^2$, which leads to reduction of the exchange energy to:

$$E_{exch}^{Bloch} = \frac{JS^2 \pi^2}{Na^2} \quad (1.15)$$

From equation 1.15, it can be understood that the exchange energy of the walls decreases with increasing N . This in turn leads to gradual rotation of the spins inside the DW leading to increasing width of the wall. However, it should be noted that with increase in wall thickness the anisotropy energy of the system gets enhanced which tends to align the spins along the EA. The anisotropy energy for a DW in bulk can be represented as (by ignoring higher order terms) [12]:

$$E_{ani}^{Bloch} = \sum_{i=1}^N K \sin^2 \epsilon_i \cong \frac{NKa}{2} \quad (1.16)$$

Hence, a competition between the anisotropy and exchange energies, expressed by equations 1.15 and 1.16, leads to stabilization of the width of the DW. In this case, the total energy is represented as [12]:

$$E^{BW} = \frac{JS^2\pi^2}{Na^2} + \frac{NKa}{2} \quad (1.17)$$

The first term in equation 1.17 favours a large number of N whereas the second term favours small N . The energy minimum can be determined by putting the first derivative of equation 1.17 to zero, which yields $N = \pi S \sqrt{\frac{2J}{a^3K}}$. The DW width (δ) can be expressed as [12]:

$$\delta = Na = \pi \sqrt{A/K} \quad (1.18)$$

where, $A = \frac{2JS^2}{a}$.

There are two major types of magnetic DWs namely Bloch and Néel wall (figure 1.6). In a Bloch wall [91] (figure 1.6(a)) the spin rotation inside the DW occurs in out-of-plane direction where the moments inside the wall are oriented parallel to the wall. Inside a Bloch wall the total magnetic charge is zero due to normal components of magnetization in both side of the wall being same. However, accumulation of magnetic charges will occur on the surface leading to strong demagnetizing field across the sample surface. Therefore, the

occurrence of Bloch walls is usually expected in bulk ferromagnetic materials or in thick films.

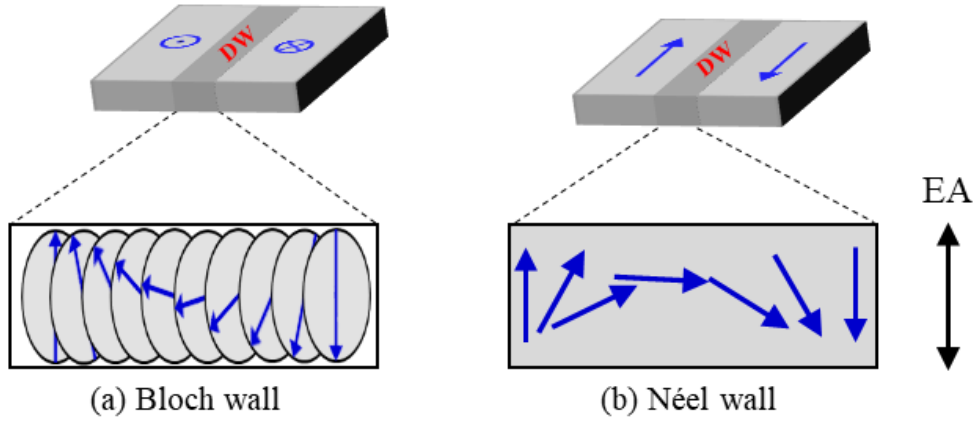


Figure 1.6: Schematic representation of (a) Bloch wall and (b) Néel wall showing the out-of-plane and in-plane spin rotations, respectively.

However, formation of the Bloch walls becomes energetically unfavored for ultrathin films as the thickness of the film becomes comparable to the width of the wall. In such cases, Néel wall [92] (figure 1.6(b)) is formed where the spin rotates in the in-plane direction. Here, the magnetization inside the wall rotates perpendicular to the wall. For Néel wall the demagnetization energy caused by the surface magnetic charges is less in comparison to that in the Bloch walls. The width of the Bloch and Néel walls can be written as [12]:

$$\delta_{Bloch} = \pi \sqrt{A/K}, \text{ and } \delta_{Néel} = \pi \sqrt{\frac{2A}{\mu_0 M_s^2}}, \text{ where } A = \frac{2JS^2}{a}.$$

It should be noted that the work presented in this thesis mostly focuses on the formation and propagation of the Néel walls.

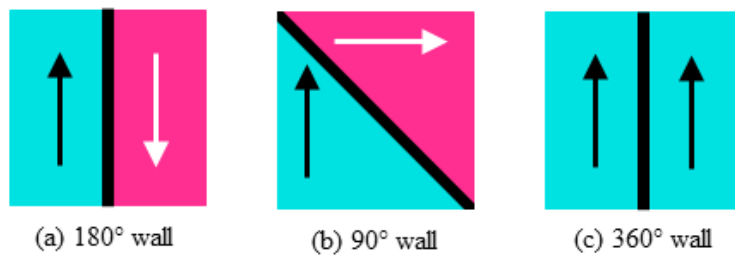


Figure 1.7: Schematic diagram for (a) 180°, (b) 90°, and (c) 360° DWs.

Further, depending on the orientation of magnetization between two neighboring domains, the DWs can be classified into different types e.g. 90°, 180°, 360° DWs etc. The schematics of such DWs are depicted in figure 1.7 (a) – (c). Systems with uniaxial anisotropy usually leads to formation of 180° DW motion [82,93] (figure 1.7(a)) during the magnetization reversal. The systems having cubic anisotropy exhibits 90° DWs [17] (figure 1.7(b)) since the easy direction of magnetizations are 90° away from each other. Therefore, under the application of external magnetic field, the magnetization reversal from positive to negative direction happens via two 90° DW motions. However, for a very few specific cases, 360° DWs [94] (figure 1.7(c)) are observed. Apart from these, 109°, 71° DWs etc. also exist which are observed in specific conditions in materials like fcc-Ni, BiFeO₃, etc.[95,96] The samples discussed in this thesis exhibits both 180° and 90° DWs depending on the anisotropy symmetry present in the samples.

1.2.7. Magnetization reversal:

Magnetization reversal (switching) is a phenomenon where the spontaneous magnetization of a ferromagnet reverses (switches) from one saturated state to another under the presence of an external magnetic field. Under the application of an external magnetic field, a torque ($\boldsymbol{\tau} = \boldsymbol{M} \times \boldsymbol{H}$) acts on the magnetic spins and the later changes its configuration to minimize the total energy of the system. The magnetization reversal phenomenon can be broadly subdivided into two major parts: coherent rotation (all the spins rotating together from one saturation to the other) and DW motion (aligning of magnetization from one state to another by movement of the DWs). The reversal process depends on the initial distribution of magnetization (the history) in the sample. Further, it should be noted that the reversal phenomenon strongly depends on the speed of reversal field. For example, if magnetic pulses shorter than 10^{-9} s are applied, the precessional motion of the magnetization becomes

dominant. The subsequent discussion is focused on the quasistatic magnetization reversal occurring under the influence of slowly changing applied field.

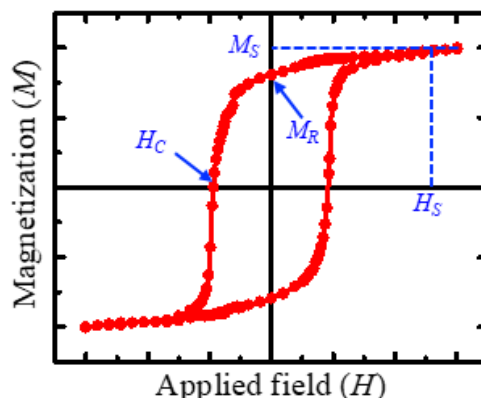


Figure 1.8: Hysteresis loop showing the typical magnetization (M) behavior as a function of the applied field (H) in a ferromagnet.

Since, the magnetization of a ferromagnetic sample does not follow the change in applied field linearly, this gives rise to the hysteresis loop. Hysteresis is a nonlinear, non-equilibrium, complex first order phase transition [97]. Further complexity in the loop arises due to the effect of local microstructure, structural, and morphological defects, etc. in the system [98]. A typical hysteresis loop in a ferromagnetic sample is depicted in figure 1.8. When a sufficiently large external magnetic field is applied, all the spins inside a system align towards the applied field direction. This state is called magnetic saturation state. Magnetization of the system in this state is called the saturation magnetization (M_S) and the required field is called saturation field (H_S). Starting from this state, by reducing the applied field to zero remanent (M_R) state can be obtained with non-zero magnetization. The coercive field (H_C) is the required reverse magnetic field to reduce the magnetization of the system to zero. The positions of M_R , M_S , H_C , and H_S for a typical hysteresis loop during the magnetization reversal are shown in figure 1.8. The hardness of a magnetic material is measured by the required saturation field of that system. The squareness of the hysteresis

loop is defined as $S = \frac{M_R}{M_S}$. In an ideal ferromagnetic system, S should be either 1 and 0 along the EA and HA, respectively. In the following we discuss the processes involved in the magnetization reversal phenomena:

1.2.7.1. Domain wall motion:

In ferromagnetic substances, domain formation occurs to reduce the magnetic stray field energy of the system. Further, domain nucleation can occur from the defects or imperfections present in the real system [99]. In such systems, the magnetization reversal mechanism takes place via propagation of the domain walls, known as domain wall (DW) motion. The process of DW motion can be both reversible and irreversible depending on the magnitude of the external magnetic field. At small applied external field, the DWs can move a small distance and come back to its initial position upon removal of the field. This is known as reversible displacement which corresponds to the initial curved part of a typical hysteresis loop (figure 1.8). In this region the DWs are pinned by the structural inhomogeneity (energy barrier) present in the sample. This expansion of the DWs, known as the DW relaxation, is similar to the stretching of elastic membrane [100]. The reversible expansion of the DWs can often turn irreversible if the wall shape as well as position is deformed sufficiently under the high applied field. This can also happen due to the depinning of the DWs from defects. Application of higher magnetic fields helps in overcoming the anisotropy of the system and the magnetization rotates from one saturation to the next crystallographic EA. At further high magnetic field the process is collective rotation of the domains towards the applied field direction, irrespective of that being along the EA or HA of the system. However, this requires sufficient energy to overcome the pinning potential. This can be observed as small discontinuous jumps in the hysteresis loop which is known as the Barkhausen effect. The Barkhausen jumps in the loop occur when the DW proceeds from one local minima to the other of the potential [101,102].

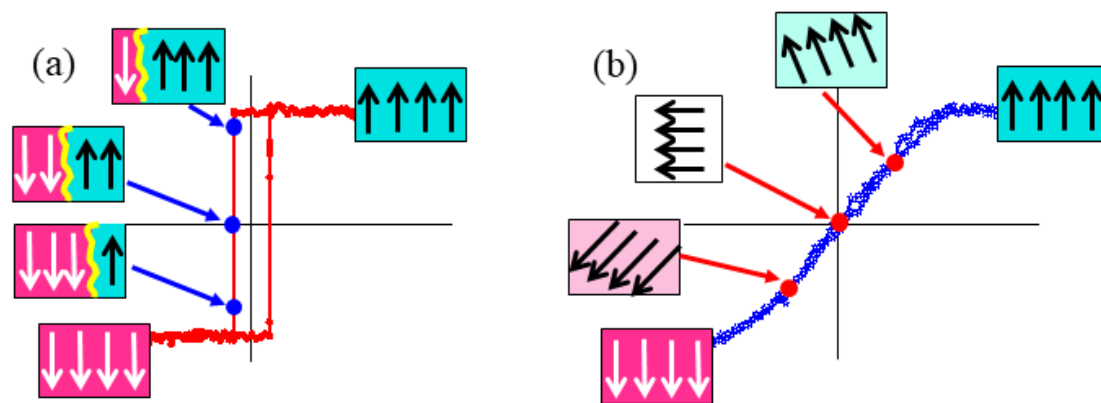


Figure 1.9: Schematic representation of the magnetization reversal process via (a) DW motion along EA and (b) coherent rotation along HA.

Figure 1.9(a) shows a schematic representation of the steps of a magnetization reversal phenomenon via DW motion. When sufficiently large positive magnetic field is applied to a demagnetized sample, all the spins point towards the applied field direction resulting in a single domain state known as positive saturation state. While decreasing the applied field, some amount of spins gets switched to opposite direction by nucleation of a reverse domain state. In the schematic (figure 1.9(a)) the yellow line corresponds to the 180° DW between two domains. By further increasing the field in reverse direction more spins get reversed by enlarging the area of the negative domain state i.e. by shifting the position of the DW. Therefore, the magnetization reversal from the positive to negative saturation occurs via repositioning of the DW throughout the sample. In reality domains can nucleate from different positions of a sample. Eventually they grow via DW motion and finally merge with each other to form the negative saturation domain state. More details regarding the magnetization reversal via DW motion have been discussed in the results section to explain the reversal mechanism of different thin films (Fe, Co etc.).

1.2.7.2. Coherent rotation:

Coherent rotation describes the magnetization reversal of a single domain nanoelement [103]. However, this can be also extended to understand the magnetization reversal of the thin films

typically around the HA where the spins rotate coherently to complete the reversal. When the dimension of a ferromagnetic particle/entity is reduced to low value, the energy required for DW formation becomes significantly high leading to alignment of all the atomic moments in one specific direction. In such a scenario, the exchange energy of the system will be minimum due to the parallel orientation of the atomic spins. Hence, the magnetic free energy under application of magnetic field can be written as the sum of Zeeman and anisotropy energy:

$$E = K\sin^2\theta - \mu_0HM_S\cos(\phi - \theta) \quad (1.19)$$

where, the orientation of θ and ϕ with respect to H , M , the EA is depicted in figure 1.10. The equilibrium of magnetization can be derived by minimizing equation 1.19 with respect to θ . The saturation field along the HA ($\phi = 90^\circ$) can be obtained by minimizing E (equation 1.19) with respect to θ . By taking $\partial E / \partial \theta = 0$, we obtain,

$$2K\sin\theta\cos\theta - \mu_0HM_S\sin(\phi - \theta) = 0 \quad (1.20)$$

The condition for stable equilibrium needs $\partial^2 E / \partial \theta^2 > 0$. Solving equation (1.20) for the HA ($\phi = 90^\circ$) the expression for the anisotropy field (H_K) can be obtained as:

$$H_K = \frac{2K}{\mu_0M_S} \quad (1.21)$$

Hence, for the EA ($\phi = 0^\circ$), when a field is applied along the reverse direction, the orientation of magnetization remains unaffected until the magnitude of the field is equal to H_K . Along the EA, if the field is further applied along $\phi = 180^\circ$, there is essentially no change in torque on M_S . However, in presence of the external field, the magnetization will become unstable at $\phi = 0^\circ$ and flip over to $\phi = 180^\circ$. Further, when the applied field is at an angle away from the EA ($0^\circ < \phi < 90^\circ$), the magnetization reversal initially occurs by reversible rotation of the spins. This aligns the spins away from the applied field direction by aligning them towards the EA. Along the HA ($\phi = 90^\circ$), when the field is applied in the reverse direction, all the

atomic spins rotate coherently which leads to the formation of ‘S’ shaped hysteresis loop (figure 1.9(b)). In such cases, all the spins rotate parallelly (always in a single domain state) from the positive to negative saturation state with respect to the change in the applied field direction. A schematic representation of coherent rotation process in a thin film along the HA has been depicted in figure 1.9(b).

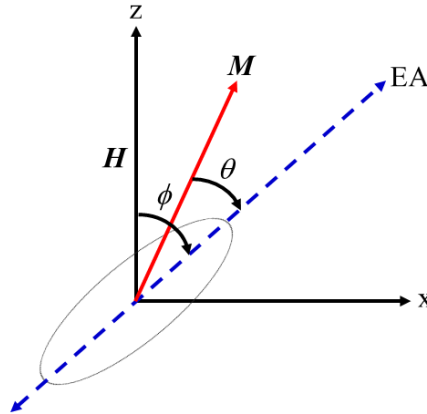


Figure 1.10: Schematic of the coordinate system to understand the coherent rotation process known as Stoner Wohlfarth model.

Hence it should be noted that in thin films the magnetization reversal occurs both via coherent rotation of the spins as well as DW motion. In a few cases, the magnetic switching occurs via partial rotation of spins followed by the DW motion depending on the pinning energy landscape of the system.

1.2.8. Magnetization dynamics:

The dynamic properties of a magnetic system can be expressed in terms of Landau-Lifshitz-Gilbert (LLG) equation. Followings are the details behind the formulation of the LLG equation: let us consider an electron is moving in a circular loop with radius r . Current i will be generated in the reverse direction of the electron motion in the loop. The magnetic moment of an electron in such condition can be expressed as: $\mu = iA$, where, A is the area of

the circular loop. Now, the angular momentum of the electron is $\mathbf{L} = m_e \mathbf{v} \times \mathbf{r}$, where m_e is the mass of an electron. Therefore, the magnetic moment of the electron can be written as:

$$\boldsymbol{\mu} = i\mathbf{A} = -\frac{e}{t}\mathbf{A} = -\frac{e\mathbf{v}}{2\pi r} \times \pi r^2 = -\frac{e\mathbf{v} \times \mathbf{r}}{2} = -\frac{e}{2m_e}\mathbf{L} = -\gamma\mathbf{L} \quad (1.22)$$

where, $\gamma = \frac{e}{2m_e}$ is the Gyromagnetic ratio. Differentiating eq. 1.22, we can obtain,

$$-\frac{1}{\gamma} \frac{d\boldsymbol{\mu}}{dt} = \frac{d\mathbf{L}}{dt} = \boldsymbol{\tau}$$

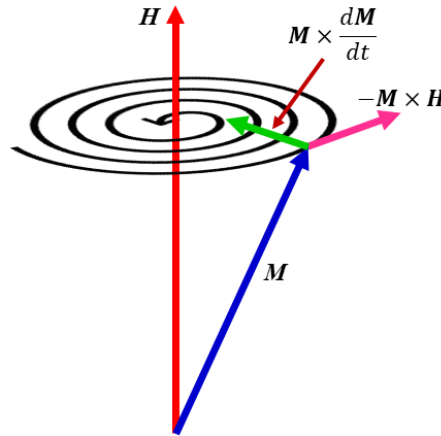


Figure 1.11: Schematic representation of the precessional motion of magnetization (\mathbf{M}) along with a damping factor around the applied field (\mathbf{H}) direction.

If an electron is placed under a magnetic field (\mathbf{H}), then the torque ($\boldsymbol{\tau}$) experienced by the electron can be expressed as: $-\frac{1}{\gamma} \frac{d\boldsymbol{\mu}}{dt} = \boldsymbol{\mu} \times \mathbf{H}$. This is the equation of motion for an electron flowing through a loop. In this scenario, the magnetic moment ($\boldsymbol{\mu}$) starts precessing around \mathbf{H} by forming a cone. Now, the total magnetic moment of a ferromagnetic material having N atomic spins can be written as: $\mathbf{M} = N\boldsymbol{\mu}$. Hence, the equation of motion for a ferromagnetic material is represented as:

$$\frac{d\boldsymbol{\mu}}{dt} = -\gamma(\mathbf{M} \times \mathbf{H}) \quad (1.23)$$

It should be noted that the precessional motion of equation 1.23 does not depend on the angle between \mathbf{M} and \mathbf{H} , which further indicates infinite motion of the moment. This term was

predicted by Landau and Lifshitz, which represents damp free motion of the electrons [90]. However, this is not true in reality as the magnetic moment eventually damps towards the applied field direction. Figure 1.11 shows the precession of magnetization around the applied field direction. Gilbert introduced the damping term in the system which is represented by $\tau_D = \frac{\alpha}{M_S} (\mathbf{M} \times \frac{d\mathbf{M}}{dt})$, where α is a positive damping parameter [104]. Hence the final form of the LLG equation becomes:

$$\frac{d\mathbf{M}}{dt} = -\gamma(\mathbf{M} \times \mathbf{H}) + \frac{\alpha}{M_S} (\mathbf{M} \times \frac{d\mathbf{M}}{dt}) \quad (1.24)$$

The damping constant α can be determined using ferromagnetic resonance measurement and are discussed further in chapter 5 and 6 of the thesis.

1.2.9. Inverted thin films:

In general, the anisotropy field (H_K) of a sample having uniaxial anisotropy is more than the coercivity (H_C) along the easy axis. If, the reverse scenario is observed in a sample i.e. H_K becomes less or comparable to H_C , then such sample is known as the inverted thin film [105]. This may happen due to the presence of randomness in the system due to grain size, misalignment of local easy axis etc. The presence of local dispersion in the anisotropy symmetry is the cause of inverted nature of the loops. The dispersion in anisotropy can arise due to inhomogeneous strain between crystallites [106], different grain sizes [107], and insufficient magnetic field during deposition etc. [108] Formation of ripple and labyrinth domains are the characteristics of inverted thin film. More details about inverted thin films are discussed in chapter 3 and chapter 7 for Co thin films prepared on MgO (001) substrates. The magnetization reversal mechanism for such inverted thin films are detailed in the aforesaid chapters.

1.2.10. Organic Semiconductors:

Organic materials are mostly composed of Carbon and Hydrogen though other elements may also be present. It has been found that the elements of the organic compound share different kind of bonds between them. Carbon is the perfect example to show the need for hybrid orbitals. The electronic configuration of carbon atom in the ground state is $1s^2 2s^2 2p^2$. The carbon atom can bond with other elements of an organic compound through covalent bonds. The formation of such covalent bonds and their arrangement in space significantly regulates the property of the material. The hybridization of orbitals is also favored as the energy of the hybridized orbitals are lower in comparison to their separated un-hybridized counterparts [109]. Various types of hybridizations are discussed in the following sub-section:

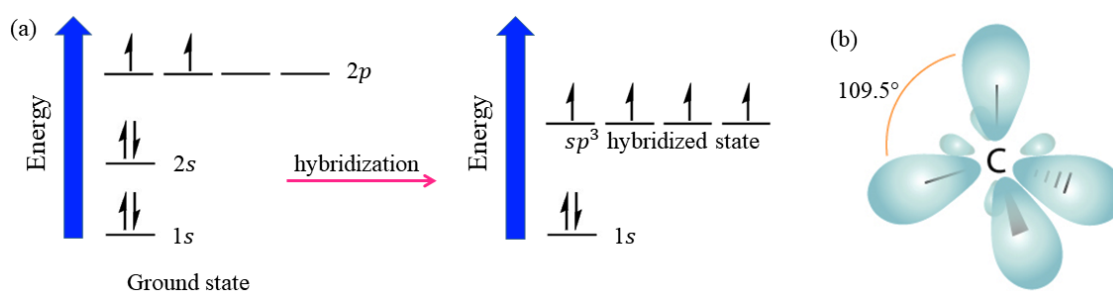


Figure 1.12: (a) Schematic for the energy diagram of carbon ground state and sp^3 hybridized state. (b) A cartoon showing the sp^3 hybridized carbon in Methane structure [110].

1.2.10.1. sp^3 hybridization: According to this form of hybridization, the 2s orbital and all three 2p orbitals hybridize to form four sp orbitals (figure 1.12(a)). Each of these four hybridized orbitals comprises 25% s and 75% p characteristics. Figure 1.12(b) shows the sp^3 hybridized geometry for Methane where the frontal lobes align themselves in a tetragonal manner to minimize the electron repulsion [109,111].

1.2.10.2. sp^2 hybridization: Here, the 2s orbital and two of the 2p orbitals hybridize to form three sp orbitals (figure 1.13(a)). Each of the sp orbitals consists of 67% p and 33% s

character. The frontal lobes align themselves in trigonal planar structure where they point along the corners of a triangle in order to minimize electron repulsion (figure 1.13(b)). The remaining p orbital remains unchanged and is perpendicular to the plane of the three sp^2 hybridized orbitals [109,111].

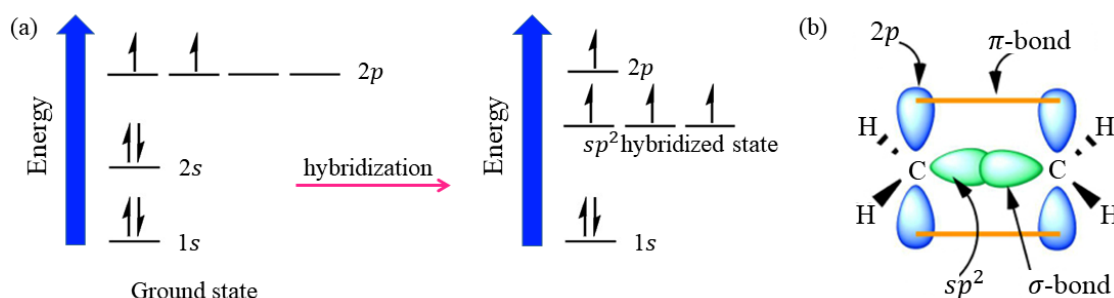


Figure 1.13: (a) Schematic for the energy diagram of carbon ground state and sp^2 hybridized state. (b) A cartoon showing the sp^2 hybridized carbon in Ethene structure [110].

1.2.10.3. sp hybridization: This can explain the linear structure of molecules. Here, the 2s orbital and one of the 2p orbitals hybridize to form two sp orbitals (figure 1.14(a)). Each of them comprises of 50% s and 50% p character. The front lobes face away from each other to form a straight line with a 180° angle between the two orbitals (figure 1.14(b)). The electron repulsion is minimum in this configuration. As only one p orbital participate in the hybridization, two unaltered 2p orbitals are left. These p orbitals are at right angles to each other and to the line formed by the two sp orbitals [109,111].

Depending on the hybridization present in the compound, carbon can form three types of bonds: single, double, and triple bonds. The single bond is the σ -bond formed by two sp^3 hybridized electrons. The bonding energy of σ -bond is large and the electrons in σ -bond are strongly localized. The double bond consists of two carbon-carbon bonds namely σ -bond and π -bond. The σ -bond is formed by two sp^2 hybridized electrons and are strongly localized. The π -bond perpendicular to the plane is formed by two neighboring p_z orbital electrons. The

characteristics of the electrons associated to p_z orbital is different from the sp^2 or sp^3 hybridized electrons. Further, the p_z orbital electron is weakly bonded (delocalized) to the carbon nuclei and the bonding energy of π -bond is relatively smaller in comparison to that of the σ -bond. Similarly, for the triple bond one σ -bond and two π -bonds are present. Similar to the double bond, σ -bond electrons are localized and π -bond electrons are delocalized. The movement of electrons within organic materials is dependent on the delocalization of the electrons in the covalent chemical bonds. For example, if all carbon atoms are connected by σ -bonds, which means that all the electrons in the covalent bonds are strongly localized, the material will behave as an insulator [70].

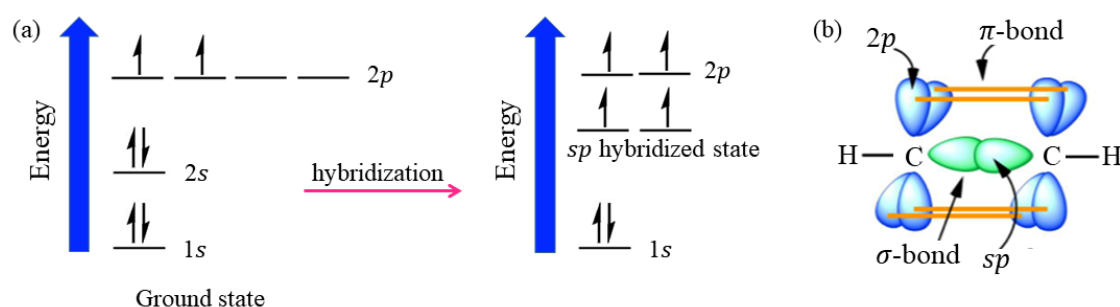


Figure 1.14: (a) Schematic for the energy diagram of carbon ground state and sp hybridized state. (b) A cartoon showing the sp hybridized carbon in Ethyne structure [110].

For organic semiconductors (OSCs), the electric conductivity arises from the π -conjugated electrons where single bond and double bonds are formed alternatively. In the π -conjugated OSC chains, two neighboring carbon atoms will share bonds (σ -bond) and another σ -bond will be formed with hydrogen (mostly). The fourth electron will form the π -bond (and π^* anti-bond) with the p_z orbital. Because of the electron-electron repulsion (Hubbard interaction) and electron-phonon interaction, the π -bond molecular orbital is completely filled, while the π^* -bond molecular orbital is completely empty. In a molecule the number of π -molecular orbitals increases with increase in the formation of π -bonds and the energy band

(π -band and π^* -band) starts to form [111]. The highest orbital of the filled π -band is called the highest occupied molecular orbital (HOMO), and the lowest orbital of the empty π -band is called the lowest unoccupied molecular orbital (LUMO). HOMO and LUMO in OSCs are analogous to the valence and conduction bands in inorganic semiconductors, respectively. In general, the band gap is in the order of 1.5-3.5 eV. This energy is relatively easy to overcome in π -conjugated OSCs. In this thesis, C₆₀ has been considered as the OSC with a band gap of ~1.8 eV at RT[112,113].

1.2.11. Ferromagnet/Organic semiconductor interface: 'SPINTERFACE':

One of the key topics in the organic spintronics is the study of spin injection from FM to OSC. When in contact to each other, the unpaired electrons from 3d orbitals (for the conventional FM materials namely Fe, Co and Ni) can be coupled to the OSC molecular orbitals through *p-d* hybridization [7,8,114]. It is possible to obtain a large interfacial spin polarization via hybridization effects by formation of 'spinterface' [5]. Usually charge transfer occurs from the FM to OSC at the interface by formation of covalent bonds [115]. This phenomenon involves the frontier orbitals of the OSC and the valence band states of the FM metal. Such chemisorption may result in large interfacial magnetoresistance effect [49,52]. Sanvito *et al.* have shown that the DOS of the OSC modifies strongly when in contact with a FM material. Figure 1.15 shows a schematic of modified DOS of the OSC when brought in contact with a FM material. The DOS of the OSC at the Fermi level may get broadened (figure 1.15(b)) or shifted (figure 1.15(c)) depending on the way OSC molecule sits on top of the FM material i.e. the types of bonds are shared[5]. However, the microscopic mechanism governing the spin transport at the FM/OSC interface is still ill understood. Moreover, the reverse effect i.e. the effect of such hybridized spinterfaces on the FM material has not been studied systematically so far.

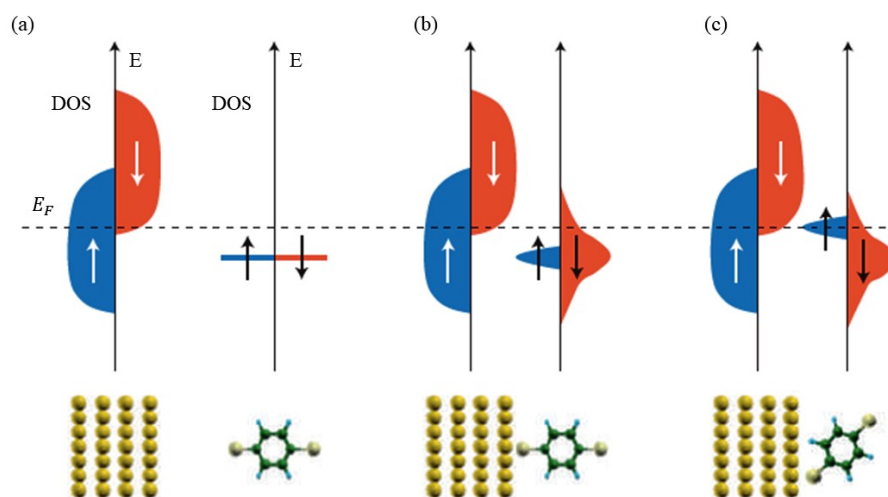


Figure 1.15: Schematic diagram to show the effect of orbital hybridization on the density of states (DOS) of the organic molecules. (a) DOS for the ferromagnet and organic semiconductor when they are separated from each other. (b) and (c) show the DOS for the same when they are brought close enough to participate in the orbital hybridization. This figure has been taken from the ref [5].

1.2.12. State-of-art of spinterfaces:

After the discovery of the spinterface [5,28], immense research interest has been grown to understand the unusual properties at the FM/OSC interfaces. The formation of spinterface is not only helpful for the spin transferring from one FM electrode to another through OSC, but also interesting for fundamental magnetization studies. The spurious MR behaviors observed earlier for FM/OSC/FM spin valves has been understood using the concept of spinterface [26,27]. Theoretical calculation predicts that the DOS of an OSC molecule can get modified when deposited next to a FM layer either by broadening or shifting of the DOS [5,55]. It has been observed that magnetic moment can be induced in C_{60} for Co/ C_{60} and Fe/ C_{60} heterostructures [6-8]. Further, suppression of ferromagnetic moment has also been observed in these multilayers. The hybridization between the p and d orbitals of OSC and FM layers, respectively, is the reason behind the spin transfer from FM to OSC. The strength of

hybridization depends significantly on the adsorption geometry of C_{60} w.r.t. the crystallographic orientation of the FM film [56-58]. Such hybridization leads to modification of the anisotropy of the systems by altering the shape of the orbitals [18,61]. Recently, it has been found that it is possible to alter the electronic state of non-ferromagnetic materials (Sc, Mn, Cu, Pt etc.) and create ferromagnetism at RT when in contact with organic materials [62-64]. However, the effect of spinterface on the magnetization reversal mechanism and the domain structure has not been studied so far. Also, the dependence of the spinterface properties on the crystallinity of the system is still unknown. Further, the effect of hybridization on the global anisotropy symmetry of the systems is not explored so far. Therefore, understanding the interfacial properties at FM/OSC heterostructures will lead to a step forward in unfolding the mysteries associated to the spinterfaces.

Chapter 2: Experimental Techniques

In this chapter, the details of the experimental techniques utilized to prepare the samples and characterize their structural as well as the magnetic properties are discussed. The Fe and Co thin films have been prepared on either MgO (001) or oxidised Si (100) substrates using dc magnetron sputtering technique. Bilayer or tri-layer of Fe/C₆₀ and Co/C₆₀ samples have also been prepared where the C₆₀ layer was deposited using thermal evaporation technique. The topography of the films has been studied using atomic force microscopy (AFM). The structural parameters like the crystallinity, thickness, roughness etc. of the samples have been obtained from the x-ray diffraction (XRD) and x-ray reflectivity (XRR) measurements. For a few Fe/C₆₀ bilayer samples, secondary ion mass spectroscopy (SIMS) has been performed to investigate the structural quality of the interfaces. The SIMS measurements have been performed via a collaboration with Dr. Manas K. Dalai at National Physical Laboratory (NPL), New Delhi. The magnetization and magnetic moments of the samples have been probed using superconducting quantum interference device (SQUID). Simultaneous domain imaging along with the hysteresis measurement of all the samples have been performed by state-of-the-art Kerr microscopy. The layer dependent magnetic properties and the interfacial magnetic moments have been obtained from the polarized neutron reflectivity (PNR) measurement performed at the large scale facilities at MARIA, and NREX reflectometers at MLZ, Garching, Germany. The anisotropy constants of the samples and the dynamic magnetic properties like the damping constant have been measured using ferromagnetic resonance (FMR) technique.

2.1. Physical vapor deposition:

A cumulative set of processes fall under physical vapor deposition (PVD) techniques that are used to deposit thin coating of materials typically in the range of several angstroms to a few

microns. It is an environment friendly (does not deal with chemical reactions and toxic substances like fluid precursors, acids etc.) process involving three steps:

- (i) Vaporization of the target material from the solid state stimulated by high temperature or gaseous plasma.
- (ii) Transportation of that vapor to the substrate through high vacuum.
- (iii) Condensation of the vapor at the substrate and formation of thin film.

There are a few types of deposition processes involved within PVD techniques namely cathodic arc deposition [116], e-beam evaporation [117], evaporative or thermal deposition [118], pulsed laser deposition [119], sputtering [118], pulsed electron deposition [120], sublimation sandwich method, [118] etc. Among these aforementioned techniques sputtering and thermal evaporation are two most popular methods. The samples discussed in this thesis are prepared by either sputtering or thermal evaporation method. The techniques are illustrated below in detail.

2.1.1. Sputtering:

Sputtering is very popular due to its advantage in producing large area samples with high uniformity and ability to deposit both conductive and insulating materials. In this process, a gaseous plasma of a typically inert gas is formed to bombard on the target material inside a vacuum chamber. As a result, the target materials get ejected and eventually deposited on the objects present within its line of sight [121,122]. In our deposition chamber Ar is used as the inert gas to create the plasma. By applying sufficient negative bias voltage to the target, ionization of the Ar gas is achieved. Therefore, the target acts as a cathode and the positively charged Ar^+ ions are accelerated towards it. Further, the Ar^+ transfer its momentum to the target particles due to both elastic and inelastic collision. The target atoms then fly out from the target surface with the transferred momentum and get deposited on the substrate if it is mounted within the line of sight of the ejected target atoms. The secondary electrons

produced by the ionization of the Ar gas bombards with the neutral Ar atoms and help in producing denser plasma of Ar^+ . A schematic of the sputtering process is shown in figure 2.1.

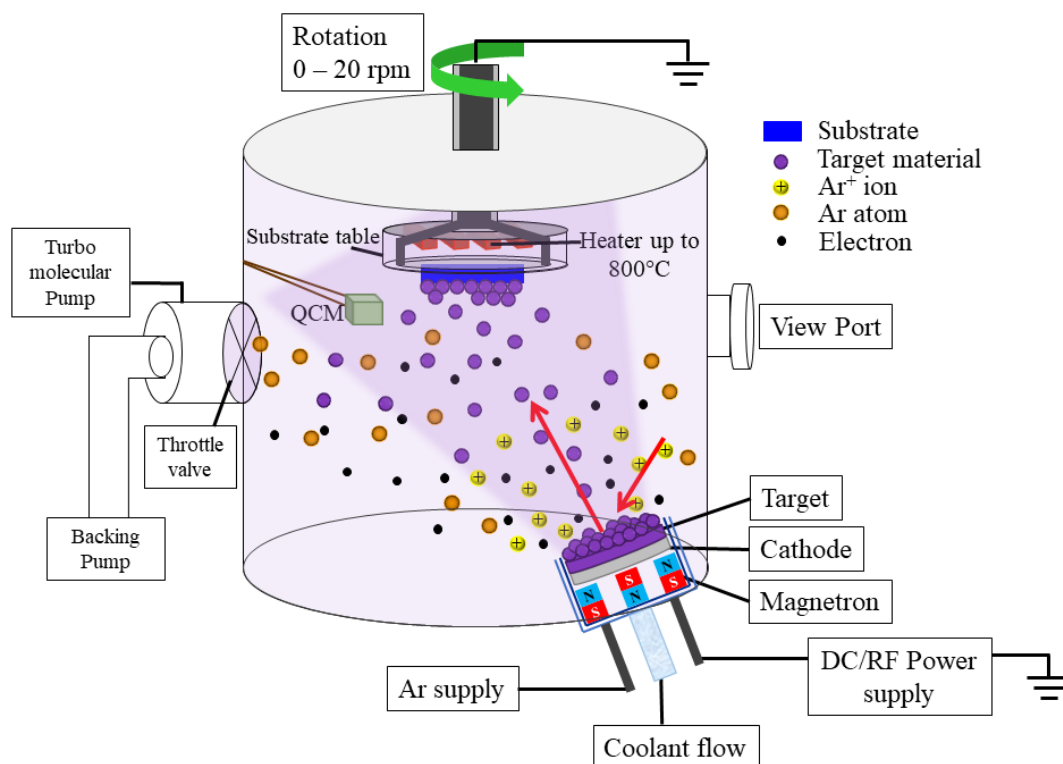


Figure 2.1: A schematic representation of the sputtering process where the vacuum components required for this process are also depicted. The light violet solid cone inside the vacuum chamber represents the plasma. Different atoms involved in this process are shown with different colored balls and labeled in the image. A few extra facilities available in our deposition chamber viz. substrate heating, rotation, thickness monitor (QCM), pressure controlling throttle valve, etc. are also shown in the image.

To obtain higher deposition rates in this process a very high pressure of Ar is required which is unacceptable in an ultrahigh vacuum chamber. To overcome this problem, magnetron sputtering technique is introduced where a permanent magnet is installed just below the target. The geometry of the magnet is designed in such a way that one pole of the magnet (N) remains just below the center of the target and the opposite pole (S) is formed at the radius of the target (see the magnet geometry in figure 2.1). As the electric field is applied

perpendicular to the magnet, the electrons present near the target experience the magnetic field. It is known that due to the Lorentz force, the path of an electron becomes helical in presence of a magnetic field. Therefore, the electrons become trapped within the vicinity of the target resulting denser plasma with high deposition rate but with less Ar pressure. This also overcomes another issue of electron bombardment at the substrate as they are trapped near the target. Here the magnet used to trap the electrons is a balanced magnet having equal strength of the poles and thus canceling the field lines from each other. However, with a balanced magnetron sputtering plasma is created only in the vicinity of the target. To obtain greater vicinity even up to the substrate, an unbalanced magnet can be used with different strength of the central and radial poles. If the strength of the radial poles is greater than that of the central one, the uncompensated field lines extend towards the substrate. As a result, the yield becomes more near the substrate [123].

There are two types of the sputtering process to deposit materials having different conductivities such as (i) dc sputtering and (ii) rf sputtering [124].

(i) Dc sputtering: In this technique direct current (dc) is applied to the target to produce the negative bias. The Ar^+ ions are attracted towards the target and get neutralized after the bombardment by transferring its momentum to the target. If the target is conducting in nature, the negative bias is evenly distributed throughout the target and Ar^+ ions get neutralized by transferring its charge at the target surface. However, for insulating target the negative voltage cannot be distributed over the whole target. Consequently, the positively charged Ar ions get accumulated over the target resulting the plasma extinguishment. Therefore, dc sputtering cannot be used to deposit insulating materials [124].

(ii) Rf sputtering: Radio frequency (rf) sputtering is the technique where the electrical potential of the current is alternated at radio frequencies to avoid the charge

accumulation problem occurred in dielectric materials. A radio frequency of 13.56 MHz is used internationally for rf power supply equipment. There are two halves in each cycle of the rf sputtering. In the negative cycle, Ar^+ ions get bombarded to the target material and the target particle gets ejected resulting in deposition on the substrate. Eventually positive charges build up on the target surface. In the positive cycle, the electrons are attracted towards the surface and bombarded on the target surface by neutralizing the accumulated positive charge of the opposite cycle. In this way the surface of the target material can be cleaned and free of charge accumulation problem. Rf sputtering can be used to deposit both the conductive as well as dielectric materials. However, the rate of deposition in rf sputtering is less in comparison to the dc sputtering as the deposition occurs only during one half of the full cycle [125]. Another drawback of this technique is much higher voltage is required to achieve similar deposition results as compared to direct current which results in overheating issues. Therefore, adequate cooling facility and advanced circuitry is necessary to overcome the additional overheating problem [124].

2.1.2. Thermal evaporation

Thermal evaporation is a quite popular PVD technique due its simplicity. Using this method thin films can be deposited simply by heating the target material above its evaporation point. The advantage of this method is almost every type of materials such as metals, non-metals, oxides, nitrides, even organic compounds can be used to prepare thin films [126]. A pair of high current vacuum feed-through are employed to flow large current (~ 200 A) through a narrow sheet of refractory materials like molybdenum, tungsten etc. This narrow sheet, known as the thermal boat, gets hotter due to joule heating and the material kept in the boat starts melting. Eventually the material starts evaporating from the thermal boat and the vapor of the material travels through high vacuum to the substrate. Increase in the current leads to

higher rate of deposition. Finally, the material vapor condenses at the substrate by formation of thin film [125].

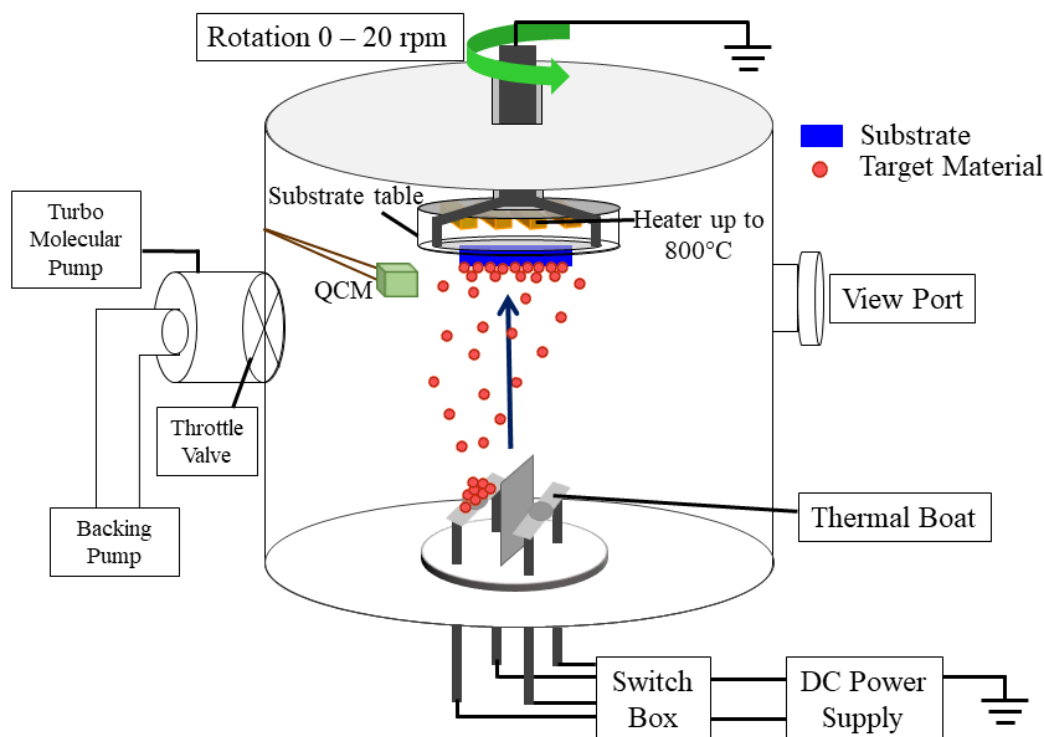


Figure 2.2: A schematic representation of the thermal evaporation process where the vacuum components required for this process are also depicted. The atoms involved in this process are shown with different colored balls and labeled in the image. The design of the chamber has been kept the same as the sputtering process as both the techniques are present inside the same chamber in our deposition unit.

A schematic diagram showing the thermal evaporation technique is depicted in figure 2.2. It is necessary to have high vacuum during the process because the mean free path of the vaporized material needs to be long enough to get deposited on the substrate. The mean free path of a particle is the length which can be travelled without having a collision. If the vacuum is low, the probability of collision of a particle becomes larger due to the existence of many gases in high pressure range. In this case, the probability of the material vapor reaching the substrate becomes less. Therefore, one of the necessary conditions for thermal

evaporation is the vacuum inside the deposition chamber needs to be high enough so that the mean free path of the vapor material becomes more than the distance between the thermal boat and the substrate. As the material is heated to its melting point and becomes liquid, usually the thermal source is located at the bottom of the chamber which is another condition to use this technique. Therefore, the deposition chambers having upside down sample mounting geometry are required for this process.



Figure 2.3: Image of QPrep multi-deposition unit present in our lab. The inset shows the inside top view of the chamber. The numbers correspond to different sources available in the chamber. 1 to 3 are dc sputtering sources, 4 is the MAT60 (for creating atomic plasma out of the molecular gases like O_2) source, 5 to 6 are rf sputtering sources, 7 is the e-beam evaporation source, 8 is the nanogen supply and 9 is the thermal evaporation source (having two boats). Except the thermal evaporation source all other sources are distributed at 45° angle with respect to each other in the horizontal plane. These sources are at 30° angle with respect to the substrate plane (vertical plane).

The samples discussed in this thesis are prepared using QPrep multi-deposition unit manufactured by Mantis deposition Ltd., UK [127]. The components of the multi-deposition

unit are depicted in figure 2.3. The main chamber is equipped with turbo molecular pumps (TMP) along with backing pumps which help in pumping down the chamber pressure in ultrahigh vacuum range. The maximum vacuum it can reach is 5×10^{-10} mbar. The pressure of the chamber can be measured using INFICON Bayard – Alpert pirani combination gauge (BPG400) which can work within 5×10^{-10} mbar to atmosphere range. A throttle valve is present in front of the TMP to control the pressure of the chamber during deposition. To maintain the vacuum of the deposition chamber in ultrahigh range, load lock facility is attached with the main chamber to transfer the sample without breaking the vacuum. The lower periphery of the chamber is designed with 8 equidistant sources (45° to each other in horizontal plane) by keeping the thermal evaporation source at the center (figure 2.3 inset).

The specifications of the sources are listed below:

- a. 3 dc unbalanced magnetron sputtering sources
- b. 2 rf unbalanced magnetron sputtering sources
- c. An e-beam evaporator with 4 pockets where the electron beam is targeted towards the crucibles and evaporation of the materials occur by transferring the energy.
- d. Mat60 unit which can be used for producing atomic oxygen from the plasma of the molecular oxygen gas for the preparation of oxide-based materials.
- e. Nanogen which is a nanoparticle generator broadly based on the sputtering process [128,129]. Another TMP is present to evacuate the nanogen assembly.
- f. Two thermal evaporation sources.

To accommodate all the aforementioned sources inside a chamber, the geometry of the sources mentioned in ‘a – e’ are fixed in tilted way where the incident flux direction from each source is at 30° with respect to the substrate normal. Only the thermal evaporation sources are kept at the bottom center of the chamber with normal deposition angle to the

substrate. In this multi-deposition unit all the sources have individual shutters to protect the target/pellets/powder materials from contamination of other materials during deposition. The substrate table is held vertically at the center of the top surface so that the substrate can be at the center of the solid cones produced by each source. The substrate can be heated up to 800°C by the halogen lamps fixed inside the substrate table (shown in figure 2.1). Substrate rotation during deposition is also possible in the range of 0 to 20 *rpm*. To monitor the thickness of the sample as well as the deposition rate quartz crystal monitor (QCM) is present inside the chamber for which its position can be changed based on the source position.

2.1.3. Sample details:

As the main aim of the thesis is to study spinterface with fullerene, bilayers of Fe/C₆₀ and Co/C₆₀ as well as tri-layers of Fe/C₆₀/Fe have been prepared on MgO (001) and Si (100) substrates. To understand the change in the properties of the ferromagnetic layer due to the presence of C₆₀, single layer Fe and Co reference samples have also been prepared on MgO (001) and Si (100) substrates. Prior to deposition, all the substrates have been cleaned using an ultrasonicator at RT. The substrates have been sonicated for 10 minutes each time with Acetone and Isopropyl alcohol separately. Afterwards, the substrates have been blow dried using 99.999% pure N₂ gas. The base pressure of the deposition chamber for all the samples was better than 3×10^{-8} mbar. Fe and Co layers have been prepared using dc sputtering technique. The deposition pressure for the ferromagnetic layer (Fe or Co) has been chosen to be 5×10^{-3} mbar. The rate of depositions for Fe and Co layers have been kept constant at 0.022 nm/s and 0.021 nm/s, respectively. Different thicknesses of single layer Fe (t_{Fe}) and Co (t_{Co}) samples have been prepared on MgO (001) and Si (100) substrates. To prepare bilayer or tri-layer of FM/C₆₀ samples, C₆₀ has been deposited using thermal evaporation technique on top of the FM layer. The deposition pressure of C₆₀ has been kept to be $\sim 1 \times 10^{-7}$ mbar. The rate of deposition for C₆₀ has been chosen to be ~ 0.01 nm/s. All the

samples have been capped with Ta or Au or Al₂O₃ layers to prevent from the oxidation. Ta, Au and Al₂O₃ layers are prepared using dc sputtering, e-beam evaporation and rf sputtering techniques, respectively. For a few samples, MgO (001) substrates have been annealed at $T_{ann} \geq 650^\circ\text{C}$ for 1 hour, prior to deposition. MgO substrates have been annealed before deposition to remove any surface impurity or water vapor as MgO is hydrophilic in nature. Also, the surface atoms of the substrate recrystallize with the heat energy produced due to pre-annealing [130]. To control the uniaxial anisotropy present in the system, a few samples have been prepared by changing the substrate rotation R_{sub} in between 0 to 20 rpm. The detailed sample structures are discussed in the respective chapters related to them. A specific way of sample naming has been followed to mark the samples throughout the thesis. The samples name has a structure of (chapter number)(layer structure)_code. For an example, for sample 3S_A, 3 denotes the chapter number 3, S stands for single layer and A is the sample code. Similarly, for bilayer and tri-layer samples 'S' has been replaced by 'B' and 'T', respectively. It should also be noted that if the sample code is same for a single layer and bi-layer sample then the thickness of the FM layer is same for both the samples. For an example, samples 4S_A and 4B_A both are discussed in chapter 4 where 4S_A is single layer 3.2 nm Fe sample and 4B_A is Fe/C₆₀ bilayer sample with 3.2 nm Fe thickness. In this way the comparison between respective samples have been easier to follow.

2.2. Atomic force microscopy:

Atomic force microscopy (AFM) is a type of high-resolution scanning probe microscopy (SPM) technique used to study the surface topography, grain structure etc. of the thin films. As the name suggests it has a resolution of angstroms [131]. The advantage of AFM over optical microscopy and electron microscopy is that it does not suffer from a limitation in spatial resolution due to diffraction and aberration, as lenses or beam irradiation is not used in

this technique. A small spring like cantilever is oscillated by a piezoelectric element and a sharp tip made of Si or Si₃N₄ is fixed to the free end of the cantilever.

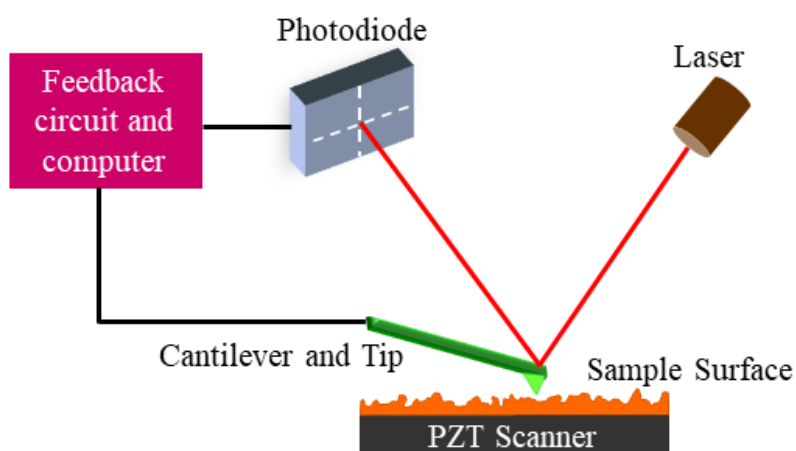


Figure 2.4: Schematic diagram showing the working principle of atomic force microscopy.

The tip raster scan over the sample surface and depending on the distance between the tip and the sample surface, the force between them changes. For longer distance between the tip and the sample surface the force will be attractive and vice-versa. Change in the height of the sample surface will change the deflection of the cantilever depending on the force experienced by it. A laser beam is pointed on top of the cantilever. The deflection of the cantilever can be measured by recording the laser intensity reflected from it. A four-segment photo detector is used to probe this and the deflection of the laser can be converted into electrical signal. In this way, the intensity of this signal will be proportional to the displacement of the cantilever. Therefore, a three-dimensional shaped image of the sample surface can be produced in this technique where the surface topography is commonly displayed in a pseudocolor plot. A feedback circuit helps in avoiding any damage due to the sample - tip collision by maintaining a constant distance between the tip and the sample surface. The feedback loop takes the cantilever deflection as input and it controls the distance between tip and the sample surface by the output. When the height variation in the sample

change the deflection, the feedback automatically adjusts the height of the tip so that the deflection is restored to a user-defined set-point. Figure 2.4 shows the schematic for AFM to understand the aforesaid working principle.

AFM can work in different modes depending on the distance between the tip and the sample surface. The interactive force also changes for various working modes [132].

- (i) **Contact mode:** The tip is in direct contact with the surface in this mode. The topography of the sample is measured using the feedback signal which keeps the cantilever at a fixed position. Low stiffness cantilevers i.e. low spring constant cantilevers are used in this mode to avoid the noise and drift arose by the static signal. In this way large deflection is achieved even with low interaction force. The contact mode is performed in the repulsive region of the force diagram (Figure 2.5(d)). However, in this mode the surface can get damaged easily as the tip directly drags over the surface. Also, the tip longevity becomes less due to the contamination from the sample surface.
- (ii) **Non-contact mode:** In this mode the tip and the sample surface are kept at a distance and the cantilever is oscillated either at or above the resonant frequency. This resonance frequency decreases due to the van der Waal force between the tip and the sample surface. This force is strongest within the range of 1 nm to 10 nm above the surface. The decrease in the resonance frequency is recorded and the feedback loop adjusts the sample – tip distance automatically to maintain a constant oscillation amplitude or frequency. The topography of the sample is imaged by recording the variation of the distance between sample and tip at each point of the scan area. The non-contact mode is performed in the attractive region of the force diagram (Figure 2.5(d)). In this mode, the probability of the damage of sample surface or the tip is much lesser in comparison to the contact mode. This mode is popular for measuring soft samples viz. biological samples or organic thin films.

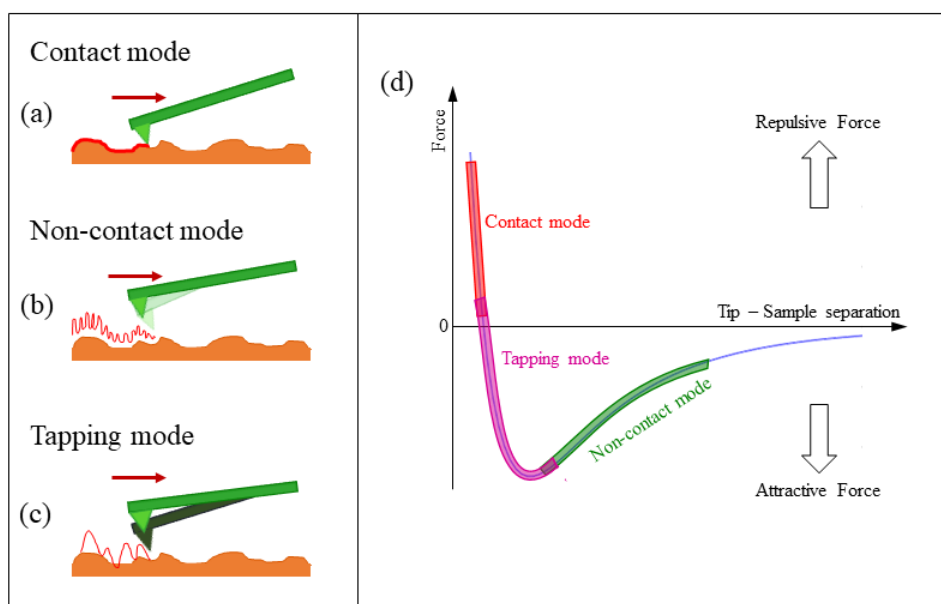


Figure 2.5: Different modes of operation of AFM techniques i.e. contact mode, non-contact mode, tapping mode, are shown in (a) to (c), respectively. (d) The force diagram of AFM is shown in the plot. Different force regions for different modes of operation of AFM are marked in the graph. The concept of the image has been taken from ref. [133].

(iii) **Tapping mode:** In this mode, the cantilever oscillates the tip near its resonance frequency in such a way that it taps over the surface constantly. In ambient conditions, many samples develop a humid layer on the surface. This hinders in detecting the short-range force in non-contact mode and also sticks the tip to the surface in the contact mode. The tapping mode prevents these problems to occur. The working principle of tapping mode is similar to the non-contact mode. The frequency and the amplitude of oscillation of the cantilever gets affected due to the van der Waal force and the feedback loop restores them by adjusting its height to the set-point. In this mode the image is produced by imaging the force of the intermittent contacts of the tip with the sample surface. The range of the operation of this mode can be seen from the figure 2.5(d). Similar to the non-contact mode, the damage of the sample surface and the tip is lesser in

this mode in comparison to the contact mode. Nowadays, this is the most frequently used AFM mode when operating in ambient conditions.

The single layer Co thin films prepared by varying the growth conditions related to this thesis are measured in tapping mode using the Nano-observer AFM machine manufactured by Concept Scientific Instrument (CSI), France [134]. The probes used for the measurements were made of Si having radius lesser than 10 nm, fabricated by AppNano. The resonance frequency and the force constant of the cantilever were 43 – 81 kHz and 0.6 – 3.7 N/m, respectively.

2.3. X-ray diffraction and reflectivity:

2.3.1. X-ray diffraction:

X-ray analysis is a widely used tool to determine structural information of a sample viz. crystal structure, thickness, density, site occupancy, etc. The wavelength of x-rays (~ 0.1 nm) is close to the atomic spacing of a crystal [135,136]. Thus, it is useful in determining the crystal structure. The reflection of a monochromatic x-ray beam from a crystal surface depends on the angle of incidence, the wavelength of the x-ray, the lattice constant of sample material, etc. Let us consider that the crystal is represented by a set of parallel planes (Figure 2.6). Monochromatic x-ray beam is incident at an angle θ to the planes and the reflected rays interfere at the detector after specular reflection. According to physical optics, the interference is constructive only if the path difference between two consecutive rays is an integral multiple of the wavelength i.e. path difference = $n\lambda$. If the inter-planar separation of the crystal is d then the path difference between two consecutive rays (yellow colored block in figure 2.6) can be calculated as $2d\sin\theta$. This is known as Bragg's law [137].

$$2d\sin\theta = n\lambda \quad (2.1)$$

For a specific experiment the wavelength is always constant. Therefore, constructive interference is possible only for a specific set of combinations of d and θ . In equation 2.1, n

corresponds to the order of the interference. The intensity of the reflected beam decreases as the order increases. It should be noted that the diffraction is possible if the condition $\lambda < 2d$ is fulfilled. After recording the diffraction data, peak will be observed for specific θ position and d can be calculated using equation 2.1. Hence, it is possible to deduce the crystallographic planes in terms of the Miller indices by using $d = a/(h^2 + k^2 + l^2)^{1/2}$, where a is the lattice constant of the material [136].

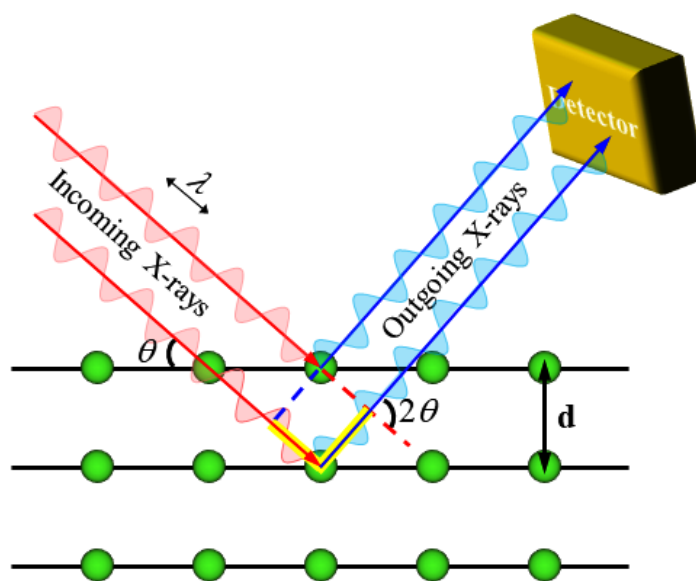


Figure 2.6: Schematic representation of x-ray diffraction phenomena in specular geometry on a crystallographic plane where the separation between the planes are denoted by d . The incoming rays fall on the planes in θ angle and diffraction is measured at 2θ angle. The wavelength of x-ray is denoted by λ . The path difference between two consecutive beams of x-rays is shown by the yellow colored lines.

Similar formalism was proposed by Laue in the reciprocal space where ad hoc assumptions on specular reflection were not imposed. Also, any specific lattice plane was not considered to formulate the theory. Let us consider, \mathbf{k} and \mathbf{k}' are the incident and scattered wavevector. According to the Laue condition i.e. $\mathbf{K} = \mathbf{k}' - \mathbf{k}$, constructive interference is possible if \mathbf{K}

is a vector of the reciprocal lattice. However, both Laue and Bragg conditions are equivalent through the relation [138],

$$\mathbf{K} = \mathbf{k}' - \mathbf{k} = \frac{4\pi}{\lambda} \sin\theta \quad (2.2)$$

The samples discussed in this thesis are measured using SmartLab, an automated multipurpose X-ray diffractometer, manufactured by Rigaku corporation, Japan [139] and D8-Advance reflectometer supplied by Bruker Corporation, USA [140]. Both the SmartLab diffractometer as well as D8-Advance reflectometer are equipped with a Cu K_α source having a wavelength of 0.154 nm. The crystalline quality of the samples was measured by performing intensity vs 2θ measurement. Also, the degree of texture was determined for textured Co thin films prepared on MgO (001) substrates by calculating the FWHM of each Co peak.

2.3.2. X-ray reflectivity:

Another way of using x-ray in probing the structural parameters viz. thickness, roughness, density, etc. of multilayer thin films is by measuring its reflectivity. The advantage of measuring the x-ray reflectivity is that it can be used on crystalline as well as amorphous multilayers with thickness from few angstroms to several hundred nanometers. When an x-ray beam impinges on the surface of a sample, the refractive index can be written as

$$n = 1 - \delta + i\beta \quad (2.3)$$

where, $\delta = \frac{\lambda^2}{2\pi} r_e \rho_e$ and $\beta = \frac{\lambda}{4\pi} \mu_x$ [135,141]. Here, λ is the wavelength of x-ray, r_e , ρ_e , and μ_x are the radius of electron, electron density and absorption length, respectively.

For a multilayer sample, the incident x-rays are reflected from both top as well as bottom interfaces of the films and experience the change in electron density and the refractive index. Due to constructive and destructive interference of the reflected rays Kiessig fringes forms. If the dissipative part (β) of the equation 2.3 is considered to be negligible, then it is possible to observe Kiessig fringes for $\delta < 0$ i.e. $n > 1$. However, for $\delta > 0$ i.e. $n < 1$, total internal

reflection takes place. Considering Snell's law from vacuum to the sample medium, the critical angle for total internal reflection becomes $\theta_c = \sqrt{2\delta}$ [135]. If the first medium is not vacuum, then the relation modifies to $\theta_c = \sqrt{2(\delta_2 - \delta_1)}$ where, δ_1 and δ_2 are the dissipative part of equation 2.3 for the medium 1 and 2, respectively [135].

In specular reflectivity geometry, the angle of incidence is equal to the angle of reflection. In figure 2.7, the angle of incidence θ_i and reflection θ_f are equal and defined with respect to the surface plane. In this mode, the x-ray beam is reflected from the sample at the grazing angle of θ_f and the intensity of the reflected beam is measured by the detector at an angle of $2\theta_f$. In this mode the momentum transfer vector $\mathbf{Q} = \mathbf{k}_f - \mathbf{k}_i$ is measured along the surface normal (Figure 2.7) [135]. For a given wavelength λ , momentum transfer is derived to be

$$Q_z = \frac{4\pi}{\lambda} \sin\theta_i \quad (2.4)$$

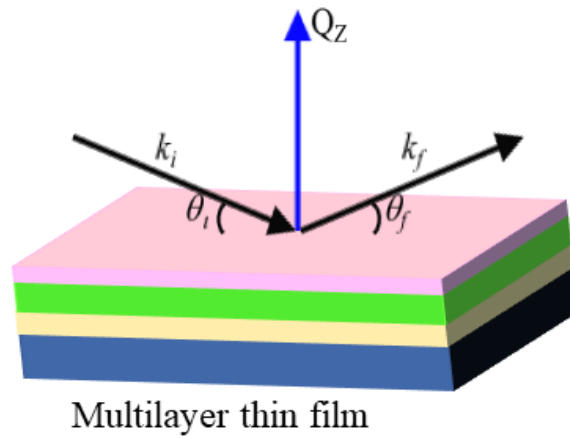


Figure 2.7: Schematic representation of X-ray reflection phenomena in specular geometry on a multilayer thin film. The incident and reflected wave vectors are denoted by k_i and k_f , respectively. The angle of incidence θ_i and reflection θ_f are equal and defined with respect to the surface plane. The momentum transfer vector Q_z is measured along the surface normal.

The reflection coefficient of the x-ray for an ideal sharp interface can be written using Fresnel's formula:

$$r = \frac{k_z - k'_z}{k_z + k'_z} \quad (2.5)$$

Where k_z and k'_z are the vertical components of incident and transmitted waves, respectively [135,141]. If δ is considered to be small, the relation between k_z and k'_z becomes $k'_z = k\sqrt{(\theta^2 - \theta_c^2)}$. Therefore, in the total internal reflection region, k'_z is purely imaginary i.e. $k'_z = ik\sqrt{(\theta_c^2 - \theta^2)}$. Above the critical angle, where k'_z is not very different from k_z , the reflected intensity falls off rapidly following the relation $|r|^2 \propto \frac{1}{\theta_i^4}$. In reality, the reflectivity of a surface with certain roughness can be written as [135]

$$r_{rough} = r_{ideal} e^{-2k_z k'_z \sigma^2} \quad (2.6)$$

If the sample has several interfaces like multilayer thin films then the reflected and the transmitted amplitude from each interface has to be calculated separately. To simplify this problem, Parratt developed a formalism with the ratio of reflected and transmitted amplitude in the medium between interfaces j and $j+1$ for multilayer consisting of N interfaces [142].

The formalism can be written as

$$X_j = \frac{R_j}{T_j} = e^{-2ik_{z,j} z_j} \frac{r_{j,j+1} + X_{j+1} e^{2ik_{z,j+1} z_j}}{1 + r_{j,j+1} X_{j+1} e^{2ik_{z,j+1} z_j}} \quad (2.7)$$

where, $r_{j,j+1} = \frac{k_{z,j} - k_{z,j+1}}{k_{z,j} + k_{z,j+1}}$.

The recursion is solved by considering $T_1 = 1$ and $R_{N+1} = 0$. Due to interference of waves, reflected from different interfaces, the intensity for the reflectivity oscillates by producing Kiessig fringes. The periodicity in Q_z of the Kiessig fringes can be related to the thickness d of the film via $\frac{2\pi}{d}$. The density of the layer is directly proportional to the height of the fringe related to that specific layer of the sample. The roughness of the surface or interface can be

incorporated by modifying equation 2.6 as $r_{rough_{i,j+1}} = r_{ideal_{i,j+1}} e^{-2k_{z,j} k_{z,j+1} \sigma_j^2}$ provided the roughness is much smaller than the thickness of the respective layer.

It is possible to extract the structural information of a multilayer from XRR data using another formalism known as the Master formula. Using the kinematical approximation, the reflectivity of an arbitrary electron density profile $\rho_e(z)$ can be described by the Master formula [135,141].

$$R(Q_z) = R_F \left| \frac{1}{\rho_e(z \rightarrow \infty)} \int_{-\infty}^{+\infty} \frac{d\rho_e}{dz} e^{iQ_z z} dz \right|^2 \quad (2.8)$$

Though this formula works very well in the $\theta \gg \theta_c$ regime, however, this approximation does not hold near the $\theta \approx \theta_c$ regime.

XRR measurement has been performed on all the bilayer and tri-layer samples studied in this thesis to extract the layer specific thickness, density, roughness etc. and also the structural parameters related to each interface. All the XRR measurements have been performed using SmartLab diffractometer, manufactured by Rigaku corporation, Japan [139]. The XRR data was then simulated using GenX software [143] which is formulated using python script, uses the wxpython package for the Graphical User Interface (GUI) and based on Parratt formalism. The extracted structural parameters of these samples have been used for fitting the polarized neutron reflectivity data.

2.4. Secondary ion mass spectroscopy:

Secondary ion mass spectrometry (SIMS) is a technique where the sputtering process is used to dig out elements from the surface of a thin film to analyze the composition of the surface [144,145]. In SIMS, a focused primary ion beam is used to sputter the surface. SIMS is one of the most effective surface sensitive technique and elemental detection limit range from parts per million to parts per billion. It can be considered as a qualitative technique due to the huge variation in the ionization probabilities of all available materials. However, with proper calibration and standardization it is possible to make quantitation using this technique [146].

An ion gun is used to generate primary ion beam using electron ionization of noble gases, surface ionization or by liquid metal ion gun. The primary ion beam is accelerated through focusing lenses towards the sample. After focusing of the ion beam deflection plates help in positioning and raster scanning the beam.

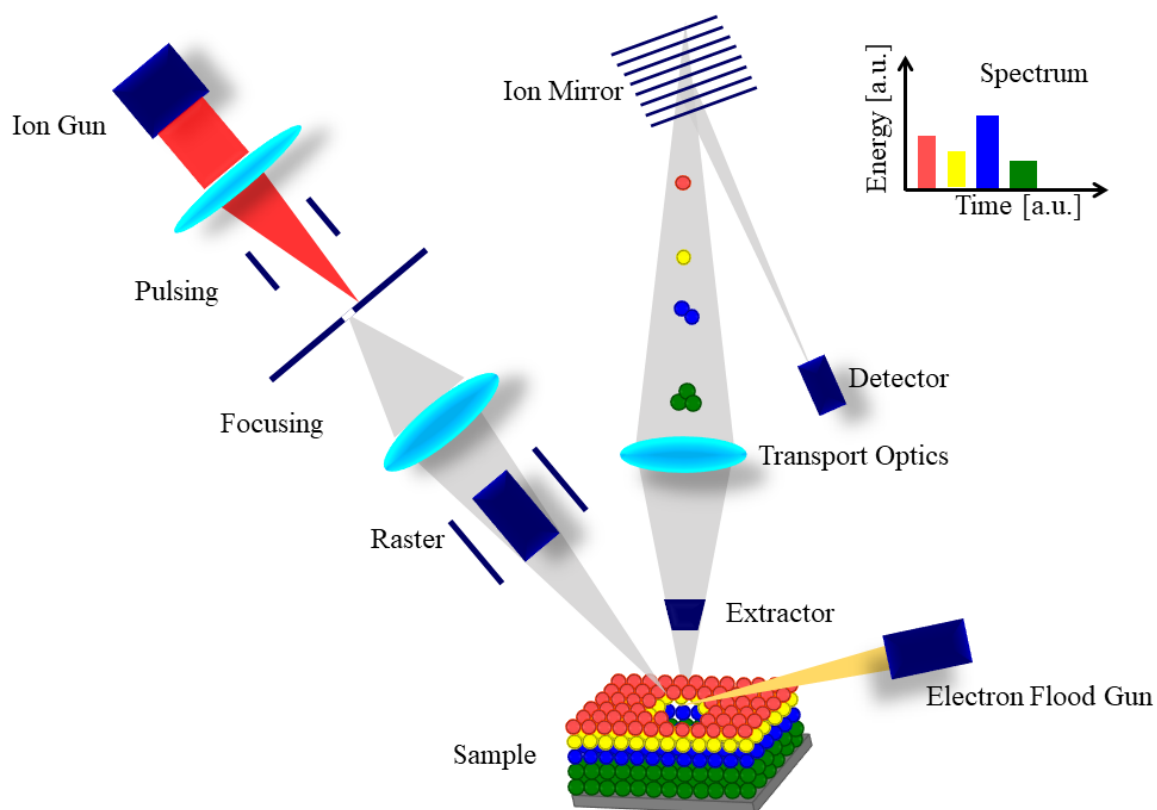


Figure 2.8: Schematic diagram showing the working principle of secondary ions mass spectroscopy. The concept of the image has been taken from ref. [147]

Further the ion beam falls on the sample which is kept within a high vacuum chamber. It is required to maintain high vacuum so that the mean free path of the secondary ions is large enough to reach the detector before colliding with background gases. Also creating high vacuum prevents the surface contamination of the sample during the measurement. There are three types of basic analyzer available such as sector, quadrupole, and time-of-flight (TOF). In case of thin film samples only the surface layers of the film are characterized which is known as static SIMS. This kind of measurement is performed usually with a pulsed ion beam as the source and a time of flight mass spectrometer as the analyzer. The time of flight

mass analyzer separates the ions in a field-free drift path according to their velocity. Depending on their mass, the time of flight of the molecules sputtered from the sample surface will be different. The intensity of the molecules is plotted with respect to the time they reach to the detector. TOF is the only analyzer type able to detect all generated secondary ions simultaneously and is the standard analyzer for static SIMS instruments. A Faraday cup is used as the detector which measures the ion current hitting a metal cup. In order to get information about the depth, the x-axis i.e. the time scale can be converted to the depth of the film by proper calibration. The depth of the sputter crater can be measured using a profilometer where the vertical depth of the crater can be measured.

SIMS measurements were performed on Fe/C₆₀ bilayers using time-of-flight analyzer to acquire the depth profile and information related to the interface of the layers. The measurements were performed using ION-TOF GmbH, in collaboration with Dr. Manas K. Dalai at National Physical Laboratory, New Delhi [148]. A 25 KeV 'Bi' ion source was used as the primary pulsed ion beam to excite secondary ions. Those secondary ions were analyzed by a reflectron based time of flight mass analyzer. Another ion source of Cs (500 eV) was used to sputter out the layers in order to have the depth profile analysis. In order to calibrate the SIMS data, thickness profilometry experiment was performed on the specific hole from where the materials have been dug out during the SIMS measurement. The sputtering area was kept at 300 × 300 μm and the analysis area was at 100 × 100 μm, respectively.

2.5 Superconducting Quantum Interference Device magnetometer:

Superconducting QUantum Interference Device (SQUID) magnetometer is used to quantify the direct magnetization of a sample with very high sensitivity. It is capable to detect magnetic moment up to 10⁻¹¹ Am². The principle of SQUID is based on two parallel Josephson junctions where two superconductors are separated by a thin insulator [149-151]. The wavefunction associated to each cooper pair present in a superconductor is equal and

similar to the wave-function of a free electron. While tunneling through a Josephson junction, the wavefunctions of the cooper pairs suffer from a phase shift which is proportion to the current i.e. $i_S = i_C \sin \Delta \varphi$. Here, i_S is the superconducting current, i_C is the critical current and $\Delta \varphi$ is the phase difference. Except the Josephson junctions, phase shift is additionally influenced by the presence of external magnetic field. According to the property of the Josephson junction, the total phase shift is quantized i.e. $\Delta \varphi(B) + 2\Delta \varphi(i) = n2\pi$. Therefore, the great sensitivity of the SQUID is associated to the change in magnetic field which is directly related to the flux quantization of Josephson junction. In a constant biasing current the voltage oscillates between two Josephson junctions where one period of oscillation of the voltage is equal to one quanta $\varphi_0 = h/2\pi = 2.07 \times 10^{-15}$ Wb.

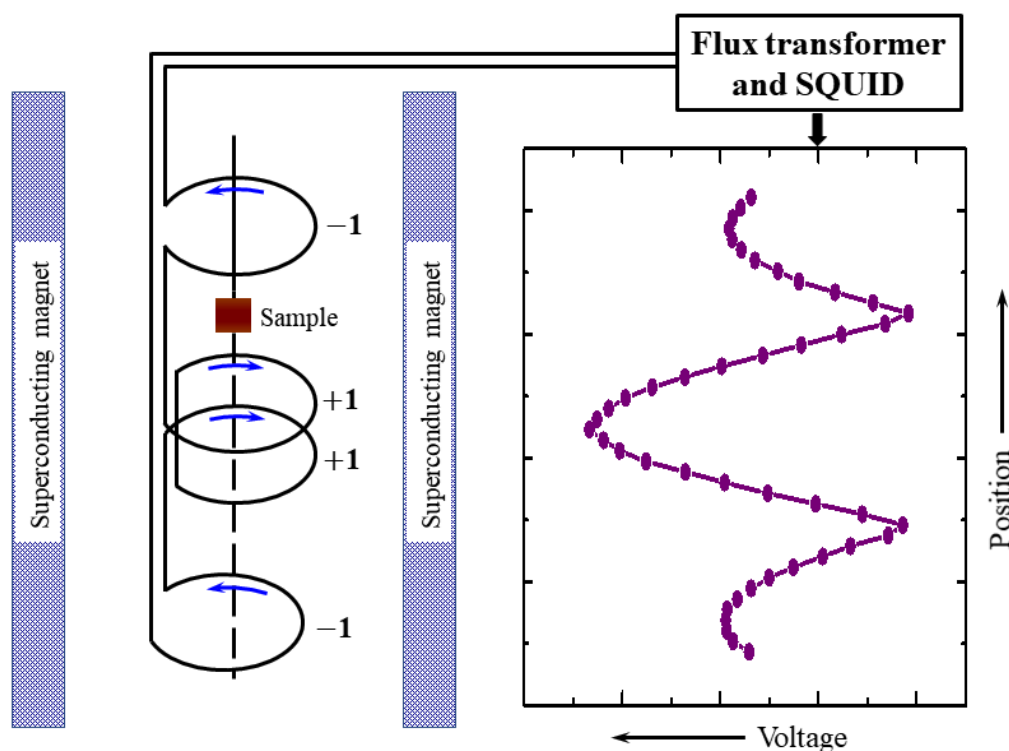


Figure 2.9: Schematic diagram showing the pick-up-coil geometry and a demo plot for the response signal while centering the sample in MPMS SQUID magnetometer [100].

The sample is placed in the superconducting sensing coil where the coil consists of a superconducting wire wound in three-coil configuration known as second order gradiometer

geometry. The upper coil is a single turn wound clockwise, the center coil consists of two turns anti-clockwise wound, and the bottom coil is again a single turn wound clockwise similar to the upper coil (Figure 2.9). This assembly is located in between two superconducting magnets which are capable to maintain uniform field distribution in the coil region. When the sample is moved up and down, it produces an alternating magnetic flux in the pick-up coil. It induces a persistent current in the coil which is proportional to the induced flux. The magnetic flux is then transferred to a rf SQUID device which is located away from the sample in the liquid helium bath and acts as magnetic flux-to-voltage converter. Further the voltage can be converted to the magnetic moment of the sample. Finally, the output signal is measured with respect to the scan position of the sample (Figure 2.9).

SQUID measurements were performed on single layer of Fe and Co thin films as well as bilayer samples of Fe/C₆₀ and Co/C₆₀ using MPMS3 Evercool system manufactured by Quantum Design, USA [152]. All the measurements were performed at RT and within an applied field of 500 mT. By measuring hysteresis along the hard axis of the sample, it is possible to calculate the hard axis saturation field (H_K). The saturation magnetization (M_S) can also be calculated from the hysteresis loop. Thus, the net anisotropy of the sample can be estimated using the relation $K_{in} = \mu_0 H_K M_S / 2$.

2.6 Kerr microscopy:

Imaging of magnetic domains is possible using the optical wavelengths where the rotation of the plane-polarized light is measured after getting reflected or transmitted from the magnetic sample. Depending on the way the plane-polarized light gets rotated after transmission or reflection from the magnetic sample, the phenomena is known as the Faraday effect or the Kerr effect, respectively [153,154]. Both these effects can be interpreted as birefringence of circularly polarized light. Another similar effect is used for imaging of magnetic domains where the principle of the birefringence of linearly polarized light is used. It is known as the

Voigt or Cotton–Mouton effect. However, Kerr effect is the dominant one among the aforementioned three magneto optic effects and is the most commonly used technique for domain imaging.

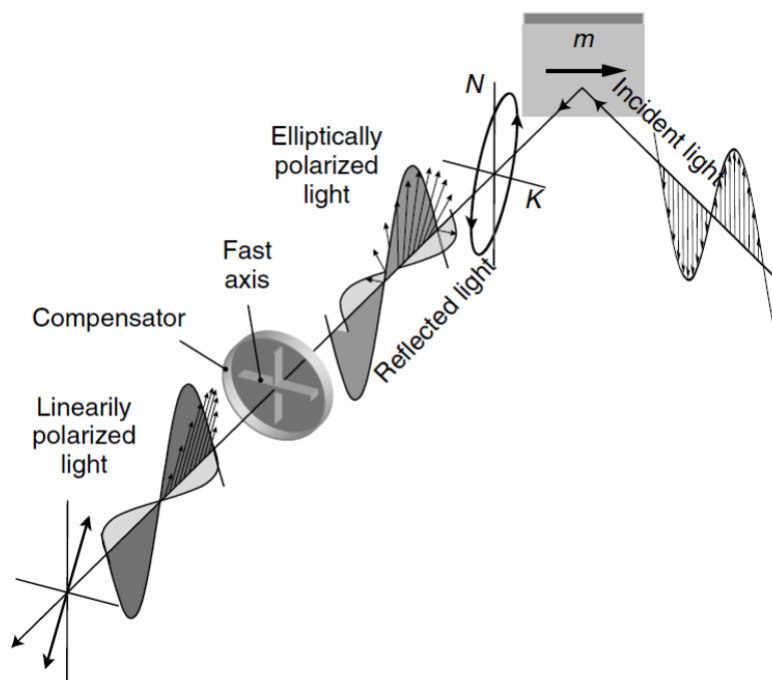


Figure 2.10: Schematic diagram showing the elementary magneto optical interaction for the longitudinal Kerr effect. This image has been taken from the ref [155]. Due to the interaction between incident light wave and the magnetic dipoles of the samples, the incident plane polarized light becomes elliptically polarized light along with a rotation after getting reflected from the sample. The phase shift can be corrected using a compensator and the rotation of the light is measured which is proportional to the magnetization of the sample.

Magneto optic Kerr effect (MOKE) is presently explained in terms of both macroscopic dielectric theory as well as microscopic quantum theory [156]. The rotation of the plane polarized light after getting reflected from the magnetic element can be expressed by the

dielectric law $\mathbf{D} = \boldsymbol{\varepsilon}\mathbf{E}$ where $\boldsymbol{\varepsilon}$ is an antisymmetric tensor. This relation can also be written in the form:

$$\mathbf{D} = \varepsilon(\mathbf{E} + iQ\mathbf{m} \times \mathbf{E}) \quad (2.9)$$

where ε is the regular dielectric constant and Q is a complex material parameter proportional to the saturation magnetization of the sample and describes the strength of the Kerr effect. From the macroscopic point of view, MOKE arises from the antisymmetric off-diagonal elements in the 3×3 dielectric tensor. The symmetric part of the dielectric tensor does not contribute to the magneto optic effect. The dielectric tensor describing the magnetic material can be written as: [157]

$$\boldsymbol{\varepsilon}' = \varepsilon \begin{pmatrix} 1 & iQ_v m_z & -iQ_v m_y \\ -iQ_v m_z & 1 & iQ_v m_x \\ iQ_v m_y & -iQ_v m_x & 1 \end{pmatrix} \quad (2.10)$$

where, Q_v is the Voigt constant and $(m_x, m_y, m_z) = m$ is the normalized magnetization vector.

The second term of the equation 2.9 reflects similarity to the Lorentz force equation. The Kerr amplitude (\mathbf{K}) is obtained if the Lorentz movement \mathbf{v}_{Lor} is projected to the plane perpendicular to the propagation direction of the reflected light wave. If \mathbf{N} is considered to be the amplitude of regular reflected light in the same plane of the incident one, then \mathbf{K} will be perpendicular to \mathbf{N} . Considering the small angle approximation, the angle of Kerr rotation (θ_K) of the polarization vector of light can be obtained as $\theta_K = \frac{K}{N}$. The amplitude of Kerr rotation K is opposite for domains with opposite magnetization. It is possible to obtain a domain contrast using this principle if the reflected light from one of the magnetization directions is blocked by the analyzer. The signal obtained from the relative contrast between the dark and bright domains can be expressed as

$$S \approx 4\xi KN \quad (2.11)$$

Where ξ is the angle between the analyzer and \mathbf{N} [12]. Three properties can be understood from equation 2.11. (i) The Kerr signal is proportional to the Kerr amplitude K which implies

that S is also proportional to the respective magnetization components according to equation (2.9). (ii) The Kerr signal can be enhanced by increasing angle ξ beyond θ_K , which will increase the signal-to-noise ratio and the sensitivity of the detector will be adjusted accordingly. (iii) The visibility of domains is determined by the Kerr amplitude and not by the Kerr rotation [155].

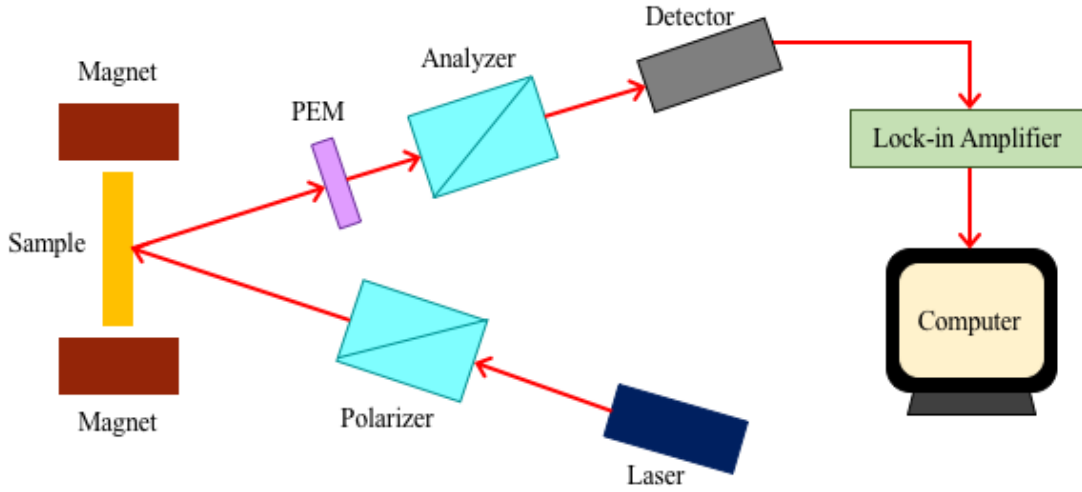


Figure 2.11: Schematic diagram of magneto optic Kerr effect setup showing all the optical and electrical components. The concept of the image has been taken from ref. [100]

The optical and electronic components required to measure the Kerr effect are shown in figure 2.11. It is possible to quantify the intensity of the reflected light measured at the detector in terms of the Kerr rotation (θ_K) and ellipticity (ϵ_K). Using the Jones matrix formalism, every optical element used to perform MOKE can be represented by a matrix form [157]. Let us start with the first optical component encountered by the incident light i.e. the polarizer (P). The matrix form of the polarizer can be written as:

$$P = \begin{pmatrix} \cos^2\beta & \sin\beta \cos\beta \\ \sin\beta \cos\beta & \sin^2\beta \end{pmatrix} \quad (2.12)$$

where β is the angle between the planes of incidence and polarization. Next the matrix form of the ferromagnetic sample (S) can be expressed as:

$$S = \begin{pmatrix} \tilde{r}_{pp} & \tilde{r}_{ps} \\ \tilde{r}_{sp} & \tilde{r}_{ss} \end{pmatrix} \quad (2.13)$$

where, the diagonal terms are $\tilde{r}_{pp} = r_{pp}e^{i\delta_{pp}}$ and $\tilde{r}_{ss} = r_{ss}e^{i\delta_{ss}}$. The off-diagonal cross terms can be written as $\tilde{r}_{ps} = r_{ps}e^{i\delta_{ps}}$ and $\tilde{r}_{sp} = r_{sp}e^{i\delta_{sp}}$. Equation 2.13 consists of both the p-polarized and s-polarized components of the incident as well as reflected light. The coefficients r_{ij} are the ratio of the incident j polarized and reflected i polarized electric field of light. δ_i is the corresponding phase angle.

The photoelastic modulator (PEM) (O) with the orientation of the transmission axis at 0° can be expressed as:

$$O = \begin{pmatrix} e^{i\varphi/2} & 0 \\ 0 & e^{-i\varphi/2} \end{pmatrix} \quad (2.14)$$

φ is the periodic retardation with the relation $\varphi = \varphi_0 \sin \omega t$ where φ_0 is the phase amplitude of the PEM. Further, Fourier decomposition of $\sin \varphi(t)$ and $\cos \varphi(t)$ can be used for PEM matrix expansion. [157]

$$\sin \varphi(t) = 2 \sum_{m=0}^{\infty} J_{2m+1}(\varphi_0) \sin[(2m+1)\omega t] \quad (2.15)$$

$$\cos \varphi(t) = J_0(\varphi_0) + 2 \sum_{m=1}^{\infty} J_{2m}(\varphi_0) \cos(2m\omega t) \quad (2.16)$$

Here, J_k is the Bessel function of order k .

The matrix representation for the analyzer (A) is exactly the same as the polarizer with a different angle (ζ) between the plane of incidence and plane of polarization.

$$A = \begin{pmatrix} \cos^2 \zeta & \sin \zeta \cos \zeta \\ \sin \zeta \cos \zeta & \sin^2 \zeta \end{pmatrix} \quad (2.17)$$

Now, the incident and the reflected light can be represented as electric field vectors $E^i =$

$$\begin{pmatrix} E_p \\ E_s \end{pmatrix}^i \text{ and } E^r = \begin{pmatrix} E_p \\ E_s \end{pmatrix}^r, \text{ respectively.}$$

Therefore, the final equation to calculate the reflected intensity of the light using the Jones matrix formalism can be written as:

$$\begin{pmatrix} E_p \\ E_s \end{pmatrix}^r = AOSP \begin{pmatrix} E_p \\ E_s \end{pmatrix}^i \quad (2.18)$$

The intensity of the reflected light measured by the detector can be represented by:

$$I \propto |E^r|^2 \quad (2.19)$$

Now let us consider two different polarization of light and calculate the final intensity of the reflected light after reflecting from the sample.

A. For, s-polarized light $\beta = 90^\circ$ i.e. $P = \begin{pmatrix} 0 & 0 \\ 0 & 1 \end{pmatrix}$.

(i) At the beginning the electric field vector of the incident light is considered to be $E^i = \begin{pmatrix} 0 \\ 1 \end{pmatrix}$.

(ii) After the polarizer: $\begin{pmatrix} 0 & 0 \\ 0 & 1 \end{pmatrix} \begin{pmatrix} 0 \\ 1 \end{pmatrix} = \begin{pmatrix} 0 \\ 1 \end{pmatrix}$

(iii) After the sample: $\begin{pmatrix} \tilde{r}_{pp} & \tilde{r}_{ps} \\ \tilde{r}_{sp} & \tilde{r}_{ss} \end{pmatrix} \begin{pmatrix} 0 \\ 1 \end{pmatrix} = \begin{pmatrix} \tilde{r}_{ps} \\ \tilde{r}_{ss} \end{pmatrix}$

(iv) After PEM: $\begin{pmatrix} e^{i\varphi/2} & 0 \\ 0 & e^{-i\varphi/2} \end{pmatrix} \begin{pmatrix} \tilde{r}_{ps} \\ \tilde{r}_{ss} \end{pmatrix} = \begin{pmatrix} \tilde{r}_{ps} e^{i\varphi/2} \\ \tilde{r}_{ss} e^{-i\varphi/2} \end{pmatrix}$

(v) After the analyzer (considering $\zeta = 45^\circ$): $\begin{pmatrix} 1/2 & 1/2 \\ 1/2 & 1/2 \end{pmatrix} \begin{pmatrix} \tilde{r}_{ps} e^{i\varphi/2} \\ \tilde{r}_{ss} e^{-i\varphi/2} \end{pmatrix} = \frac{1}{2} (\tilde{r}_{ps} e^{\frac{i\varphi}{2}} + \tilde{r}_{ss} e^{-\frac{i\varphi}{2}}) \begin{pmatrix} 1 \\ 1 \end{pmatrix}$

Therefore, the final intensity is given by

$$\begin{aligned} I &\propto \frac{1}{2} \left| (\tilde{r}_{ps} e^{\frac{i\varphi}{2}} + \tilde{r}_{ss} e^{-\frac{i\varphi}{2}}) \right|^2 \\ &= \frac{1}{2} [r_{ps} e^{i(\delta_{ps} + \varphi/2)} + r_{ss} e^{i(\delta_{ss} - \varphi/2)}] [r_{ps} e^{-i(\delta_{ps} + \varphi/2)} + r_{ss} e^{-i(\delta_{ss} - \varphi/2)}] \\ &= \frac{1}{2} [r_{ps}^2 + r_{ss}^2 + 2r_{ps}r_{ss} \cos(\delta_{ps} - \delta_{ss} + \varphi)] \\ &= \frac{1}{2} r_{ss}^2 \left[\left(\frac{r_{ps}}{r_{ss}} \right)^2 + 1 + 2 \frac{r_{ps}}{r_{ss}} [\cos(\delta_{ps} - \delta_{ss}) \cos\varphi - \sin(\delta_{ps} - \delta_{ss}) \sin\varphi] \right] \end{aligned}$$

Substituting equation 2.15 and 2.16,

$$= \frac{1}{2} r_{ss}^2 \left[\left(\frac{r_{ps}}{r_{ss}} \right)^2 + 1 + 2J_0(\varphi_0) \theta_k^s + 4J_2(\varphi_0) \theta_k^s \cos(2\omega t) - 4J_1(\varphi_0) \varepsilon_k^s \sin(\omega t) \right]$$

where, $\theta_k^s = \frac{r_{ps}}{r_{ss}} \cos(\delta_{ps} - \delta_{ss})$ and $\varepsilon_k^s = \frac{r_{ps}}{r_{ss}} \sin(\delta_{ps} - \delta_{ss})$ [158].

Therefore, the first and the second harmonics are:

$$I_\omega = -2r_{ss}^2 J_1(\varphi_0) \varepsilon_k^s \sin(\omega t)$$

$$I_{2\omega} = 2r_{ss}^2 J_2(\varphi_0) \theta_k^s \cos(2\omega t)$$

Similarly, for analyzer angle $\zeta = 135^\circ$, the first and second harmonics become:

$$I_\omega = 2r_{ss}^2 J_1(\varphi_0) \varepsilon_k^s \sin(\omega t)$$

$$I_{2\omega} = -2r_{ss}^2 J_2(\varphi_0) \theta_k^s \cos(2\omega t)$$

B. For, p-polarized light $\beta = 0^\circ$ i.e. $P = \begin{pmatrix} 1 & 0 \\ 0 & 0 \end{pmatrix}$.

(i) The electric field vector of the incident light modifies to be $E^i = \begin{pmatrix} 1 \\ 0 \end{pmatrix}$.

(ii) After the polarizer: $\begin{pmatrix} 1 & 0 \\ 0 & 0 \end{pmatrix} \begin{pmatrix} 1 \\ 0 \end{pmatrix} = \begin{pmatrix} 1 \\ 0 \end{pmatrix}$

(iii) After the sample: $\begin{pmatrix} \tilde{r}_{pp} & \tilde{r}_{ps} \\ \tilde{r}_{sp} & \tilde{r}_{ss} \end{pmatrix} \begin{pmatrix} 1 \\ 0 \end{pmatrix} = \begin{pmatrix} \tilde{r}_{pp} \\ \tilde{r}_{sp} \end{pmatrix}$

(iv) After PEM: $\begin{pmatrix} e^{i\varphi/2} & 0 \\ 0 & e^{-i\varphi/2} \end{pmatrix} \begin{pmatrix} \tilde{r}_{pp} \\ \tilde{r}_{sp} \end{pmatrix} = \begin{pmatrix} \tilde{r}_{pp} e^{i\varphi/2} \\ \tilde{r}_{sp} e^{-i\varphi/2} \end{pmatrix}$

(v) After the analyzer (considering $\zeta = 45^\circ$): $\begin{pmatrix} 1/2 & 1/2 \\ 1/2 & 1/2 \end{pmatrix} \begin{pmatrix} \tilde{r}_{pp} e^{i\varphi/2} \\ \tilde{r}_{sp} e^{-i\varphi/2} \end{pmatrix} = \frac{1}{2} (\tilde{r}_{pp} e^{i\varphi/2} +$

$$\tilde{r}_{sp} e^{-i\varphi/2}) \begin{pmatrix} 1 \\ 1 \end{pmatrix}$$

Therefore, the final intensity is given by

$$\begin{aligned} I &\propto \frac{1}{2} \left| (\tilde{r}_{pp} e^{i\varphi/2} + \tilde{r}_{sp} e^{-i\varphi/2}) \right|^2 \\ &= \frac{1}{2} [r_{pp} e^{i(\delta_{pp} + \varphi/2)} + r_{sp} e^{i(\delta_{sp} - \varphi/2)}] [r_{pp} e^{-i(\delta_{pp} + \varphi/2)} + r_{sp} e^{-i(\delta_{sp} - \varphi/2)}] \\ &= \frac{1}{2} [r_{pp}^2 + r_{sp}^2 + 2r_{pp}r_{sp} \cos(\delta_{pp} - \delta_{sp} + \varphi)] \end{aligned}$$

$$= \frac{1}{2} r_{pp}^2 \left[\left(\frac{r_{sp}}{r_{pp}} \right)^2 + 1 + 2 \frac{r_{sp}}{r_{pp}} [\cos(\delta_{pp} - \delta_{sp}) \cos\varphi - \sin(\delta_{pp} - \delta_{sp}) \sin\varphi] \right]$$

Substituting equation 2.15 and 2.16,

$$= \frac{1}{2} r_{pp}^2 \left[\left(\frac{r_{sp}}{r_{pp}} \right)^2 + 1 + 2J_0(\varphi_0)\theta_k^p + 4J_2(\varphi_0)\theta_k^p \cos(2\omega t) + 4J_1(\varphi_0)\varepsilon_k^p \sin(\omega t) \right]$$

where, $\theta_k^p = \frac{r_{sp}}{r_{pp}} \cos(\delta_{sp} - \delta_{pp})$ and $\varepsilon_k^p = \frac{r_{sp}}{r_{pp}} \sin(\delta_{sp} - \delta_{pp})$ [158].

Therefore, the first and the second harmonics are:

$$I_\omega = 2r_{pp}^2 J_1(\varphi_0)\varepsilon_k^p \sin(\omega t)$$

$$I_{2\omega} = 2r_{pp}^2 J_2(\varphi_0)\theta_k^p \cos(2\omega t)$$

Similarly, for analyzer angle $\zeta = 135^\circ$, the first and second harmonics become:

$$I_\omega = -2r_{pp}^2 J_1(\varphi_0)\varepsilon_k^p \sin(\omega t)$$

$$I_{2\omega} = -2r_{pp}^2 J_2(\varphi_0)\theta_k^p \cos(2\omega t)$$

Using similar formalism, it is possible to obtain the harmonics for different configurations of the polarizer and analyzer. However, literature reveals that for most of the MOKE set-ups analyzer angle $\zeta = 45^\circ$ produces the highest signal to noise ratio. While performing the experiment, voltages corresponding to dc (V_{dc}), 1st harmonic (V_{1f}) and 2nd harmonics (V_{2f}) are measured with the help of lock-in amplifier and voltmeter. Following relations are used to obtain the Kerr signals:

$$\theta_k = \frac{\sqrt{2}V_{2f}}{4J_2V_{dc}} \quad \text{and} \quad \varepsilon_k = \frac{\sqrt{2}V_{1f}}{4J_1V_{dc}}.$$

From the microscopic point of view, MOKE arises due to the coupling between the electrical field of the light and the electron spin within a magnetic medium through the spin-orbit interaction [159]. A plane-polarized light can be considered as a sum of left and right circularly polarized light. In the absence of external magnetic field, a left-circularly polarized electric field will drive the electrons into left circular motion, and a right circularly polarized

electric field will drive the electrons into right circular motion. Consequently, the radius of the electron orbit for left and right circular motion will be the same. However, in presence of an external magnetic field, an additional Lorentz force will be acting on each electron. This force points toward or away from the circle's center for left or right circular motion. Thus, the radius for left circular motion will be reduced and the radius for right circular motion will expand. The difference in the radii of the left- and right-circularly polarized modes will give different dielectric constants correspondingly. Thus, it is the Lorentz force of the external magnetic field that generates the Kerr effect [159].

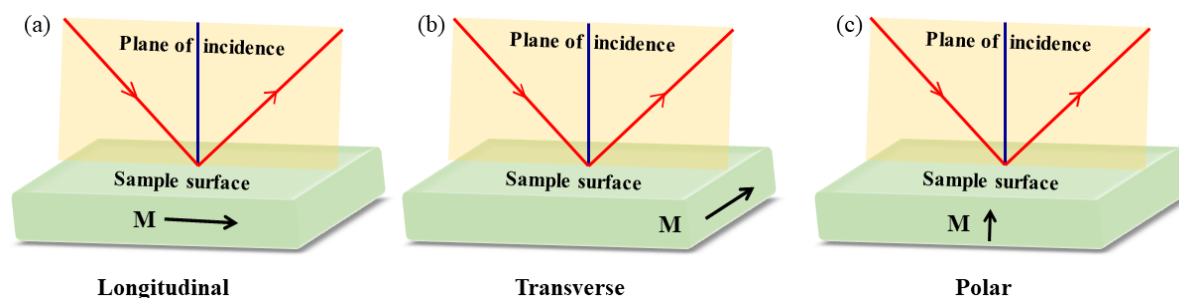


Figure 2.12: Different geometries of MOKE measurements are depicted with respect to the magnetization of the sample and plane of incidence of the light. (a), (b) and (c) show the longitudinal, transverse and polar geometries, respectively.

Figure 2.12 shows the geometries for the MOKE sensitivity depending on the plane of incidence and the direction of the net magnetization of the sample:

- (i) Longitudinal Mode: The spontaneous magnetization direction is parallel to both the plane of incidence and sample plane (Figure 2.12(a)). It is possible to measure the domain contrast in this mode using both the s as well as p polarized light.
- (ii) Transverse Mode: The spontaneous magnetization direction is parallel to the sample plane but perpendicular to the plane of incidence (Figure 2.12(b)). In this configuration, only p polarized light can lead to measurable signal.

(iii) Polar Mode: The spontaneous magnetization points towards the out-of-plane to both the plane of incidence and sample surface (Figure 2.12(c)).

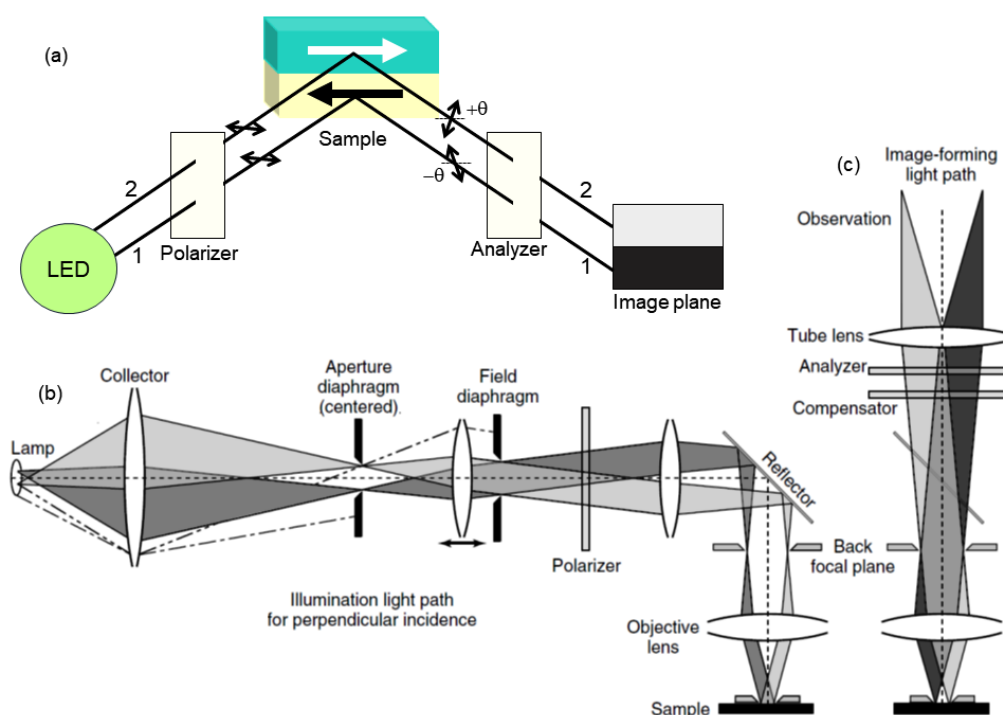


Figure 2.13: (a) Schematic diagram showing the principle of domain formation in Kerr microscope. (b) The essential components and ray paths for perpendicular light incidence and (c) image-forming path. Images shown in (b) and (c) are taken from the ref [155].

Figure 2.13 shows the schematic of the Kerr microscopy principle to form domain contrast. Unpolarized light is incident on the polarizer and linearly polarized light is obtained. It is then incident on the magnetic sample. For simplicity let us consider that the magnetic sample consists of two domains with opposite magnetization. According to the aforementioned Kerr effect principle, the linearly polarized light will rotate in opposite directions after interacting with two opposite magnetizations. As the linearly polarized light distorts to elliptically polarized light after interacting with the magnetic sample, a variable quarter wave plate is used before the analyzer to compensate for the phase shift. If the axis of the analyzer is aligned in such a way that it blocks the transmittance of one of the rotated lights then dark

contrast will appear in the image plane. However, bright contrast will be observed for the light reflected from another domain as analyzer will allow it to pass through. A CCD camera is used to record the light intensity. Therefore, the domain structure in the sample will be represented in the image plane through different contrasts. The net grey value of the domain image is proportional to the net magnetization.

Domain imaging were performed for all the samples discussed in this thesis using the Kerr microscope manufactured by Evico Magnetics Ltd., Germany [160]. It is possible to apply maximum of 1300 mT and 900 mT magnetic field along in-plane and out-of-plane direction, respectively. The microscope is equipped with 8 LED sources and it is possible to choose the sensitivity of the measurement by choosing the proper combination of the LEDs. KerrLab software allows acquiring domain images at each point of the hysteresis loop. It also offers the possibility to record real time videos to understand the DW motion. The software also permits to subtract the background to avoid any effect from the topography. Initially, a background image is recorded at the saturation field which is the reference image. Further that reference image is subtracted from all other images taken at different points of the hysteresis loop to avoid any topographical contrast. The sample stage can be rotated in plane from 0° to 360° with a step resolution of 1°. The angle dependent magnetic properties like magnetic anisotropy, hysteresis and domains can be studied using this.

2.7 Polarized neutron reflectivity:

Neutrons are non-destructive powerful tool to study the layer specific structural as well as magnetic properties of multi-layered samples. Being neutral in charge, they are highly penetrating and non-perturbing. This allows significant flexibility in sample environments and in use of delicate materials like biological specimens. Though neutrons are spin-half particles, still they have wave-like properties according to the de Broglie theory where the wavelength of the neutrons can be expressed as $\lambda = \frac{h}{mv}$. The wavelength of a neutron is

typically in the range of 0.2 – 1 nm which is comparable to the lattice spacing. Therefore, neutrons can be used to probe the structural information in a similar way to x-rays. However, the magnetic moment associated with neutrons provides an additional degree of freedom to probe magnetism in various magnetic compounds and thin films. The energies of thermal neutrons are of the same order of the energy associated with the elementary excitations in solid. Therefore, they can be used to study the spin waves, lattice vibrations, dynamics of atomic motion, lattice modes etc. Neutrons interact directly with the nuclei of materials rather than electron density which enables it to measure lighter elements e.g. Hydrogen, Carbon, Nitrogen, Oxygen etc. Along with that it is sensitive in distinguishing the isotopes and has better contrast change for neighboring elements of the periodic table in comparison to the x-rays. Similar reflectivity techniques viz. optical reflectivity, x-ray reflectivity operates in the same working principles, however, neutron measurements are advantageous in a few notable ways. X-ray exposure may damage some materials and optical laser can modify properties of some materials like photoresists [161]. Besides this, optical techniques may include ambiguity due to optical anisotropy [162], which can be resolved by neutron measurements. However, the unique advantage of neutrons over other techniques is that neutrons possess a magnetic moment which can be used to study the magnetic properties like spin ordering, micromagnetic structures, magnetic fluctuations, the coupling between different magnetic sites etc. If μ_n is considered to be the magnetic moment of neutron then in presence of a homogeneous field \mathbf{B} the magnetic potential will be $V_m = -\mu_n \cdot \mathbf{B}$ where the negative sign corresponds to the antiparallel alignment between the spin and the magnetic field.

Polarized neutron reflectivity is a very powerful technique to study the magnetic properties in multi-layered thin films. It is possible to understand many important phenomena viz. exchange coupling [163-166], antiferromagnetic coupling of ferromagnetic layers separated by non-ferromagnetic layers [163,164], intricate non-collinear coupling [167], helical

magnetic structure [168] etc. Apart from these, PNR is very popular in quantifying the exact magnetic moment in ultrathin ferromagnetic thin films induced due to surface and size effects [169-171]. One major advantage of PNR is that it does not include any magnetic effect from the substrate unlike the conventional magnetometries where diamagnetic signals from the substrates dominate if the magnetic signal is not sufficiently large from the sample.

When a neutron beam falls on the sample surface, the refractive index can be written in a similar way to equation 2.3 i.e. $n = 1 - \delta + i\beta$ where $\delta = \frac{\lambda^2}{2\pi} b_{coh}\rho_n$ and $\beta = \frac{\lambda}{4\pi}\mu_n$ [135,141]. Here, λ is the wavelength of the neutrons, b_{coh}, ρ_n , and μ_n are the coherent scattering length, atomic number density and absorption length of neutron, respectively.

Similar to the x-ray reflectivity, Kiessig fringes are observed due to the constructive and destructive interference of incident and reflected neutron beams from different layers of the sample. Let us consider the dissipative part β be negligible and therefore the condition for total internal reflection becomes $\delta > 0$ i.e. $n > 1$. Considering Snell's law from vacuum to the sample medium, the critical angle for total internal reflection becomes $\theta_c = \sqrt{2\delta}$ i.e.

$\sqrt{4\pi \frac{b_{coh}\rho_n}{k^2}}$ [135]. The dissipative part δ can be written as $\delta = \frac{\lambda^2}{2\pi} b_{coh}\rho_n = \frac{2\pi}{k^2} b_{coh}\rho_n = \frac{2\pi}{\hbar} V_n$ where V_n is the neutron-nucleus pseudo-potential. Since neutrons have magnetic moment, it will also contribute to the refractive index of the ferromagnetic material. The refractive index of the ferromagnetic material can be expressed as –

$$n(Q) = 1 - \frac{2\pi}{\hbar} (V_n \pm V_m) \quad (2.20)$$

where, V_m is the magnetic potential. The sign (+) and (–) corresponds to the parallel and antiparallel alignment of the initial neutron polarization to the magnetization [172]. Equation 2.20 shows that the refractive index of the magnetic material depends on the relative orientation of \mathbf{B} with respect to the neutron spin.

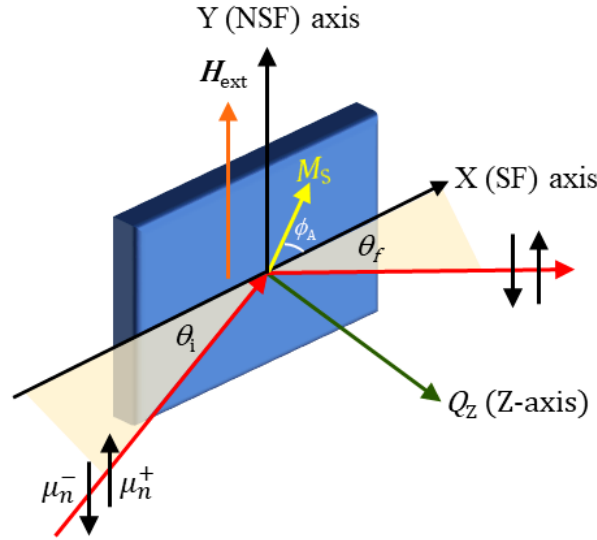


Figure 2.14: Schematic diagram of the scattering geometry for polarized neutron reflectivity in specular reflection mode. The Y-axis is the quantization axis for the neutrons known as the non-spin flip (NSF) axis and the X-direction is the spin flip (SF) axis. The resultant Q_z vector points towards the perpendicular to the surface along z-axis.

In specular reflectivity mode, the angle of incidence (θ_i) is equal to the angle of reflectance (θ_f). Figure 2.14 shows the scattering geometry of the PNR experiment. In this geometry the scattering vector is along the Z-axis i.e. the normal to the sample surface. The momentum transfer is similar to equation 2.4 i.e. $Q_z = \frac{4\pi}{\lambda} \sin\theta_i$. Depending on the neutron source, the range of Q_z during measurement can be decided either by varying θ_i and keeping the λ fixed, or by keeping θ_i fixed and changing λ within a specific range [173]. From the condition for the total internal reflection it can be inferred that the reflectivity will be 1 up to $Q_z < Q_c$ where $Q_c = \sqrt{16\pi\rho_n(b_{coh} + \rho_m)}$ where ρ_m is the magnetic scattering length related to the magnetic induction of the sample [174]. After the plateau of total internal reflections, the Keissig fringes are observed and the intensity of the neutron reflectivity decreases following

$\frac{1}{Q_z^4}$ relation. For a multi-layer sample, the reflectivity can be expressed using the first Born approximation in the $Q_z \gg Q_C$ range as follows:

$$R \approx \frac{1}{Q_z^4} |4\pi \sum_{l=1}^L [(\rho_n b_{coh})_l - (\rho_n b_{coh})_{l-1}] e^{iQ_z d_l}|^2 \quad (2.21)$$

where dl is the distance of the l^{th} layer's top interface from the surface [174]. The neutrons can be considered as a plane wave before it interacts with the sample and the magnetic field. Therefore, the interaction potential will only be a function of Z , which reduces the 3D Schrödinger equation to 1D. Let us consider that the magnetization of the sample lies in-plane and it can point towards any direction at an angle ϕ with respect to the scattering plane. Two major interactions take place upon exposing to the sample to the polarized neutron beam. (i) Short range nuclear interaction of the neutron with the atomic nucleus and (ii) Zeeman interaction between the magnetic moment of the neutron and the magnetic field produced by spin and orbital magnetic moments of the electrons. Therefore, the effective potential for the i^{th} layer of the multilayer can be written as –

$$V_{i,eff} = V_{i,n} + V_{i,m} \quad (2.22)$$

where V_n and V_m are given by $\frac{2\pi\hbar^2}{m} \rho_n b_{coh,n}$ and $-\boldsymbol{\mu}_n \cdot \mathbf{B}$, respectively. Here, m is the mass of the neutron. The magnetic induction \mathbf{B} can be decomposed as $\mathbf{B} = \mathbf{B}_{spin} + \mathbf{B}_{orbital}$. Hence equation 2.22 reduces to –

$$V_{eff} = \frac{2\pi\hbar^2}{m} \rho_n b_{coh,n} + \mu_n \boldsymbol{\sigma} \cdot \mathbf{B} \quad (2.23)$$

Therefore,
$$V \propto (\rho_n \pm \rho_m) \quad (2.24)$$

where, $\boldsymbol{\sigma}$ is the operator associated with the Pauli-spin matrices and $\boldsymbol{\mu}_n$ is the neutron magnetic moment. The positive and negative sign in equation 2.24 indicates the spin up and down state of the incident neutron. This signifies that the scattering length density of a magnetic sample is either the sum or the difference between the nuclear (ρ_n) and magnetic (ρ_m) scattering length densities [173]. The reflectivity can be expressed with the help of time

independent Schrödinger equation where the neutron wave functions can be expressed as the linear combination of up and down spin states: [173]

$$|\psi(r)\rangle = |\psi^+(r)|\chi^+\rangle + |\psi^-(r)|\chi^-\rangle = \begin{pmatrix} \psi^+ \\ \psi^- \end{pmatrix} \quad (2.25)$$

By solving the equation for both the non-spin flip (NSF) and spin flip (SF) scattering reflectivity can be obtained. The NSF scattering amplitude is expressed as $\rho_n \pm \rho_m \cos\phi_A$ where the information related to magnetization parallel or anti-parallel to the applied field is obtained. The y-component is the NSF one along which magnetic field is applied and the change in the effective potential occurs only due to this component. The specular reflectivity from the NSF channel (R^{++} and R^{--}) contains information related to the structural as well magnetic parameters. On the other hand, information related to the magnetization perpendicular to the applied field is obtained from the SF channel and it is expressed as $\rho_m^2 \sin^2\phi_A$ [173]. This component does not change the effective potential and causes a perturbation to the polarization to flip the neutron spins from the positive state to the negative state and vice versa. Spin flip is a purely magnetic property obtained from the R^{+-} and R^{-+} channels and does not occur in coherent nuclear scattering. Hence, the net magnetization vector can be obtained from the combination of the magnetization vectors from both the NSF and SF channels [175].

We have mostly performed PNR at MARIA reflectometer at MLZ, Garching, Germany to measure our Fe/C₆₀ and Co/C₆₀ bilayer as well as tri-layer samples discussed in the thesis [176]. At MLZ, neutrons are produced through fission process and the measurements are performed by choosing a specific wavelength of neutron and changing the incident angle. The ultrathin single layer Fe sample has been measured using NREX reflectometer at MLZ, Garching, Germany where the instrument is an angle dispersive fixed wavelength machine [177]. The default wavelength of NREX is 0.428 nm. However, the working principle of both the reflectometers are similar in nature and discussed in the following section. The schematic

layout of both the instruments are shown in figure 2.15. Neutrons travel through guides before interacting with the samples. The guides are constructed with supermirrors which are basically multilayers of thin metallic films viz. Ni and Ti. Inside the neutron guide neutrons are total internally reflected by the supermirrors so that neutrons cannot leave the guide until they reach the sample. Magnetic supermirrors are also used as a polarizer where multilayers are deposited with increasing value of the artificial periodicity. Before the sample spin flippers are used to change the neutrons to up or down state. After interacting with the sample, depending on the interaction the neutrons spin state may change. A second spin flipper is used after the sample which verifies if the incident spin state is changed or not after the reflection. Four possible scattering cross sections are R^{++} , R^{-} , R^{+-} and R^{-+} depending on the incident and final spin state of the neutron. The first and second signs in the scattering cross sections correspond to the incident and final neutron state, respectively. Finally, the neutrons are detected using ^3He analyzer.

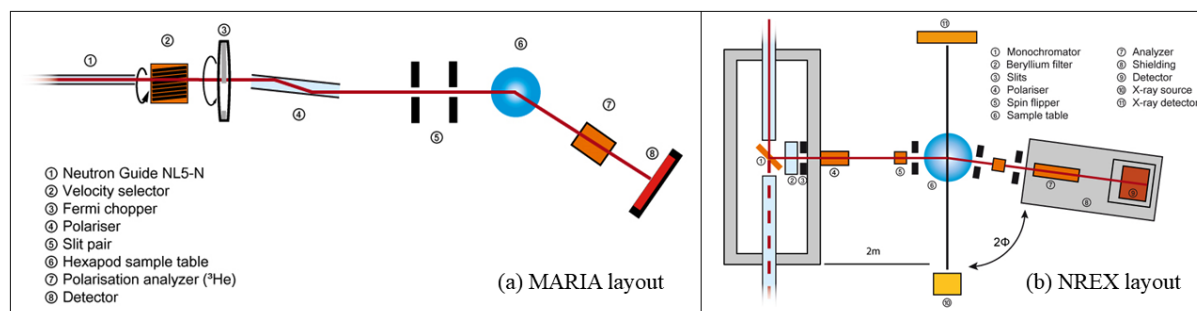


Figure 2.15: Schematic layout of the reflectometers (a) MARIA [176] and (b) NREX [177] at MLZ, Garching, Germany. The image has been taken from the respective websites. In both the facilities spin polarized neutrons interact with the sample and the reflected state (+ or -) of the neutron is measured using the ^3He detector. Spin flipper helps in measuring the non-spin flip and spin flip reflectivity.

MARIA is optimized to measure 3 – 300 Å thick samples. The available range of polarized neutron wavelengths at MARIA is $4.5 \text{ \AA} < \lambda < 10 \text{ \AA}$. A wide angle ^3He -cell analyzer was

used. In the standard configuration 1.3 T magnetic fields are provided and cryogenic temperatures down to 4K is available. Beside this standard setup magnetic fields up to 5T and temperatures from 50 mK to 500 K can be adopted with special arrangements. All parts of MARIA are remote controlled through software with automatic scan programs. The ultrathin single layer Fe sample has been measured using NREX reflectometer at the same place where similar measurement facilities are available. All the PNR data were fitted using GenX software [143] based on Parratt formalism [142] as discussed earlier in this chapter.

2.8 Ferromagnetic Resonance:

Ferromagnetic resonance (FMR) is a technique used to measure the dynamic magnetic properties of a ferromagnetic sample [178,179]. The magnetization of a ferromagnetic sample will align along a specific direction if a constant dc magnetic field is applied in that direction. Now it is possible to excite oscillation of the spins by applying a small perturbing field. Consequently, the spins will start precessing and will continue to do so until it gets back to its equilibrium through damping. The resonance phenomena in the magnetic sample can be explained both classically and quantum mechanically. According to the classical explanation, the resonance is observed when a transverse ac field is projected at the Larmor frequency i.e. $\omega = \gamma H$.

Quantum mechanically it can be explained by the Zeeman splitting of the energy levels with an external magnetic field. The energy levels of a magnetic sample are quantized when the electronic and nuclear moments of that sample are quantized. In presence of a uniform external magnetic field, the system absorbs energy from an oscillating magnetic field at specific frequencies corresponding to the transitions from the Zeeman splitted one energy level to another one. The phenomenon of absorption at a specific combination of magnetic field and frequency is known as the resonance. Figure 2.16 (a and b) shows the resonance phenomena in quantum mechanical path and a typical absorption spectrum at the resonance.

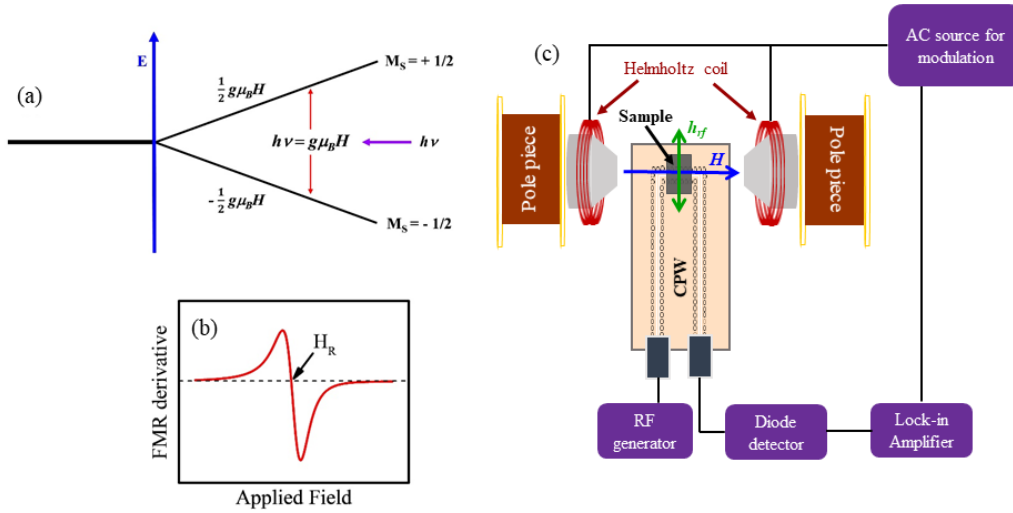


Figure 2.16: (a) Zeeman splitting of the energy levels of a ferromagnetic sample on application of uniform external magnetic field. (b) A typical FMR spectrum showing the resonance phenomenon occurred due to transitions between the energy levels shown in (a). (c) Schematic overview of the CPW FMR set-up used in our lab [180].

Figure 2.16 (c) shows the schematic diagram of the FMR set-up used in our lab. The yellow dotted rectangular plate where the sample is placed is the coplanar waveguide (CPW) with a ground-signal-ground (G-S-G) configuration. Here, the h_{rf} field travelling through the CPW acts as the perturbing field. Resonance occurs when the frequency of h_{rf} matches with the frequencies of the precessing spins of the ferromagnetic sample. Transmission coefficient is measured throughout the measurement and a remarkable decrease in the transmission coefficient is observed at the resonance due to absorption of energy. During a specific measurement, the external field is swept within a specific range by keeping the frequency of h_{rf} constant. It is possible to record frequency dependent H_{res} field by repeating the aforementioned procedure for a range of frequencies. The Kittel formula $f_r = \frac{\gamma}{2\pi} \sqrt{(4\pi M_S + H_{res} + H_K)(H_{res} + H_K)}$ is used to fit the data and the saturation magnetization (M_S) and anisotropy field H_K are obtained [178,179]. The dynamic behavior of the spin excitation such as the intrinsic damping of the ferromagnetic material can be

obtained from $\alpha = \frac{\Delta H \cdot \gamma}{4\pi f_r}$ relation where, ΔH is the line width of the derivative of the FMR spectra, γ is the gyromagnetic ratio of the ferromagnetic material and f_r is the measurement frequency^{55, 56}. In addition to the information on magnetization and damping, the FMR technique can provide information on the in-plane anisotropy constants. By choosing a constant frequency for h_{rf} , FMR spectra are measured to record the angle dependent H_{res} field. The total energy of a system can be expressed as: [76]

$$E_T = E_Z + E_a + E_d + E_{ex} + \dots \quad (2.26)$$

where, E_Z, E_a, E_d and E_{ex} are Zeeman, magnetocrystalline anisotropy, demagnetization and ferromagnetic exchange energy, respectively. The dispersion relation can be derived from equation 2.26 as follows,

$$\left(\frac{\omega}{\gamma}\right)^2 = \frac{1}{M^2 \sin^2 \theta} \left[\frac{\partial^2 E}{\partial \theta^2} \frac{\partial^2 E}{\partial \phi^2} - \left(\frac{\partial^2 E}{\partial \theta \partial \phi}\right)^2 \right] \quad (2.27)$$

Where, θ is the angles between the z-axis and the magnetization direction and ϕ is the angle between the x-axis and projection of the magnetization direction in the x-y plane. This analysis was used in this thesis to calculate the anisotropy constants of different Fe and Co samples possessing different combinations of magnetocrystalline anisotropies. The details of the anisotropy constant calculations are discussed in the respective chapters.

All the anisotropy, damping etc. measurements shown in this thesis are performed using a CPW-FMR manufactured by NanoOsc Instruments, Sweden [180]. The FMR Bandwidth of the system is 2-17 GHz and the maximum applied field is ~ 0.42 T.

Chapter 3: Study of magnetic properties in ultrathin Fe and Co films on MgO (001) substrates

A detailed understanding of the magnetization reversal mechanism in ultrathin films is necessary for both the fundamental research as well as technological applications [35,181-183]. Study of the magnetic properties viz. magnetic anisotropy, magnetization reversal mechanism, domain structures etc. in ultrathin ferromagnetic (FM) films will aid better control of each of these parameters. It is expected that FM films having good crystallinity will provide definite and better control of the intrinsic properties. Therefore, the growth conditions play a major role in controlling the magnetic properties of a thin film [24,184]. It should be noted that both Fe and Co exhibit epitaxial growth on MgO (001) substrate when deposited with required growth parameters. Urano *et al.* first reported the epitaxial growth of bcc Fe on MgO (001) substrate with $\text{Fe}(001)[110] \parallel \text{MgO}(001)[100]$ epitaxial relation [15]. Similarly, Nukaga *et al.* showed the possibility of epitaxial growth of Co on MgO substrate by following the relation $\text{Co}(11\bar{2}0)[0001] \parallel \text{MgO}(100)[001]$ and $\text{Co}(11\bar{2}0)[1\bar{1}00] \parallel \text{MgO}(100)[001]$ [22]. However, due to ~16% mismatch between Co and MgO lattice constants, textured or polycrystalline growth of Co is more probable on MgO (001) substrate. It should be noted that different crystalline structure leads to the induction of different anisotropy symmetry in the sample. Cubic lattice symmetry gives rise to an in-plane fourfold magnetic anisotropy in magnetic thin films [185]. Similarly, textured or hexagonal lattice symmetry induces uniaxial or six-fold anisotropies in the system [24]. Apart from the crystallinity induced anisotropy, uniaxial anisotropy can be induced in magnetic thin films by means of different techniques viz. self-shadowing effect due to oblique angle of deposition [77-82], preparation under a magnetic field [83], post-annealing under a field [84], interface effect arising from the bonding between the magnetic film and the substrate, [85,86] etc. In case of oblique angle deposition induced uniaxial anisotropy, the grains become elongated along the

perpendicular to the projection of the in-plane flux direction. Long range dipolar interaction between the elongated grains are the origin of this induced uniaxial anisotropy [78,79,186]. A systematic investigation on the effect of deposition angle on the uniaxial magnetic anisotropy for a series of 3 nm polycrystalline cobalt films on Si (111) substrates reveals that the direction of the uniaxial anisotropy is perpendicular to the flux direction for lower angle of deposition [81]. However, it becomes parallel to the deposition direction for a deposition angle $\geq 75^\circ$ [81].

Along with the anisotropy symmetry, the magnetization reversal can also be significantly influenced by the crystallinity and the grain structure of the film. Initially, the reversal mechanism for single crystalline Fe thin film having cubic anisotropy has been explained via a combination of 180° or 90° DW motion depending on the angle between the cubic easy axis and the applied field direction. Afterwards, a theoretical model by Zhan *et al.* expressed that two simultaneous or separate 90° DW motions can explain the reversal mechanism for a Fe sample having both cubic and uniaxial anisotropies [187]. Similarly, a theoretical study on polycrystalline Co thin film reveals that large grain size results in higher switching field [188]. Recently, Idigoras *et al.* showed the dependence of domain structures and anisotropy dispersion on the grain disorder of a partially epitaxial Co film on Si substrate [189-191]. The presence of ripple domains has been observed in polycrystalline Co films when the field is applied (in the film plane) at certain angles to the easy axis, which can be explained from the inverted nature of the hysteresis loop [82].

Apart from the inherent grain structure, the magnetization reversal is also affected by interfacial properties. The magnetization reversal of 3 nm Fe thin film on MgO (001) substrate has been discussed in section 3.1. Further, the effect of growth condition on the anisotropy, magnetization reversal and damping properties of ultrathin Co (3 nm) films on MgO (001) substrate has been discussed in section 3.2 [21].

3.1. Study of magnetization reversal in Fe (3 nm) thin film on MgO (001) substrate:

Ultrathin Fe film of 3 nm thickness has been prepared on commercially available MgO (001) substrate using dc magnetron sputtering. The base pressure of the vacuum chamber has been better than 3×10^{-8} mbar. The deposition pressure and the rate of deposition for Fe have been chosen to be 5×10^{-3} mbar and 0.022 nm/s, respectively. The substrate has been annealed at 700°C prior to deposition for 1 hour and the substrate temperature during Fe deposition has been kept fixed at 150°C. Due to the geometry of the deposition chamber the Fe plume was incident at 30° angle with respect to the substrate normal. To avoid the oxidation of the Fe layer, 7 nm Ta has been deposited in-situ as a capping layer. The sample structure is as follows: sample 3S_A: MgO (001)/Fe(3 nm)/Ta(7 nm).

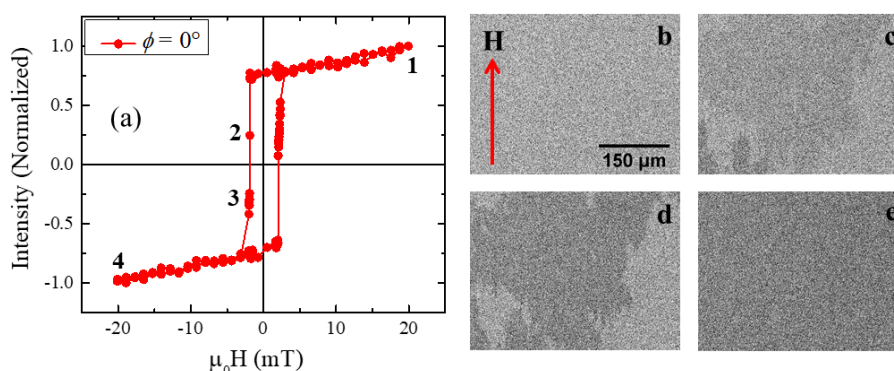


Figure 3.1:(a) Hysteresis loop measured along the easy axis ($\phi = 0^\circ$) for sample 3S_A in longitudinal mode at RT using MOKE microscope. (b) – (e) show the domain states corresponding to the field points marked by points 1 – 4, respectively, in the hysteresis loop (a). The applied field direction is shown with the red arrow. The scale bar shown in (b) is same for all the images.

The hysteresis loops and the corresponding domain images have been measured simultaneously using magneto optic Kerr effect (MOKE) microscope in longitudinal mode at RT. The angle ϕ between the easy axis and the applied field direction has been rotated at 10° interval during the measurement. Figure 3.1 shows the hysteresis loop and corresponding domain images along the easy axis ($\phi = 0^\circ$) of the sample. A single jump has been observed

in the hysteresis loop suggesting a 180° reversal. At the positive saturation (point 1 of the hysteresis loop shown in figure 3.1(a)) all the spins point toward the applied field direction producing a single domain state with white contrast (figure 3.1(b)) in the image plane. It should be noted that a positive slope is observed in the hysteresis loop (figure 3.1(a)) at the high fields. A possible reason for such a slope can be Faraday contribution from the transparent MgO substrate. Upon decreasing the magnetic field from the saturation, black contrast domains appear (figure 3.1(c)) corresponding to point 2 in the hysteresis loop (a). Large domains with irregular fractal boundaries have been observed (figure 3.1(d)). Previous reports suggest that such domains are observed for samples having poor crystalline quality and dispersed anisotropy symmetry [12]. Therefore, it can be inferred that the growth of Fe may not be proper in the ultrathin limit. Fe follows the Volmer-Weber growth mechanism where the grains form islands at the initial stage and eventually becomes a continuous layer. Probably the topmost Fe sub-layers could not form a continuous structure at the ultrathin limit [192]. Therefore, 3 nm of Fe was grown in polycrystalline form instead of the expected single crystalline structure.

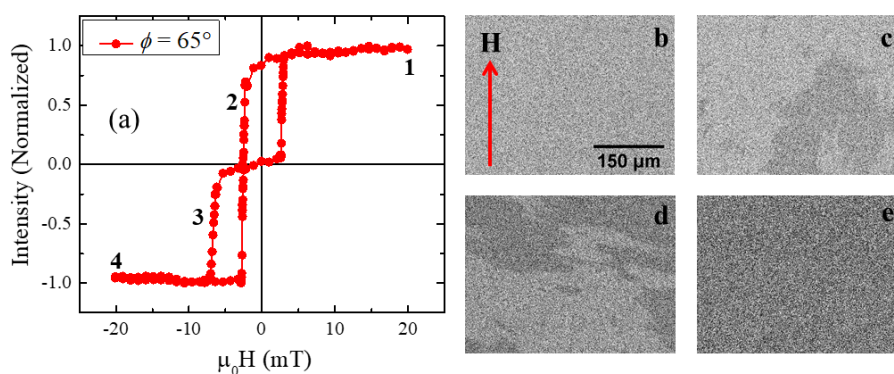


Figure 3.2:(a) Hysteresis loop measured along $\phi = 65^\circ$ for sample 3S_A in longitudinal mode at RT using MOKE microscope. (b) - (e) show the domain states corresponding to the field points marked by points 1 – 4, respectively, in the hysteresis loop (a). The applied field direction is shown with the red arrow. The scale bar shown in (b) is same for all the images.

While going away from the easy axis, double step loops are observed for $\phi > 45^\circ$. Figure 3.2 shows the hysteresis loop and corresponding domain images for $\phi = 65^\circ$. The reversal is governed via two separate DW motions. Theoretical model by Zhan *et al.* suggests that in the case of epitaxial Fe thin films having cubic anisotropy, two 90° DW motions are expected. However, sample 3S_A has not grown epitaxially at the ultrathin limit. Consequently, the features of two 90° DW motion are not prominent for all the angles. It should be noted that the hysteresis loop is not symmetric along $\phi = 65^\circ$. This may happen due to the presence of transverse component of magnetization in the sample. Such transverse components have also been observed previously in Fe thin films [193-197].

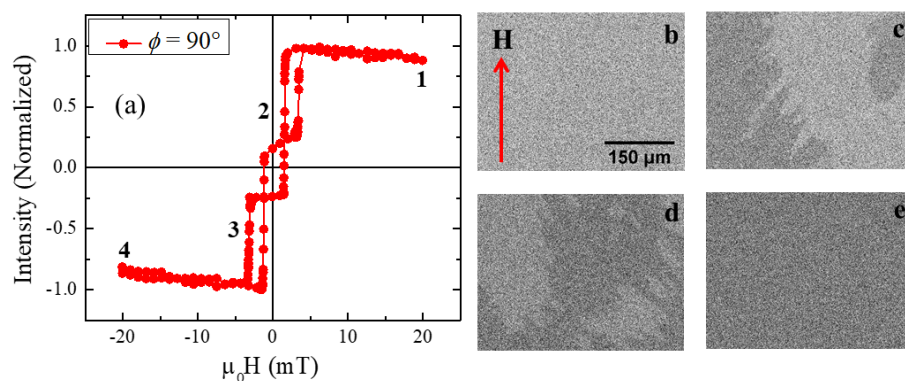


Figure 3.3:(a) Hysteresis loop measured along $\phi = 90^\circ$ for sample 3S_A in longitudinal mode at RT using MOKE microscope. (b) - (e) show the domain states corresponding to the field points marked in the hysteresis loop (a). The applied field direction is shown with the red arrow. The scale bar shown in (b) is same for all the images.

A complex shape of hysteresis loop has been observed along $\phi = 90^\circ$ for sample 3S_A. Figure 3.3 shows the hysteresis loop and corresponding domain images along $\phi = 90^\circ$. While decreasing the applied field from the positive saturation state (point 1 in figure 3.3(a)), first reversal occurs through 90° DW motion (figure 3.3(c) corresponding to point 2 in figure 3.3(a)) even before the switching of the field direction. By further decreasing the magnitude, the direction of the field gets switched. Afterwards, the second reversal happens via another 90° DW motion (figure 3.3(d) corresponding to field point 3 in figure 3.3(a)). Therefore, the

expected reversal mechanism with two 90° DW motions is observed here. The complex shape of the hysteresis loop can be explained by the presence of a transverse component in the sample. In sample 3S_A, uniaxial anisotropy is expected due to the oblique angle of deposition of the Fe layer. Along with this, a weak contribution from the cubic anisotropy may be present due to the substrate pre-annealing effect. However, both of them may not be aligned with each other and the anisotropy contribution is not clear enough (not shown here). As a consequence, presence of transverse component of magnetization is expected in the sample.

To obtain the direction of the net magnetization of the Fe layer, polarized neutron reflectivity (PNR) measurement has been performed at saturation, remanence and coercivity states along different ϕ directions. The measurements have been performed in specular reflectivity mode at NREX reflectometer at MLZ, Garching, Germany [177]. The wavelength (λ) of the neutrons during the PNR measurements has been chosen to be 0.428 nm. Both the non-spin flip (NSF) and spin flip (SF) scattering cross sections R^{++} (up - up), R^{--} (down - down), R^{+-} (up - down) and R^{-+} (down - up) have been measured at RT. The first and second signs in the scattering cross section correspond to the polarization of the incident and the reflected neutrons, respectively. The intensity of the reflected neutrons has been measured as a function of the momentum transfer (Q_z). The relation between Q_z and the incidence/reflected angle of neutron is $Q_z = \frac{4\pi}{\lambda} \sin\theta$ where θ is the angle of incidence/reflection. Figure 3.4(a) shows the PNR data (open circles) and the corresponding fits (solid lines) for sample 3S_A measured at the positive saturation state ($\mu_0 H = 450$ mT) along $\phi = 0^\circ$. The red and blue open circles represent the data measured for the R^{++} and R^{--} channels, respectively (Figure 3.4(a)). At saturation the presence of spin-flip scattering is not expected. Therefore, spin-flip measurements were not been performed at saturation. The fitting was performed using GenX software [143] which is based on the Parratt formalism [142]. The figure of merit (FOM) for all the fits are less than 7×10^{-2} .

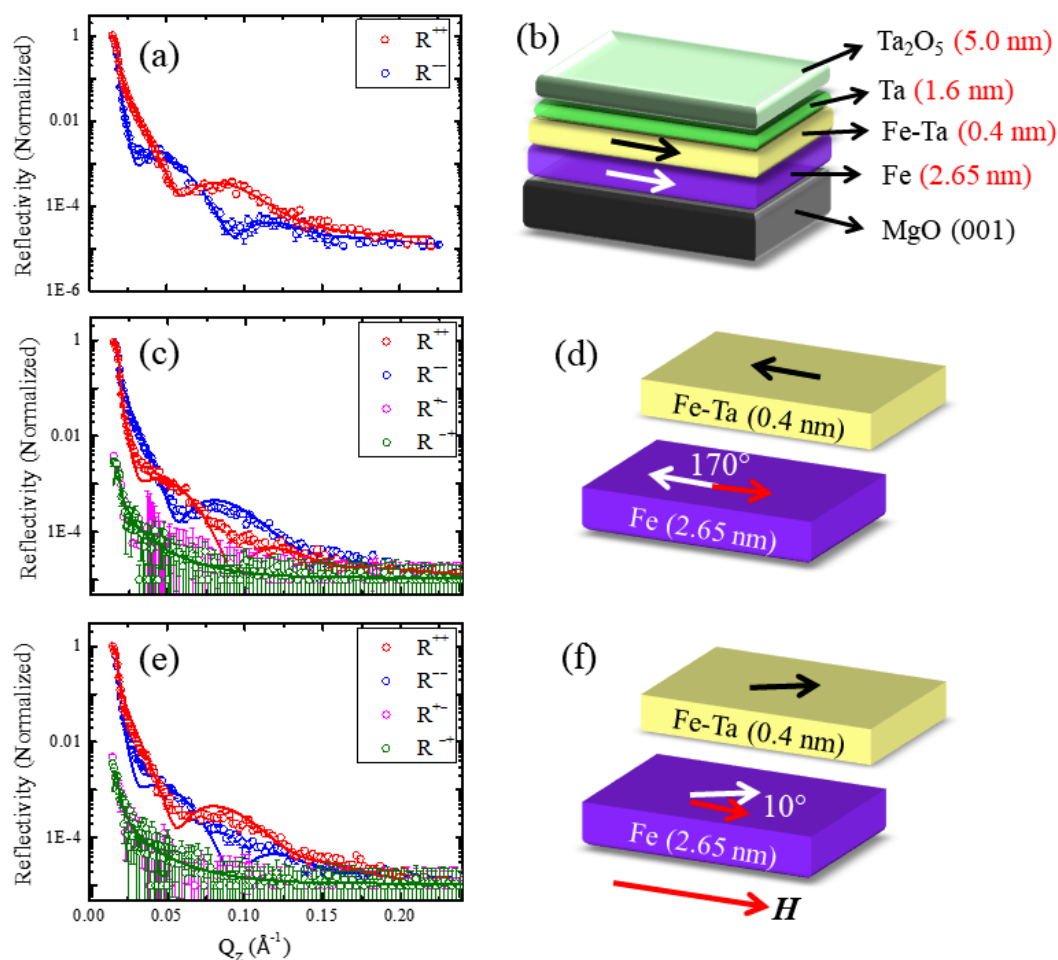


Figure 3.4: (a) Polarized neutron reflectivity data measured at the saturation state along $\phi = 0^\circ$ at RT and its corresponding fits for sample 3S_A. The red and blue open circles represent the data measured for the R^{++} , and R^{--} channels, respectively. The solid lines correspond to their respective fits. (b) A schematic representation of the sample structure obtained by fitting the PNR data shown in (a). The numbers written in brackets correspond to the fitted thickness of the respective layer. (c) and (e) show the PNR data and fits near the remanence and coercivity, respectively. Similar to R^{++} , and R^{--} channels, pink and green open circles represent the data measured for the R^{+-} and R^{-+} channels, respectively. (d) and (f) show the schematic representation of the ferromagnetic layers. The arrows shown in (b), (d) and (f) correspond to the net magnetization direction of the respective layer. The red arrow shows the direction of the applied field for (a) – (c).

The layer structure of the sample obtained from the best fitted PNR data has been shown in figure 3.4(b). A thin layer of interdiffusion (0.40 ± 0.05 nm) between the Fe and Ta layers has been found (denoted as Fe-Ta) from the PNR fit. It has also been observed that 71% of the Ta capping layer has become oxidized. For this sample, the PNR measurement has been performed after ~ 1.5 years of its preparation. Probably, within this long time the capping layer has become oxidized. However, the magnetic properties of the FM layer have not been affected as the capping layer was not fully oxidized. From the best fit of the PNR data it has been obtained that at the saturation the Fe and interdiffused Fe-Ta layers exhibit magnetic moment of 2.20 ± 0.05 and $1.44 \pm 0.30 \mu_B/\text{atom}$, respectively. The angle between the applied field direction and the net magnetization of each layer has been obtained from the fitting of the spin-flip data. The direction of the net magnetization of Fe and Fe-Ta layers are shown by white and black arrows, respectively in figure 3.4(b). At the saturation all the spins in both Fe and Fe-Ta layers point along the applied field direction (figure 3.4(b)).

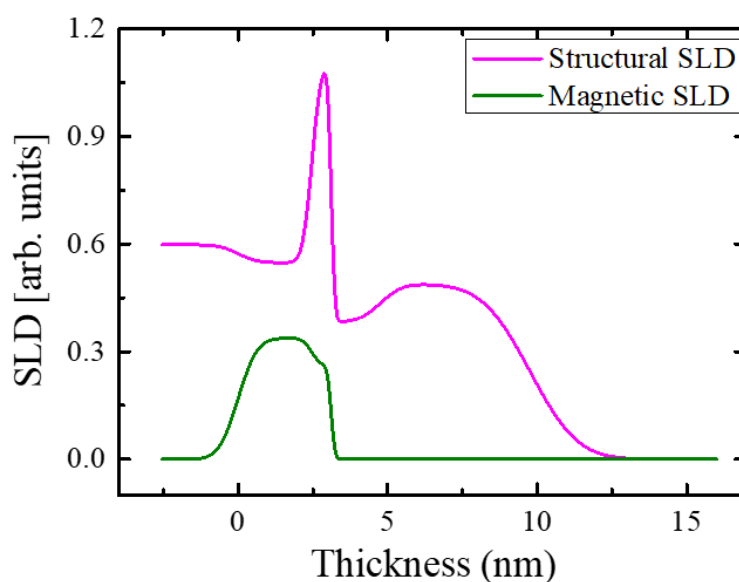


Figure 3.5: Structural and magnetic scattering length density (SLD) vs thickness for sample 3S_A

To understand the layer structure of sample, a plot showing the structural and magnetic scattering length density (SLD) with respect to the sample thickness is depicted in figure 3.5. For the first ~ 2.6 nm of the sample the structural and magnetic SLD is very high. This indicates the presence of Fe layer. Further, for a very low thickness (~ 0.5 nm) a slight drop in the SLD is observed for the Fe-Ta interdiffused layer. The magnetic SLD drops to zero after crossing the Fe-Ta layer. The structural SLD line indicates the presence of Ta and Ta₂O₅ layer in this region.

This sample has been also measured near remanence (1 mT) and coercivity (2.1 mT) to elucidate the net magnetization direction of the layers during the reversal. Figure 3.4 (c) – (f) show the PNR data and the schematic for the net magnetization of the magnetic layers near the remanence and the coercivity states. It has been observed from the best fit of the remanence data (figure 3.4(c) and (d)) that the Fe layer spins point in negative direction at an angle of 170° with respect to the saturation magnetization direction. The Fe-Ta layer follows the same reversal mechanism as the Fe layer showing negative moment with a net magnetization direction $\sim 170^\circ$. As the magnetic moment and the thickness is less for the Fe-Ta layer in comparison to the Fe layer, Fe-Ta follows the magnetization directions for the Fe layer. The measurement near the coercive field provides the direction of the net magnetization of both the Fe and Fe-Ta layer to be at 10° (figure 3.4(f)) i.e. almost positive saturation state. Therefore, very weak transverse component is present along $\phi = 0^\circ$ where the reversal occurs via 180° DW motion as obtained from the MOKE measurement.

Similar measurements have been performed in sample 3S_A along $\phi = 65^\circ$ to observe the transverse components expected from the previously discussed Kerr measurements. The PNR measurement at the saturation state along $\phi = 65^\circ$ (data not shown here) provides similar information like the saturation state along $\phi = 0^\circ$. All the spins from both the Fe and Fe-Ta layers stay parallel along the applied field direction.

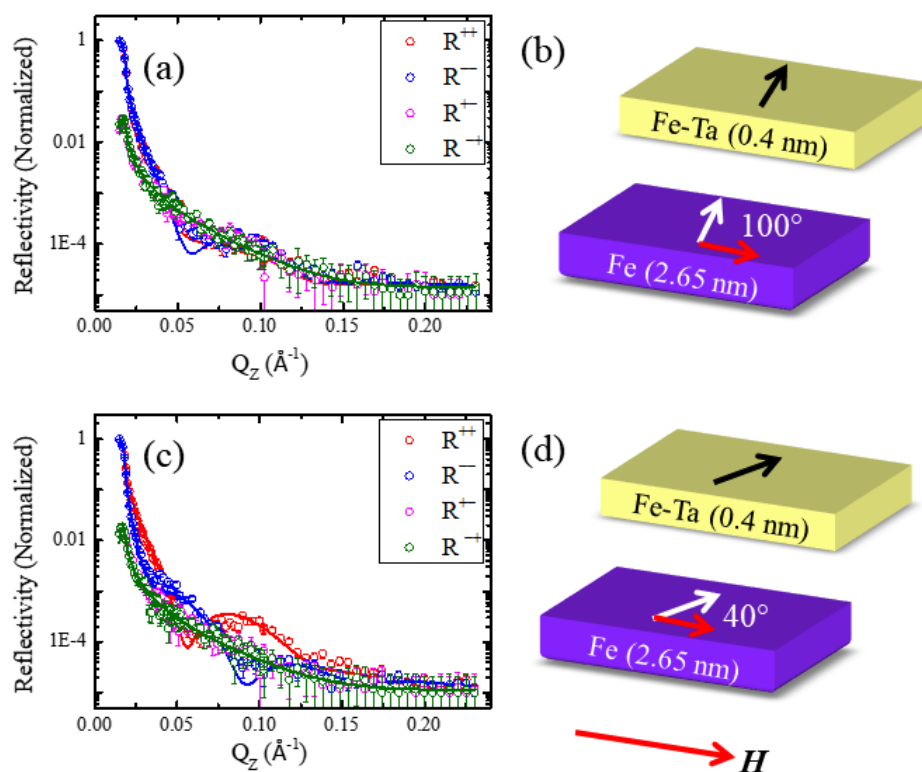


Figure 3.6: Polarized neutron reflectivity data and its corresponding fits for sample 3S_A along $\phi = 65^\circ$ at (a) remanence and (c) coercivity state. The red, blue, pink and green open circles represent the data measured for the R^{++} , R^{--} , R^{+-} and R^{-+} channels, respectively. The solid lines correspond to their respective fits. (b) and (d) show the schematic representation of the ferromagnetic layers where the arrows correspond to the net magnetization direction of the respective layer. The red arrow shows the direction of the applied field.

However, near the remanence state, the net magnetization direction for the Fe layer points along 100° with respect to the saturation magnetization direction (figure 3.6(b)). This indicates that already $\sim 90^\circ$ reversal has taken place. By further increasing the magnetic field amplitude towards the coercive field yields the net magnetization direction of the Fe layer to be at 40° angle (figure 3.6(d)). Therefore, the reversal happens via two steps with the presence of transverse component along 100° . This observation is in good agreement

with the domain images obtained from the MOKE measurements. It should be noted that the Fe-Ta layer always follows the net magnetization of the Fe layer.

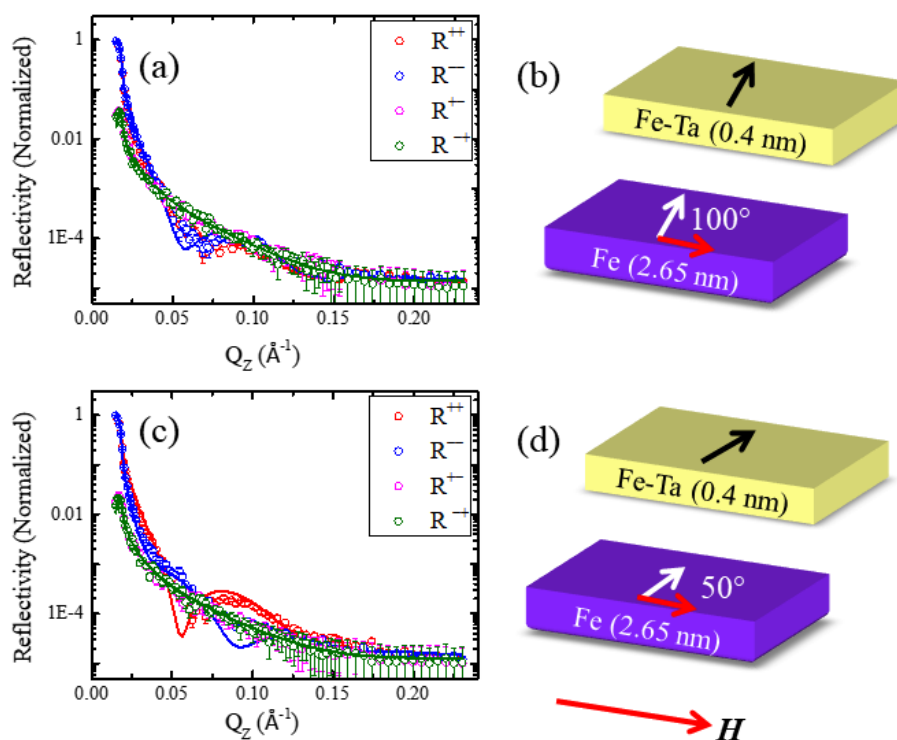


Figure 3.7: Polarized neutron reflectivity data and its corresponding fits for sample 3S_A along $\phi = 90^\circ$ at (a) remanence and (c) coercivity state. The red, blue, pink and green open circles represent the data measured for the R^{++} , R^{--} , R^{+-} and R^{-+} channels, respectively. The solid lines correspond to their respective fits. (b) and (d) show the schematic representation of the ferromagnetic layers where the arrows correspond to the net magnetization direction of the respective layer. The red arrow shows the direction of the applied field.

Figure 3.7 shows the PNR data and the net magnetization directions of the Fe and Fe-Ta layers along $\phi = 90^\circ$ near the remanence and coercive state. Similar to $\phi = 65^\circ$, transverse component has been observed along $\phi = 90^\circ$. Near the remanence state the net magnetization of both the Fe and Fe-Ta layers point along 100° (figure 3.7(b)). Further, near the coercive state the net magnetization direction rotates at 50° angle. Therefore, the magnetization

reversal happens through two 90° DW motions along $\phi = 90^\circ$ as expected from the previously discussed domain images. Therefore, the PNR measurement confirms the presence of transverse components for $\phi > 45^\circ$. Also, the reversal mechanism for ultrathin Fe film on MgO (001) substrate has been understood by fitting the PNR data measured along different ϕ for different fields. As the sample structure obtained from the PNR fit shows oxidation of the capping layer (Ta) with time, we have measured zero field cooled and field cooled hysteresis loop of sample 3S_A at 10K to check the presence of exchange bias (if any) using SQUID magnetometer. However, no shift in the hysteresis loop has been observed for the field cooled hysteresis loop (data not shown). This confirms that the oxidation of the Ta layer is stopped after a certain thickness and the Fe layer is prevented from oxidation.

3.2. Study of anisotropy, magnetization reversal and damping properties in Co (3 nm) thin films on MgO (001) substrate:

Co thin films of 3 nm thickness have been deposited on MgO (001) substrates using dc magnetron sputtering. The base pressure of the deposition chamber was better than 3×10^{-8} mbar. Two samples with a structure of MgO(001)/Co(3 nm)/Ta(3 nm) have been prepared by varying the pre-annealing conditions. For sample 3S_B, the substrate has been annealed at 650°C for 1 hour prior to deposition whereas no pre-annealing of the substrate has been performed for sample 3S_C. Similar to the Fe film, the Co films also have been deposited at a substrate temperature of 150°C for both the samples. The rate of Co deposition has been chosen to be 0.02 nm/s. Due to the geometry of the deposition chamber, the Co layer has been grown at an oblique angle of 30° with respect to the substrate normal. To prevent from oxidization, 3 nm of Ta has been deposited in-situ as a capping layer on top of the Co layer for both the samples.

The hysteresis loops have been measured for both the samples at RT in longitudinal mode using MOKE based microscopy. Figure 3.8 depicts the angle dependent ($\phi = 0^\circ, 30^\circ, 60^\circ$ and

90°) hysteresis loops for samples 3S_B and 3S_C, respectively. It should be noted from figure 3.8(a) that the coercive field increases while going away from the easy axis for sample 3S_B. This is the reverse situation as usually the coercivity is largest along the easy axis. The coercivity behavior in sample 3S_B may be explained by the presence of two anisotropies in the system which is discussed later in this section. In contrary, sample 3S_C exhibits usual ferromagnetic behavior with a well-defined uniaxial anisotropy by showing the largest coercivity value along its easy direction (figure 3.8(b)).

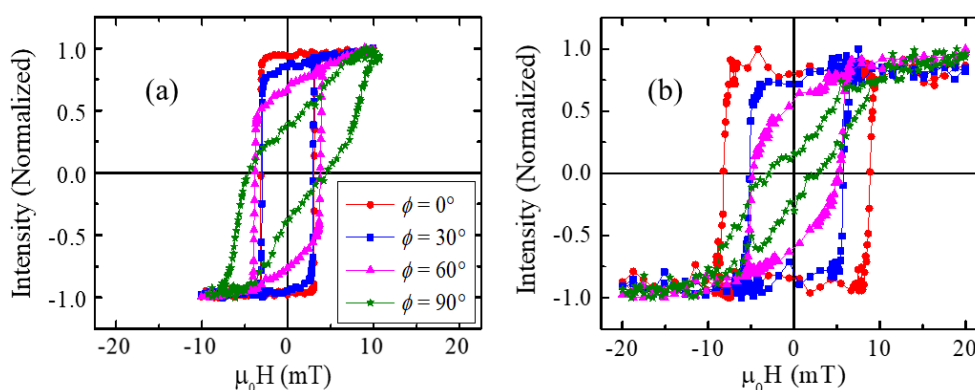


Figure 3.8: Hysteresis loops measured using longitudinal MOKE microscopy for (a) sample 3S_B, and (b) sample 3S_C along $\phi = 0^\circ$ (EA), 30° , 60° and 90° . The legends to represent different angles for both the samples are shown in (a). Both the graphs are plotted in the same scale for better comparison.

Another way of determining the easy axis is by taking the ratio between the remanent magnetization (M_r) and saturation magnetization (M_s). Figure 3.9 shows the anisotropy behavior as a function of ϕ . Sample 3S_B exhibits uniaxial anisotropy like behavior with an asymmetry along the two-fold axis. Uniaxial anisotropy is expected in the samples due to the oblique angular deposition of Co. As discussed earlier, the grains formed due to the oblique deposition are elongated in a specific direction which in turn induces a preferential direction in the sample [10,198]. In case of epitaxial or textured growth of Co, cubic anisotropy is expected in the sample. However, for ultrathin film of 3 nm Co (sample 3S_B) the cubic

symmetry is not profound. According to the Volmer-Weber growth mechanism, the Co atoms first form island like structures on the substrate and eventually the islands grow on the substrate plane to form continuous thin film. Due to the lattice mismatch between Co and MgO atoms, grain misalignment is expected in our samples. The grain misalignment may induce a preferential growth direction in sample 3S_B. The presence of two anisotropies can be observed from the blue colored curve in figure 3.9 for sample 3S_B. However, it is not possible to understand the exact anisotropy symmetry as the anisotropies are misaligned to each other. On the other hand, sample 3S_C shows purely uniaxial anisotropy behavior due to the presence of oblique angular deposition and absence of pre-annealing.

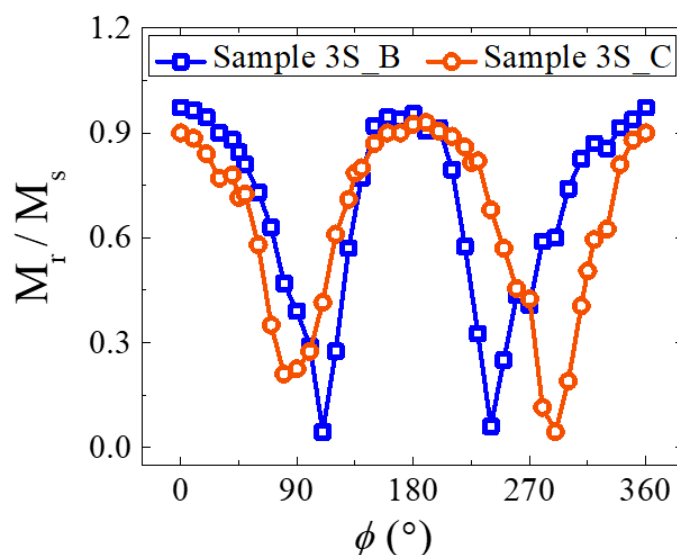


Figure 3.9: M_r/M_s vs. ϕ plot for samples 3S_B (blue colored squares) and 3S_C (orange colored circles) measured using MOKE microscopy showing the anisotropy behavior.

Figure 3.10 depicts the domain images of both the samples at coercivity measured by MOKE based microscopy in longitudinal mode along 0° (EA), 30° , 60° and 90° . For sample 3S_B, the magnetization reversal is governed by nucleation followed by propagation of DWs. In this case, the nucleation occurs at a few sites and the reversal gets completed via DW motion. However, for sample 3S_C the magnetization reversal is governed by simultaneous

nucleation and propagation of branched domains. The domain size decreases for sample 3S_C in comparison to sample 3S_B. It is expected that the growth of sample 3S_B will be better than sample 3S_C due to the substrate pre-annealing effect which may lead to bigger grain size in case of sample 3S_B. Increase in grain size leads to enhancement in exchange coupling which in turn results in bigger domain size [11,82,199]. While going away from the easy axis the domains get tilted along the field direction for both the samples (figure 3.10(b), (c), (f) and (g)).

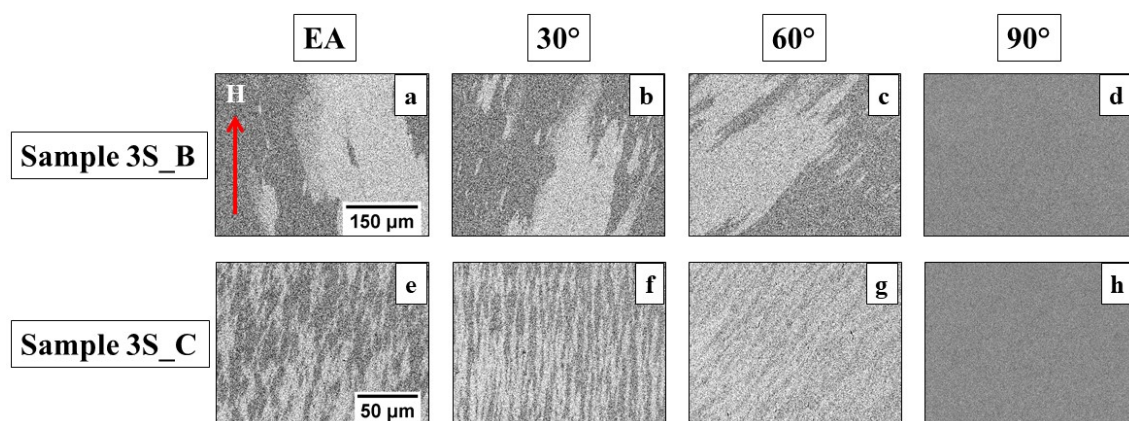


Figure 3.10: Domain images measured using longitudinal MOKE microscopy at coercivity for sample 3S_B (a) – (d) and sample 3S_C (e) – (h) along 0° (EA), 30°, 60° and 90°. The arrow shown in (a) represents the applied field direction for all the measurements. The scale bars in (a) and (e) are same for all other images for samples 3S_B and 3S_C, respectively.

For angles close to the hard axis the magnetization reversal occurs via coherent rotation (figure 3.10 (d) and (h)). Unlike sample 3S_B, branched domains are observed in sample 3S_C. This type of branched domain is mostly observed in case of strongly misoriented surface in highly anisotropic materials like NdFeB[12]. However, for lower anisotropy materials like Co, the character of the branched domain pattern remains same in the macroscopic view, but differs in the fine structure [12]. In sample 3S_C, the branched domains appear due to the poor growth of Co on non-annealed MgO (001) substrate. The

decrease in domain size in sample 3S_C can be explained in terms of the smaller grain size [11]. The magnetization reversal is dominated by coherent rotation near the hard axis (figure 3.10(d) and (h)) due to the uniaxial nature of both the samples.

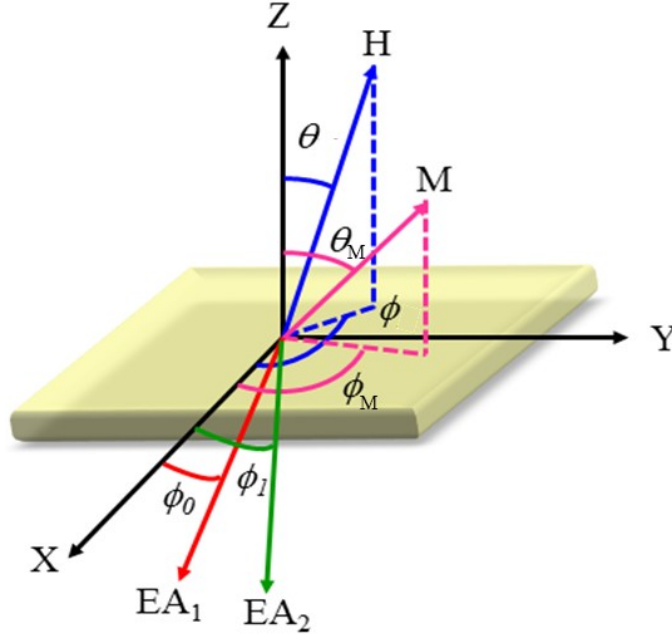


Figure 3.11: Schematic of the direction of the magnetization, applied field, easy axis with respect to the sample orientation considered for the analysis of the FMR data.

To understand the anisotropy symmetry of thin films, angle (ϕ) dependent (FMR) measurements have been performed by applying the field along the sample plane and at a fixed frequency of 6.5 GHz. The total magnetic free energy density of the system having two in plane anisotropies can be written as [200]:

$$E = -HM_S[\sin\theta\sin\theta_M \cos(\phi_M - \phi) + \cos\theta\cos\theta_M] - 2\pi M_S^2 \sin^2\theta_M + K_U \sin^2\theta_M + K_{2a} \sin^2\theta_M \sin^2(\phi_M - \phi_0) + K_{2b} \sin^2\theta_M \sin^2(\phi_M - \phi_1) \quad (3.1)$$

where K_U is the perpendicular uniaxial anisotropy constant and K_{2a} , K_{2b} are the in-plane two-fold anisotropy constants. According to figure 3.11 the sample is placed in the x-y plane. ϕ_M is the angle between the x-axis and projection of the magnetization direction in the x-y plane. ϕ_0 , ϕ_1 denote the angles between the in-plane easy axis directions and the x-axis and ϕ is the angle between the x-axis and the projection of applied field in x-y plane. θ_M and θ are the

angles between the z-axis and the magnetization direction and the applied field direction, respectively. To evaluate the strength of the anisotropies present in sample 3S_B, angle dependent resonance fields (H_R) have been fitted using the following dispersion relation derived from equation 3.1:

$$\left(\frac{\omega}{\gamma}\right)^2 = [H \cos(\phi_M - \phi) - h_U + h_{2a} \sin^2(\phi_M - \phi_0) + h_{2b} \sin^2(\phi_M - \phi_1)] [H \cos(\phi_M - \phi) + h_{2a} + h_{2b} + 2h_{2a} \sin^2(\phi_M - \phi_0) + 2h_{2b} \sin^2(\phi_M - \phi_1)] \quad (3.2)$$

$$\text{Here, } h_U = 2 \frac{K_U}{M_S} - 4\pi M_S \quad (3.3)$$

$$\text{and } h_{2a,b} = 2 \frac{K_{2a,b}}{M_S} \quad (3.4)$$

where, h_U is uniaxial anisotropy representation (perpendicular to surface), h_{2a} , h_{2b} are in-plane anisotropy representations and ϕ_0 , ϕ_1 are the angles associated with h_{2a} and h_{2b} , respectively. As both the applied field and the magnetization are in-plane in our case, therefore, θ and θ_M are considered to be zero. The angle-dependent resonance field (H_R) data and the curves fitted by equation 3.2 are shown in figure 3.12. The blue dotted curve exhibits the fit with one uniaxial anisotropy i.e. by keeping h_{2b} and ϕ_1 zero. It can be clearly seen from figure 3.12 that the data do not fit if only one anisotropy is considered to be present in sample 3S_B. However, the solid red line in figure 3.12 follows the data behavior when fitted with two anisotropies. The strength of both the anisotropies h_{2a} and h_{2b} are 24.22 ± 0.79 and 16.79 ± 1.57 mT, respectively. The corresponding ϕ_0 and ϕ_1 values are $-9.8 \pm 0.9^\circ$ and $8.4 \pm 1.3^\circ$, respectively. Therefore, it can be concluded that the anisotropy contribution from h_{2a} is $\sim 31\%$ stronger than that of h_{2b} and are misaligned by $\sim 18^\circ$. Hence, it is believed that the uniaxial anisotropy induced due to the oblique angular growth is the stronger one (h_{2a}). Another uniaxial anisotropy contribution may have arisen from the disorientation of the Co grains due to the lattice mismatch (16%) between the Co and the MgO (001) substrate. The

expected texture growth of Co on pre-annealed MgO (001) substrate may lead to some preferential growth directions of Co grains, which in turn induces a uniaxial anisotropy.

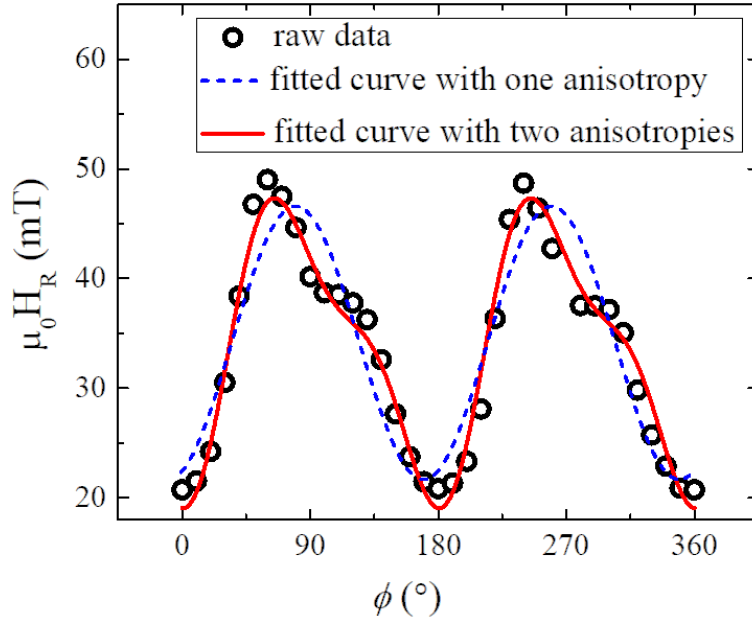


Figure 3.12: Anisotropy symmetry plot and the fits for sample 3S_B measured using FMR keeping the frequency fixed at 6.5 GHz.

It is expected that an additional out-of-plane anisotropy will exist in case of ultrathin films due to the interface between Co and Ta layer [201-203]. The fitting yields an additional out-of-plane interfacial anisotropy to be $h_U = 17.68 \pm 0.58$ mT. Both the out-of-plane and in-plane anisotropy constants are calculated by using equations 3.3 and 3.4, respectively. The out-of-plane and average in-plane anisotropy constants K_U and K_2 are 1.01×10^6 and 1.53×10^4 J/m³, respectively. The comparative lower value of the in-plane anisotropy constant indicates that the preferred magnetization direction lies in the plane of the sample and much higher field is needed to saturate the sample when field is applied along the out-of-plane direction.

To verify the anisotropy values calculated from the FMR measurement, the magnetization of the sample 3S_B (figure 3.13) has been measured using a SQUID magnetometer by applying the field in both in-plane and out-of-plane directions at RT. It has been observed that the

hysteresis loops measured by applying the field in the film-plane, can be saturated at ~ 20 mT. However, the same sample 3S_B needs much higher magnetic field ~ 1.6 T to saturate when the field has been applied in the out-of-plane geometry. The values of the K_U and K_2 calculated from the SQUID measurements are 1.01×10^6 and 1.50×10^4 J/m³, respectively. These values are in good agreement with the ones calculated from the FMR measurements.

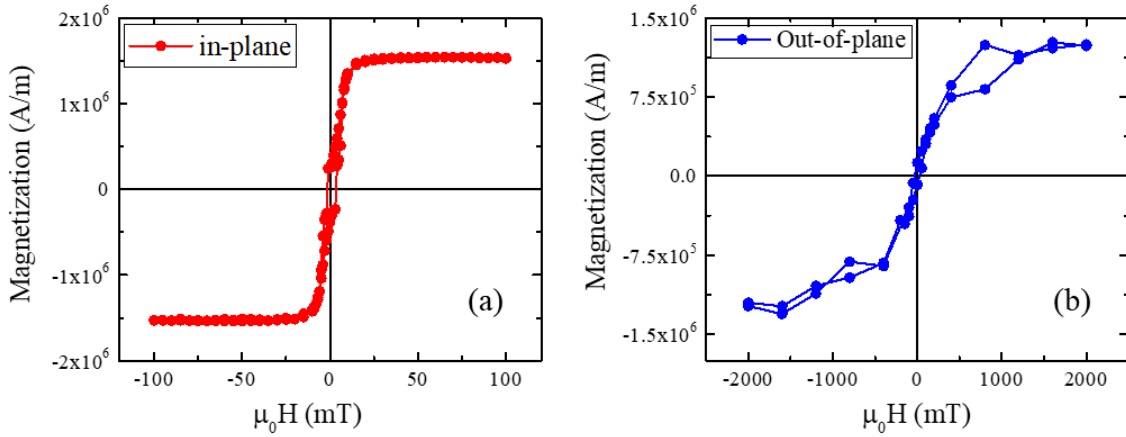


Figure 3.13: Hysteresis loops measured by SQUID for sample 3S_B when the field is applied along (a) in-plane and (b) out-of-plane direction.

It should be noted that K_U is larger than K_2 by two orders of magnitude. Further, the positive sign of h_U indicates that (from equation 3.3) K_U is dominating over the shape anisotropy ($4\pi M_S$). This means when the magnetic field is applied in the film plane the spins can switch from one saturated state to the reverse one via in-plane rotation. However, with sufficient large perpendicular magnetic field to the film plane it is possible to rotate the spins out of the plane. Further, for a magnetic field applied at certain polar angle to the film plane it may lead to both in-plane and out-of-plane magnetization components because h_U , h_{2a} and h_{2b} have comparable values. Nevertheless, it should be noted that in this work we have focused on the magnetization reversal only for in-plane magnetic fields.

In summary, the magnetic properties of ultrathin Fe and Co films grown on MgO (001) have been studied. Both the Fe and Co growth have not been found to be single

crystalline/textured at the ultrathin limit probably due to high deposition rate or absence of substrate rotation during deposition. A thorough understanding of the magnetization reversal mechanism of ultrathin Fe films reveals the presence of transverse component away from the easy direction. Further, ultrathin Co films exhibit presence of additional uniaxial anisotropy due to the substrate pre-annealing along with the uniaxial anisotropy induced by oblique angular deposition. The misalignment between both the anisotropies has been calculated. However, to obtain better crystalline Fe and Co thin films, bilayers of fullerene (organic material)/ferromagnet have been prepared with thicker Fe and Co layers on MgO (001) substrate and have been chosen to study the spinterfacial properties. However, future studies are required to control the growth of the ultrathin films to tune their properties to be used for spinterface studies.

Chapter 4: Thickness dependence of spinterfaces in polycrystalline Fe/C₆₀ films

In this chapter the thickness dependent magnetic properties of polycrystalline Fe thin films have been discussed. Fe shows polycrystalline nature when deposited on Si (100) substrate at RT. Si substrates possess naturally grown native oxide (SiO₂) layers in its surface (if not treated separately to remove the native oxide layer) due to the surface oxidation. If Fe is deposited on top the SiO₂ layers, the growth of Fe becomes polycrystalline in nature due to the lattice mismatch between Fe and SiO₂. The magnetic properties viz. magnetization reversal, domain images, anisotropy etc. of single layer polycrystalline Fe thin films with variable thicknesses have been discussed in section 4.1 of this chapter. Further, bilayers and tri-layers of Fe/C₆₀ have been prepared to study the effect of the spinterface on the aforesaid magnetic properties. Spinterface plays a crucial role in organic spintronics devices by controlling the spin polarization in magnetic field sensors [54], generating spin-filtering effects in nonmagnetic electrodes [52], altering the anisotropy symmetry [18], inducing exchange bias property [204], or giving rise to a RT ferromagnetism in nonmagnetic elements [62]. However, the effect of such spinterfaces on the magnetization reversal and domains of the FM/OSC systems are not much explored. It has been reported in previous literature that magnetic moment can be induced in C₆₀ at the FM/C₆₀ interface due to hybridization of FM and Carbon molecular orbitals [6,8]. However, the dependence of the induced moment and the thickness of the spinterfaces on the crystalline quality and the thickness of the underneath FM layer is not discussed so far. Further, the tunability of the anisotropy symmetry of polycrystalline Fe/C₆₀ systems due to such hybridization of orbitals is discussed in this chapter. The effect of spinterface on the magnetic properties of bilayer and tri-layer Fe/C₆₀ samples prepared on Si (100) substrates is discussed in section 4.2 and 4.3, respectively.

4.1. Study of magnetization reversal and anisotropy symmetry in single layer Fe thin films with variable thickness:

Single layer Fe thin films of different thicknesses have been deposited at RT using dc magnetron sputtering technique. The samples were grown on commercially available Si (100) substrates with a layer of native oxide (SiO₂). The base pressure of the system has been better than 3×10^{-8} mbar. The deposition pressure and rate for Fe have been chosen to be 5×10^{-3} mbar and 0.02 nm/s, respectively. To prevent Fe from the oxidation, a capping layer of Ta was deposited in-situ in all samples using dc magnetron sputtering. The details of the sample structures are discussed in table 4.1.

Table 4.1. Details of single layer polycrystalline Fe samples prepared on Si (100) substrate

Sample name	Sample structure
Sample 4S_A	Si (100)/SiO ₂ (native oxide)/Fe (3.5 nm)/Ta (3 nm)
Sample 4S_B	Si (100)/SiO ₂ (native oxide)/Fe (7.5 nm)/Ta (3 nm)
Sample 4S_C	Si (100)/SiO ₂ (native oxide)/Fe (18 nm)/Ta (3 nm)

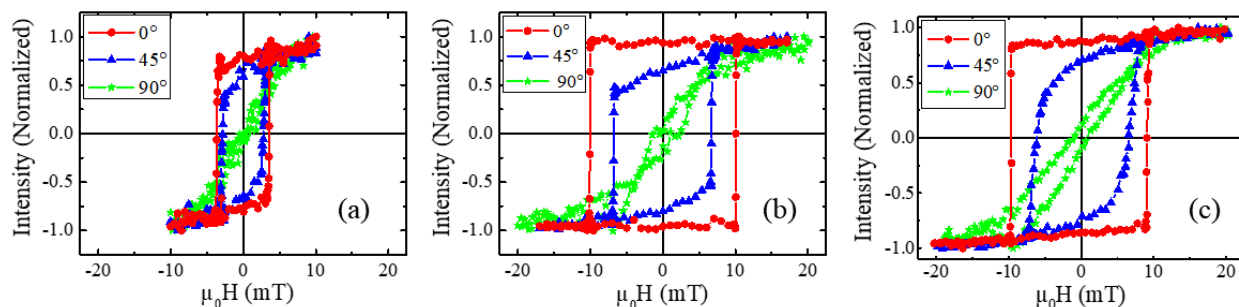


Figure 4.1: Angle dependent hysteresis loops shown in (a) – (c) for samples 4S_A, 4S_B and 4S_C, respectively. The measurements have been performed using MOKE microscopy in longitudinal mode at RT. The loops have been plotted in the same scale for better comparison of the coercivity w.r.t. the thickness of the Fe layer.

Due to the in-built geometry of our deposition system, the Fe plume is always inclined at 30° angle w.r.t. the substrate normal [9,11,17,82,93]. As discussed earlier, the oblique angle of

deposition promotes the columnar growth of the material with a preferential direction of uniaxial anisotropy [10]. Therefore, presence of uniaxial anisotropy is expected in all the samples discussed in this chapter.

The hysteresis loops and the corresponding domain images have been measured simultaneously using magneto optic Kerr effect (MOKE) based microscopy. All the measurements in MOKE microscopy have been performed in longitudinal mode at RT within a field range of ± 20 mT. The hysteresis loops have been measured by varying ϕ i.e. the angle between applied field direction and the easy axis. The angle dependent hysteresis loops for all three samples are shown in figure 4.1. It has been observed that the coercivity (H_C) along the easy axis increases with increase in the thickness of the Fe layer. This can be explained in terms of the Fe growth on Si (100) substrate with native oxide. The lattice constants of bcc Fe and hcp SiO₂ are $a_{Fe} = 0.278$ nm and $a_{SiO_2} = 0.491$ nm, $c_{SiO_2} = 0.54$ nm, respectively. Due to this large lattice mismatch the growth of Fe will be strained on SiO₂ layer. For $t_{Fe} = 3.5$ nm, the effect of strain is even more as the growth of Fe is poor at ultrathin limit when deposited using sputtering technique with high deposition rate (0.02 nm/s). However, with increase in thickness of the Fe layer ($t_{Fe} = 7.5$ nm), the strain will be reduced as the Fe adatoms can relax with more thickness. Therefore, the exchange coupling between the Fe atoms will increase with thickness and consequently the coercivity will also increase. However, the coercivity remains almost similar for further increase of Fe thickness from $t_{Fe} = 7.5$ to 18 nm. Therefore, the strain experienced by the Fe layer due to the lattice mismatch does not change after a certain thickness of Fe. Uniaxial anisotropy has been observed in all the three samples due to the oblique angular growth of Fe.

The domain images for all the samples along the easy axis are shown in figure 4.2. The series of domain images for each sample correspond to the domain states observed at the points marked in the respective hysteresis loop. Along with H_C , the domain size also increases with

Fe thickness. This can also be attributed to the increase in exchange coupling with the reduction in strain and increase in Fe thickness.

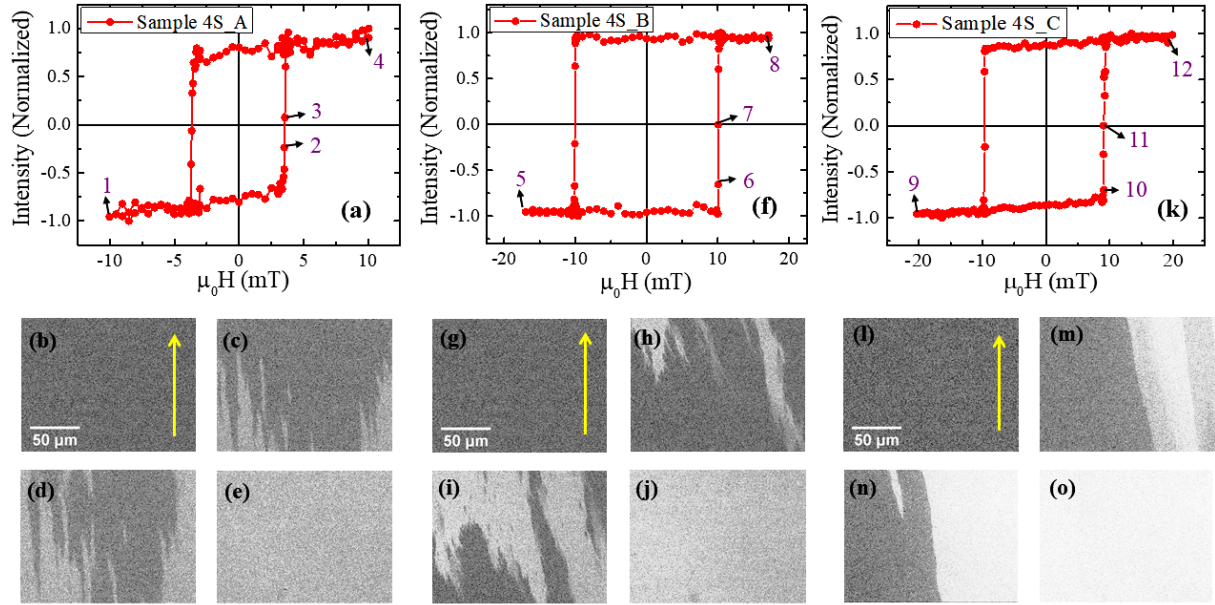


Figure 4.2: The hysteresis loops ((a), (f), (k)) and the corresponding domain images ((b) – (e), (g) – (j), (l) – (o)) measured along the easy axis for samples 4S_A, 4S_B and 4S_C, respectively. The images shown in (b) – (e) correspond to the domain states observed in sample 4S_A at the field points 1 – 4, respectively marked in (a). Similarly, the images shown in (g) – (j) and (l) – (o) correspond to the domain states observed in samples 4S_B and 4S_C at the field points 5 – 8 and 9 – 12 as marked in (f) and (k), respectively. All the domain images are in same length scale shown in (b), (g) and (l). The arrows shown in image (b), (g) and (l) represent the direction of the applied field.

Branch domains are observed for samples 4S_A and 4S_B. Generally, branch domains are characteristics of strongly misoriented samples with high anisotropic materials like NdFeB [12]. However, for less anisotropic samples, such domain patterns appear due to poor growth of the sample. Therefore, branch domains are observed in samples 4S_A and 4S_B due to poor growth of Fe in low thickness regime. Instead of branch domains, large stripe domains are observed in sample 4S_C. It should be noted that the induced strain in the Fe layers may

add dispersion in the oblique angle deposition induced uniaxial anisotropy direction. Stripe domains are characteristics of films having dispersed uniaxial anisotropy due to strain [12]. It has also been reported that stripe domains are observed for obliquely grown materials due to their columnar growth [12].

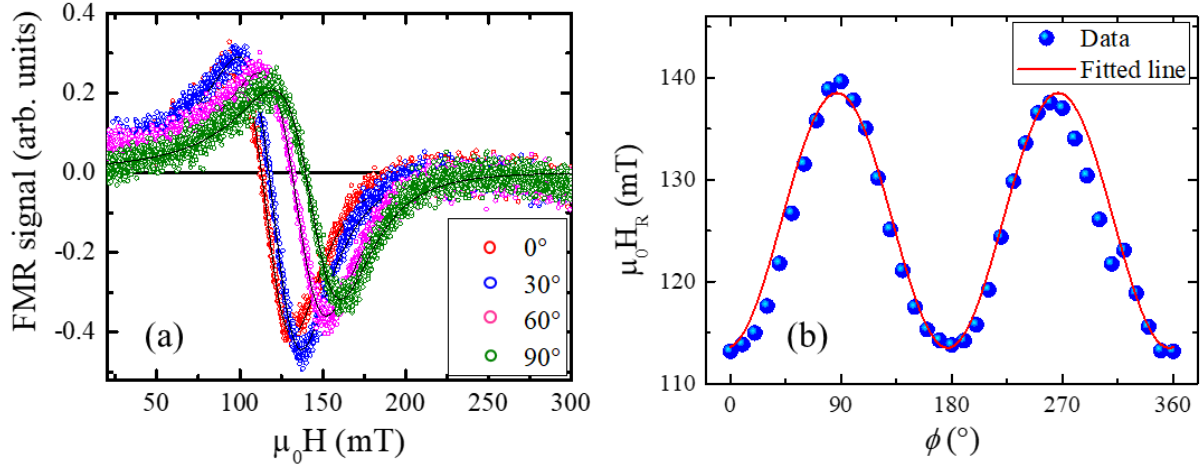


Figure 4.3: (a) FMR signal vs applied field measured at various angles for sample 4S_C. (b) Anisotropy symmetry plot and its fit for sample 4S_C measured using ferromagnetic resonance (FMR) technique by keeping the frequency fixed at 12 GHz. The blue colored solid circles and the red line correspond to the measured data and the fit to equation 4.2, respectively.

The quantification of the anisotropy is performed using Phase FMR spectrometer. Due to low thickness and strained growth of Fe on SiO₂/Si (100) substrate, the FMR data measured for samples 4S_A and 4S_B were very noisy. Therefore, any interpretation was not possible using those FMR data. The angle dependent FMR measurement has been performed at a fixed frequency of 12 GHz on sample 4S_C to quantify the anisotropy. The angle ϕ between the easy axis and the applied field direction have been varied at an interval of 10° in the full 360° sample rotation. The FMR signals vs field for $\phi = 0^\circ, 30^\circ, 60^\circ$ and 90° are shown in figure 4.3(a). The resonance field H_R has been recorded for each angle and the anisotropy nature of the sample has been extracted by plotting H_R as a function of ϕ (figure 4.3(b)). The

anisotropy constant of the sample can be derived by fitting the data in terms of the energies present in the system. The total magnetic free energy density of the system can be written as [200]:

$$E = -HM_S[\sin\theta\sin\theta_M \cos(\phi_M - \phi) + \cos\theta\cos\theta_M] - 2\pi M_S^2 \sin^2\theta_M + K_U \sin^2\theta_M + K_2 \sin^2\theta_M \sin^2\phi_M \quad (4.1)$$

where K_2 is the in-plane uniaxial anisotropy constant and K_U is the perpendicular contribution of the anisotropy. ϕ is the angle between the easy axis and the projection of the applied field direction in the sample plane. ϕ_M is the angle between the easy axis and the projection of magnetization in sample plane. θ and θ_M are the angles between the z-axis w.r.t. the applied field direction and the magnetization direction, respectively. However, our sample is in-plane magnetized and the external field is also applied in the sample plane. Therefore, θ_M and θ are considered to be 90° .

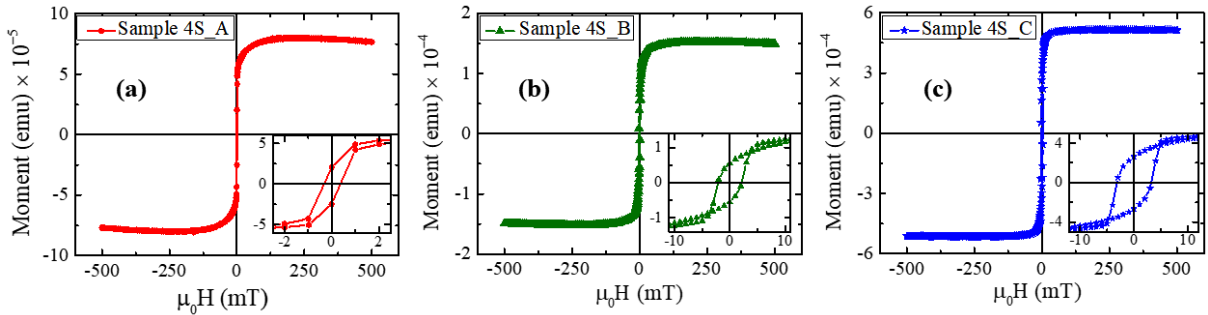


Figure 4.4: (a) – (c) M–H loops measured at RT using superconducting quantum interference device (SQUID) for samples 4S_A, 4S_B and 4S_C, respectively. The insets of the figures show the zoomed in version of the loops near the coercivity.

To evaluate the strength of the uniaxial anisotropy present in sample 4S_C, angle dependent H_R values have been fitted using the following dispersion relation [200]:

$$\left(\frac{\omega}{\gamma}\right)^2 = [H_R \cos(\phi_M - \phi) - h_U + h_2 \sin^2\phi_M][H_R \cos(\phi_M - \phi) - h_2 + 2h_2 \sin^2\phi_M] \quad (4.2)$$

where, h_2 is the in-plane anisotropy representations and can be written as $h_2 = 2 \frac{K_2}{M_S}$ (K_2 is the in-plane uniaxial anisotropy constant). The red solid line in figure 4.3(b) show the fitted curve for the angle dependent H_R data using equation 4.2. The anisotropy field h_2 is extracted to be 25 mT for sample 4S_C. The value of saturation magnetization (M_S) has been measured using SQUID magnetometer (figure 4.4(c)). The uniaxial anisotropy constant K_2 is calculated to be 2.16×10^4 for sample 4S_C.

To evaluate the magnetic moment in single layer Fe samples, M–H loops were measured at RT within ± 500 mT using a superconducting quantum interference device (SQUID) magnetometry. The hysteresis loops are shown in figure 4.4. The number of Fe atoms present in each sample was estimated from the volume of the Fe layer. The moment per atom in the Fe layer is calculated by dividing the saturation moment with the number of Fe atoms of the respective samples. The moments are calculated to be 1.49 ± 0.08 , 1.77 ± 0.04 and $1.98 \pm 0.05 \mu_B/\text{atom}$ for samples 4S_A, 4S_B and 4S_C, respectively. The moment in Fe decreases with thickness due to the poor growth of Fe at low thicknesses on Si (100) substrate.

4.2. Study of Fe/C₆₀ spinterface induced magnetic properties in polycrystalline Fe/C₆₀ bilayer thin films with variable thickness:

The bilayer of Fe/C₆₀ thin films have been prepared with similar thicknesses of Fe as discussed in the previous section to study the effect of the spinterface on the magnetic properties of the systems. However, the thickness of the C₆₀ layer has not been kept constant for all the samples to probe the exact thickness of the spinterface depending on t_{Fe} . Therefore, two samples have been prepared by keeping same t_{Fe} but changing the C₆₀ thickness, to study the effect of C₆₀ thickness on the spinterfaces. The Fe and C₆₀ layers were prepared in-situ at RT using dc magnetron sputtering and thermal evaporation, respectively. The deposition pressure and rate for C₆₀ were $\sim 1 \times 10^{-7}$ mbar and 0.012 nm/s, respectively.

The C₆₀ was deposited normal to the substrate. To prevent damage of C₆₀, a capping layer of Ta was deposited in-situ in all samples using dc magnetron sputtering. The details of the samples are shown in table 4.2.

Table 4.2. Details of bilayer polycrystalline Fe/C₆₀ samples prepared on Si (100) substrate

Sample name	Sample structure
Sample 4B_A	Si (100)/SiO ₂ (native oxide)/Fe (3.5 nm)/C ₆₀ (10 nm)/Ta (3 nm)
Sample 4B_B	Si (100)/SiO ₂ (native oxide)/Fe (7.5 nm)/ C ₆₀ (15 nm)/Ta (3 nm)
Sample 4B_C	Si (100)/SiO ₂ (native oxide)/Fe (18 nm)/ C ₆₀ (40 nm)/Ta (3 nm)
Sample 4B_D	Si (100)/SiO ₂ (native oxide)/Fe (18 nm)/ C ₆₀ (7 nm)

To understand the structural quality of the interface between the layers, time of flight secondary ion mass spectroscopy (TOF-SIMS) [205,206] has been performed on sample 4B_C. Figure 4.5 shows the depth profile for the layer structure of sample 4B_C obtained from the SIMS measurement. The rising and falling of different colors in the figure represents the appearance of the respective layers w.r.t. the depth from the surface of the sample. The depth profile data clearly shows the multilayer structure of Si(100)/Fe(18 nm)/C₆₀(40 nm)/Ta(3 nm) (sample 4B_C) accordingly as per the proper growth structure. The profile starts with high intensity of Ta (green) along with O (red) represents the top most layer and it starts decreasing when the intensity of C₆₀ (blue) rises up. The C₆₀ layer continues till the next layer of Fe (pink) come up. The Fe layer is just above the Si substrate with SiO₂ layer (Si is black and O is red). The thickness of each layer has been determined approximately from figure 4.5 as $\sim 19.7 \pm 6.6$ nm, $\sim 45.1 \pm 2.4$ nm, $\sim 3.99 \pm 1.59$ nm for Fe, C₆₀ and Ta, respectively. However, the thickness of the SiO₂ layer could not be calculated from the SIMS plot. The nature of the interface, i.e. the presence of inter-diffusion, depends on the position of the intercept between the falling and rising edge of two consecutive layers. It can be seen from figure 4.5 that the coordinate of the intercept between all the consecutive

layers lie a little above the 50% of the highest intensity. This confirms the presence of a very thin layer of inter-diffusion (<1 nm) between all the consecutive layers. However, it was not possible to calculate the exact thicknesses of the inter-diffusion layers as it was beyond the resolution limit of the technique.

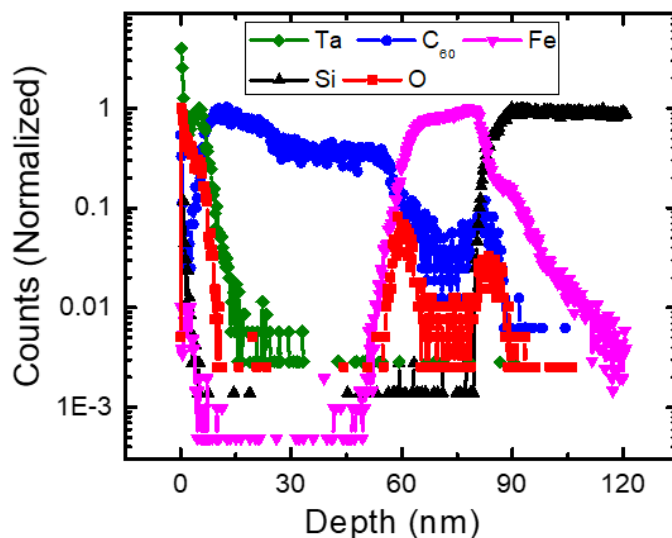


Figure 4.5: Depth profile of sample 4B_C measured by secondary ion mass spectroscopy.

Polarized neutron reflectivity (PNR) has been performed on the bilayer samples (samples 4B_A, 4B_B, 4B_C) in specular reflectivity mode at the MARIA reflectometer [176] at MLZ, Garching, Germany, to investigate the formation of the spinterface at the interfaces between Fe and C₆₀. The wavelength (λ) of the neutrons during the PNR measurements has been chosen to be 0.65 nm. The non-spin flip (NSF) scattering cross sections R^{++} (up - up) and R^{--} (down - down) have been measured at RT. All the PNR measurements have been performed by applying the magnetic field along the easy axis of each sample at saturation, near remanence and coercivity. The incident polarized neutrons interact with the magnetic spins of the sample and flip their sign according to the sign of the interacting spin. The intensity of the reflected neutrons (both up and down) has been measured as a function of the component of the momentum transfer (Q_Z) which is perpendicular to the sample surface.

Figure 4.6(a) shows the PNR data (open circles) and the corresponding fits (solid lines) for sample 4B_A measured at the positive saturation state ($\mu_0 H = 100$ mT). The reflectivity for the non-spin flip (NSF) scattering cross section (i.e. R^{++} and R^{--}) has been recorded where the red and blue open circles represent the data measured for the up – up and down – down channels, respectively (Figure 4.6(a)). The fitting was performed using GenX software [143] which is based on the Parratt formalism [142]. The fits reveal the presence of interdiffusion in between all the layers of sample 4B_A. The schematic sample structure obtained from the fitting is depicted in figure 4.6(b) where the thicknesses of each layers are mentioned beside the respective layers. From the PNR data analysis the magnetic moment of the Fe layer in sample 4B_A is obtained to be only $1.06 \pm 0.02 \mu_B/\text{atom}$. Earlier it has been discussed that the single layer Fe sample with similar thickness (sample 4S_A) exhibits $1.49 \pm 0.08 \mu_B/\text{atom}$ magnetic moment. Therefore, a loss of 29% of magnetic moment is observed for sample 4B_A w.r.t. its single layer reference sample 4S_A. An interdiffusion layer of 1.20 ± 0.03 nm is observed between the Fe and C₆₀ layer. Next to this mixed layer, 1.10 ± 0.08 nm of pure C₆₀ layer exhibits a magnetic moment of $1.37 \pm 0.18 \mu_B/\text{cage}$ of C₆₀. The interdiffusion layer shows a magnetic moment of $1.80 \pm 0.01 \mu_B$ per unit where 1 unit consists of one Fe atom and one C₆₀ cage. The moment in the interdiffusion layer is higher as it contains moment from both the Fe and magnetic C₆₀. The reason behind the loss of moment in Fe and induction of moment in C₆₀ cage can be ascribed to the hybridization of d and p orbitals between the Fe and C, respectively. Due to the electronic configuration of C atoms it is prone to sp hybridization and one of the p orbitals of C gets hybridized with the d orbital of Fe atom. Due to this $p - d$ hybridization, the density of states of the C₆₀ get modified which leads to ferromagnetism in fullerene [5]. However, the length of charge/spin transfer from Fe layer to C₆₀ layer is limited to 1.10 ± 0.08 nm for this sample. Next to the magnetic C₆₀ layer, remaining 7.30 ± 0.02 nm of C₆₀ layer does not exhibit any signature of ferromagnetism.

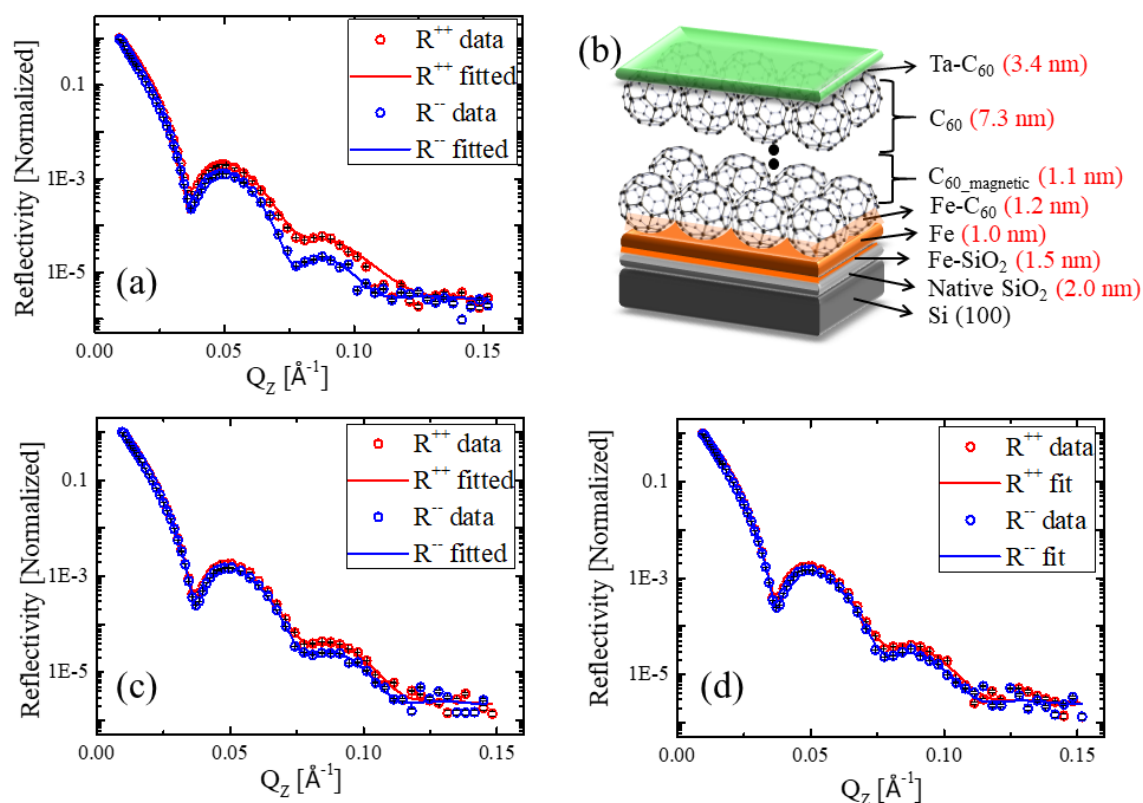


Figure 4.6: (a) Polarized neutron reflectivity data measured at the saturation state at RT and its corresponding fits for sample 4B_A. The red and blue open circles represent the data measured for the R^{++} and R^{--} channels, respectively. The solid lines correspond to their respective fits. (b) A schematic representation of the sample structure obtained by fitting the PNR data shown in (a). The numbers written in brackets beside each layer correspond to the thickness of various layers obtained from the best fit. (c) and (d) show the PNR data and corresponding fits for the near remanence and coercivity measurement for sample 4B_A, respectively.

This sample has been also measured near remanence and coercivity to elucidate the magnetization direction of the layers during the reversal i.e. away from the saturation (figure 4.6(c) and (d)). It has been observed from the best fit of the remanence data that 76% of the Fe layer spins point in negative direction whereas the magnetic C₆₀ layer shows positive moment. This indicates that the Fe and magnetic C₆₀ layers are anti-parallel to each other close to the remanence.

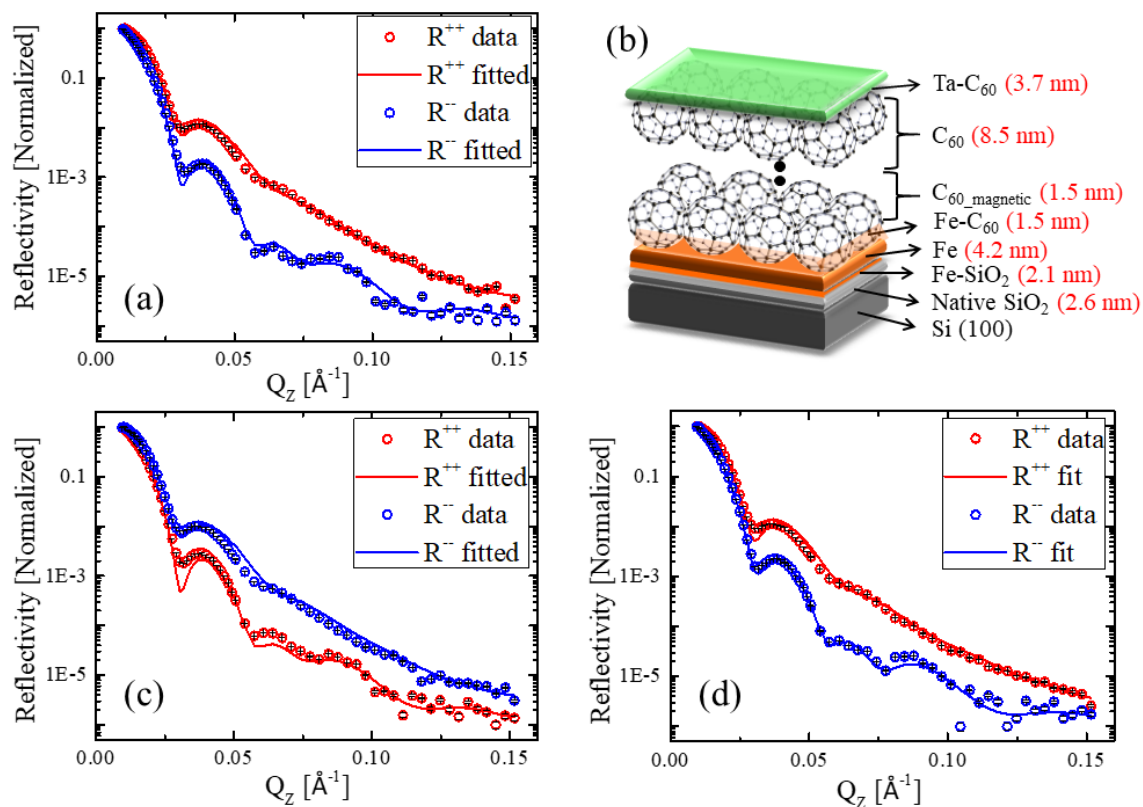


Figure 4.7: (a) Polarized neutron reflectivity data measured at the saturation state at RT and its corresponding fits for sample 4B_B. The red and blue open circles represent the data measured for the R^{++} and R^{-} channels, respectively. The solid lines correspond to their respective fits. (b) A schematic representation of the sample structure obtained by fitting the PNR data shown in (a). The numbers written in brackets beside each layer correspond to the thickness of various layers obtained from the best fit. (c) and (d) show the PNR data and corresponding fits for the near remanence and coercivity measurement for sample 4B_B, respectively.

To understand the effect of the Fe layer thickness on the induced moment in the C₆₀ layer, PNR measurements have been performed on samples 4B_B and 4B_C. The PNR data and their corresponding fits at the saturation state for samples 4B_B and 4B_C are shown in figure 4.7(a) and 4.8(a), respectively. Sample 4B_B exhibits a spinterface of 1.50 ± 0.07 nm of C₆₀ (figure 4.7(b)) which is close to a monolayer thickness of C₆₀. The induced moment in

C₆₀ is extracted to be $1.52 \pm 0.05 \mu_B/\text{cage}$. Therefore, sample 4B_B shows more induced moment than that of sample 4B_A. The Fe layer exhibits $1.77 \pm 0.04 \mu_B/\text{atom}$ (figure 4.4(b)) and $1.36 \pm 0.08 \mu_B/\text{atom}$ in samples 4S_B and 4B_B, respectively. The loss in Fe moment is 23% for sample 4B_B in comparison to its corresponding reference sample 4S_B. The PNR data and its fit for sample 4B_B near the remanence and coercivity states are shown in figure 4.7(c) and (d). Similar to the sample 4B_A, the Fe and C₆₀ layers exhibit anti-parallel coupling at the remanence state. In this sample, the Fe layer is 87% reversed near the remanence whereas the C₆₀ layer is still in the positive state.

By fitting the saturation data for sample 4B_C, it has been observed that $1.90 \pm 0.04 \mu_B/\text{cage}$ of magnetic moment is induced in C₆₀ at the interface. The thickness of the magnetic C₆₀ further increases to $1.80 \pm 0.06 \text{ nm}$ (figure 4.8(b)) which is even more than a monolayer of C₆₀. This indicates that the induced moment in C₆₀ increases monotonically with the increase in Fe thickness. In this sample the interdiffusion layer between the Fe and C₆₀ exhibits $2.4 \pm 0.6 \mu_B/\text{unit}$ moment. The Fe moment in its reference sample 4S_C have been obtained to be $1.98 \pm 0.05 \mu_B/\text{atom}$ by SQUID magnetometry (figure 4.4(c)). Whereas in sample 4B_C the moment in Fe is observed to be only $1.56 \pm 0.06 \mu_B/\text{atom}$ which corresponds 21% loss in the Fe moment. The PNR data and fits near the remanence and corecivity states for sample 4B_C is shown in figure 4.8(c) and (d). Here, the Fe layer shows $\sim 80\%$ negative moment and the C₆₀ layer is completely in a positive state. Therefore, it can be concluded that irrespective of the Fe layer thickness, the magnetic C₆₀ and the Fe layer shows anti-parallel magnetization at the remanence state. The growth of Fe on Si (100) substrate with native oxide is poor in the ultrathin limit as the roughness of the Fe layer becomes nearly in the order of its thickness. Also, the interdiffusion between the Fe and C₆₀ layer is even more than the pure Fe layer thickness (Figure 4.6(b)). Due to the presence of such disorder in the growth of the Fe, the

moment decreases rapidly. As a consequence, the induced moment in C₆₀ as well as the thickness of the spinterface decreases with decrease in Fe thickness.

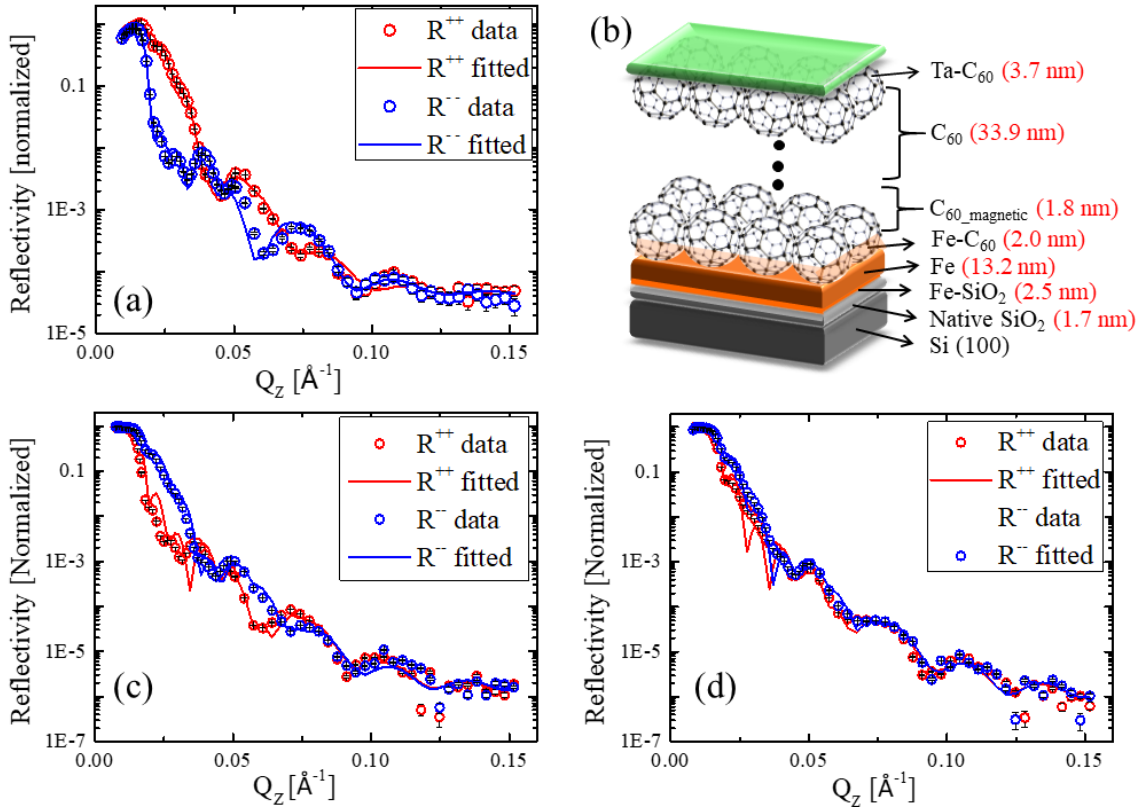


Figure 4.8: (a) Polarized neutron reflectivity data measured at the saturation state at RT and its corresponding fits for sample 4B_C. The red and blue open circles represent the data measured for the R^{++} and R^{--} channels, respectively. The solid lines correspond to their respective fits. (b) A schematic representation of the sample structure obtained by fitting the PNR data shown in (a). The numbers written in brackets beside each layer correspond to the thickness of various layers obtained from the best fit. (c) and (d) show the PNR data and corresponding fits for the near remanence and coercivity measurement for sample 4B_C, respectively.

PNR measurement has been performed on sample 4B_D to study the effect of the non-magnetic C₆₀ on the induced moment and the thickness of the spinterface. The data measured at the saturation state and the corresponding fits are shown in figure 4.9(a). It has been observed from the fits that both the induced moment ($1.90 \pm 0.05 \mu_B/\text{cage}$) and the thickness

of the spinterface (1.80 ± 0.04 nm) remains unchanged w.r.t. sample 4B_C. Therefore, it can be concluded that the thickness of non-magnetic C₆₀ does not contribute to the spinterface properties whereas the thickness of the underlying Fe layer plays a major role in determining it. Sample 4B_D has been prepared without any capping layer and still it exhibits similar magnetic properties (spinterface moment and thickness) like sample 4B_C. It infers that the capping layer of the sample does not have any effect on the spinterface induced magnetic properties.

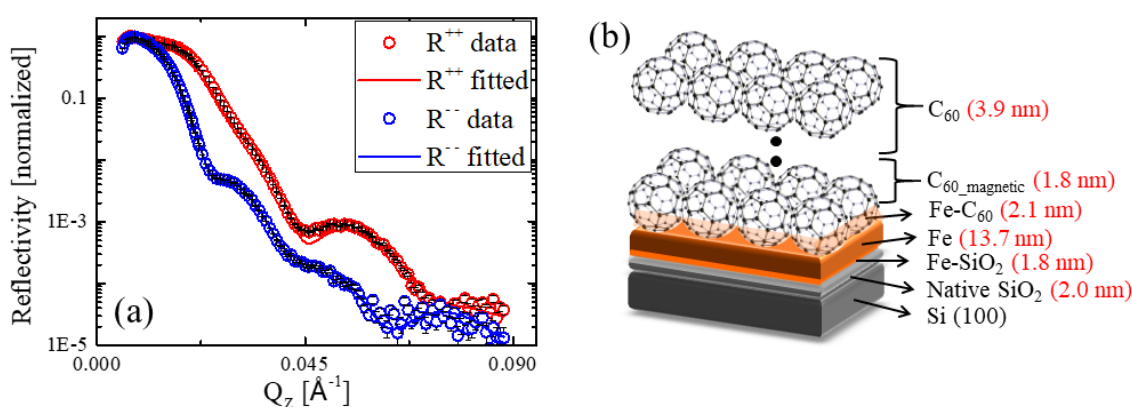


Figure 4.9: (a) Polarized neutron reflectivity data measured at the saturation state at RT and its corresponding fits for sample 4B_D. The red and blue open circles represent the data measured for the R^{++} and R^{--} channels, respectively. The solid lines correspond to their respective fits. (b) A schematic representation of the sample structure obtained by fitting the PNR data shown in (a). The numbers written in brackets beside each layer correspond to the thickness of various layers obtained from the best fit.

The angle dependent hysteresis loops and the corresponding domain images have been measured simultaneously using MOKE microscopy to observe the effect of spinterfaces on the magnetization reversal mechanism of the samples. Figure 4.10 shows the hysteresis loops for samples 4B_A ($t_{Fe} = 3.5$ nm), 4B_B ($t_{Fe} = 7.5$ nm) and 4B_C ($t_{Fe} = 18$ nm) measured along $\phi = 0^\circ$, 45° and 90° . The coercivity of the bilayer samples decreases in comparison to the respective single layer samples (figure 4.2). Due to the lattice mismatch between Fe and

C₆₀, the bilayer samples become even more disordered which leads to decrease in coercivity. Similar to their single layer counterparts, the bilayer samples also exhibit uniaxial anisotropy due to the oblique angular deposition of Fe. However, the difference of the coercivity between easy and hard axis is less for the Fe/C₆₀ bilayer samples in comparison to their corresponding single layer reference samples. This indicates reduction in the strength of the uniaxial anisotropy in the bilayer samples. Presence of C₆₀ increases the dispersion in anisotropy due to the poor growth of C₆₀ on polycrystalline Fe.

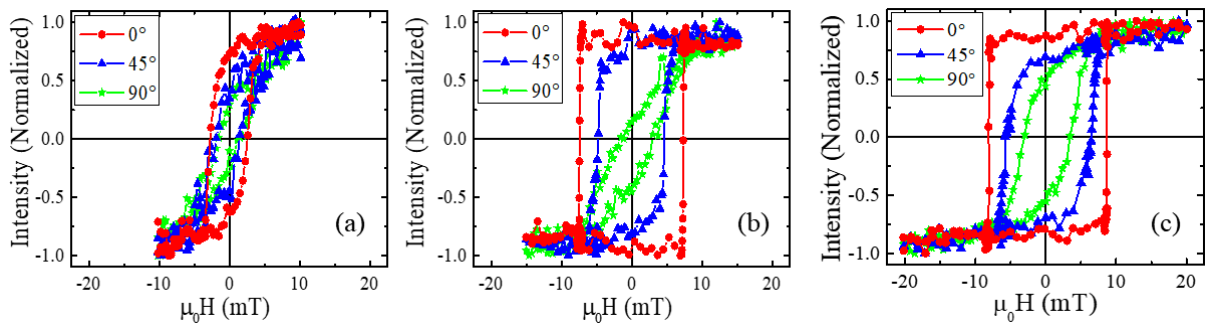


Figure 4.10: Angle dependent hysteresis loops (a – c) for samples 4B_A ($t_{Fe} = 3.5$ nm), 4B_B ($t_{Fe} = 7.5$ nm) and 4B_C ($t_{Fe} = 18$ nm), respectively. The measurements have been performed using MOKE microscopy in longitudinal mode at RT. The loops have been plotted on the same scale for better comparison of the coercivity w.r.t. the thickness of the Fe layer.

The domain structures along the easy axis of the bilayer samples are shown in figure 4.11. Along with the coercivity, the domain size also decreases in the bilayer samples due to the presence of C₆₀. In case of sample 4B_A, domains could not be observed (figure 4.11(b) – (e)) using the same magnification of the objective lens used to probe other samples. Probably the domains become such small (fragmented) that it was not possible to image them using same magnification as used to image the domains from the respective single layer (sample 4S_A). Both the samples 4B_B and 4B_C exhibit branch (figure 4.11(g) – (j)) and stripe domains (figure 4.11(l) – (o)), respectively along the easy axis similar to their corresponding

single layer samples. However, the domain size decreases due to the increase in disorder in the samples. The branches in sample 4B_B and the stripe domains in sample 4B_C become fragmented and denser in comparison to their reference samples which indicates increase in dispersion in the net anisotropy of the bilayer samples [12].

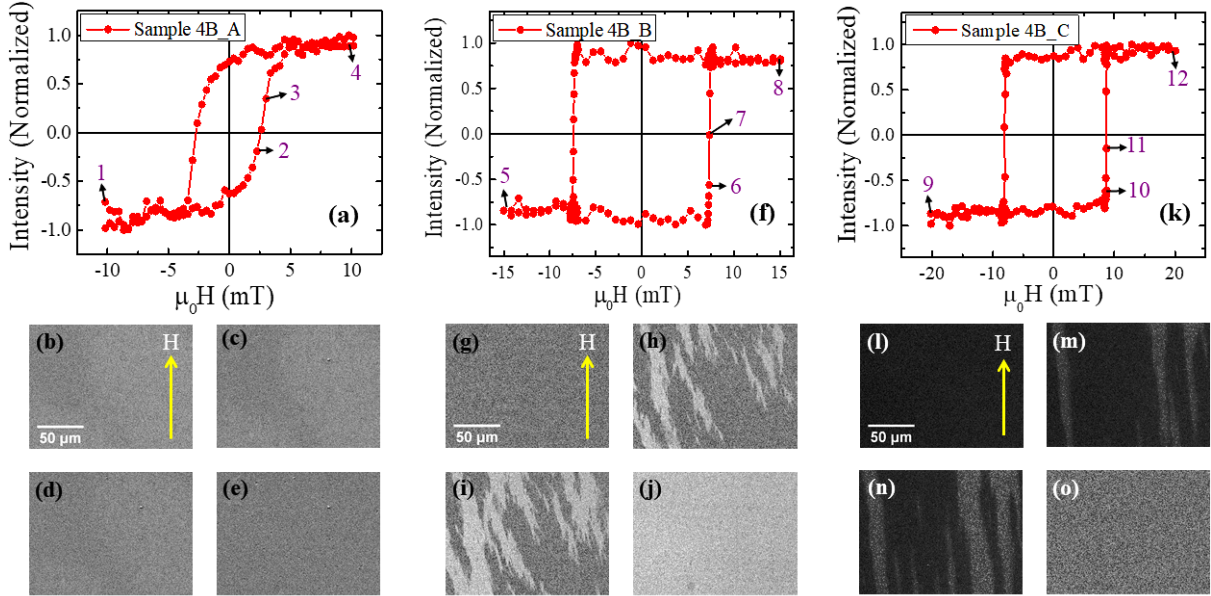


Figure 4.11: The hysteresis loops ((a), (f), (k)) and the corresponding domain images ((b) – (e), (g) – (j), (l) – (o)) measured along the easy axis for samples 4B_A, 4B_B and 4B_C, respectively. The images shown in (b) – (e) correspond to the domain states observed in sample 4B_A at the field points 1 – 4 marked in (a), respectively. Similarly, the images shown in (g) – (j) and (l) – (o) correspond to the domain states observed in samples 4B_B and 4B_C at the field points 5 – 8 and 9 – 12, respectively. All the domain images are in same length scale shown in (b), (g) and (l). The arrows shown in image (b), (g) and (l) represent the direction of the applied field.

To quantify the change in anisotropy due to the presence of magnetic Fe/C₆₀ spinterface, angle dependent FMR measurements have been performed on sample 4B_C at a fixed frequency of 12 GHz. As discussed in section 4.1, due to the low thickness of Fe and presence of disorder in the samples, FMR measurement could not be possible on samples

4B_A and 4B_B. A representative plot to show the angle dependent FMR signals for sample 4B_C along $\phi = 0^\circ, 30^\circ, 60^\circ$ and 90° is depicted in figure 4.12(a). The angle dependent resonance fields (H_R) and its fit for sample 4B_C are shown in figure 4.12(b). As the bilayer samples exhibit only uniaxial anisotropy, the energy equation remains the same (equation 4.1) to its respective single layer sample 4S_C. The angle dependent H_R is fitted using the dispersion equation 4.2. However, a deviation in the fitted line from the data points is observed for $\phi > 320^\circ$ which may be because of some experimental error.

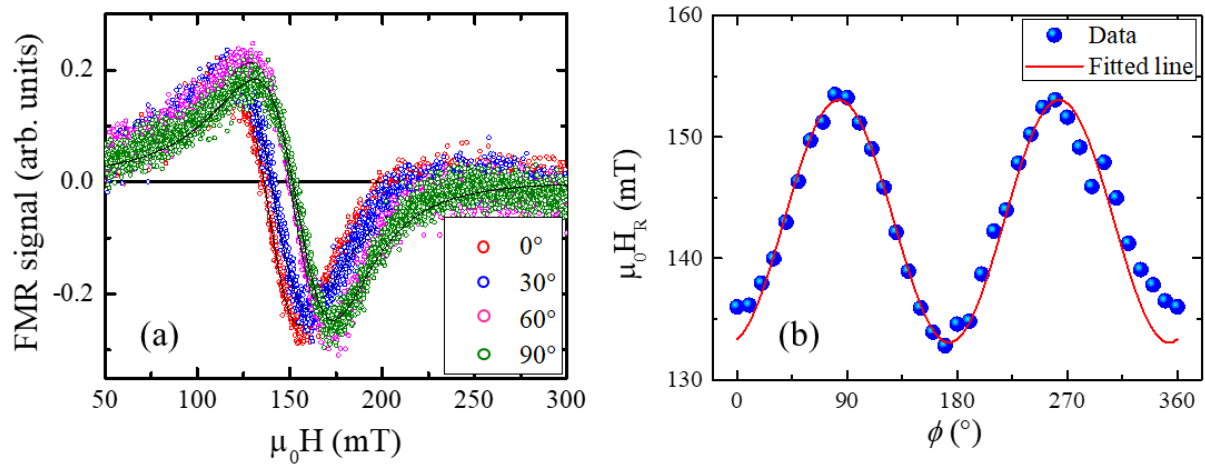


Figure 4.12: (a) FMR signal vs applied field measured at various angles for sample 4B_C. (b) Anisotropy symmetry plot and its fit for sample 4B_C measured using ferromagnetic resonance (FMR) technique by keeping the frequency fixed at 12 GHz. The blue colored solid circles and the red line correspond to the measured data and the fit to equation 4.2, respectively.

The uniaxial anisotropy constant K_2 is calculated to be $1.05 \times 10^4 \text{ J/m}^3$ for sample 4B_C. Earlier it has been found that the uniaxial anisotropy constant K_2 is $2.16 \times 10^4 \text{ J/m}^3$ for sample 4S_C. Therefore, it can be concluded that the anisotropy decreases by $\sim 51\%$ for sample 4B_C than that of its corresponding single layer reference sample 4S_C. Hence, it is believed that the dispersion in the anisotropy in sample 4B_C, due to the lattice mismatch

between C₆₀, Fe, SiO₂, and Si (100) substrate, is the reason behind the decrease in net uniaxial anisotropy of the system.

4.3. Effect of two spinterfaces on the thickness, induced moment and magnetization reversal of tri-layer Fe/C₆₀ system:

In this section, spinterfaces have been created in both sides of the C₆₀ layer by sandwiching it between two Fe layers. To study the effect of number of spinterfaces on the magnetic properties of the samples, two tri-layer Fe/C₆₀ samples have been prepared with similar thicknesses of the Fe layer. The details of the prepared samples are listed in table 4.3.

Table 4.3. Details of tri-layer polycrystalline Fe/C₆₀ samples prepared on Si (100) substrate

Sample name	Sample structure
4T_A	Si (100)/SiO ₂ (native oxide)/Fe (3.5 nm)/C ₆₀ (15 nm)/Fe (3.5 nm)/Ta (3 nm)
4T_B	Si (100)/SiO ₂ (native oxide)/Fe (7.5 nm)/ C ₆₀ (20 nm)/Fe (7.5 nm)/Ta (3 nm)

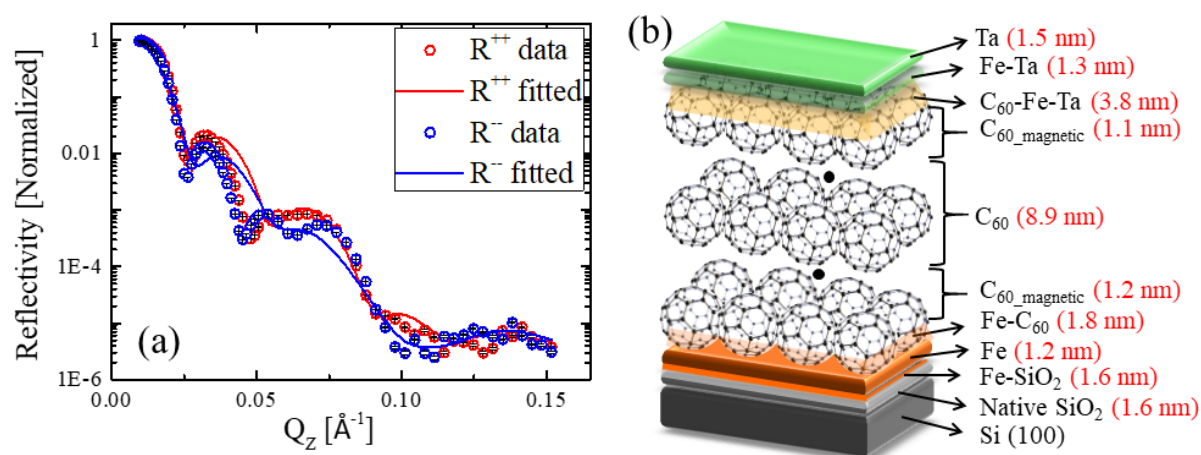


Figure 4.13: (a) Polarized neutron reflectivity data measured at the saturation state at RT and its corresponding fits for sample 4T_A. The red and blue open circles represent the data measured for the R^{++} and R^{--} channels, respectively. The solid lines correspond to their respective fits. (b) A schematic representation of the sample structure obtained by fitting the PNR data shown in (a). The numbers written in brackets beside each layer correspond to the fitted thickness of the respective layer.

PNR data and the corresponding fits for sample 4T_A exhibit that the magnetic moment induced in the C₆₀ next to the bottom Fe layer is similar to the induced moment in its respective bilayer sample 4B_A. The fitted data and its corresponding layer structure are shown in figure 4.13(a) and (b), respectively. The thickness of the bottom spinterface is also of same order w.r.t. its corresponding bilayer sample. However, due to the huge lattice mismatch between C₆₀ and Fe, the growth of the top Fe layer is very poor in quality. The structural parameters obtained from the PNR fits suggest that the entire Fe layer has been interdiffused within the C₆₀ layer. Along with Fe, some amount of Ta (topmost layer of the sample) also got intermixed with C₆₀. Therefore, choosing the proper model to fit the PNR data was rigorous which results in poor quality of fitting. Due to intermixing of all the layers above C₆₀, the magnetic properties of these layers are not properly defined. Also, such intermixed structures are not good from the application point of view. In spite of such intermixed FM layer on top the C₆₀ layer, spinterface has been observed for 1.1 ± 0.1 nm of C₆₀ between the top Fe and C₆₀ layer. The induced moment in the top spinterface has been determined as $1.37 \pm 0.20 \mu_B/\text{cage}$ which is exactly the same to the bottom spinterface.

Figure 4.14 shows the PNR fits and the simulated layer structure of sample 4T_B. The layer structure and the magnetic moments in each layer of the sample 4T_B is similar to that of the corresponding bilayer sample 4B_B up to the non-magnetic C₆₀ layer. However, a major portion of the top Fe layer got intermixed with the C₆₀ due to the lattice mismatch between them. For sample 4T_B the thickness of Fe is more than sample 4T_A. Consequently, the top Fe layer does not get completely intermixed with the C₆₀ layer. 1.80 ± 0.03 nm of pure Fe layer has been observed on top the Fe-C₆₀ intermixed layer. Analogues to the previous sample 4T_A, spinterfaces are formed in both side of the C₆₀ layer which shows similar induced moment and the thickness w.r.t. the corresponding bilayer sample 4B_B. Therefore, with increase in the number of interfaces in a sample, the induced moment and the length of

the spinterfaces remain constant for each spinterface. This indicates that the strength of $p - d$ hybridization between Fe and C₆₀ remains constant for each spinterface in multilayer samples if the growth conditions and thickness of Fe layers are kept constant.

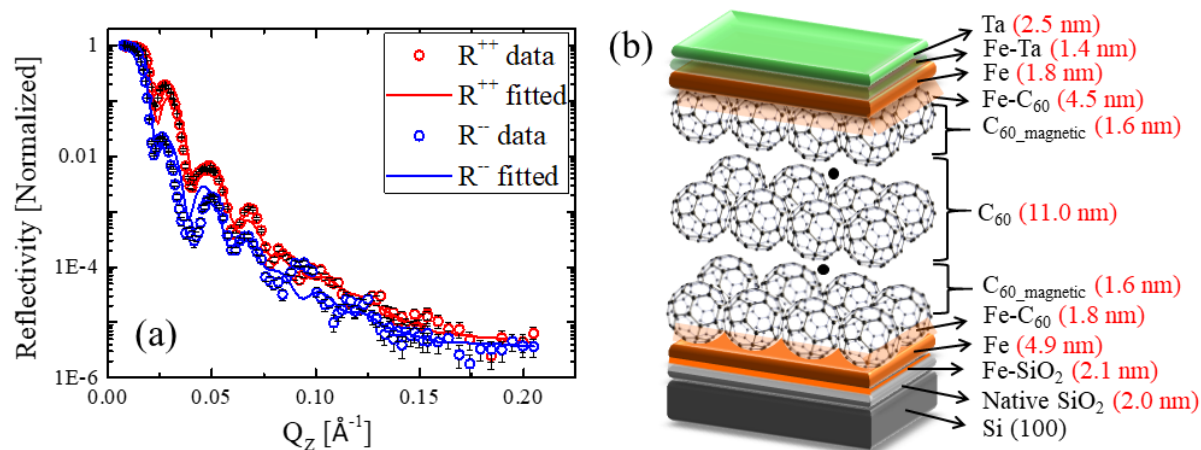


Figure 4.14: (a) Polarized neutron reflectivity data measured at the saturation state at RT and its corresponding fits for sample 4T_B. The red and blue open circles represent the data measured for the R^{++} and R^{--} channels, respectively. The solid lines correspond to their respective fits. (b) A schematic representation of the sample structure obtained by fitting the PNR data shown in (a). The numbers written in brackets beside each layer correspond to the fitted thickness of the respective layer.

The angle dependent hysteresis loops and the domain images along the easy axis for both the tri-layer samples are shown in figure 4.15. The difference in coercivity between the easy and hard axis indicates further decrease in anisotropy for both the samples w.r.t. their corresponding bilayer samples. Along with the anisotropy, the domain size also decreases for the tri-layer samples. For sample 4T_A, domains have not been observed as their size decreases below the resolution limit of the objective lens used for this measurement. Branch domains are observed for sample 4T_B analogous to its corresponding single layer (4S_B) and bilayer (4B_B) samples. The increase in fragmentation of the domain structure infers increase in dispersion in anisotropy symmetry due to the poor growth of the samples [12].

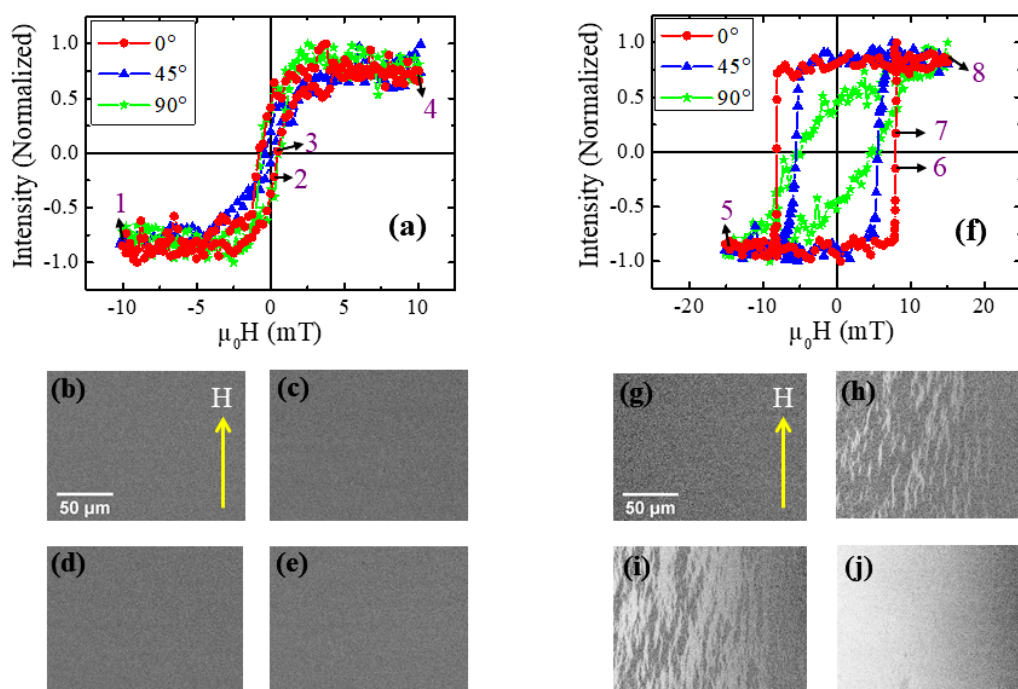


Figure 4.15: Hysteresis loops measured using MOKE microscopy in longitudinal mode by varying the angle (ϕ) between the applied field and the easy axis at RT for samples (a) 4T_A and (f) 4T_B, respectively. The images shown in ((b) – (e)) and ((g) – (j)) correspond to the domain states observed in samples 4T_A and 4T_B along the easy axis (red curve with solid circles) at the field points 1 – 4 and 5 – 8, respectively. All the domain images are in same length scale shown in (b) and (g). The arrows shown in images (b) and (g) represent the direction of the applied field.

In summary, the formation of spinterface has been observed in all the bilayer and tri-layer samples of polycrystalline Fe/C₆₀ due to the p - d hybridization between C and Fe atoms. Due to the lattice mismatch between Fe and SiO₂, the growth of Fe is polycrystalline in nature. Consequently, the Fe layer grows with a strain in its ultrathin limit. After a certain thickness of Fe, the induced strain gets relaxed. Therefore, both the induced moment and the thickness of the spinterface increase with increase in the Fe layer thickness. However, this relation may not be obeyed if the thickness of the Fe layer is increased beyond certain limit. Future analysis is necessary to find out the global relationship between the thickness of FM

layer and the induced moment in the spinterface. The formation of a spinterface leads to a decrease in uniaxial anisotropy in comparison to their reference samples without having the C₆₀ layer. The induced moment and the thickness of the spinterface remains constant for each spinterface in case of the multilayer samples. However, in the case of tri-layer samples the top spinterface exhibits poor quality and the layers above the C₆₀ are mostly interdiffused due to large lattice mismatch. Therefore, bilayer samples are chosen for further studies in this thesis. It has been observed that the spinterface properties depend significantly on the thickness and the growth of the Fe layer. Therefore, better growth (single crystalline) of thicker Fe ($t_{Fe} > 10$ nm) may give rise to better tunability of the spinterfacial properties which are discussed in the next chapter.

Chapter 5: Spinterface in epitaxial Fe and C₆₀ systems

In the previous chapter, the study of magnetic properties of polycrystalline Fe thin films with and without spinterface reveals that the magnetization reversal mechanism, domain structures, and anisotropy symmetry of Fe thin films get significantly modified due to the presence of spinterface. However, to achieve better tunability of the magnetic parameters it is essential to study the effect of crystallinity of the FM material on such spinterfaces. In this chapter the effect of Fe/C₆₀ spinterface on the magnetic properties of epitaxial Fe thin film has been discussed. The Fe films can exhibit polycrystalline as well as epitaxial nature depending on the lattice mismatch between the Fe and the substrate. However, the physical properties of a system strongly depend on the crystalline quality and are improved with better crystallinity. The crystallinity is determined by the growth conditions like substrate pre-annealing, high temperature growth of the film, substrate rotation during deposition etc. MgO being an insulating, non-interactive material shows high potential to promote better growth of materials with proper growth conditions. The indispensable condition to grow an epitaxial film is lattice matching between the sample material and the substrate. Bcc Fe can grow in single crystalline form on MgO (001) substrate by following the epitaxial relation Fe(001)[110]||MgO(001)[100] [15]. The lattice constants of bcc Fe and cubic MgO are $a_{Fe} = 0.287$ nm and $a_{MgO} = 0.4213$ nm, respectively. The epitaxial relation suggests that the lattice constant of MgO matches with that of the bcc Fe along the diagonal plane. The magnetic properties of single layer epitaxial Fe thin film prepared on MgO (001) substrate have been discussed in section 5.1 [17]. Further the effect of Fe/C₆₀ spinterface on the magnetic properties of the bilayer system has been discussed in section 5.2 [9].

5.1. Study of magnetization reversal, domain structure and anisotropy in single layer epitaxial Fe thin film:

Study of single layer epitaxial Fe thin film on MgO (001) substrate is exciting due to its fascinating properties viz. intricate hysteresis loop shapes, complex reversal mechanism, higher magnetic moment etc. A monolayer of Fe on MgO (001) substrate exhibits $3.07\mu_B$ magnetic moment which is even more than the bulk magnetic moment of Fe ($2.2\mu_B$) [21]. This finding makes Fe/MgO system suitable for magnetic data storage and spintronic devices as high magnetic moment is strongly desirable for technological applications. Besides this, it is utmost necessary to control the magnetization reversal mechanism and anisotropy symmetry in such systems. Growth of bcc Fe in epitaxial form leads to emergence of in-plane cubic magnetic anisotropy (CMA) [22]. As discussed in previous chapter, extra uniaxial magnetic anisotropy (UMA) can be induced in the system by means of many processes [83-86] among which oblique angular deposition is quite popular [77,78,82]. One, two and three step hysteresis loops have been reported so far for epitaxial Fe thin films on various substrates [23,184,207]. Initially the reversal mechanism has been explained via nucleation and propagation of 180° DWs. Afterward Zhan *et al.* explained the reversal mechanism for angle $\phi \leq 45^\circ$ via two 90° DW motions for an epitaxial Fe film having CMA [208]. However, if another anisotropy contribution is superimposed with the cubic symmetry then the aforementioned model fails to predict the reversal mechanism for $\phi > 45^\circ$ angles. Due to the particular angle dependence of the target materials in our deposition chamber, a uniaxial anisotropy is always induced in our samples. Therefore, it is required to understand the anisotropy symmetry and the magnetization reversal mechanism for a system having a superposition of cubic and uniaxial anisotropies.

Fe films were grown by dc magnetron sputtering on MgO (001) substrates supplied by MTI Corporation. The base pressure of the sputtering chamber was better than 3×10^{-8} mbar. The

substrates have been annealed at 690 – 695°C for an hour prior to the deposition and held at 150°C during the deposition. For these samples also, the Fe beam in the sputtering chamber has been incident at an angle of 30° w.r.t. the surface normal of the substrate. Two samples have been prepared without and with substrate rotation (R_{sub}) with the following structure: MgO (001)/Fe (15 nm)/Al₂O₃ (3.5 nm). The latter was deposited with $R_{sub} = 10 \text{ rpm}$ in order to minimize the effect of the growth-induced anisotropy. The details of the prepared samples are listed in table 5.1. As discussed earlier, Fe layers grow epitaxially on MgO (001) substrate, however, there might be a small lattice mismatch accompanied by a tetragonal distortion [15,24,208]. To prevent oxidation of the Fe layer, a capping layer of 3.5 nm thick Al₂O₃ has been deposited on both the samples using rf sputtering. Fe and Al₂O₃ layers have been deposited at a rate of 0.022 and 0.008 nm/s, respectively.

Table 5.1. Details of the epitaxial single layer Fe samples

Sample name	Sample structure	Substrate rotation (R_{sub})
Sample 5S_A	MgO (001)/Fe (15 nm)/Al ₂ O ₃ (3.5 nm)	0 rpm
Sample 5S_B	MgO (001)/Fe (15 nm)/Al ₂ O ₃ (3.5 nm)	10 rpm

Hysteresis loops for the Fe thin films have been measured using MOKE magnetometer in both longitudinal and transverse geometries. The domain imaging for both the samples have been carried out at RT using MOKE microscope within the applied field range of $\pm 40 \text{ mT}$ by rotating the sample w.r.t. the applied field in 10° interval. Figure 5.1 shows the coordinate system for the anisotropy configuration in Fe thin film having both cubic and uniaxial anisotropies. The angle between applied field H and Fe [100] direction (easy axis) is denoted by ϕ . It should be noted that the easy axes of both the uniaxial and cubic anisotropies lie along [100]. This is the global easy axis of the sample and the energy is lowest along this direction (blue solid line in figure 5.1). However, along [010] direction another easy axis of

CMA and hard axis of UMA coincides (red solid line in figure 5.1). The cubic hard axes lie along [110] and $[\bar{1}\bar{1}0]$ directions (green dotted lines in figure 5.1).

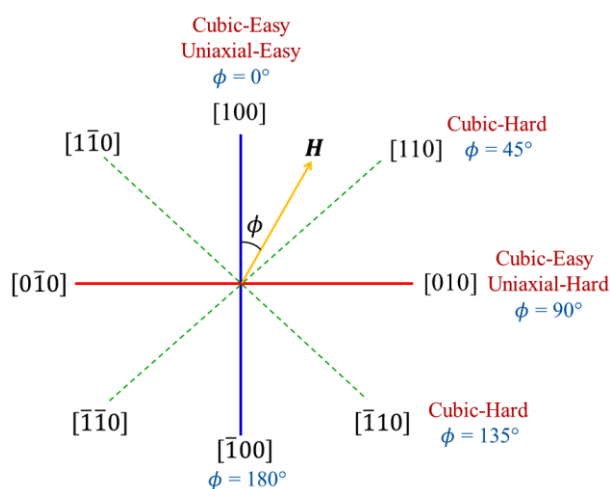


Figure 5.1: Coordinate system used to describe the anisotropy configuration of epitaxial Fe thin film on MgO (001) substrate having both cubic and uniaxial anisotropies.

In both samples 5S_A and 5S_B, one and two stepped hysteresis loops are observed depending on the angle (ϕ) between the applied field direction and the easy axis. Single step hysteresis loops are observed for $\phi \cong 0$ or 180° within a range of $\pm \sim 30^\circ$. Similarly, two stepped loops are observed for $\phi \cong 90$ or 270° within a range of $\pm \sim 60^\circ$. Similar hysteresis loops with one or more steps have been observed by other groups in Fe thin films having superposition of uniaxial and cubic anisotropies [23,187,208]. The anisotropy symmetry of these samples can be plotted by extracting the switching fields from all the hysteresis loops. The switching field for single stepped loop is defined as H_{C1} . Whereas, the lower and higher switching fields for the double stepped loops are defined as H_{C1} and H_{C2} , respectively. Figure 5.2 shows the anisotropy symmetry of both the samples. From the coercivity plot of sample 5S_A (figure 5.2(a)), H_{C1} shows maxima at 0° [100] and 90° [010] and minima at 45° [110] confirming the presence of cubic anisotropy in the sample. For the additional UMA, $\phi = 0^\circ$ and 90° correspond to the easy and hard axes, respectively, which explains the pronounced maxima of H_{C2} at 0° as compared to 90° . For sample 5S_B, similar anisotropy behavior

(figure 5.2(b)) has been observed with less difference between the H_{C2} values at 0 and 90°. However, H_{C1} still exhibits pronounced maxima at $\phi = 0^\circ$ than 90°. Therefore, it can be inferred that $R_{Sub} = 10$ rpm is not sufficient to remove the oblique angular deposition induced UMA. It can only suppress the UMA contribution in the sample by lowering the H_{C2} [82,208]. Rotation at higher rpm may suppress further or remove the additional UMA.

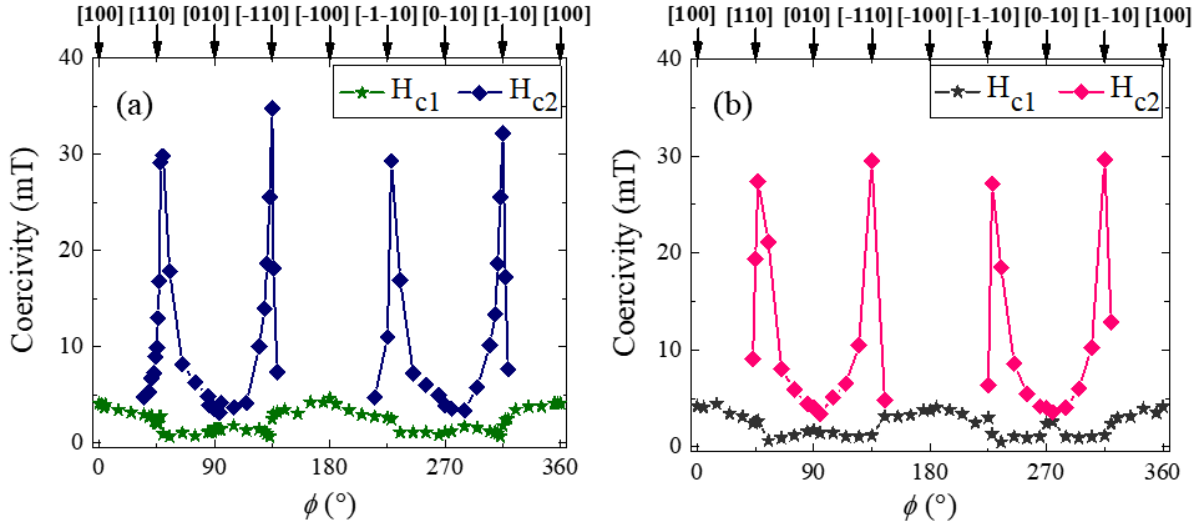


Figure 5.2: Coercivity (H_C) vs. angle (ϕ) plot for (a) sample 5S_A and (b) sample 5S_B. H_{C1} and H_{C2} values are extracted from hysteresis loops measured by longitudinal MOKE.

Figure 5.3 shows the hysteresis loops for different angles measured at RT using both longitudinal and transverse modes for sample 5S_A. Along the uniaxial cum cubic easy axis ($\phi = 0^\circ$) single step loop has been observed (figure 5.3(a)). The transverse loop measured along this direction does not indicate presence of any transverse component (figure 5.3(d)). Double stepped loop has been observed along the cubic hard axis ($\phi = 45^\circ$) in longitudinal mode (figure 5.3(b)). The clear asymmetry in the loop shape indicates contribution from the higher order Kerr components (quadratic terms) which has been observed by other groups for such Fe thin films [209-213]. The loop shape in figure 5.3(e) indicates presence of transverse component at this angle. Along the cubic easy cum uniaxial hard axis ($\phi = 90^\circ$) a small step

has been observed due to the interplay of both the anisotropies (figure 5.3(c)). In this configuration clear presence of transverse component has been evidenced from figure 5.3(f) where the sudden increase and decrease in intensity occurs exactly at H_{C1} and H_{C2} field values obtained from the longitudinal loop.

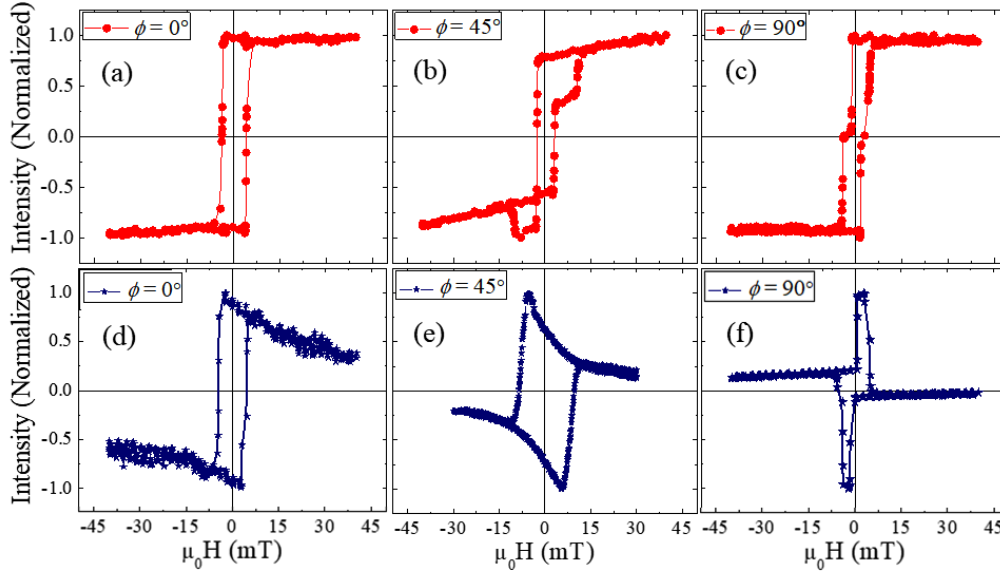


Figure 5.3: Hysteresis loops measured at RT by longitudinal (a – c) and transverse (d – f) MOKE for different ϕ (0° , 45° and 90°) for sample 5S_A.

According to the theoretical model adopted by Zhan *et al.*, Fe film on MgO (001) substrate exhibits two simultaneous 90° DW motion along $\phi = 0^\circ$. When $H = H_{C1}$, domains nucleate along the intermediate axis [010] with corresponding energy $\Delta E_{180^\circ \rightarrow 90^\circ} = C_{90^\circ}$. In order to achieve the full 180° reversal from [100] to $[\bar{1}00]$ via [010] directions another nucleation of domain occurs simultaneously from [010] to $[\bar{1}00]$ as the required energy $\Delta E_{90^\circ \rightarrow 0^\circ}$ is already present at H_{C1} [214]. Therefore, two simultaneous 90° DW motion result in single step in the hysteresis loop. Figure 5.4 shows the hysteresis loops and corresponding domain images for sample 5S_A along $\phi = 0^\circ$ ([100] direction). We have observed a similar reversal mechanism as discussed earlier in the theoretical model. It can be observed from the domain images that two 90° domains appear simultaneously (image 5.4(c) at point 2 of 5.4(a)) and 180° reversal occurs with a single jump in the hysteresis loop. It has been reported in previous literature

that such kind of domain structures are known as 90° domain [192]. From the domain image near the coercivity (image 5.4(d) at point 3 of 5.4(a)), two different shades (black and grey) are observed simultaneously over the white shade. This can be observed clearly from the high-resolution domain images shown in figure 5.5.

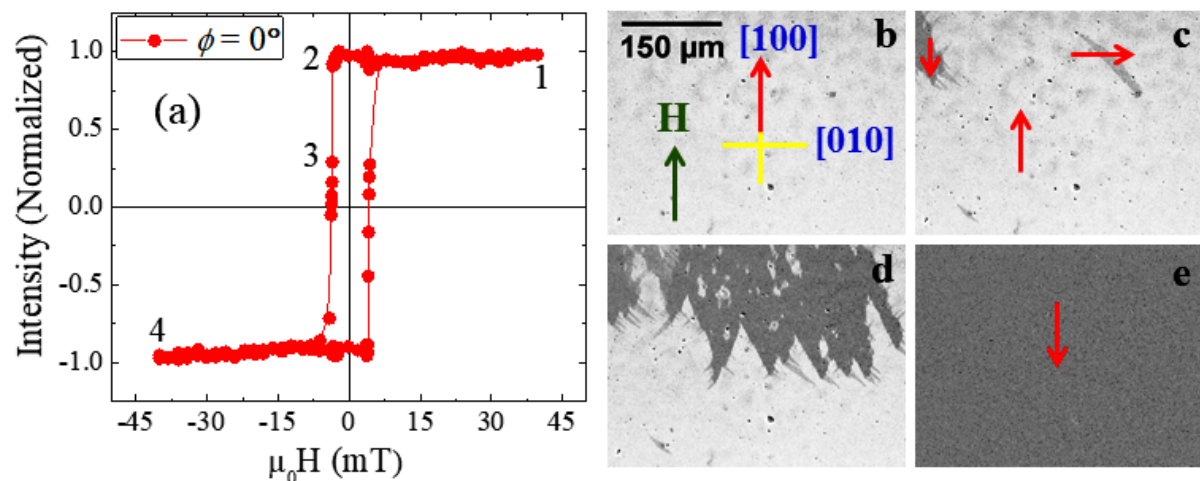


Figure 5.4: Hysteresis loop (a) and its corresponding domain images (b – e) measured by longitudinal Kerr microscope along $\phi = 0^\circ$ for sample 5S_A. The images shown in (b) – (d) correspond to the domain states in the hysteresis loop for the numbers 1 – 4, respectively. The red arrows in the images represent the net magnetization of that particular area of the sample. The green arrow in (b) shows the direction of applied magnetic field (H). All the images are in same length scale as shown in (b).

At saturation all the spins are oriented along the applied field direction i.e. [100] resulting in domains with white contrast (figure 5.4(b)). Now at point 2 in the hysteresis loop, a sharp jump occurs with domains having grey contrast oriented along [010] over the white contrast domains (figure 5.4(c)) which are 90° with respect to each other. Simultaneously the second domain (black contrast) nucleates with orientation along $[\bar{1}00]$ direction (figure 5.4(c)). The angle between domains with grey and black contrast is also 90°. Both the domains expand simultaneously to complete the 180° reversal. On further increasing the applied field the film achieves a saturation state with all the spins pointing toward $[\bar{1}00]$ direction (figure 5.4(e)).

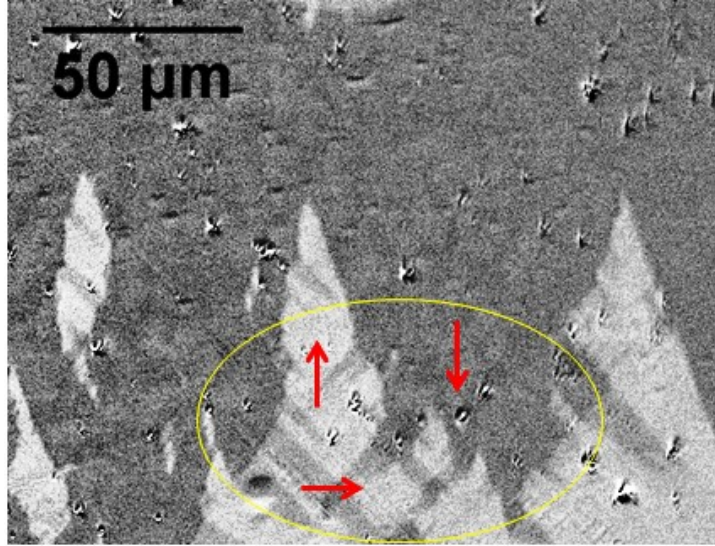


Figure 5.5: High Resolution Domain image along $\phi = 0^\circ$ for sample 5S_A captured by Kerr microscope. The area encircled shows two 90° DWs.

The two-step loops are also explained using the theoretical model by Zhan *et al.* where two separate 90° DW motion i.e. the two separate energy barriers are considered [208]. For $0^\circ < \phi < 45^\circ$ i.e. H close to cubic hard axis $[110]$ direction, the energy difference $\Delta E_{180^\circ \rightarrow 90^\circ}$ between $[110]$ to $[\bar{1}\bar{1}0]$ is comparable to C_{90° at H_{C1} . Further in order to make the reversal from $[\bar{1}\bar{1}0]$ to $[\bar{1}\bar{1}0]$ extra Zeeman energy is needed as $\Delta E_{90^\circ \rightarrow 0^\circ}$ is still smaller than C_{90° and this is achieved at H_{C2} [208]. This results in two stepped hysteresis loop with two discrete sharp jumps at H_{C1} and H_{C2} (figure 5.6(a)). However, our experimentally observed behavior differs with the theoretical model in terms of the domain orientations. When the magnetic field is applied along the cubic hard axis ($\phi = 45^\circ$) all the spins point along $[110]$ direction at saturation. However, it can be observed that at point 1 in figure 5.6(a), magnetization did not reach saturation. Therefore, in the corresponding domain image (figure 5.6(b)) the magnetization direction is pointed a bit shifted from $[110]$ towards $[100]$ direction. While increasing the field towards negative direction, the magnetization direction prefers to align along the easy axis i.e. $[100]$ direction via coherent rotation.

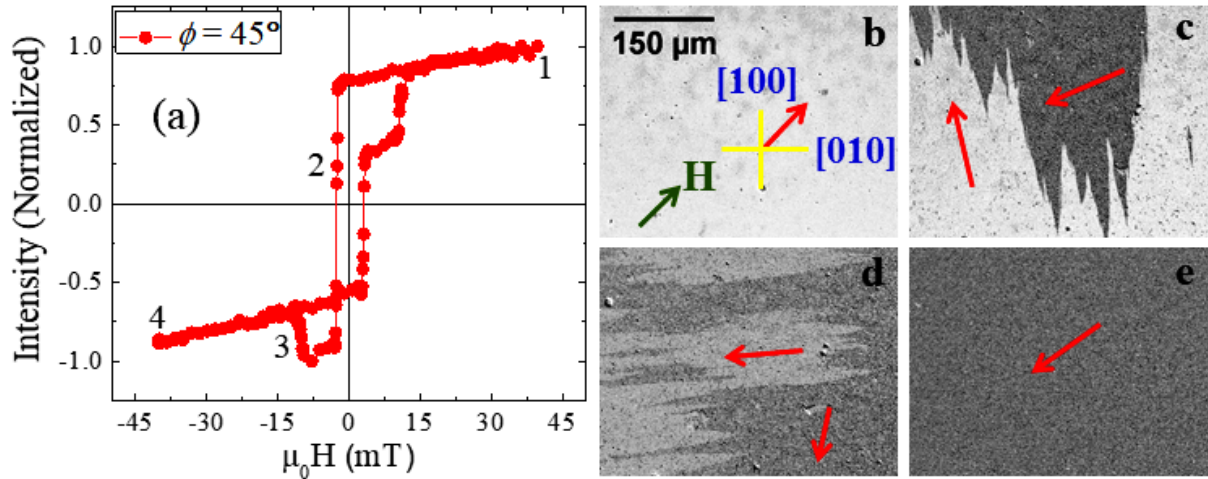


Figure 5.6: Hysteresis loop (a) and its corresponding domain images (b – e) measured by longitudinal Kerr microscope along $\phi = 45^\circ$ for sample 5S_A. The images shown in (b) – (d) correspond to the domain states in the hysteresis loop for the numbers 1 – 4, respectively. The red arrows in the images represent the net magnetization of that particular area of the sample. The green arrow in (b) shows the direction of applied magnetic field (H). All the images are in same length scale as shown in (b).

Considering the anisotropy symmetry schematic shown in figure 5.1, for $\phi \leq 45^\circ$, $[100]$ is energetically more favorable as compared to $[010]$. Referring to figure 5.6(a) we have observed that while changing the state from the positive remanence by negative magnetic field, it leads to the first reversal. Here the spins get flipped from near $[100]$ to near $[0\bar{1}0]$ direction via a 90° DW motion as observed in figure 5.6(c). A plateau is observed in this state where the net magnetization rotates from near $[0\bar{1}0]$ to $[0\bar{1}0]$ direction. Further increase in the field leads to a 2nd reversal by switching the spin direction from $[0\bar{1}0]$ to $[\bar{1}00]$ through another 90° DW motion (figure 5.6(d)). The later reversal occurs by producing a hump-like feature, where the MOKE intensity is even lower than the negative saturation. It has been reported in previous literature that this asymmetry in hysteresis loops in Fe samples occurs due to the quadratic component of the MOKE. Near the hard axis of the sample the quadratic component becomes dominant over the linear one of the MOKE which gives rise to sudden

jumps in hysteresis loops [209-213]. Further, the reversal gets completed with partial rotation of spins from $[\bar{1}00]$ to $[\bar{1}\bar{1}0]$ by applying more negative field (figure 5.6(e)).

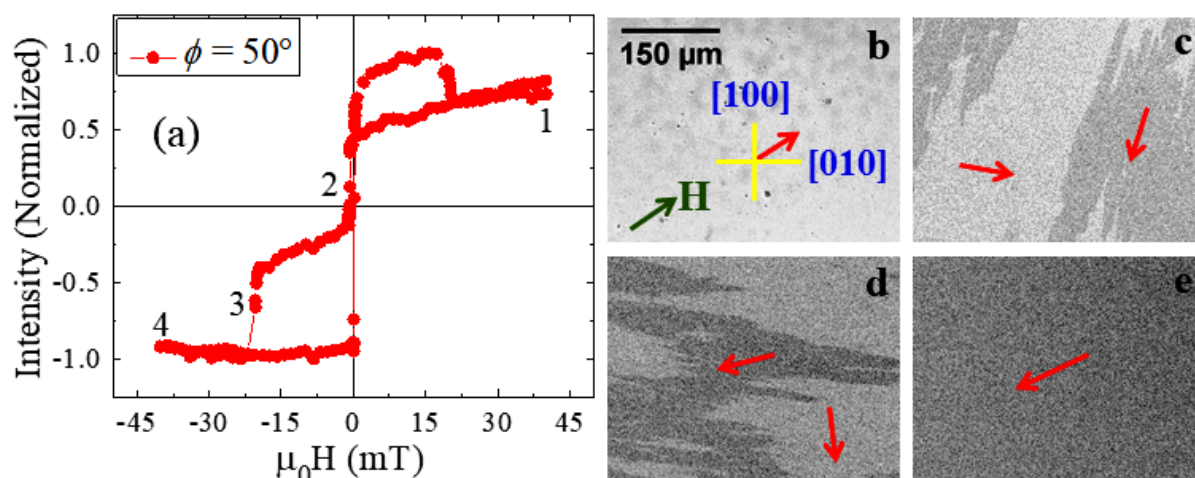


Figure 5.7: Hysteresis loop (a) and its corresponding domain images (b – e) measured by longitudinal Kerr microscope along $\phi = 50^\circ$ for sample 5S_A. The images shown in (b) – (d) correspond to the domain states in the hysteresis loop for the numbers 1 – 4, respectively. The red arrows in the images represent the net magnetization of that particular area of the sample. The green arrow in (b) shows the direction of applied magnetic field (H). All the images are in same length scale as shown in (b).

It has been found from the anisotropy symmetry plot (figure 5.2(a)) that $\phi = 50^\circ$ is the resultant hard axis of CMA and UMA. This may happen due to little mismatch in the orientation of both the anisotropies, while mounting the sample in the deposition chamber. Figure 5.7(a) shows the hysteresis loop for sample 5S_A measured along $\phi = 50^\circ$. For $\phi > 45^\circ$, while decreasing the magnetic field from the positive saturation state, the spins try to orient themselves via coherent rotation towards $[010]$ direction as it is the nearest minimum energy state. When the spins cross $[010]$ direction, first reversal occurs from near $[010]$ to near $[\bar{1}00]$ direction via a 90° DW motion (image 5.7(c) at point 2 of 5.7(a)). A wide plateau region has been observed in the loop (figure 5.7(a)) after the first reversal. In this state the spins are dragged from near the $[\bar{1}00]$ to the $[\bar{1}\bar{1}0]$ direction via coherent rotation. When the

spins cross the $[\bar{1}00]$ axis in reverse direction, further application of magnetic field in negative direction leads to one more reversal from $[\bar{1}00]$ to $[010]$ direction via another 90° DW motion (image 5.7(d) at point 3 of 5.7(a)). Afterwards, with increase in the field to negative saturation the spins are dragged towards the applied field direction via coherent rotation (figure 5.7(e)). For the other branch of the hysteresis loop (negative to positive side i.e. point 4 to 1 in figure 5.7(a)) the sudden increase of the MOKE intensity than the positive saturation state indicates presence of transverse component in the sample. As discussed earlier, this asymmetry (sudden increase) in the hysteresis loop arises due to the dominance of quadratic component of MOKE over the linear one [209-213]. It should be noted that the asymmetry present in the loop along $\phi = 45^\circ$ (figure 5.6(a)) is the reverse of the asymmetry present in the loop for $\phi = 50^\circ$ (figure 5.7(a)). This is because the path of the reversal process is just opposite for $40^\circ \leq \phi \leq 45^\circ$ and $45^\circ \leq \phi \leq 70^\circ$.

Further increasing ϕ from 50° to 90° , we observed that the magnetization reversal mechanism for $\phi = 90^\circ$ is not similar to $\phi = 0^\circ$ as predicted by the theoretical model from Zhan *et al.*[214] It has been observed from figure 5.8(a) that along $\phi = 90^\circ$, a very small step is present in the hysteresis loop which gives rise to two separate 90° DW motion at H_{C1} and H_{C2} . Here the values of H_{C1} and H_{C2} are comparable. Being the easy axis loop for CMA, the step is present in the loop because of the fact that it is the hard axis for UMA. However, as cubic anisotropy is dominant in this system, the step is very small in this configuration. From the domain images of $\phi = 90^\circ$ (figure 5.8(c, d)), we observe that two independent 90° reversals occur just one after another. Here the domains (white contrast) are oriented along the $[010]$ at saturation (figure 5.8(b)). While approaching to H_{C1} grey contrast domains appear along $[\bar{1}00]$ (figure 5.8(c)) and quickly sweep through the whole sample. Right after this, black contrast domains appear along $[0\bar{1}0]$ (figure 5.8(d)) and get saturated (figure 5.8(e)). On further increasing from $\phi = 90^\circ$ towards $\phi = 135^\circ$ the steps become more

prominent as it reaches to another hard axis of CMA. After 135°, step size starts decreasing and becomes single step loop when ϕ approaches towards 180°. Coercivity values and hysteresis loop shapes are exactly similar for $180^\circ \leq \phi \leq 360^\circ$ as discussed for $0^\circ \leq \phi \leq 180^\circ$.

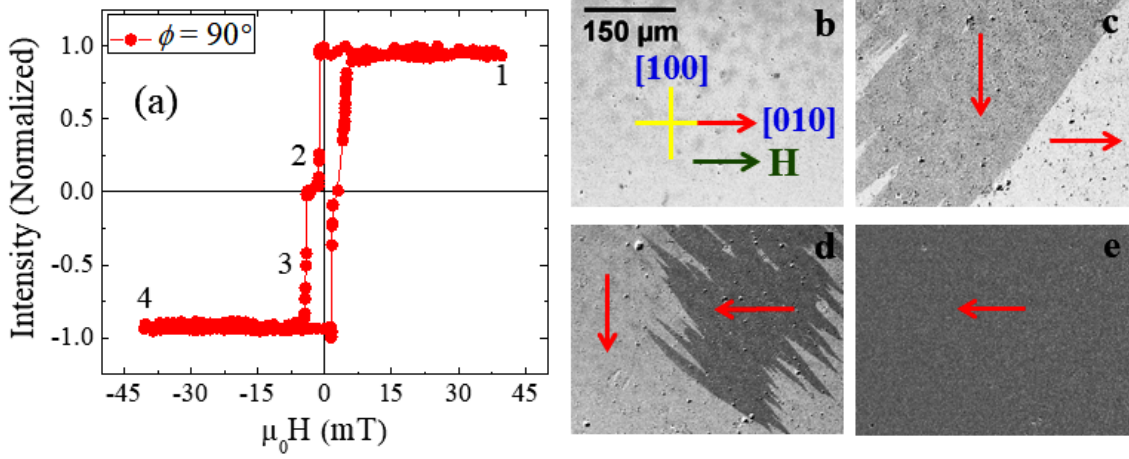


Figure 5.8: Hysteresis loop (a) and its corresponding domain images (b – e) measured by longitudinal Kerr microscope along $\phi = 90^\circ$ for sample 5S_A. The images shown in (b) – (d) correspond to the domain states in the hysteresis loop for the numbers 1 – 4, respectively. The red arrows in the images represent the net magnetization of that particular area of the sample. The green arrow in (b) shows the direction of applied magnetic field (H). All the images are in same length scale as shown in (b).

The damping properties and quantification of anisotropies have been performed using frequency (figure 5.9(a)) and angle dependent FMR measurements, respectively. The damping constant (α) can be calculated using the following formula [200]

$$\alpha = \frac{\Delta H \cdot \gamma}{4\pi\omega} \quad (5.1)$$

where, ΔH is the line width of the derivative of the FMR signal, γ is the gyromagnetic ratio of Fe and ω is the measurement frequency. The damping constant (α) of sample 5S_A is calculated by linearly fitting the frequency dependent line width data (figure 5.9(b)). The best fitted value of α has been extracted to be 0.033 ± 0.001 . Figure 5.9(c) depicts the ω vs H_R

plot for sample 5S_A. The effective magnetization (M_{eff}) and the anisotropy field (H_K) were determined by fitting the ω vs H_R data with the following Kittel equation [178].

$$\omega = \frac{\gamma}{2\pi} \sqrt{(H_R + H_K)(H_R + H_K + 4\pi M_{eff})} \quad (5.2)$$

The values of H_K and $\mu_0 M_{eff}$ for sample 5S_A are 54.19 ± 0.60 mT and 1235.75 ± 76.36 mT, respectively.

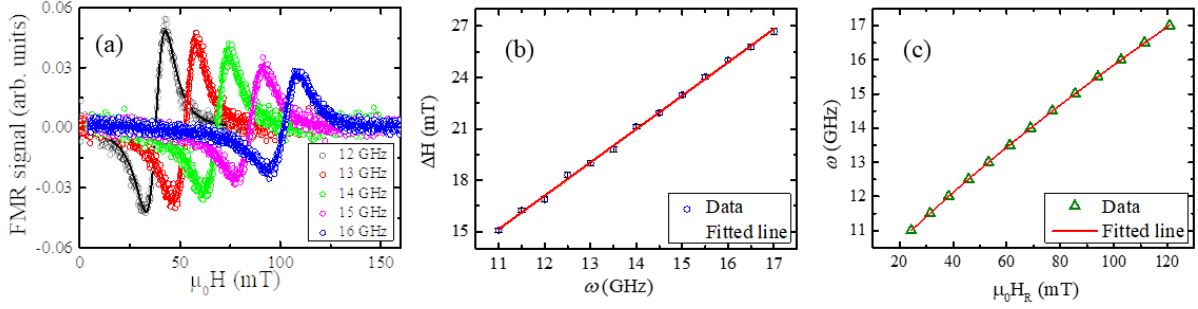


Figure 5.9: (a) Frequency dependent FMR signal for sample 5S_A. (b) ΔH vs ω and (c) ω vs H_R plots for sample 5S_A to calculate the damping constant and anisotropy field, respectively.

Figure 5.10 shows the angle dependent H_R plot for sample 5S_A. The blue solid circles represent the data points and the red line corresponds to their fit. The dispersion relation of a system having both cubic and uniaxial anisotropies can be expressed by following equation:

$$\left(\frac{\omega}{\gamma}\right)^2 = \frac{1}{4\pi} \left(H_{res} + \frac{2K_2}{M_S} \cos 2(\phi - \phi_0) - \frac{4K_4}{M_S} \cos 4(\phi - \phi_0) \right) \left(H_{res} + 4\pi M_S + \frac{2K_2}{M_S} \cos^2(\phi - \phi_0) - \frac{K_4}{M_S} (3 + \cos 4(\phi - \phi_0)) \right) \quad (5.3)$$

where, K_2 and K_4 are the uniaxial and cubic anisotropy constants, respectively, M_S is the saturation magnetization, ϕ is the angle between H and the reference direction x and ϕ_0 is the angle between EA and x axis. When $\phi_0 = 0$, ϕ becomes the angle between EA and H.

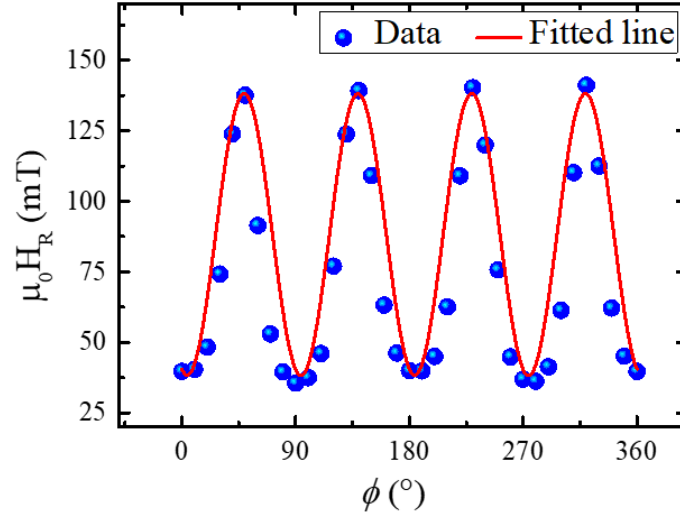


Figure 5.10: Anisotropy symmetry plot and its fit for sample 5S_A measured using ferromagnetic resonance (FMR) technique by keeping the frequency fixed at 10 GHz. The blue colored solid circles and the red line correspond to the measured data for $0^\circ < \phi < 360^\circ$ in 10° interval and the fit to equation 5.3, respectively.

To quantify the anisotropy contribution present in sample 5S_A, the angle dependent H_R data has been fitted using equation 5.3. The extracted values of K_2 and K_4 are extracted to be -49 J/m^3 and $-1.4 \times 10^4 \text{ J/m}^3$, respectively. The presence of cubic anisotropy is expected due to the intrinsic nature of Fe and the epitaxial growth on MgO (001) substrate. Due to the oblique angular deposition geometry of our chamber, uniaxial anisotropy is induced in the sample. However, the strength of uniaxial anisotropy is much weaker than the intrinsic cubic anisotropy.

5.2. Effect of magnetic C₆₀ on the magnetic properties of Fe thin film (bilayer of epitaxial Fe/C₆₀):

To study the effect of Fe/C₆₀ spinterface on the epitaxially grown Fe layer, sample 5B_A has been prepared with the following structure: MgO (001)/Fe(15 nm)/C₆₀(40 nm)/Ta(3 nm). Fe and C₆₀ layers have been prepared without breaking the vacuum using dc magnetron sputtering and thermal evaporation technique, respectively. The deposition conditions of the

Fe layer have been kept constant to sample 5S_A. To prevent from oxidation and surface damage, a capping layer of Ta has been deposited on the sample. Figure 5.11(a) shows the schematic of the layer structure of sample 5B_A. It has been reported that C₆₀ adsorption on Fe surface leads to surface reconstruction when the deposition temperature is in the temperature range of 70°C to 300°C [185,188]. Yang *et al.* have performed ab initio calculation to show that for Fe/C₆₀ interface, 4 atom hole reconstruction is the most stable adsorption structure where a pentagon of the C₆₀ cage sinks-in a 4-atom hole of top most Fe atomic layer [188]. In this context it should be noted that sample 5B_A is prepared at 150°C. Therefore, similar mechanism of four-atom hole reconstruction might be possible in sample 5B_A. However, depending on the roughness at the interface, intermixing of Fe and C₆₀ is also quite probable.

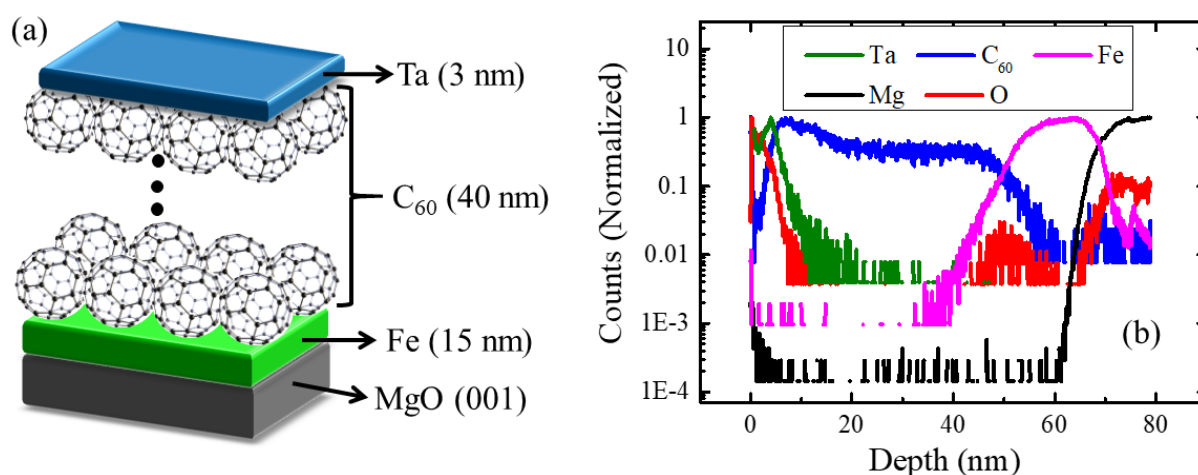


Figure 5.11: (a) Schematic layer structure of sample 5B_A. (b) Depth profile of sample 5B_A measured using secondary ion mass spectroscopy (SIMS) technique.

ION-TOF's [205,206] time of flight secondary ion mass spectroscopy (TOF-SIMS) has been performed on the bilayer sample to analyze the thickness of the individual layers and study the nature of their interfaces. Initially the material dependent SIMS data have been recorded according to the appearance of each layers with respect to the time of measurement. In order to calibrate the SIMS data, thickness profilometry experiment has been performed on the

specific hole from where the materials have been dug out during the SIMS measurement. The sputtering area and analysis area have been chosen to be $300 \times 300 \mu\text{m}^2$ and $100 \times 100 \mu\text{m}^2$, respectively. Figure 1(b) shows the depth profile for the layer structure of sample 5B_A obtained from the SIMS measurement. The plotted data clearly resolves individual layers of the multilayer structure of MgO (001)/Fe(15 nm)/C₆₀(40 nm)/Ta(3 nm) accordingly as per the proper growth structure. Initially high intensity of Ta (green) and O (red) have been observed at the top most layer. The intensity of Ta starts decreasing with the increasing intensity of C₆₀ (blue). The pink color represents the Fe layer next to the C₆₀ layer. Further, the MgO substrate (Mg is black and O is red) have been observed. The thicknesses of the layers have been calculated from figure 5.11(b) as $\sim 14.53 \pm 3.34$ nm, $\sim 44.58 \pm 3.28$ nm, $\sim 2.94 \pm 1.23$ nm for Fe, C₆₀ and Ta, respectively. It has been anticipated from the position of the intercept between two consecutive layers that very thin layer of inter-diffusion (<1 nm) might be present. However, the exact thicknesses of the inter-diffusion layers could not be calculated from the data as it was beyond the resolution limit of the technique.

Neutron is a powerful probe to provide layer selective structural as well as magnetic information in multilayers. PNR has been performed at RT on the Fe/C₆₀ sample at MARIA reflectometer at FRM II, Garching, Germany [176]. A similar sample like sample 5B_A with 6 nm Au as capping layer instead of the Ta layer has been used for the PNR measurement. The wavelength (λ) of the neutrons in the PNR measurements has been chosen to be 6.5 Å. Two scattering cross sections R^{++} and R^{--} have been measured where the intensity depends on the interaction of the neutrons with the magnetic spins in the sample. PNR measurements have been performed on the sample by applying magnetic field along $\phi \sim 45^\circ$ (cubic hard axis) and $\phi \sim 90^\circ$ (cubic easy but uniaxial hard axis). Figure 5.12(a) shows the PNR data measured at saturation ($\mu_0 H = 100$ mT). The red and blue open circles correspond to the data for R^{++} and R^{--} reflected neutron intensity, respectively. The reflectivity for R^{++}

reflectivity is more than that of the R^{--} case for lower Q values which confirms that the sample has been measured at its positive magnetized state. The data has been fitted using the same GenX software [143]. The thickness of each layer including the interdiffusion ones has been extracted from the best fit. The extracted values are of the same order with the ones evaluated from the SIMS data.

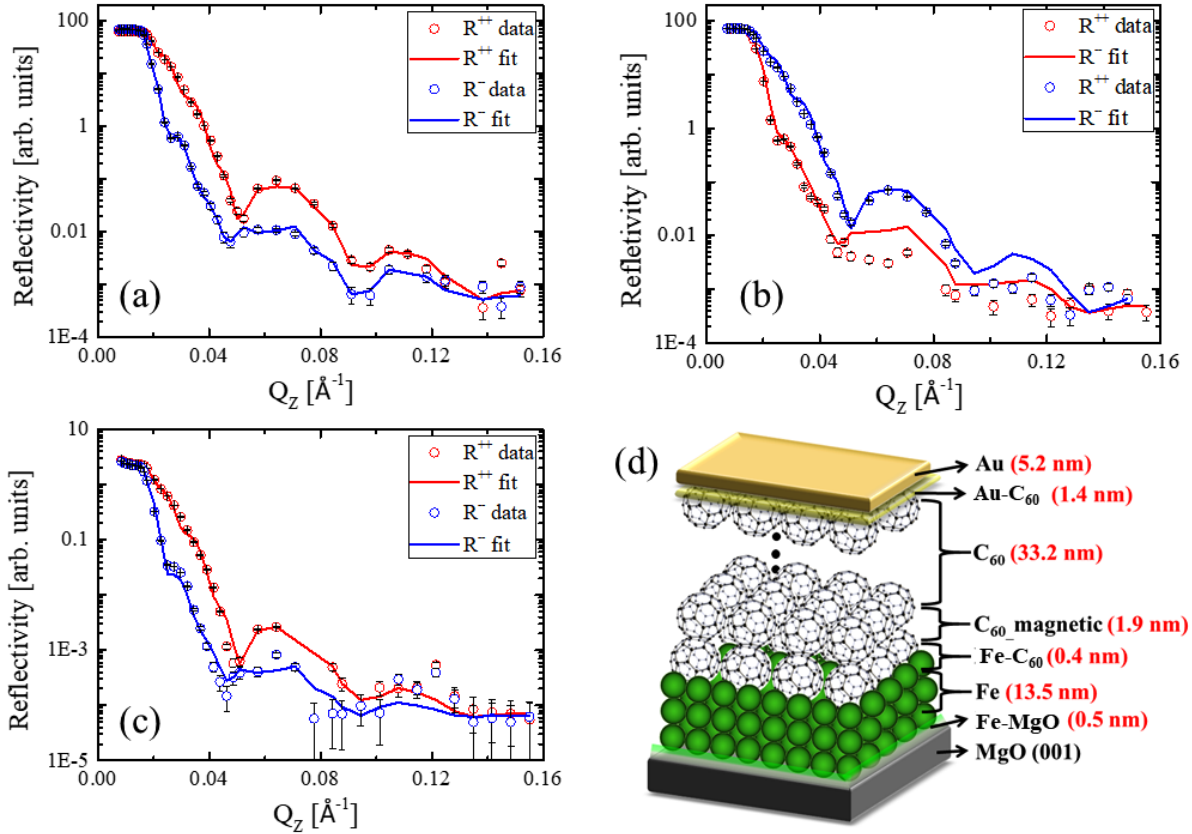


Figure 5.12: Polarized neutron reflectivity (PNR) data for sample 5B_A measured at RT at (a) saturation ($\mu_0 H = 100$ mT), (b) near remanence ($\mu_0 H = 2.1$ mT) for magnetic field applied along $\phi = 45^\circ$ and (c) saturation ($\mu_0 H = 100$ mT) for magnetic field applied along $\phi = 90^\circ$. The PNR data (open circles) and their corresponding fits (solid lines) for R^{++} and R^{--} channels are shown by red and blue color, respectively. (d) The model layer structure for sample 5B_A where the thicknesses for each layer have been obtained by fitting the PNR data.

From the PNR fits we have obtained the magnetic moments for each layer of the sample. The Fe layer exhibits magnetic moment of $1.59 \pm 0.02 \mu_B/\text{atom}$, which is less by $\sim 27\%$ than the single layer sample 5S_A ($2.20 \pm 0.01 \mu_B/\text{atom}$). The PNR fits indicate that a thin layer ($0.38 \pm 0.03 \text{ nm}$) of interdiffusion is present at the interface of Fe and C₆₀ layers. This layer consists of the top most Fe atomic layer and the lower portion of the C₆₀ cages. It should be noted that we have tried to fit the data with various thicknesses of the interdiffusion layer. However, the best figure of merit was obtained for the thickness of $0.38 \pm 0.03 \text{ nm}$. Further, we note that the roughness at the interface is high because of the high temperature growth and large lattice mismatch between Fe and C₆₀. Therefore, this interdiffusion layer may be a result of surface reconstruction or could actually be simple intermixing. The Fe-C₆₀ interdiffusion layer exhibits a magnetic moment of $5.14 \pm 0.15 \mu_B/\text{unit}$ where 1 unit is comprised of one Fe atom and one C₆₀ cage. On top of this interdiffusion layer, up to $1.9 \pm 0.1 \text{ nm}$ of C₆₀ near the Fe-Fullerene interface exhibits a magnetic moment of $2.95 \pm 0.27 \mu_B/\text{cage}$ (as per the best fit). The density parameter used to fit the data confirms that this moment arises from pure C₆₀ layer and not from any mixture of Fe and C₆₀. The reason behind the induced magnetic moment in pure fullerene cages is the hybridization between Fe and C atoms at the interface. C atom has the affinity for hybridization to obtain stable from with lower energy due to its electronic structure and Fe can get coupled with its *d* orbital to reach the lower energy configuration [8,188,191]. Due to such polarized charge/spin transfer between Fe and C atoms, the fullerene balls exhibit magnetic moment and Fe moment gets decreased than its bulk value. We have tried to fit the PNR data for various values of magnetic moment in the range of 1 to $5 \mu_B$ for the magnetic C₆₀ interface. Qualitatively similar fits have been found in comparison to figure 5.12(a) by considering C₆₀ moment in the range of 1 to $5 \mu_B$. However, for $\mu_{C60} = 2.95 \pm 0.27 \mu_B/\text{cage}$ the figure of merit (FOM)

has been found to be the lowest which indicates the best fit. This can be further confirmed from the FOM vs moment of C₆₀ plot shown in figure 5.13.

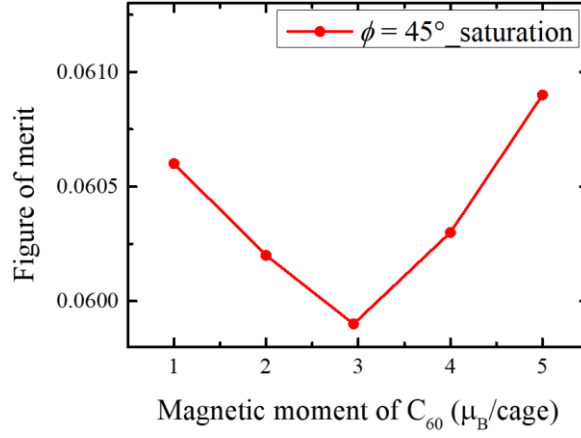


Figure 5.13: Figure of merit (FOM) versus different values of induced magnetic moment of C₆₀ to show the best fitted value of the induced moment.

It should be noted that the DFT calculation by Moorsom *et al.* have shown that 1.3 e charge transfer between the metallic ferromagnet to the C₆₀ interface can yield magnetic moment up to 3 μ_B [6]. This implies that our obtained moment of 2.95 μ_B may not be due to the result of direct charge transfer of 3 e. However, if we consider that the induced magnetic moment in C₆₀ is a result of equivalent charge transfer of ~ 3 e, then the potential at the Fe/C₆₀ interface becomes ~2 V which may be unphysical. The potential can be calculated using Helmholtz equation i.e.

$$\Delta V = \mu \times \frac{\cos\vartheta}{(\epsilon_r \times \epsilon_0)}$$

where, μ is the dipole moment per unit area, ϑ ≈ 0 is the angle between dipole and surface normal, ε_r ~ 4.2 (typical value for C₆₀ is between 4 to 4.5), and ε₀ is the permittivity of vacuum. The exact thickness of the C₆₀ cage immersed in the topmost Fe sublayer has been obtained from the PNR data analysis. The area of the C₆₀ cage lying on the Fe surface will participate in the interfacial voltage calculation. Therefore, the area of interface which is probably directly interacting with the magnetic C₆₀ has been calculated to be ~ 1.3 nm²

(figure 5.14). Though the thickness of magnetic C₆₀ is quite high, maximum charge transfer is probable at the vicinity of the interface and the induced moment in C₆₀ will decrease with increasing distance from the interface. If the distance between point charges at C₆₀ and Fe sites is considered about 0.2 nm near interface, then the dipole moment per unit area with a charge transfer of 3 electron per C₆₀ will be,

$$\mu = (3 \times 0.2)/1.3 \text{ e/nm} = 0.462 \text{ e/nm}$$

$$\text{So, } \Delta V = (0.462 \times 1.6 \times 10^{-19} \times 10^9) / (4.2 \times 8.85 \times 10^{-12}) \text{ V} = 1.99 \text{ V}$$

Considering this argument of spin moment directly coupled to equivalent charge transfer the induced magnetic moment in our case might be $\sim 1.5 \mu_B$. Nevertheless, the actual phenomena of spin transfer coupled to charge transfer needs to be understood via future theoretical calculations to elucidate if such high moment of $\sim 3 \mu_B$ is possible to be induced in C₆₀ interface.

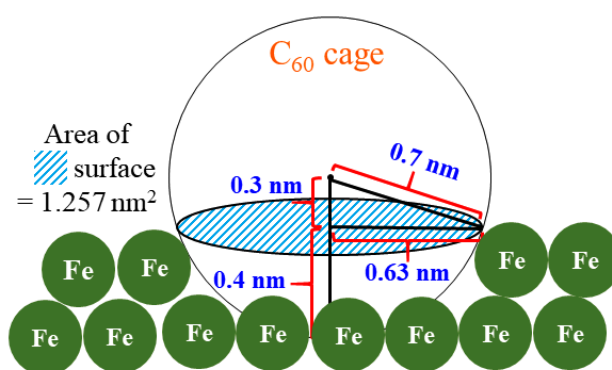


Figure 5.14: Schematic of one C₆₀ cage sitting on top of the Fe layer to calculate the area of contact between C₆₀ and Fe surface.

Figure 5.12(b) shows the PNR data for sample 5B_A measured near the remanence ($\mu_0 H = 2.1 \text{ mT}$). We have incorporated the structural parameters used in the best fit for the saturation data (figure 5.12(a)) for fitting the PNR data measured at remanence (figure 5.12(b)). It is found that near the remanence about 88% of the Fe spins have reversed in comparison to the saturation state. However, the magnetic C₆₀ layer exhibits a positive magnetic moment of

$2.95 \pm 0.27 \mu_B/\text{cage}$ in the vicinity of the interface (~ 0.2 nm). However, next to the interface (~ 1.7 nm) the induced moment in the magnetic C₆₀ becomes weaker. It should be noted that, the fullerene layer is antiferromagnetically coupled to the Fe layer at the remanence state. Figure 5.12(c) shows the PNR fit for saturation state along $\phi = 90^\circ$. The PNR fit exhibits similar information obtained from the saturation measurement along $\phi = 45^\circ$. The layer structure and the thicknesses of each layers obtained from the PNR fit is depicted in figure 5.12(d).

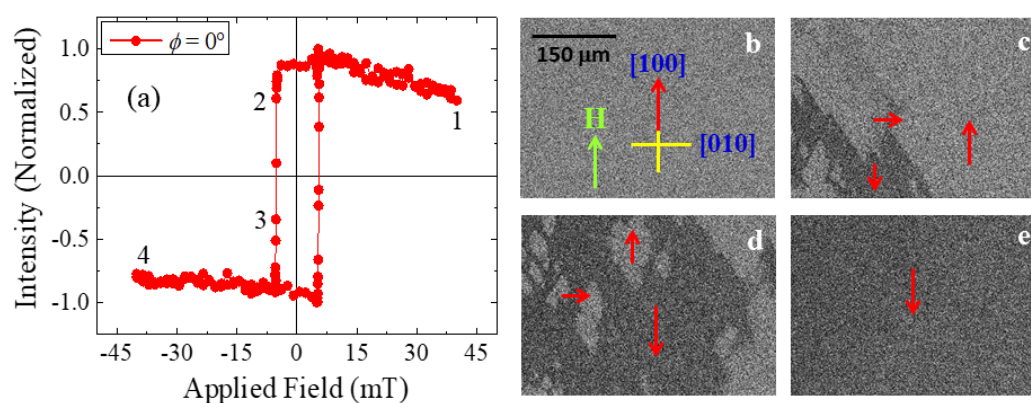


Figure 5.15: Hysteresis loop (a) and its corresponding domain images (b – e) measured by longitudinal Kerr microscope along $\phi = 0^\circ$ for sample 5B_A. The images shown in (b) – (d) correspond to the domain states in the hysteresis loop for the numbers 1 – 4, respectively. The red arrows in the images represent the net magnetization of that particular area of the sample. The green arrow in (b) shows the direction of applied magnetic field (H). All the images are in same length scale as shown in (b).

The hysteresis loops along with simultaneous domain images have been measured at RT by a MOKE based microscope in longitudinal mode to detect the change in loop shapes and domain structures due to the presence of the spinterface. Similar to the single layer sample 5S_A, MOKE measurements have been performed on 5B_A by varying the angle (ϕ) between the external magnetic field and the easy axis of the sample at an interval of 5° . Depending on ϕ , single, double even triple step loops have been observed in sample 5B_A

due to the interplay of both cubic and uniaxial anisotropies. Figure 5.15 shows the hysteresis loop and corresponding domain images in longitudinal mode for $\phi = 0^\circ$. The reversal mechanism of sample 5B_A along $\phi = 0^\circ$ is exactly similar to that of the single layer sample. By decreasing the field from positive saturation, the reversal follows the path $[100] \rightarrow [010] \rightarrow [100]$ via two simultaneous 90° DW motion. A single jump in the hysteresis loop has been observed with a small increase in coercive field (H_C) (figure 5.15(a)). The reason for the increase in H_C might be due to the strong exchange coupling between Fe and the magnetic C₆₀ interface. The domain images for sample 5B_A along $\phi = 0^\circ$ are shown in figure 5.15(b) – (e). It should be noted that near the cubic hard axis ($45^\circ < \phi < 70^\circ$), a major change in the shape of the hysteresis loops has been observed for sample 5B_A in comparison to sample 5S_A. Therefore, it can be inferred that the presence of magnetic fullerene at the interface between Fe and C₆₀ modifies the magnetization reversal. The most stable energy configuration for a sample is along its easy axes ($\phi = 0^\circ$ and/or 90°). However, the energy is maximum along the hard axis and the spins can get easily disturbed even with small deviation from the saturation state. As a consequence, significant change in the hysteresis loop shape for the bilayer sample has been observed around the CMA hard axis.

The reversal mechanism for sample 5B_A along $\phi = 45^\circ$ (figure 5.16(a)) is similar to sample 5S_A. The reversal is governed by the combination of partial rotation and two 90° DW motions. The change in the net magnetization directions of the domains observed during the reversal are shown with red arrows in figure 5.16(b) – (e). However, unlike the single layer sample, a plateau region between two 90° reversals is not observed in the bilayer sample. Here, the second 90° reversal is favoured by the magnetic C₆₀ layer and the coercivity for the second reversal is less in sample 5B_A (figure 5.16(a)) in comparison to that of sample 5S_A. The hysteresis loop is not symmetric with respect to the y-axis. This is due to the

presence of a transverse component and appearance of a quadratic MOKE component in the signal, similar to the single layer sample.

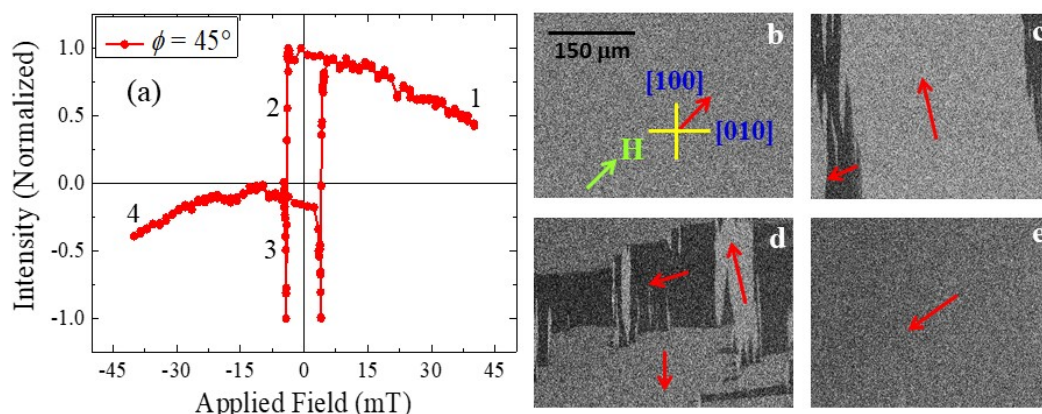


Figure 5.16: Hysteresis loop (a) and its corresponding domain images (b – e) measured by longitudinal Kerr microscope along $\phi = 45^\circ$ for sample 5B_A. The images shown in (b) – (d) correspond to the domain states in the hysteresis loop for the numbers 1 – 4, respectively. The red arrows in the images represent the net magnetization of that particular area of the sample. The green arrow in (b) shows the direction of applied magnetic field (H). All the images are in same length scale as shown in (b).

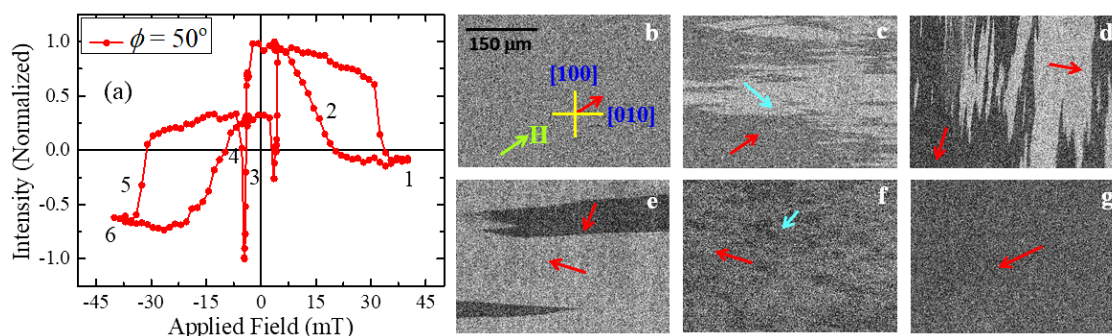


Figure 5.17: Hysteresis loop (a) and its corresponding domain images (b – g) measured by longitudinal Kerr microscope along $\phi = 50^\circ$ for sample 5B_A. (b) – (g) correspond to the domain images in the hysteresis loop for the numbers 1 – 6, respectively. The red and cyan arrows in the images represent the net magnetization of that particular area of the Fe and C₆₀ layers, respectively. The green arrow in (b) shows the direction of applied magnetic field (H). All the images are in same length scale as shown in (b).

Maximum change in the hysteresis loop shape and the reversal mechanism has been observed along the resultant hard axis ($\phi = 50^\circ$) of the sample. In case of sample 5B_A, the magnetization reversal (figure 5.17(a)) starts with coherent rotation similar to sample 5S_A. It should be noted that the effective magnetic field is $H_{eff} = H + H_{dipolar}$, where, H and $H_{dipolar}$ are the external applied field and the dipolar field generated by the Fe underlayer on the interfacial magnetic C₆₀ layer, respectively [190]. $H_{dipolar}$ is large enough to promote the reversal of the C₆₀ layer with less change in the H field. Therefore, even before the switching of the field direction the reversal of the magnetic C₆₀ layer has been observed (figure 5.17(c) corresponding to the point 2 in figure 5.17(a)). Reversal of one layer before the switching of the field direction implies the presence of antiferromagnetic coupling in the sample [35,181,215], which is corroborated by the PNR analysis of figure 5.12(b). By further reduction in the field (figure 5.17(d) corresponding to the point 3 in figure 5.17(a)) first reversal from the Fe layer is observed via 90° DW motion (i.e. similar to sample 5S_A). Immediately afterwards, the second reversal for the Fe layer takes place via another 90° DW motion (figure 5.17(e) corresponding to the point 4 in figure 5.17(a)). This sudden occurrence of the second reversal is probably due to the strong exchange coupling at the interface between Fe/magnetic C₆₀. Upon increase in applied magnetic field in the negative direction, the magnetic C₆₀ layer undergoes another reversal (figure 5.17(f), corresponding to point 5 in figure 5.17(a)), to complete full 180° reversal of the magnetic C₆₀ layer.

As discussed earlier, $\phi = 90^\circ$ is the easy direction for the cubic anisotropy but the hard direction for the uniaxial one. Similar to sample 5S_A, two stepped hysteresis loop is observed for sample 5B_A along $\phi = 90^\circ$ (figure 5.18(a)). The reversal process for sample 5B_A is exactly similar to that of sample 5S_A. The reversal follows $[010]$ to $[100]$ to $[0\bar{1}0]$ path via two successive 90° DW motions. The domain images with proper net magnetization directions for sample 5B_A are shown in figure 5.18(b) – (e).

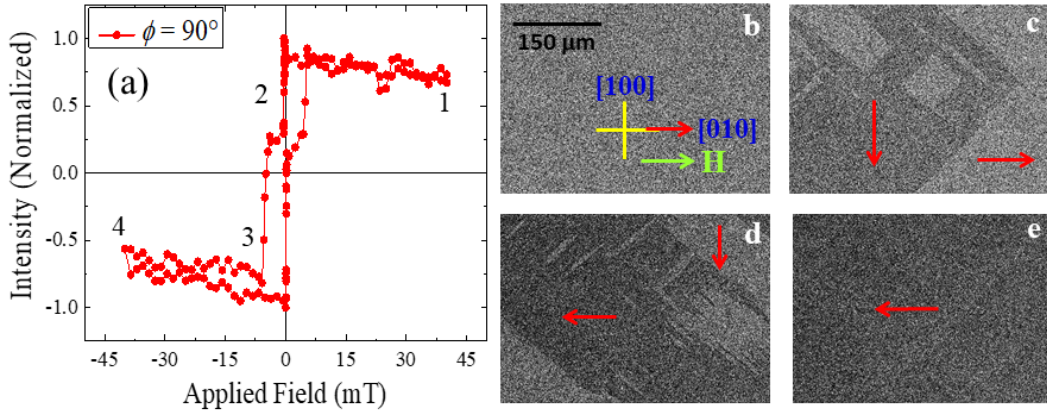


Figure 5.18: Hysteresis loop (a) and its corresponding domain images (b – e) measured by longitudinal Kerr microscope along $\phi = 90^\circ$ for sample 5B_A. The images shown in (b) – (d) correspond to the domain states in the hysteresis loop for the numbers 1 – 4, respectively. The red arrows in the images represent the net magnetization of that particular area of the sample. The green arrow in (b) shows the direction of applied magnetic field (H). All the images are in same length scale as shown in (b).

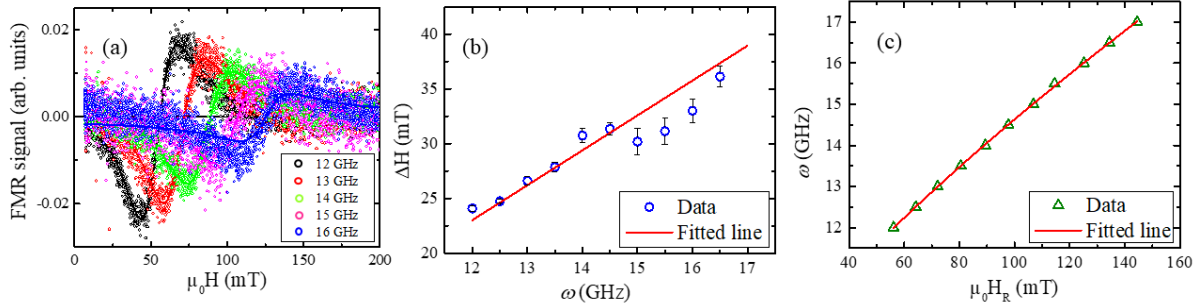


Figure 5.19: (a) Frequency dependent FMR signal for sample 5B_A. (b) ΔH vs frequency ω plot to calculate the damping constant and (c) frequency ω vs $\mu_0 H_R$ plot for sample 5B_A.

Frequency dependent FMR signals for sample 5B_A is shown in figure 5.19(a). The damping constant (α) of the sample has been calculated by taking the slope from figure 5.19(b) and substituting it in equation 5.1. The value of α for sample 5B_A is 0.052 ± 0.008 . The increase in α for sample 5B_A with respect to sample 5S_A can be expressed by the large interface roughness between Fe and C₆₀ layers. Further, it has been reported in various literature that

the damping constant increases in bilayer samples due to various extrinsic damping contribution such as interface roughness, spin pumping, and proximity effect [216-219]. It can be observed from figure 5.19(b) that the data measured in higher frequency ($\omega > 15$) exhibits non-linear nature. As the interface roughness between Fe and C₆₀ layer is quite high, it is expected that two magnon scattering will occur for such samples at higher frequencies [182]. Therefore, we have calculated the α value for sample 5B_A by considering the fit for $\omega < 15$ GHz. The values for H_K and $\mu_0 M_{eff}$ are 43.3 ± 4.8 mT and 1240.4 ± 177.5 mT for sample 5B_A, respectively. These values are extracted by fitting the data shown in figure 5.19(c) with the Kittle formula (equation 5.2).

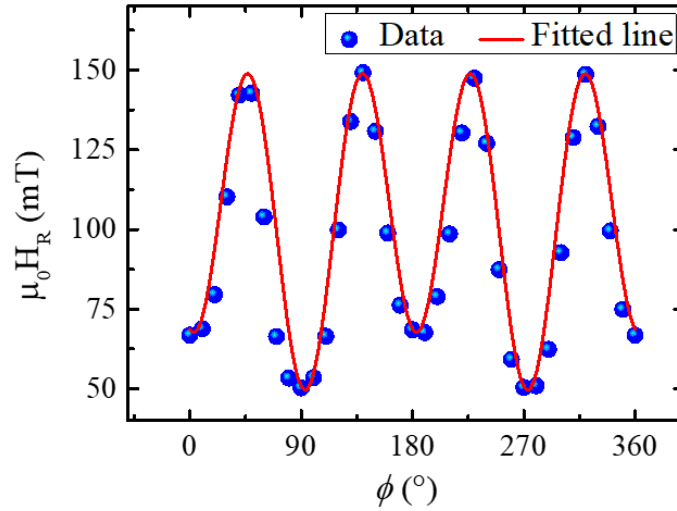


Figure 5.20: Anisotropy symmetry plot and its fit for sample 5B_A measured using ferromagnetic resonance (FMR) technique by keeping the frequency fixed at 10 GHz. The blue colored solid circles and the red line correspond to the measured data and the fit to equation 5.3, respectively.

Angle dependent measurement of resonance field (H_R) have been performed on sample 5B_A in a fixed frequency of 10 GHz to quantify the contributions from both the anisotropies (figure 5.20). The fitting performed using equation 5.3 on the data for sample 5B_A yields K_2 and K_4 to be -4.7×10^3 J/m³ and -1.2×10^4 J/m³, respectively. The value of the cubic

anisotropy for the bilayer sample is of the same order in comparison to the single layer sample. However, it can be noticed that the uniaxial anisotropy is larger by two orders in case of sample 5B_A. The ferromagnetic layer of both the samples have been prepared with same growth conditions which infers that there should not be any change in the anisotropy symmetry. Therefore, the enhancement of the uniaxial anisotropy in sample 5B_A may be due to the additional contribution from the interfacial anisotropy. The later might be because of orbital hybridization. However, future theory may elucidate the exact origin for this enhancement of anisotropy. In the previous chapter, decrease in uniaxial anisotropy has been found in polycrystalline Fe/C₆₀ sample due to the $p - d$ hybridization. However, for the epitaxial Fe/C₆₀ sample, the enhancement in the anisotropy suggests that better crystallinity of Fe layer promotes the uniaxial anisotropy. Therefore, it has been possible to tune the anisotropy of Fe/C₆₀ heterostructures by controlling the crystallinity of the Fe layer.

In summary, a spinterface has also been observed in epitaxial Fe/C₆₀ bilayer sample. The induced moment in C₆₀ and the thickness of the spinterface for Fe/C₆₀ bilayer on MgO (001) substrate are higher than those observed for a similar spinterface grown on Si (100) substrate. Therefore, the crystallinity of the FM layer is an important factor to be controlled to optimize the spinterface properties. Better crystallinity of the FM layer provides higher induced moment and thickness of the spinterface. The magnetic C₆₀ certainly has profound effect on the magnetization reversal and the domain microstructure when compared to the results obtained on a single layer Fe film. Further, the UMA gets enhanced remarkably for the bilayer sample due to the orbital overlap between Fe and C₆₀ molecules. However, reduction of anisotropy has been observed earlier in case of polycrystalline Fe/C₆₀ samples. Therefore, the growth of the FM layer plays a major role in tuning the anisotropy symmetry of a system.

Chapter 6: Spinterface in polycrystalline Co and C₆₀ systems

In the previous chapters, it has been observed that formation of spinterface is possible at the Fe/C₆₀ interface for various thickness, growth, crystallinity of the parent ferromagnetic thin film. Also, the tunability of anisotropy symmetry, domain structures, induced moment and thickness of spinterfaces have been achieved in Fe/C₆₀ heterostructures by varying the characteristics of the FM layers. However, modulation of such properties can be accomplished further by varying the material of the FM layer as the strength of the orbital hybridization strongly depends on the electronic structure of the material. In this chapter, spinterface properties in polycrystalline Co/C₆₀ bilayers have been discussed. According to the electronic structure, Co possesses 3 unpaired electrons in its outermost shell (d - orbital) which is less than that of the Fe. Therefore, it is expected that the spinterface induced properties of Co/C₆₀ bilayers will be different than that of the Fe/C₆₀ bilayers. Previous literature revealed the observation of Co/C₆₀ spinterfaces by XMCD and PNR techniques [6]. Modification of anisotropy like inverse spin reorientation has been observed in Co thin film due to the presence of C₆₀ [18]. However, the effect of Co/C₆₀ spinterface on the properties like magnetization reversal, domain structures, in-plane anisotropy symmetry etc. has not been discussed so far in literature. Before studying the spinterfaces, the magnetic properties of single layer Co parent thin film have been studied and discussed in section 6.1. The quantification of the induced moment, thickness of interfacial C₆₀ and the magnetic properties viz. magnetization reversal, domain structures, anisotropy symmetry etc. for a Co/C₆₀ bilayer have been discussed in section 6.2. Further, the aforementioned properties are compared with that for the single layer parent Co thin films to understand the effect of spinterfaces.

6.1. Study of magnetic properties in Co thin film on Si (100) substrate:

Co thin film of 10 nm thickness has been prepared by dc sputtering on Si (100) substrate with native oxide SiO₂. The deposition pressure and rate of deposition for Co layer were 5×10^{-3} mbar and 0.02 nm/s, respectively. It has been discussed in chapter 4 that direct deposition of Fe film on Si substrate leads to poor growth of Fe which in turn affects the magnetic properties strongly. In order to grow polycrystalline Co films by avoiding such huge lattice mismatch the Co layers have been fabricated on a seed layer of 5 nm Ta. The lattice constant of Ta (a_{Ta}) is more than that of Co (a_{Co}) and less than Si (a_{Si}). As a consequence, the growth of Co is better on Ta than the Si (100) substrate. Besides the seed layer, Ta has also been used as a capping layer to prevent from the oxidation of Co. The following is the complete structure of the prepared sample: Sample 6S_A: Si (100)/Ta(5 nm)/Co(10 nm)/Ta(3 nm).

The Co target is at 30° angle w.r.t. the substrate normal due to the in-built geometry of our deposition system. Therefore, a uniaxial anisotropy is expected in our samples due to the oblique angle of deposition [17,21,25,220,221]. The hysteresis loops and the corresponding domain images have been measured using MOKE based microscopy. The RT hysteresis measurements have been performed within a field range of ± 20 mT by varying the angle ϕ in longitudinal mode. ϕ denotes the angle between the easy axis and applied field direction. Figure 6.1 depicts the angle dependent hysteresis loops for sample 6S_A where the shape of the hysteresis loops changes with ϕ due to the presence of anisotropy in the sample. The change in coercivity (H_C) between the easy (EA) and hard axis (HA) loops is a qualitative measure of the anisotropy present in the sample. It should be noted that the difference in H_C values between EA and HA for sample 6S_A is nominal (figure 6.1). The inset of figure 6.1 shows the zoomed image of the hysteresis loops for sample 6S_A near the coercivity. The change in the H_C values between EA and HA is clearly visible here.

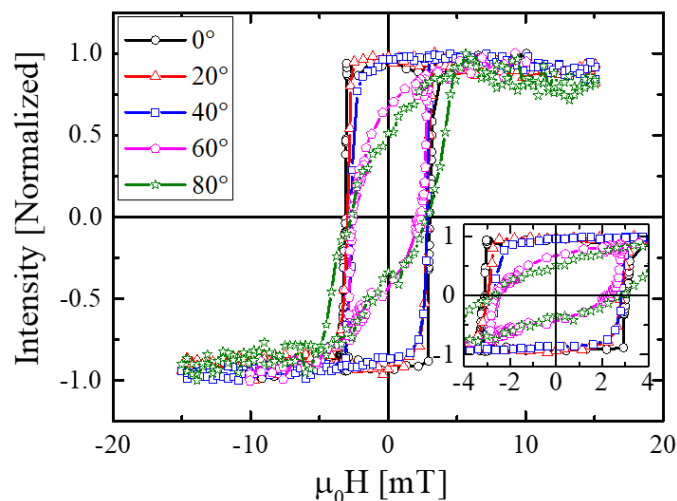


Figure 6.1: Hysteresis loops measured using MOKE based microscopy at RT in longitudinal mode by varying the angle (ϕ) between the easy axis and the applied field direction for sample 6S_A. The inset of the figure shows the zoomed in view of the hysteresis loops near the coercivity for better visibility.

Uniaxial anisotropy is expected in the sample due the oblique angular growth of Co. Similar to the samples discussed earlier, the easy axis of the oblique angle incidence induced uniaxial anisotropy lies perpendicular to the projection of the in-plane plume direction [77-79,186]. The anisotropy symmetry of sample 6S_A is discussed in the later part of this section using angle dependent FMR measurement.

Figure 6.2 shows the hysteresis loop (a) and corresponding domain images (b – e) measured along the easy axis of sample 6S_A. At the positive saturation all the magnetic spins point towards the applied field direction and white contrast is observed in the domain image (figure 6.2(b)). Upon decreasing the field from the saturation, branch domains are observed (figure 6.2(c)) after the switching of the field direction. Branch domains are characteristics of the samples having poor crystallinity which is expected due to the lattice mismatch between Ta and Co. The reversal happens with a sharp jump in the hysteresis loop with sweeping of black contrast branch domains (figure 6.2(d)). Further, the sample reaches to its negative saturation

state where all the spins point along the negative field direction exhibiting black contrast in the domain image (figure 6.2(e)).

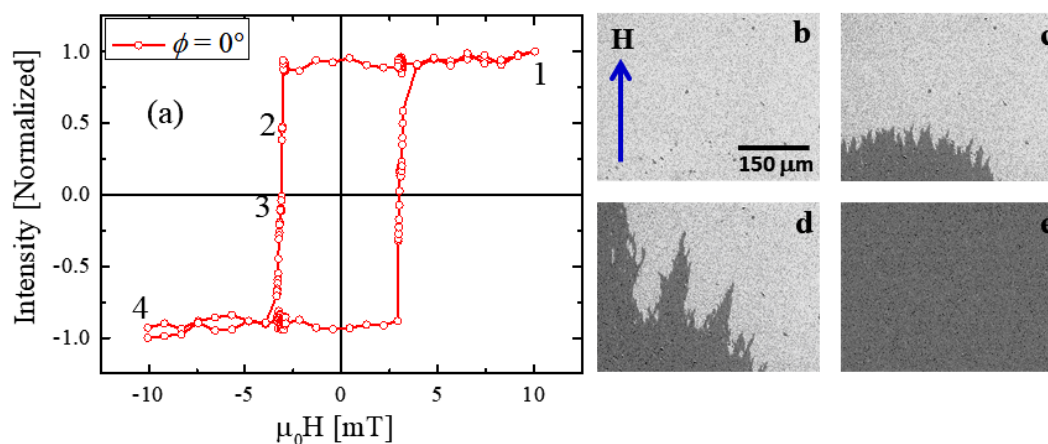


Figure 6.2:(a) Hysteresis loop measured along the easy axis ($\phi = 0^\circ$) at RT in longitudinal mode for sample 6S_A. (b) – (e) show the domain images correspond to the field points 1 – 4 in the hysteresis loop, respectively. All the domain images are in the same scale shown in (b).

The domain images captured near the coercive field of the loops measured along different ϕ for sample 6S_A are shown in figure 6.3. As discussed earlier, large branch domains are observed along the EA. By rotating the ϕ away from the EA, domain size decreases and modifies to stripe domains. It should be noted that stripe domains are characteristics of films having dispersed uniaxial anisotropy due to strain [12]. Therefore, due to the polycrystalline growth of Co, branch and stripe domains are observed for different angles. In case of thin films having well defined uniaxial anisotropy, the domain size decreases monotonically from EA towards HA. However, due to the presence of dispersion in anisotropy symmetry, the domain size increases in between $30^\circ < \phi < 60^\circ$. The average domain width for each angles have been calculated using ImageJ software. A specific field (close to the coercive field) has been chosen for all the angles and width of different domains has been measured at various positions of the image. Further, the average domain width has been calculated by taking the

mean value. The variation of average domain widths with respect to ϕ is shown in figure 6.3(f). The dispersion in anisotropy can also be attributed to the fact that the crystallinity of Co is not well defined due to the lattice mismatch between Co and Ta.

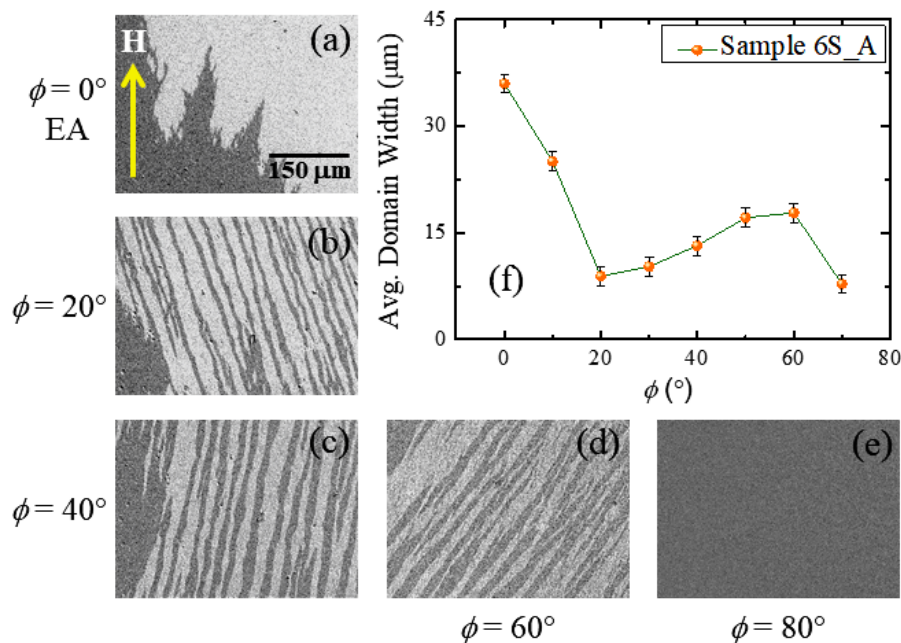


Figure 6.3: Angle (ϕ) dependent domain images near the coercivity for sample 6S_A are shown in (a) - (e). The domain images are measured using MOKE based microscopy at RT in longitudinal mode. The scale bars of the images are shown in image (a). The applied field direction shown in image (a) has been kept constant during all the measurements and the sample was rotated accordingly. (f) Plot for the angle dependent average domain width.

The damping property of the sample has been measured using frequency dependent ferromagnetic measurement (FMR). The damping constant (α) can be evaluated using the formula: $\alpha = \frac{\Delta H \cdot \gamma}{4\pi\omega}$ [200] where ΔH is the line width of the derivative of the FMR signal, γ is the gyromagnetic ratio of Co and ω is the measurement frequency. Figure 6.4(a) shows the frequency dependent linewidth data (magenta solid circles) and the corresponding fit (green solid line) for sample 6S_A. The damping constant (α) is calculated by linearly fitting the

frequency dependent line width data. The best fitted value of α has been extracted to be 0.0072 ± 0.0009 .

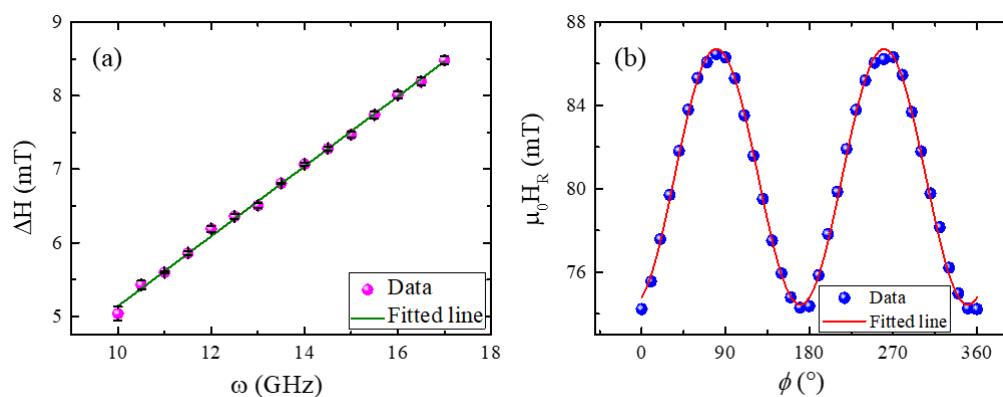


Figure 6.4:(a) Plot for frequency dependent linewidth and corresponding fit for sample 6S_A. (b) Angle dependent resonance field (H_R) plot for sample 6S_A to evaluate the anisotropy constants of the system.

To quantify the uniaxial present anisotropy in sample 6S_A, angle dependent FMR measurement has been performed. The angle ϕ has been rotated in 10° interval at a constant frequency of 10 GHz. The corresponding resonance field (H_R) has been recorded for each angle. Figure 6.4(b) shows the H_R vs ϕ data (solid blue circles) and corresponding fits (red solid line) for both the samples. The energy equation for a system having uniaxial anisotropy is discussed in chapter 4 in equation 4.1 [200]. The dispersion relation obtained from the energy equation is given in equation 4.2 [200]. The angle dependent resonance field shown in figure 6.4(b) can be fitted using equation 4.2. The uniaxial anisotropy constant K_2 is extracted to be $8.78 \times 10^3 \text{ J/m}^3$ for sample 6S_A.

6.2. Study of spinterface induced magnetic properties in Co/C₆₀ bilayer thin films on Si (100) substrate:

Bilayer of Co/C₆₀ sample has been prepared in our multi-deposition vacuum chamber. The seed layer (Ta) and Co have been prepared keeping all the deposition parameters same as used to prepare the single layer Co sample 6S_A. 12 nm C₆₀ layer has been deposited in-situ

on top the Co layer using thermal evaporation technique. The deposition pressure and the rate of deposition for C₆₀ have been chosen to be $\sim 1 \times 10^{-7}$ mbar and 0.015 nm/s, respectively. The C₆₀ layer has been capped with 3 nm Ta layer to protect from the surface corrosion. The sample is denoted by sample 6B_A with the structure of Si (100)/Ta(5 nm)/Co(10 nm)/C₆₀(12 nm)/Ta(3 nm).

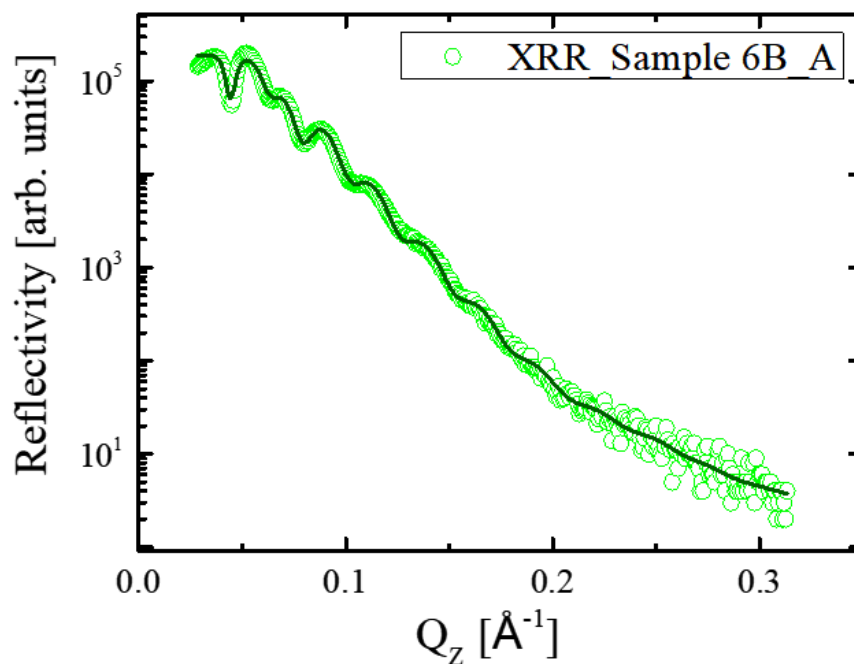


Figure 6.5: X-ray reflectivity (XRR) data and its corresponding fit for sample 6B_A.

The structural parameters viz. thickness, roughness etc. of sample 6B_A have been calculated by fitting the x-ray reflectivity (XRR) data. The fitting has been performed using the GenX software [143]. Figure 6.5 shows the XRR data and its corresponding fit for sample 6B_A. The extracted thickness of each layer of the sample matches well with our expected sample structure. It has been observed from the fit that the roughness of the Co layer ($\sim 2.00 \pm 0.03$ nm) is quite high. This aspect can be attributed to the high deposition rate of Co and lattice mismatch between Co and Ta layers. Further, the roughness of C₆₀ layer is $\sim 1.80 \pm 0.04$ nm which is expected due to its growth on rough Co surface and large lattice mismatch between Co and C₆₀.

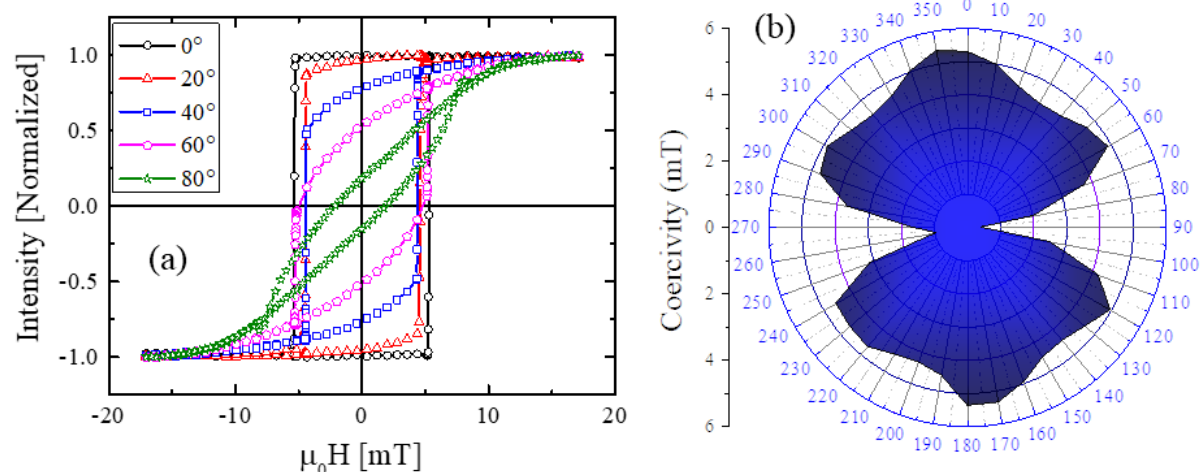


Figure 6.6:(a) Hysteresis loops measured using MOKE based microscopy at RT in longitudinal mode by varying the angle (ϕ) between the easy axis and the applied field direction for sample 6B_A. The inset of figure (a) shows the zoomed version of the hysteresis loops near the coercivity for better visibility. (b) Angle dependent coercivity plot for sample 6B_A.

The hysteresis loops are measured for sample 6B_A by varying ϕ in 10° interval using MOKE microscopy in longitudinal mode. Figure 6.6(a) shows the angle dependent hysteresis loops for sample 6B_A. In comparison to sample 6S_A, the variance in H_C values while changing ϕ is quite prominent for sample 6B_A. This indicates that the anisotropy increases in sample 6B_A in comparison to sample 6S_A due to the presence of the Co/C₆₀ interface. Further, the H_C along the EA for sample 6B_A increases in comparison to that of the sample 6S_A. This can be explained from the increased exchange coupling at the interface of Co/C₆₀ in sample 6B_A. It is expected from the electronic structures of Co and C₆₀ that hybridization is probable between d and p orbitals of Co and C atoms, respectively. Due to such hybridization, the C₆₀ molecules at the interface may exhibit ferromagnetism resulting in higher exchange coupling in the bilayer sample than its parent single layer film. Detailed information on the induced magnetism in C₆₀ is discussed later in this section. Figure 6.6(b) depicts the polar plot of H_C vs ϕ for sample 6B_A to understand the anisotropy symmetry

present in the sample. A minor contribution from another anisotropy has been observed along with the oblique deposition induced uniaxial anisotropy. The presence of local minima (30°, 150°, 200°, 320°) and maxima (60°, 120°, 240°, 300°) other than 90°, 270° and 0°, 180°, respectively in the anisotropy plot (figure 6.6(b)) indicates the increase in dispersion or appearance of another anisotropy in sample 6B_A in comparison to that of the sample 6S_A. The dispersion may increase due to the large lattice mismatch between Co and C₆₀. According to the XRR data shown in figure 6.5, the roughness at the Co/C₆₀ interface is high due to the absence of lattice matching. As a result, the anisotropy becomes more dispersed in the bilayer sample. It should be noted that the hybridization at the Co/C₆₀ interface may promote the strength of the present anisotropy or endorse the appearance of another anisotropy in the bilayer system. However, theoretical calculation is required in future to unravel the exact mechanism.

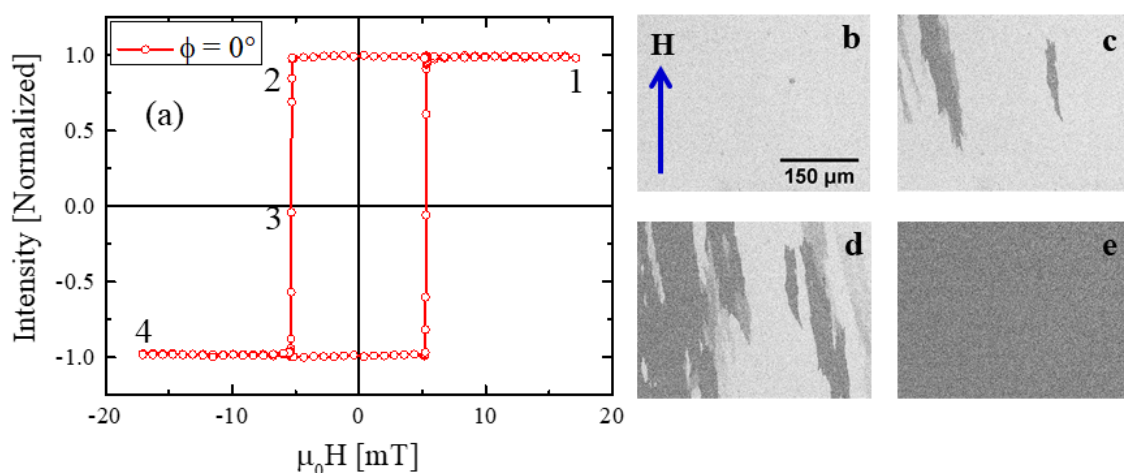


Figure 6.7:(a) Hysteresis loop measured along the easy axis ($\phi = 0^\circ$) at RT in longitudinal mode for sample 6B_A. (b) – (e) show the domain images correspond to the field points 1 – 4 in the hysteresis loop, respectively. All the domain images are in the same scale shown in (b).

Figure 6.7 shows the hysteresis loop and corresponding domain images for sample 6B_A along the easy axis ($\phi = 0^\circ$). Similar to the single layer sample 6S_A, branch domains are

observed along during the reversal. In this sample, disorder is present due to following two reasons: the lattice mismatch between Co and Ta and presence of C₆₀ on top of Co layer. As a consequence, branch domains are formed in this sample. The domain size increases for sample 6B_A in comparison to that of the sample 6S_A. The increase in domain size in the bilayer sample may occur due to the presence of added exchange coupling at the Co/C₆₀ interface.

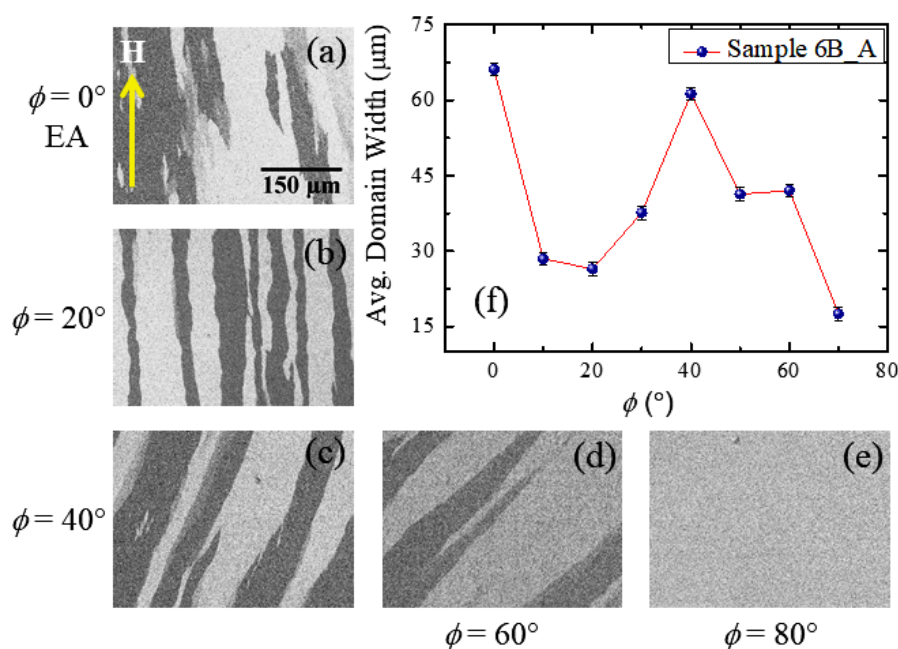


Figure 6.8: Angle (ϕ) dependent domain images near the coercivity for sample 6B_A are shown in (a) - (e). The domain images are measured using MOKE based microscopy at RT in longitudinal mode. The scale bars of the images are shown in image (a). The applied field direction shown in image (a) has been kept constant during all the measurements and the sample was rotated accordingly. (f) Plot for the angle dependent average domain width.

Figure 6.8 corresponds to the domain states measured for sample 6B_A for different angles of rotation (ϕ). Similar to sample 6S_A, the branch domains observed along the EA change to stripe domains while going away from the EA for sample 6B_A. The nature of the domains indicates dispersion in the anisotropy due to the presence of Co/C₆₀ interface. Further for

sample 6B_A the domain width increases when the field is applied away from the EA direction. Due to the presence of more dispersion or another anisotropy contribution, the domain width at $\phi = 60^\circ$ becomes similar to that of at EA. For $\phi > 70^\circ$, domains are not observed during the reversal as it may happen via coherent rotation. Therefore, a gradual change in the contrast have been observed for $\phi > 70^\circ$ while the field is swept from the positive to negative saturation. The change in the domain width with respect to ϕ for sample 6B_A is depicted in figure 6.8(f).

The layer specific magnetic moments and interfacial magnetic properties have been studied using polarized neutron reflectivity (PNR) technique in specular mode at MARIA, MLZ Germany on sample 6B_A. Figure 6.9(a) shows the PNR data and the corresponding fit measured at positive saturation ($\mu_0 H = 100$ mT) of the sample at RT for sample 6B_A. The reflectivity has been measured for the non-spin flip (NSF) scattering cross sections R^{++} and R^{--} . The red and blue open circles represent the data obtained from the R^{++} and R^{--} channels, respectively. The data has been fitted using the same GenX software which we have used for other sample as described in this thesis earlier [143]. The sample structure obtained from the best fit is shown in figure 6.9(b) with thicknesses extracted for each layer. From the fitting, it has been observed that the Co layer exhibits magnetic moment of $1.60 \pm 0.01 \mu_B/\text{atom}$. The magnetic moment of the single layer Co sample has also been calculated from the SQUID loop (figure 6.10). The moment for sample 6S_A is obtained to be $1.70 \pm 0.03 \mu_B/\text{atom}$. Therefore, a reduction of $\sim 6\%$ of magnetic moment in Co is observed in the bilayer sample. Next to the Co layer, $\sim 1.99 \pm 0.18$ nm of pure C₆₀ shows $0.8 \pm 0.2 \mu_B/\text{cage}$ of magnetic moment. Further, rest of 10.1 ± 0.1 nm of C₆₀ exhibits its inherent diamagnetic behavior. The possible cause of induction of moment in C₆₀ cage and loss of moment in Co is the hybridization between d_{Co} and p_{C60} orbitals. The unpaired electrons from d orbital of Co atom can be transferred to the p orbital of C atom leading to hybridization. It is highly

probable that the density of states of the C₆₀ gets strongly modified at the interface resulting in induced ferromagnetism in fullerene [5,54].

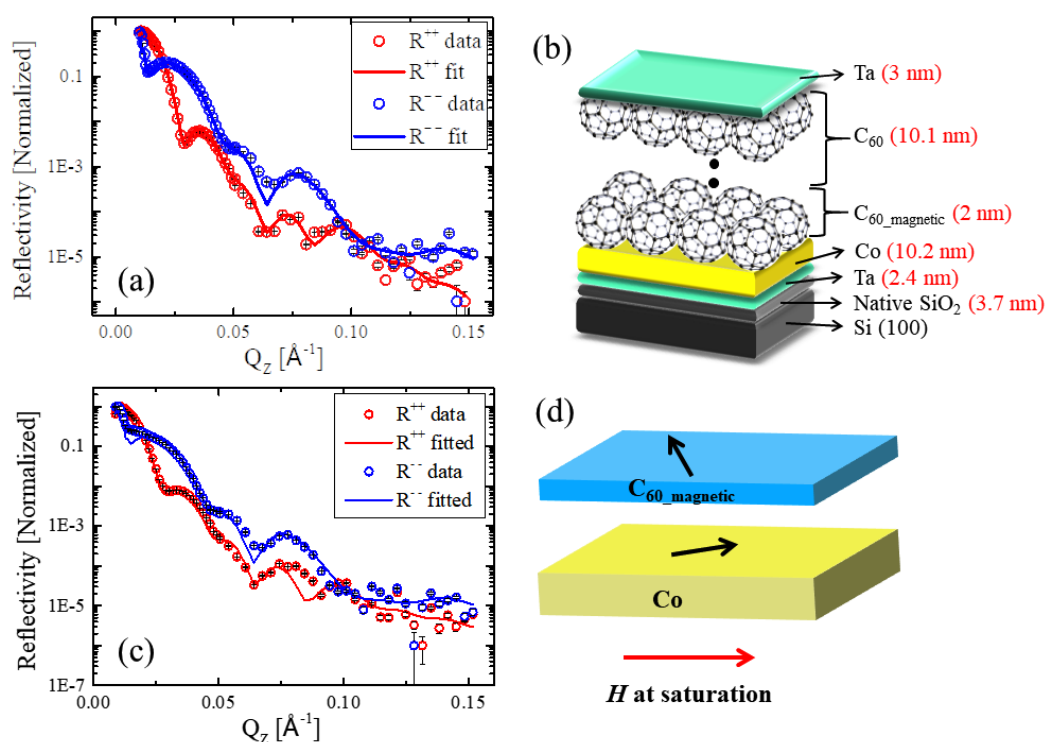


Figure 6.9:(a) Polarized neutron reflectivity (PNR) data and the corresponding fits for sample 6B_A. The red and blue open circles represent the data measured for the R^{++} and R^{--} channels, respectively. The solid lines correspond to their respective fits. The measurement was performed at the saturation state at RT. (b) A schematic representation of the sample structure obtained by fitting the PNR data is shown in (a). The numbers written in brackets correspond to the fitted thickness of the respective layer. (c) shows the PNR data and the corresponding fits for sample 6B_A near the coercive field (H_C) at RT. (d) A schematic representation of the magnetic states of the layers with respect to the saturation state.

The induced moment in C₆₀ is quite less in the Co/C₆₀ bilayers in comparison to our previously discussed spinterfaces with Fe/C₆₀. This may happen as Co possess less magnetic moment in comparison to Fe. However, the induced moment in Co may increase with better

growth of Co layer. The PNR measurement near the coercive field (figure 6.9(c)) elucidates the non-parallel coupling between C₆₀ and Co layer at the interface. At the near coercive state, 17% of the Co spins are in reversed state and rest are along the field direction. However, 63% of the magnetic C₆₀ spins point in the reverse direction. The direction of the net magnetization of the magnetic layers with respect to the magnetization at the saturation state are shown in figure 6.9(d). It should be noted that the net magnetization directions of the Co and magnetic C₆₀ layers are obtained from the percentage of the spins flipped with respect to the saturation state from the non-spin flip data. Spin-flip measurements were not performed on this sample. Therefore, it can be inferred from the PNR measurement that the change in domain structure and the anisotropy symmetry discussed earlier is possibly a result of the formation of spinterface between Co and C₆₀.

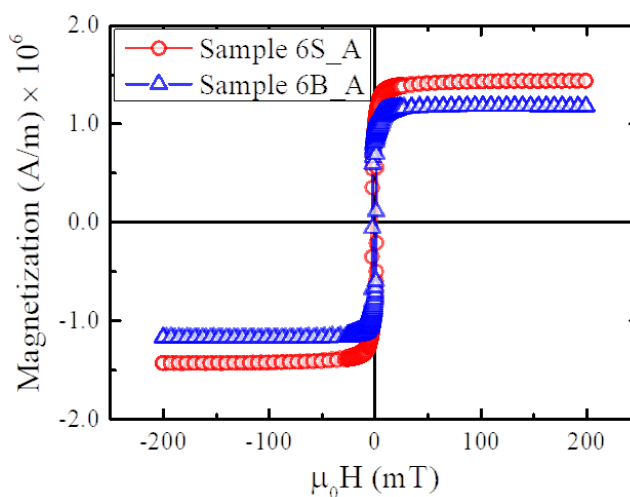


Figure 6.10: Hysteresis loops measured by superconducting quantum interference device (SQUID) to quantify and compare the net magnetization in the samples. Presence of Co/C₆₀ interface decreases the magnetization of Co significantly in sample 6B_A.

Figure 6.10 shows the hysteresis loops of both the samples measured using SQUID at RT. The magnetic moment per atom in the Co layer has been calculated from the loop for sample 6S_A. However, such calculations could not yield layer specific moment for sample 6B_A.

However, the hysteresis loops shown in figure 6.10 suggests that over all magnetization of the sample decreases in case of sample 6B_A in comparison to sample 6S_A. This is due to the reduction of magnetic moment in the Co layer due to orbital hybridization. The loss of net magnetization of the sample in case of the bilayer system is an indirect proof of presence of hybridization at the Co/C₆₀ interface.

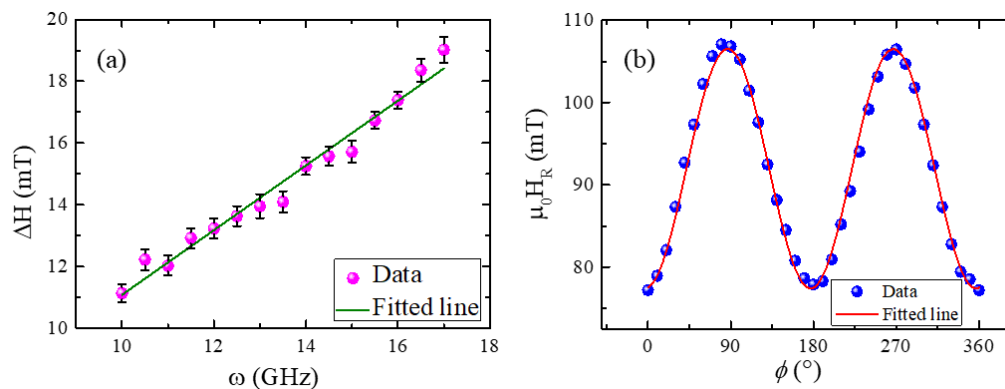


Figure 6.11: (a) Plot for frequency dependent linewidth plot and corresponding fit for sample 6B_A. (b) Angle dependent resonance field (H_R) plot for sample 6B_A to evaluate the anisotropy constants of the system.

To calculate the damping constant and anisotropy constant, FMR measurement has been performed on sample 6B_A by varying the frequency and the angle (ϕ), respectively. Figure 6.11(a) shows the measurement frequency vs linewidth data (magenta solid circles) and the corresponding fit (green solid line) for sample 6B_A. The damping constant (α) is calculated to be 0.0159 ± 0.0007 by linearly fitting the frequency dependent line width data. The increase in damping constant for the bilayer sample in comparison to the single layer sample may be due to the interfacial effects such as spin pumping. The angle dependent resonance field has been measured in sample 6B_A at a fixed frequency of 10 GHz to quantify and compare the anisotropy constant with that of the sample 6S_A. Figure 6.11(b) shows the H_R vs ϕ data (solid blue circles) and corresponding fits (red solid line) for sample 6B_A. The angle dependent resonance field shown in figure 6.11(b) can be fitted using the same

equation (equation 4.2) used for sample 6S_A. The uniaxial anisotropy constant K_2 is extracted to be $1.71 \times 10^4 \text{ J/m}^3$ for sample 6B_A. The anisotropy increases by twice in the bilayer sample 6B_A than that of the single layer sample 6S_A ($K_2 = 8.78 \times 10^3 \text{ J/m}^3$). Hence, the orbital hybridization at the interface of Co and C₆₀ leads to deformation/elongation of the shape of orbitals which in turn promotes the enhancement of anisotropy in bilayer system.

In summary, formation of a spinterface is observed at the Co/C₆₀ interface similar to the Fe/C₆₀ systems. The magnetic properties of bilayer Co/C₆₀ sample have been studied and compared with its parent single layer Co thin film. The domain size as well as the coercivity of the bilayer sample increases due to the presence of the spinterface. This can be explained in terms of the increase in exchange coupling at the Co/C₆₀ interface. About $2.00 \pm 0.18 \text{ nm}$ of C₆₀ layer next to the interface exhibits $0.8 \pm 0.2 \mu_B/\text{cage}$ magnetic moment due to the $p - d$ orbital hybridization between C and Co atoms. However, the induced moment is quite less in comparison to that of the Fe/C₆₀ samples. Better growth of Co layer may lead to increase in the induced moment in C₆₀. Such orbital hybridization at the interface leads to increase in anisotropy by twice of its value in the bilayer sample.

Chapter 7: Spinterface in textured Co and C₆₀ systems

In previous chapters, magnetic properties of spinterfaces have been studied by changing the thickness, crystalline quality and material of the ferromagnetic layer. It has been found that the spinterfacial properties get improved when the crystallinity of the FM layer modifies from polycrystalline to single crystalline (epitaxial) structure. Another crystalline phase, known as textured, exists in nature which exhibits crystalline quality better than polycrystalline but worse than single crystals. It is a special type of crystallinity where the material possesses more than one crystalline orientation due to specific growth conditions. It is expected that such textured spinterface may exhibit distinct effects on the magnetic properties in comparison to the polycrystalline or epitaxial systems. Minute lattice mismatch between the substrate and the thin film material may lead to formation of textured thin films if grown with certain deposition parameters. Though epitaxial growth of Co on MgO substrate has been reported with following relationship: Co (11 $\bar{2}$ 0)[0001] || MgO (100)[001] and Co (11 $\bar{2}$ 0)[1 $\bar{1}$ 00] || MgO (100)[001][22], however, Co thin film is not expected to be epitaxial on MgO substrate due to ~16% misfit between MgO and cubic Co lattice constants [23,24]. This lattice mismatch may lead to formation of textured or polycrystalline Co films on MgO substrate. We have prepared Co thin films on MgO (001) substrate by varying the deposition conditions for obtaining different anisotropy symmetry. Formation of textured Co film is observed when the substrate is pre-annealed over 650°C for an hour. A systematic study on the dependence of the magnetic anisotropy, domain structure and magnetic relaxation on the substrate pre-annealing condition and substrate rotation during deposition have been presented for Co thin films on MgO (001) substrates in section 7.1 [25]. Further, Co/C₆₀ bilayer film has been prepared by choosing the specific deposition condition for Co where it exhibits strong textured nature. The magnetic properties viz. anisotropy, domain structure,

induced moment, thickness of the spinterface etc. in textured Co/C₆₀ bilayer film have been discussed in section 7.2.

7.1. Effect of the growth conditions on the anisotropy, domain structures and the relaxation in Co thin films on MgO (001) substrate:

The change in anisotropy symmetry in Co thin films due to different growth conditions has been observed by a few groups. For example, Co single layer film on Ar⁺ sputtered MgO substrate with ripple surface exhibits uniaxial anisotropy [209]. However, a transformation from cubic to uniaxial anisotropy has been observed due to the change in sputtering angle of Ar⁺ from normal to oblique incidence [209]. Similarly, different crystalline structure of Co grown on MgO substrate shows different types of anisotropies. Co thin film with body centered tetragonal (bct) structure grown on MgO substrate exhibits cubic anisotropy whereas fcc and polycrystalline Co shows intricate anisotropy symmetry [23]. Cubic anisotropy has also been observed in Co thin films having twinned film structure [210]. Texture induced uniaxial anisotropy has been reported for fcc Co thin film on MgO (110) substrate [24]. Liu *et al.* have theoretically shown that the anisotropy behavior in textured films can be modeled with the incorporation of magneto-texture anisotropy [184]. We have observed in all our previously discussed samples that uniaxial anisotropy is induced due to the oblique angular deposition geometry of our vacuum chamber. Substrate rotation during deposition is a way to control such oblique angular deposition induced uniaxial anisotropy. Previous literature reveals that substrate rotation during deposition of Co thin films on Si (100) substrate has a significant effect on magnetic anisotropy and the domain structure [82]. It has been observed that among 10 and 20 rpm of substrate rotation during deposition, the former leads to better uniformity of Co on Si (100) substrate [11]. Keeping the aforementioned results in mind, we have prepared four Co single layer samples on MgO (001) substrate by varying the substrate rotation and pre-annealing conditions. Co has been deposited using dc magnetron sputtering

technique. As discussed in the earlier chapters, the incident Co plume in the sputtering chamber has been fixed at 30° with respect to the surface normal of the substrate. The deposition pressure and rate for the Co layer have been chosen to be 5×10^{-3} mbar and 0.021 nm/s, respectively. The details of the samples are shown in table 7.1. Followings are the deposition parameters varied to grow the Co samples having 25 nm thickness: (i) sample 7S_A has been grown with substrate pre-annealing at $T_{ann} = 650^\circ\text{C}$ for an hour and then Co has been deposited without rotating the substrate ($R_{sub} = 0$ rpm), (ii) sample 7S_B has been deposited without pre-annealing and substrate rotation ($R_{sub} = 0$ rpm), (iii) sample 7S_C has been prepared with substrate pre-annealing like sample 7S_A ($T_{ann} = 650^\circ\text{C}$) but by rotation during deposition at $R_{sub} = 10$ rpm in order to minimize the growth-induced anisotropy, and (iv) for sample 7S_D substrate has not been pre-annealed but rotated at $R_{sub} = 10$ rpm during deposition. A capping layer of 3.5 nm Al₂O₃ has been deposited at a rate of 0.008 nm/s on all the samples using rf sputtering to prevent from oxidation of Co. All the samples have been deposited at $T_{dep} = 150^\circ\text{C}$.

Table 7.1. Details of prepared Co samples on MgO (001) substrate

Sample Name	Sample Description	
	Pre-annealing condition	Substrate rotation (R_{sub})
Sample 7S_A	650°C for 1 hour	0 rpm
Sample 7S_B	not annealed	0 rpm
Sample 7S_C	650°C for 1 hour	10 rpm
Sample 7S_D	not annealed	10 rpm

X-ray diffraction (XRD) measurements have been performed on all the samples in $\theta - 2\theta$ mode to understand the crystalline quality of Co layers. Figure 7.1(a) – (d) depict the intensity vs. 2θ (where θ is the angle between the incident x-ray and the plane of sample surface) plot for sample 7S_A, 7S_B, 7S_C, and 7S_D, respectively. The XRD data reveals

the growth of Co in hcp structure. Since in $\theta - 2\theta$ mode the MgO substrate produces a large count in the intensity for all the samples, the normalized intensity shown here are truncated up to 0.08 in order to identify the peaks for Co and Al₂O₃. Both the samples 7S_A (figure 7.1(a)) and 7S_C (figure 7.1(c)) exhibit textured nature where the preferred directions for the Co layers are (10 $\bar{1}$ 0) and (10 $\bar{1}$ 1). This is expected as the annealing prior to deposition leads to surface reconstruction of the MgO substrate which in turn promotes the growth of Co in crystalline form. Due to the effect of substrate rotation during deposition the intensity of Co (10 $\bar{1}$ 1) peak is less for sample 7S_C in comparison to sample 7S_A. However, the intensity of Co (10 $\bar{1}$ 0) peak is similar for both the samples (figure 7.1(a) and (c)).

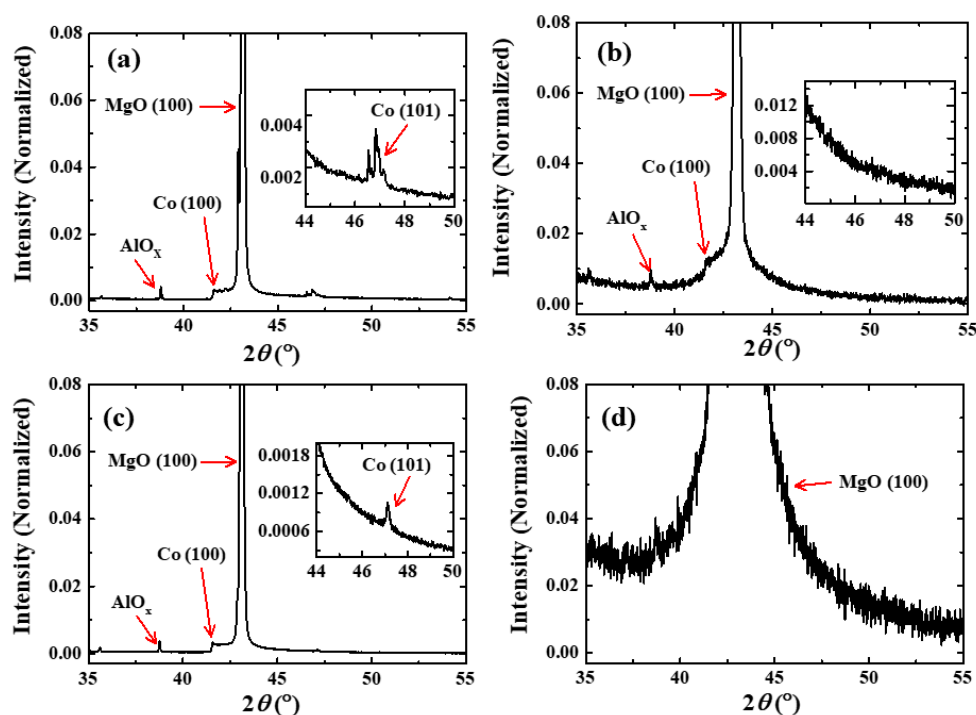


Figure 7.1: (a) – (d) Plots showing intensity vs. 2θ measured using XRD for samples 7S_A, 7S_B, 7S_C, and 7S_D, respectively. The insets of (a), (b) and (c) depict the zoomed plot for a specific range of 2θ for samples 7S_A, 7S_B, and 7S_C, respectively.

Further, the x-ray measurements with fine precision around each Co peaks have been performed for the textured samples (Samples 7S_A and 7S_C). The degree of texture has

been analyzed by fitting the peaks with Gaussian function and calculating the full width at half maxima (FWHM). Figure 7.2 shows the XRD data around each Co peak with the corresponding Gaussian fits for the samples 7S_A and 7S_C. For the Co (10 $\bar{1}$ 0) peak, it has not been possible to observe the decreasing side of the peak due to its coincidence with the increasing side of the substrate peak. It can be observed from figure 7.2 that some small peaks are present around the Co (10 $\bar{1}$ 1) peak which can be denoted as the contribution from K α ₂ radiation. For sample 7S_A the FWHM for the (10 $\bar{1}$ 0) and (10 $\bar{1}$ 1) peaks are 0.1133 and 0.0755, respectively. Similarly, for sample 7S_C the FWHM for the (10 $\bar{1}$ 0) and (10 $\bar{1}$ 1) peaks are 0.1431 and 0.079, respectively. This indicates that sample 7S_A has a better degree of texture in comparison to sample 7S_C.

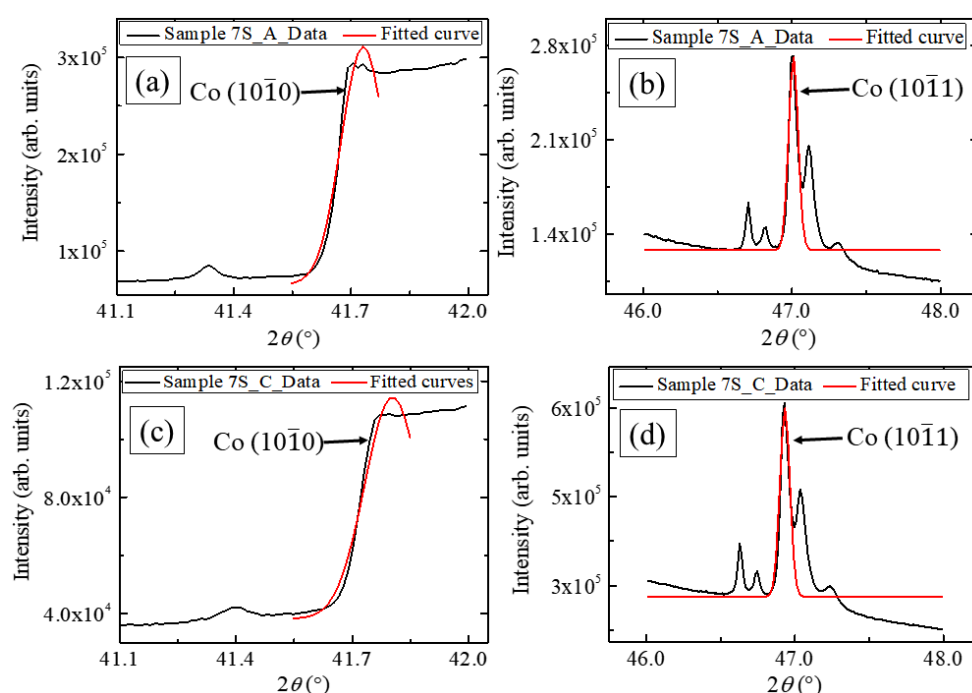


Figure 7.2: Plots showing intensity vs. 2θ measured around Co (10 $\bar{1}$ 0) and Co (10 $\bar{1}$ 1) peaks using XRD for samples 7S_A (a, b) and 7S_C (c, d), respectively.

Samples 7S_B and 7S_D exhibit polycrystalline nature due to the absence of substrate annealing before deposition. A careful observation of the data for sample 7S_B reveals the existence of Co (10 $\bar{1}$ 0) peak (figure 7.1(b)) with very weak intensity. However, the peak for

Co (10 $\bar{1}1$) is absent here (inset of figure 7.1(b)). As seen from figure 7.1(d), sample 7S_D does not show any preferred direction of Co due to the absence of pre-annealing and presence of substrate rotation during deposition. Peak corresponding to the capping layer has also been observed in all samples. It should be noted that due to the deficiency of O₂ during deposition, the capping layer of Al₂O₃ has not been grown with proper stoichiometry. Therefore, it has been denoted as AlO_x and (h,k,l) values are not mentioned in the XRD plots.

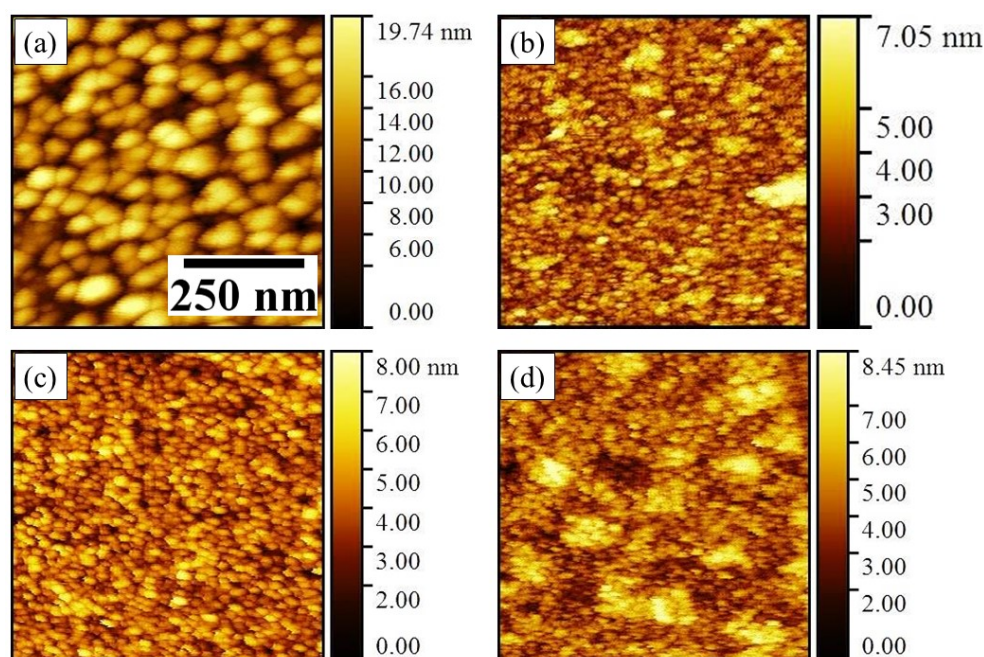


Figure 7.3: (a) – (d) Surface topography imaged using atomic force microscopy (AFM) technique for samples 7S_A, 7S_B, 7S_C, and 7S_D, respectively. All the images are in same length scale as shown in (a).

Figure 7.3 shows the surface topography for all the samples imaged using atomic force microscopy (AFM). It should be noted that, since AFM is a surface sensitive technique, we could image only the top layer of the samples i.e. the AlO_x layer. Sample 7S_A (figure 7.3(a)) exhibits the largest grain size among all the samples. The average grain size and roughness for all the samples are calculated using Gwyddion software [213]. The calculated

values are tabulated in table 7.2. The average grain sizes are 49.8 ± 3.9 , 21.0 ± 3.1 , 24.1 ± 3.9 , and 24.6 ± 3.9 nm for samples 7S_A, 7S_B, 7S_C, and 7S_D, respectively.

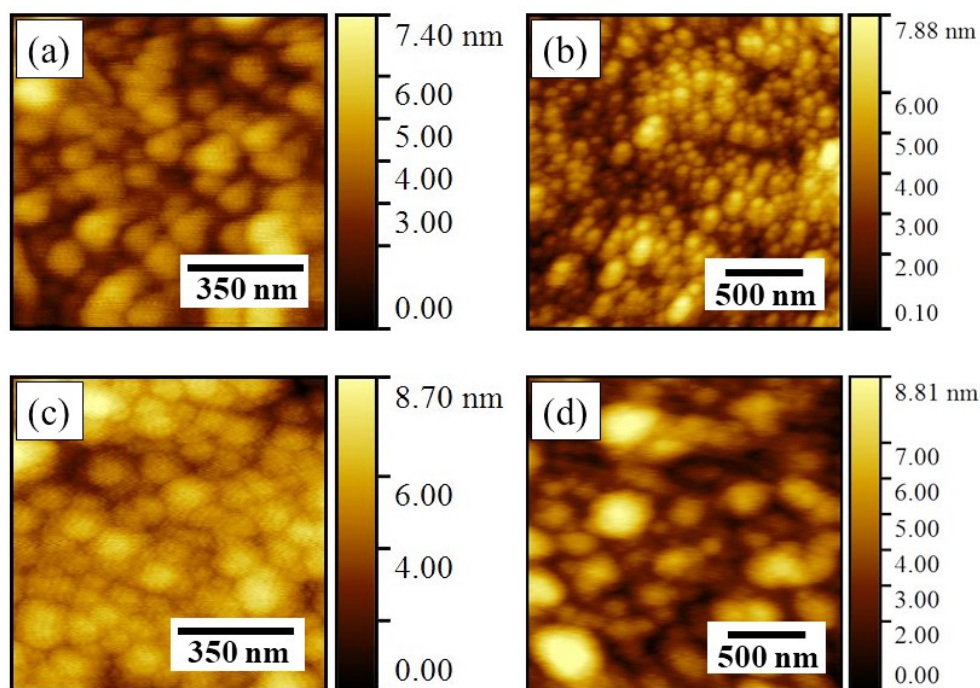


Figure 7.4: (a) – (d) Surface topography imaged by AFM for the samples 7S_A*, 7S_B*, 7S_C*, and 7S_D*, respectively, prepared without the capping (AlO_x) layer.

To obtain the actual grain size of Co, four samples termed as sample 7S_A*, 7S_B*, 7S_C*, and 7S_D* have been prepared with similar growth conditions like sample 7S_A, 7S_B, 7S_C, 7S_D but without the AlO_x capping layer. Figure 7.4 shows the topography of the Co layers for all the * samples. The grain sizes are listed in table 7.2. It can be observed that the annealing and rotation of substrate during deposition led to most dense packing of Co grains in sample 7S_C* (figure 7.4(c)). This indicates the possibility of highest exchange coupling in sample 7S_C* as well as in sample 7S_C among all the samples which is correlated to the magnetic properties of the samples in later part of this section. Further, the packing of Co grains in sample 7S_A* is less dense (figure 7.4(a)) as compared to sample 7S_C* due to the absence of substrate rotation. However, samples 7S_B* and 7S_D* show scattered distribution of grains (figure 7.4(b) and (d)) due to the absence of pre-annealing. This can be

confirmed from the XRD analysis (figure 7.1) which indicates polycrystalline nature of Co in samples 7S_B and 7S_D. In sample 7S_D, Co grains form island structures due to non-availability of sufficient time for the adatoms to relax because of the substrate rotation during deposition. Therefore, it is expected that the exchange coupling in sample 7S_D is probably more in comparison to that of sample 7S_B.

Table 7.2: Average Roughness and grain size for the samples calculated from AFM images

Sample Name	Average Grain Size with AlO _x	Average Grain Size of Co without AlO _x capping layer (from * samples)	Roughness
Sample 7S_A (annealed, 0 rpm)	49.8 ± 3.9 nm	88.5 ± 7.8 nm	1.1 nm
Sample 7S_B (not annealed, 0 rpm)	21.0 ± 3.1 nm	105.7 ± 11.7 nm	0.6 nm
Sample 7S_C (annealed, 10 rpm)	24.1 ± 3.9 nm	80.2 ± 7.8 nm	0.6 nm
Sample 7S_D (not annealed, 10 rpm)	24.6 ± 3.9 nm	182.7 ± 23.8 nm	0.5 nm

It should be noted that substrate rotation during deposition and pre-annealing lead to decrease and increase in roughness, respectively. This is confirmed from the observation that the roughness of sample 7S_A is much higher in comparison to the other samples (Table 2). Due to the combination of presence of substrate rotation and absence of pre-annealing sample 7S_D exhibits lowest roughness. Sample 7S_B and 7S_C show similar roughness as they fall in the intermediate category.

In order to study the magnetization reversal, angle dependent static hysteresis loops with simultaneous domain imaging has been performed for all the samples in longitudinal mode at RT using MOKE microscope. The angle (ϕ) has been varied between the easy axis and the

external magnetic field at an interval of 10°. Figure 7.5 shows the static hysteresis loops for all the samples along easy axis (EA), intermediate axis (IA) and hard axis (HA). It should be noted that for all the samples less magnetic field is required to saturate the sample along HA as compared to the EA. This indicates that all the samples are inverted thin films where the coercive field of the EA is either comparable or greater than the anisotropy field [105,108]. Similar inverted hysteresis loops have been observed by Chowdhury *et al.* for Co (10 nm) thin films on Si (100) substrate [82]. The origin of the inverted loop has been ascribed to the dispersion in anisotropy due to the substrate rotation during deposition [82].

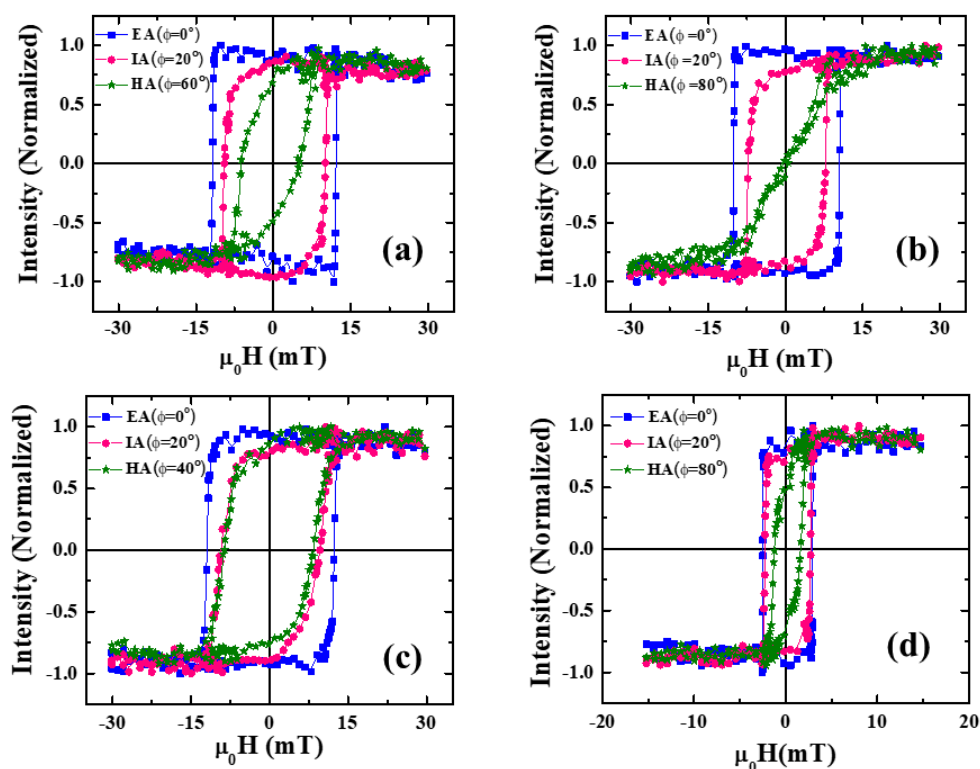


Figure 7.5: (a) – (d) Hysteresis loops measured along easy, intermediate and hard axes by longitudinal MOKE at RT for samples 7S_A, 7S_B, 7S_C and 7S_D, respectively.

The anisotropy behavior for all the samples is depicted by the polar plots of coercivity vs. ϕ data in figure 7.6(a). The red curve (square shaped dots) in figure 7.6(a) shows the anisotropy nature for sample 7S_A where $\phi = 0^\circ$ and 110° are the easy axes and $\phi = 60^\circ$ is the HA. Therefore, no clear conventional anisotropy symmetry is observed in sample 7S_A. It is

expected that uniaxial magnetic anisotropy (UMA) will be induced due to the oblique angle of deposition [17,77-79,93,186]. Further, another contribution of cubic anisotropy is present in sample 7S_A due to the substrate pre-annealing. However, these two anisotropies are not properly aligned with each other.

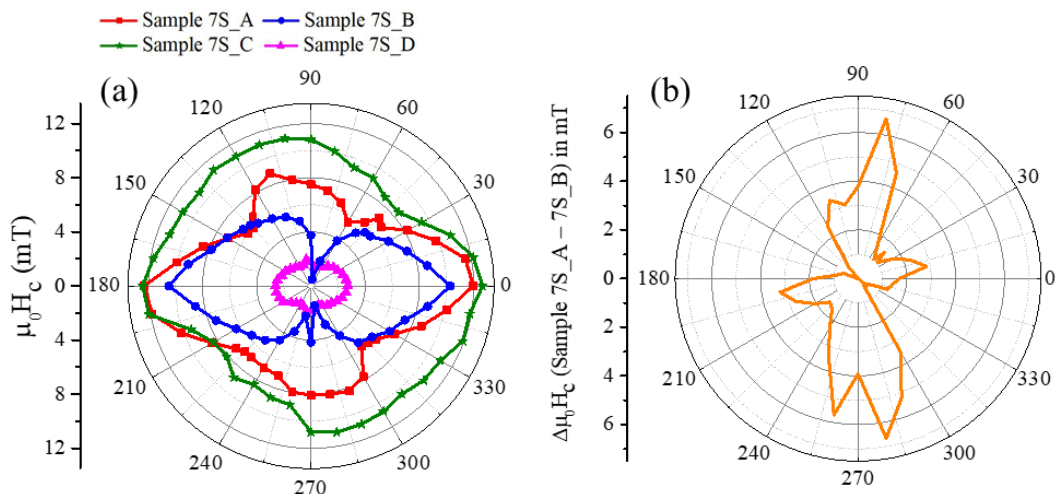


Figure 7.6: (a) Comparison of the coercivity vs. ϕ plots are shown in polar symmetry for samples 7S_A (red solid squares), 7S_B (blue solid circles), 7S_C (green solid stars) and 7S_D (pink solid triangles). (b) Polar plot for difference in coercivity between samples 7S_A and 7S_B vs. ϕ .

In order to explain the mismatch in the alignment of both the anisotropies for sample 7S_A, it is necessary to understand the anisotropy behavior of sample 7S_B. The plot for sample 7S_B (blue curve with round shaped dots) shown in figure 7.6(a) clearly indicates pure uniaxial behavior. Cubic anisotropy is not observed in sample 7S_B as the MgO substrate is not annealed before deposition. Figure 7.6(b) is obtained by subtracting the coercivity curve for sample B from its counterpart of sample A, which shows a four-fold behavior where the EA for cubic anisotropy is shifted by 10° from the EA corresponding to UMA. Therefore, for sample 7S_A both the cubic and uniaxial anisotropies are misaligned by 10° . It should be noted that an error of $\pm 5^\circ$ may occur during the mounting of the substrate in the deposition chamber. In order to suppress the uniaxial anisotropy, sample 7S_C has been prepared by

rotating the substrate at 10 rpm. While rotating the substrate during deposition the grains do not get any preferential growth direction. This may lead to the reduction of uniaxial anisotropy induced by oblique angle deposition. It should be noted that sample 7S_C displays a similar anisotropy behavior (green curve with star shaped dots shown in figure 7.6(a)) like sample 7S_A. But the variations between the coercivity values for EA and HA are much less in comparison to sample 7S_A. Therefore, substrate rotation at 10 rpm during the growth of Co thin film is not sufficient for complete removal of the uniaxial anisotropy. Sample D shows the least anisotropy (pink curve with triangle shaped dots in figure 7.6(a)) because of its preparation conditions (no substrate annealing and $R_{sub} = 10$ rpm). However, it shows a very weak uniaxial anisotropy behavior with a small peak along HA. The peak along HA can be explained due to the misalignment of the grains induced by substrate rotation [82,189].

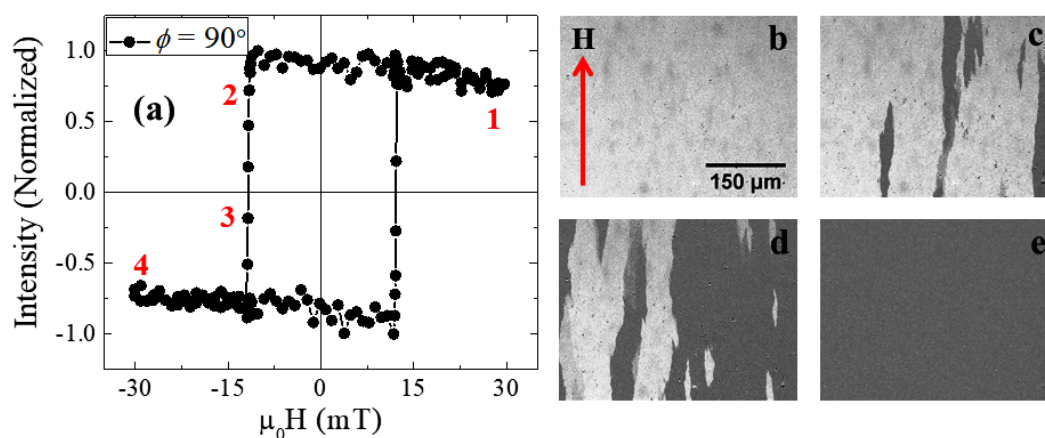


Figure 7.7: (a) Hysteresis loop measured by longitudinal Kerr microscope for sample 7S_A along the EA ($\phi = 0^\circ$). (b) – (e) are the domain images corresponding to the field points 1 to 4 marked in (a) respectively. The arrow in (b) represents the direction of applied magnetic field. The scale bar shown in (b) is same for all the images.

Figure 7.7 depicts the magnetization reversal mechanism for sample 7S_A along EA ($\phi = 0^\circ$). The domain images shown in (b) to (f) correspond to the field points 1 to 4, respectively in the hysteresis loop. Figure 7.7(b) corresponds to the positive saturation (represented by a white contrast domain) of the sample where all the spins are aligned along the applied field

direction. Upon decreasing the field from point '1' to '2' in the hysteresis loop, the spins start reversing in negative direction to initiate the nucleation of 180° domains represented by black contrast in figure 7.7(c). By increasing the field further in the negative direction, more spins get aligned along the reverse direction. This can be observed from the domain image in figure 7.7(d) where black contrast domains expand gradually over white contrast domains via 180° DW motion. At point '4' in the hysteresis loop only black contrast is observed (figure 7.7 (e)) indicating that all the spins are in negatively saturated state.

The effect of different growth modes on the anisotropy behavior can be understood clearly by comparing the domain images for all the samples. Figure 7.8 depicts the domain images for all the samples at coercivity along EA [$\phi = 0^\circ$], IA [$\phi = 20^\circ$] and HA. Figure 7.8(a) – (d) show the domain images at coercivity along the EA of samples 7S_A, 7S_B, 7S_C and 7S_D, respectively. It is observed that for all the samples magnetization reversal along EA is governed by 180° DW motion. Along $\phi = 0^\circ$ branch domain is observed in all the samples. Branch domains are observed in the systems having disorder in growth [12]. Here, the lattice mismatch between Co and MgO attributes to the disorder in the samples. While increasing the angle between the applied magnetic field and the EA of the samples, a second kind of ripple structured domains are observed (figure 7.8(e) – (h)). The ripple domain is the characteristic of inverted thin films [105]. Along all the intermediate axes, ripple domains appear in the beginning of the reversal process. Then at a critical field these ripple domains get frozen and the reversal gets completed through DW motion of a second type of domain i.e. branch domain. This phenomenon can be explained in terms of the model given by Methfessel *et al.* where the magnetization reversal has been qualitatively explained in terms of the exchange and stray field coupling [105]. Along EA the magnetization reversal occurs at $H = H_w$ via DW motion where H_w is the critical field for DW motion. In this

configuration, the field direction remains in the sector of normal behavior where $H_w < H_r$ (H_r = critical field for coherent rotation).

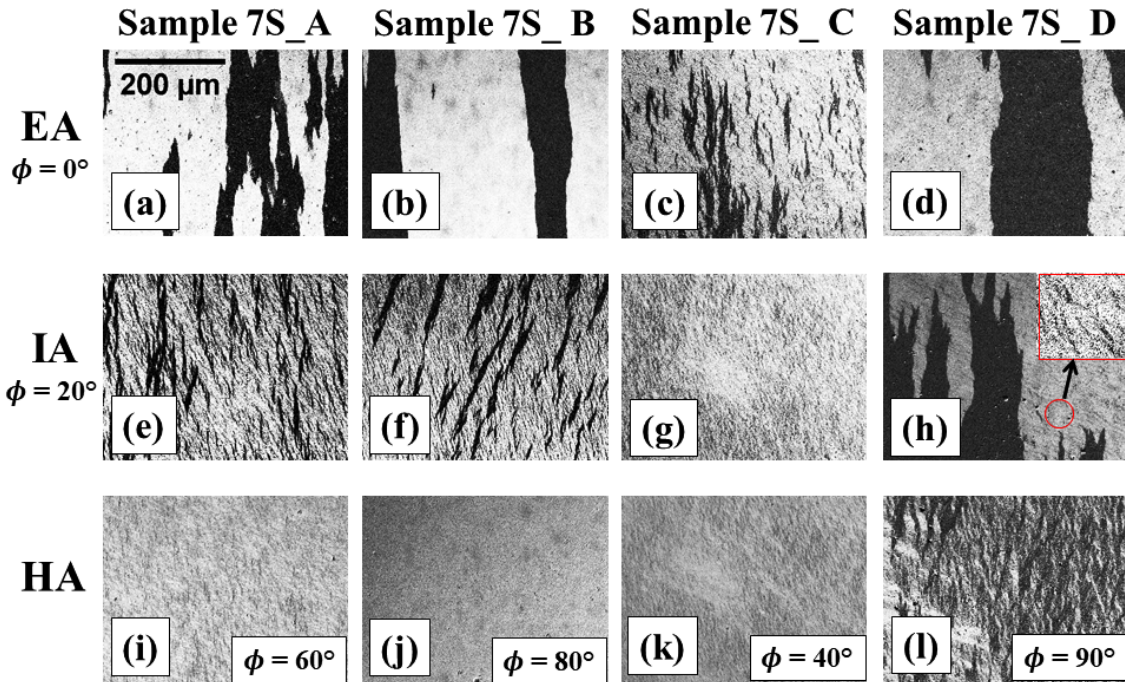


Figure 7.8: Domain images measured at the coercive field for all the samples are shown here. First to third row of the domain images are measured along EA, IA and HA, respectively. The HA was different for different samples and therefore the values of ϕ are written in the domain images in (i) – (l). Four columns of the figure correspond to four different samples 7S_A, 7S_B, 7S_C, and 7S_D. The inset of figure (h) in red square box corresponds to the zoomed image of the red circled area. The direction of the applied field (H) for all the images is shown in (a). All the images are in same length scale shown in (a).

However, when going away from the easy direction the field region enters the inversion sector $H_w > H_r$. In our samples, for IA [$\phi = 20^\circ$] initially at $H = H_r$ the magnetization reverses by partial rotation giving rise to ripple domains in order to reduce the stray field energy [105]. By further increasing the magnetic field at $H = H_w$, another type of domain (branched domain) appears and the reversal process gets completed via DW motion. It is noticed that

for all the samples the domain size decreases with increasing ϕ up to the HA. Along HA the magnetization reversal occurs due to partial rotation of spins for sample 7S_A and 7S_C. This is corroborated by the observation of only ripple domains along HA (figure 7.8 (i) and (k)). However, no domains are observed along HA for sample 7S_B as the reversal probably occurs fully via coherent rotation. For sample 7S_D, due to the misalignment of the grains, narrow domains are observed in addition to the ripple domains along HA. This is corroborated by the presence of a small peak at the HA in the coercivity vs. ϕ plot (figure 7.6 (a)) which indicates the presence of dispersion in anisotropy.

In addition to the subject of magnetic anisotropy, complete understanding of magnetization relaxation is necessary for media writability, data storage and decay of magnetic recording media. Furthermore, the knowledge of magnetization relaxation in different systems allows us to comprehend the underlying physics of magnetization dynamics [212]. Magnetization relaxation measured under sub-coercive fields for thin films [211] and antidots [199,222] of Co on Si (100) substrate shows Fatuzzo – Labrune like single exponential behavior which is common for systems with nucleation dominated aftereffects followed by DW motion [223,224]. The effect of the growth conditions on magnetic relaxation of Co films on MgO substrate has been investigated by longitudinal Kerr microscope at RT along the easy axis. The relaxation measurements have been performed at H_M such that $H_M/H_C \sim 0.99$, where H_M and H_C are the applied constant magnetic field and coercive field, respectively. First the sample has been saturated at a negative magnetic field. Then slowly the magnetic field has been switched towards the positive coercive field (H_C). At $H = H_M$ (H_M is just below H_C), the field has been kept constant and the samples have been allowed to saturate under the influence of thermal activation energy in addition to the constant Zeeman energy. During the relaxation process domain images were taken at regular intervals of ~ 0.2 seconds. The mean grayscale value of each domain image, which represents the net magnetization in the sample,

has been plotted as a function of time to investigate the temporal evolution of magnetization under the influence of constant magnetic field (H_M).

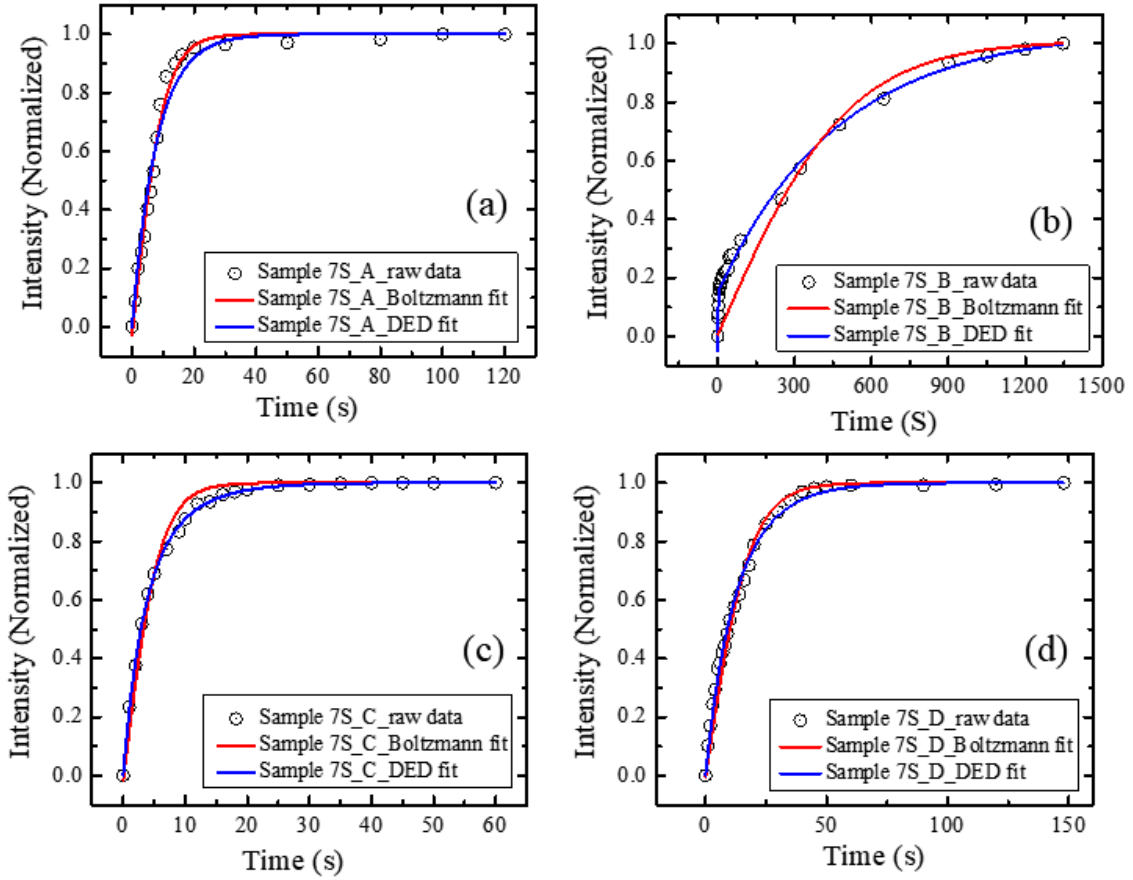


Figure 7.9: (a) – (d) Relaxation measurement along easy axis performed at $H_M/H_C \sim 0.99$ by longitudinal Kerr Microscope for samples 7S_A, 7S_B, 7S_C, and 7S_D, respectively. Open circles and solid lines represent the experimental data and the fits, respectively.

Figure 7.9 shows the relaxation behavior for all the samples where the raw data points are represented by the black hollow circles. The experimentally observed data have been fitted with Boltzmann (equation 7.1) and Double exponential decay (DED) (equation 7.2) functions with the following forms

$$I(t) = I_F + \frac{I_I - I_F}{1 + \exp\left(\frac{t - t_0}{\tau}\right)} \quad (7.1)$$

$$I(t) = I_F + I'_F \exp\left(\frac{-t}{\tau_2}\right) + I'_I \exp\left(\frac{-t}{\tau_1}\right) \quad (7.2)$$

where, $I(t)$ is the measured Kerr intensity, I_I is the initial Kerr intensity at time $t = 0$, I_F is the final Kerr intensity at saturation, τ , τ_1 , τ_2 are the relaxation time constants, I'_I , I'_F are the amplitudes of the corresponding exponents and t_0 is the time corresponding to the mean intensity. It has been reported previously that relaxation data can be well described by a single exponential decay function known as Fatuzzo – Labrune model [223,224] in magnetic thin films where the magnetization reversal occurs via domain nucleation followed by DW motion. However, it should be noted that Fatuzzo – Labrune model is a limiting case of the Boltzmann function (equation 7.1).

Table 3. Fitting parameters of relaxation data measured at $H_M/H_C \sim 0.99$

	Boltzmann Fit	DED Fit
Sample 7S_A	reduced $\chi^2 = 1.28 \times 10^{-3}$ cod $r^2 = 0.989$ $\tau = 5.06 \pm 0.23$ s	reduced $\chi^2 = 3.15 \times 10^{-3}$ cod $r^2 = 0.974$ $\tau_1 = 7.96 \pm 0.80$ s, $\tau_2 = 7.96 \pm 0.80$ s
Sample 7S_B	reduced $\chi^2 = 1.69 \times 10^{-3}$ cod $r^2 = 0.807$ $\tau = 253.37 \pm 40.86$ s	reduced $\chi^2 = 4.70 \times 10^{-4}$ cod $r^2 = 0.995$ $\tau_1 = 2.09 \pm 0.38$ s, $\tau_2 = 471.64 \pm 11.81$ s
Sample 7S_C	reduced $\chi^2 = 1.77 \times 10^{-3}$ cod $r^2 = 0.979$ $\tau = 2.92 \pm 0.18$ s	reduced $\chi^2 = 6.67 \times 10^{-5}$ cod $r^2 = 0.999$ $\tau_1 = 2.73 \pm 0.09$ s, $\tau_2 = 6.64 \pm 0.17$ s
Sample 7S_D	reduced $\chi^2 = 2.03 \times 10^{-3}$ cod $r^2 = 0.98$ $\tau = 9.09 \pm 0.46$ s	reduced $\chi^2 = 4.71 \times 10^{-4}$ cod $r^2 = 0.995$ $\tau_1 = 7.94 \pm 1.40$ s, $\tau_2 = 15.38 \pm 0.84$ s

Figure 7.9 (a) depicts the relaxation measurements performed for sample 7S_A at $\mu_0 H_M = 12.0$ mT. The blue and the red curves represent fits with Boltzmann and DED functions, respectively. The experimentally observed data for sample 7S_A has been best fitted using the Boltzmann function (equation 7.1). The value of time constant obtained from

the best fit is 5.06 ± 0.23 s. The detailed parameters for the fitting are summarized in table 3. Similar measurements on sample 7S_B, 7S_C and 7S_D revealed that the relaxation nature follows the double exponential decay (DED) behavior (equation 7.2). It can be shown that equation 2 is a manifestation of equation 1 with the assumption that the magnitude of τ is different in two different regime of the function. Rewriting equation 1:

$$\begin{aligned}
 I(t) &= I_F + \frac{I_I - I_F}{1 + \exp\left(\frac{t-t_0}{\tau}\right)} \\
 &= I_F + \frac{I_I}{1 + \exp\left(\frac{t-t_0}{\tau}\right)} - \frac{I_F}{1 + \exp\left(\frac{t-t_0}{\tau}\right)} \\
 &= \frac{I_F}{\exp\left(\frac{t_0-t}{\tau}\right) + 1} + \frac{I_I}{1 + \exp\left(\frac{t-t_0}{\tau}\right)} \\
 &= I_F \left[1 - \exp\left(\frac{t_0-t}{\tau_2}\right) \right] + I_I \exp\left(\frac{-t}{\tau_1}\right) \exp\left(\frac{t_0}{\tau_1}\right); \text{ where, } \tau = \tau_1 \ll t - t_0 \text{ and } \tau = \tau_2 > t - t_0 \\
 &= I_F - I_F \exp\left(\frac{-t}{\tau_2}\right) \exp\left(\frac{t_0}{\tau_2}\right) + I_I \exp\left(\frac{-t}{\tau_1}\right) \exp\left(\frac{t_0}{\tau_1}\right) \\
 &= I_F + I'_F \exp\left(\frac{-t}{\tau_2}\right) + I'_I \exp\left(\frac{-t}{\tau_1}\right) ; \text{ where, } I_F \exp\left(\frac{-t}{\tau_2}\right) = I'_F \text{ and } I_I \exp\left(\frac{-t}{\tau_1}\right) = I'_I
 \end{aligned}$$

The relaxation time constants (τ_1 and τ_2) for sample 7S_B, 7S_C, and 7S_D are (2.09 ± 0.38 s, 471.64 ± 11.81 s), (2.73 ± 0.09 s, 6.64 ± 0.17 s), and (7.94 ± 1.40 s, 15.38 ± 0.84 s), respectively. The DED type relaxation in sample 7S_B, 7S_C, and 7S_D indicates that the initial fast nucleation is followed by slow DW motion. Comparable values of both relaxation time constants (τ_1 and τ_2) suggest that the DED type relaxation behavior of sample 7S_C is very similar to Fatuzzo – Labrune like fast single exponential decay (SED) behavior. Samples 7S_A and 7S_C both show fast relaxation due to formation of large ordered grains (figure 7.4(a) and (c)) owing to substrate annealing prior to deposition. However, substrate rotation along with annealing leads to formation of most densely packed grains in sample 7S_C (figure 7.4(c)) yielding higher exchange coupling in comparison to sample 7S_A which is responsible for fastest relaxation in sample 7S_C (figure 7.9(c)) among all the samples.

Absence of substrate annealing before deposition results in formation of scattered polycrystalline Co grains in sample 7S_B and 7S_D (figure 7.4(b) and (d)) as explained previously. Presence of several pinning centres in the samples 7S_B and 7S_D ensures nucleation of domains. However, due to low exchange coupling between the spins, the system requires longer time to gather sufficient energy to overcome the energy barrier for DW motion to complete the magnetization reversal. This leads to the slow DED relaxation nature in samples 7S_B and 7S_D. It should be noted that, substrate rotation during deposition leads to formation of islands in sample 7S_D which results in relatively higher exchange coupling in comparison to sample 7S_B. Hence, sample 7S_B shows the slowest relaxation among all the other samples.

From the previous discussion, it should be noted that textured Co has been formed when the substrate is pre-annealed at 650°C. Further, from the XRD analysis it has been observed that the degree of texture is better in sample 7S_A in comparison to sample 7S_C. Therefore, the deposition conditions similar to sample 7S_A has been chosen further for the preparation of the bilayer Co/C₆₀ samples.

7.2. Effect of magnetic C₆₀ on the textured Co/C₆₀ bilayer thin film on MgO (001)

substrate:

To observe the effect of Co/C₆₀ spinterface on the magnetic properties of the textured Co film bilayer of Co/C₆₀ sample has been prepared on pre-annealed MgO (001) substrate. To prepare the bilayer of Co/C₆₀ sample, the deposition conditions for the Co layer have been chosen to be similar to sample 7S_A. 20 nm of C₆₀ layer has been deposited in-situ on top of 25 nm Co layer on MgO (001) substrate. C₆₀ has been prepared using thermal evaporation technique. The deposition pressure and the rate for C₆₀ have been observed to be $\sim 1 \times 10^{-7}$ mbar and 0.015 nm/s, respectively. The deposition temperature of 150°C has been maintained for the growth of C₆₀ layer also. The sample structure is as follows - sample 7B_A:

MgO(001)/Co(25 nm)/C₆₀(20 nm). The angle dependent hysteresis loops and corresponding domain images of sample 7B_A have been measured in longitudinal mode at RT using MOKE microscopy. Figure 7.10(a) shows the hysteresis loops measured by varying ϕ for sample 7B_A. It can be observed from the hysteresis loops that similar to the single layer sample 7S_A, the bilayer sample 7B_A also exhibits inverted nature [105]. The inverted nature is even more in the bilayer sample as the difference between the H_C at EA and the H_A saturation field (anisotropy field) is more in sample 7B_A than that of sample 7S_A. This indicates presence of more dispersion in the anisotropy symmetry in sample 7B_A due to the lattice mismatch at the Co/C₆₀ interface. The anisotropy symmetry for sample 7B_A can be understood from the coercivity vs ϕ plot shown in figure 7.10(b). Unlike the single layer sample 7S_A, the effect of the cubic anisotropy is quite less in the bilayer sample 7B_A in comparison to the oblique deposition induced uniaxial anisotropy. The anisotropy symmetry for sample 7B_A is similar to the ones having one dispersed uniaxial anisotropy [189]. Presence of peak at the uniaxial hard axis has also been observed in the sample [189]. This indicates that the global anisotropy is more dispersed in sample 7B_A due to the presence of Co/C₆₀ interface.

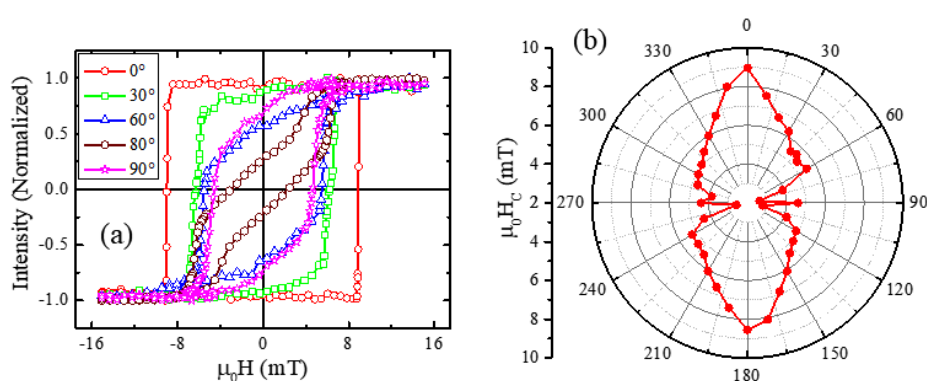


Figure 7.10: (a) Hysteresis loops measured by varying ϕ in longitudinal mode using MOKE microscopy at RT for sample 7B_A. (b) Polar plot showing the variation of coercivity with respect to ϕ which reflects the anisotropy symmetry of sample 7B_A.

The magnetization reversal mechanism for sample 7B_A along the EA ($\phi = 0^\circ$) is depicted in figure 7.11. The reversal occurs with a single jump in the hysteresis loop suggesting 180° DW motion. Large stripe domains are observed in the bilayer sample instead of branch domains as observed in the single layer sample. Such modification in domain structure from branch to stripe pattern has also been observed in case of the polycrystalline Co/C₆₀ sample on Si (100) substrate discussed in chapter 6. Stripe domains are observed in the systems having large dispersion in the anisotropy symmetry [12]. Therefore, the change in the domain pattern in case of this bilayer sample can be attributed to the increase in dispersion in the anisotropy symmetry due to the presence of Co/C₆₀ interface.

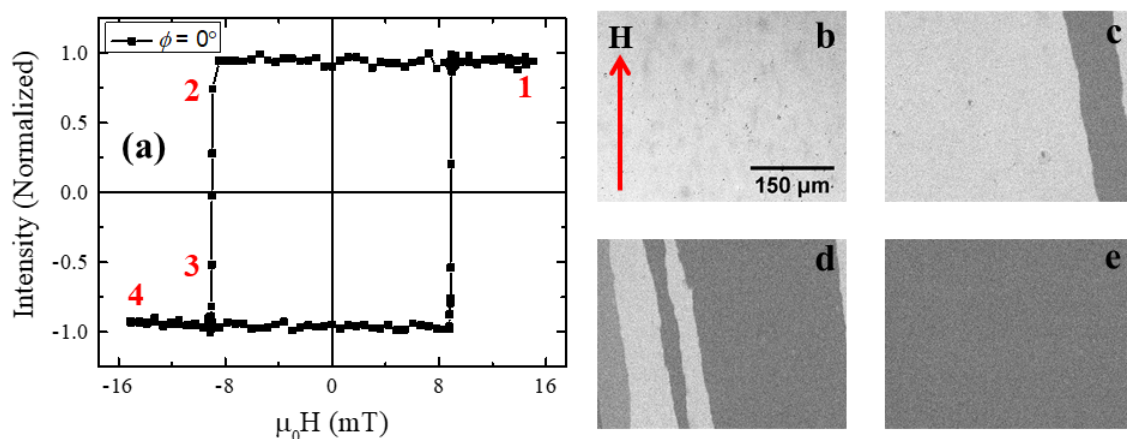


Figure 7.11: (a) Hysteresis loop measured by longitudinal Kerr microscope for sample 7B_A along the EA ($\phi = 0^\circ$). (b) – (e) are the domain images corresponding to the field points 1 to 4 marked in (a) respectively. The arrow in (b) shows the direction of applied magnetic field. The scale bar shown in (b) is same for rest of the images (c) – (e).

As the bilayer sample also exhibits inverted nature, ripple domain is observed in sample 7B_A when the field is applied away from the easy direction. Figure 7.12 shows the hysteresis loop and corresponding domain images for sample 7B_A along $\phi = 30^\circ$. Similar to the single layer sample, formation of ripple domain is observed at the beginning of the reversal (figure 7.12(c)). At a critical field the ripple domains remain static and branch

domains appear (figure 7.12(d)). Further, with increase in the applied field complete reversal is accomplished by the DW motion of the branch domains. When the applied field direction is rotated further near the HA ($\phi = 80^\circ$), a small step has been noticed in the hysteresis loop (figure 7.10(a)). During the reversal two domains have appeared separately where the first domain gets reversed before the switching of the field direction (not shown here). Reversal before the switching of the field direction indicates presence of anti-parallel spin orientation in the sample. Such behavior has also been observed for the epitaxial Fe/C₆₀ sample near the HA discussed in chapter 5.2.

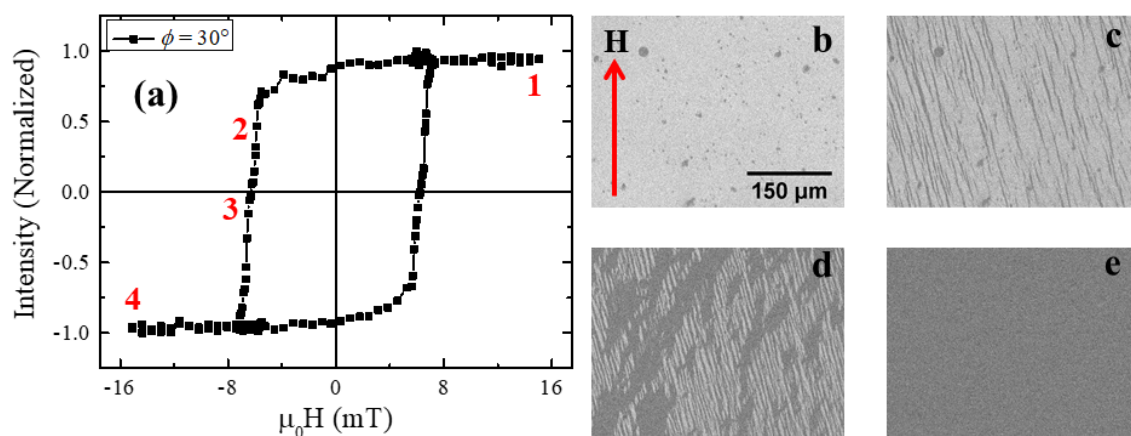


Figure 7.12: (a) Hysteresis loop measured by longitudinal Kerr microscope for sample 7B_A along IA ($\phi = 30^\circ$). (b) – (e) are the domain images corresponding to the field points 1 to 4 marked in (a) respectively. The arrow in (b) represents the direction of applied magnetic field. The scale bar shown in (b) is same for rest of the images.

Polarized neutron reflectivity (PNR) has been performed to obtain the magnetic depth profile in sample 7B_A at MARIA reflectometer. The non-spin flip scattering has been measured at RT keeping the wavelength of the neutron fixed at 0.65 nm. Figure 7.13(a) shows the PNR data and the corresponding fit measured at positive saturation ($\mu_0 H = 100$ mT) of the sample 7B_A. The red and blue open circles represent the data obtained from the R^{++} and R^{--} channels, respectively. The data has been fitted using GenX software [143]. The solid lines

show the best fits to obtain the layer specific structural as well as magnetic properties. The model layer structure of the sample to obtain the magnetic moment and spin arrangement has been shown in figure 7.13(b).

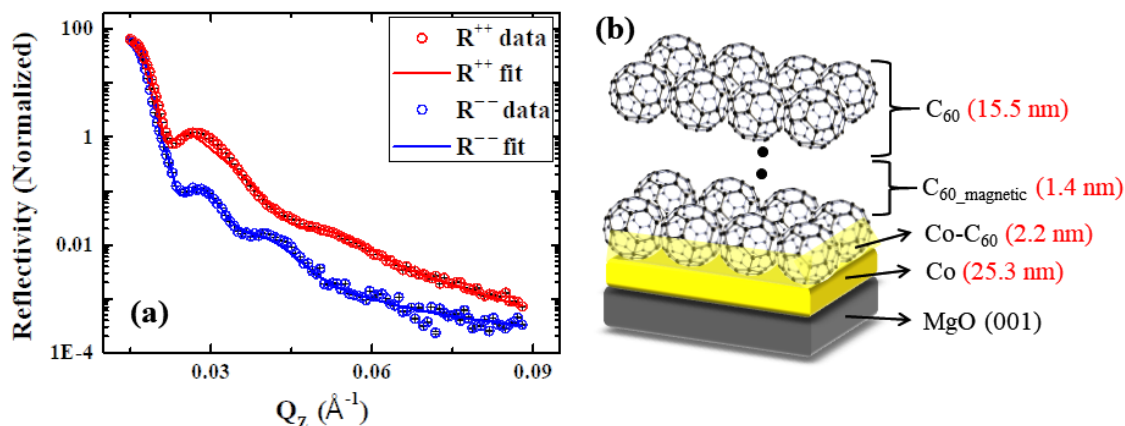


Figure 7.13: (a) Polarized neutron reflectivity (PNR) data and the corresponding fits for sample 7B_A. The red and blue open circles represent the data measured for the R^{++} and R^{--} channels, respectively. The solid lines correspond to their respective fits. The measurement has been performed at the saturation state at RT. (b) A schematic representation of the sample structure obtained by fitting the PNR data is shown in (a). The numbers written in brackets in each layer correspond to the fitted thickness of the respective layer.

The Co layer exhibits $1.33 \pm 0.02 \mu_B/\text{atom}$ magnetic moment in sample 7B_A. Next to the Co layer, an interdiffusion layer of Co and C₆₀ is observed in sample 7B_A. In previous chapter for polycrystalline Co/C₆₀ bilayer sample interdiffusion of Co and C₆₀ has not been observed. However, due to the high temperature growth ($T_{dep} = 150^\circ\text{C}$) of Co and C₆₀ in sample 7B_A, $2.20 \pm 0.01 \text{ nm}$ of interdiffusion is observed in between the Co and C₆₀ layers. The interdiffusion layer contains magnetic moment from both Co atoms and C₆₀ cages. In sample 7B_A, magnetic moment of $2.15 \pm 0.21 \mu_B/\text{unit}$ is observed in the interdiffusion (Co-C₆₀) layer where 1 unit consist of 1 Co atom and 1 C₆₀ cage. Next to the interdiffusion layer,

1.40 ± 0.01 nm of pure C₆₀ layer exhibits magnetic moment of 1.15 ± 0.32 μ_B/cage. Beyond the ferromagnetic C₆₀ layer, 15.5 ± 0.06 nm of C₆₀ does not show any magnetic moment. As discussed in the previous chapters, the cause of the induction of ferromagnetism in C₆₀ near the Co/C₆₀ interface may be attributed to the hybridization between *d*_{Co} and *p*_{C₆₀} orbitals. The induced moment in C₆₀ increases for textured sample 7B_A in comparison to that of polycrystalline Co/C₆₀ sample due to the better growth of the Co layer. The PNR fitting performed for the data measured at the coercive field reveals that Co and the magnetic C₆₀ layers are anti-parallel to each other at the interface. This finding is in good agreement with our earlier discussion of reversal before the switching of the field direction for the hysteresis loops near the hard axis.

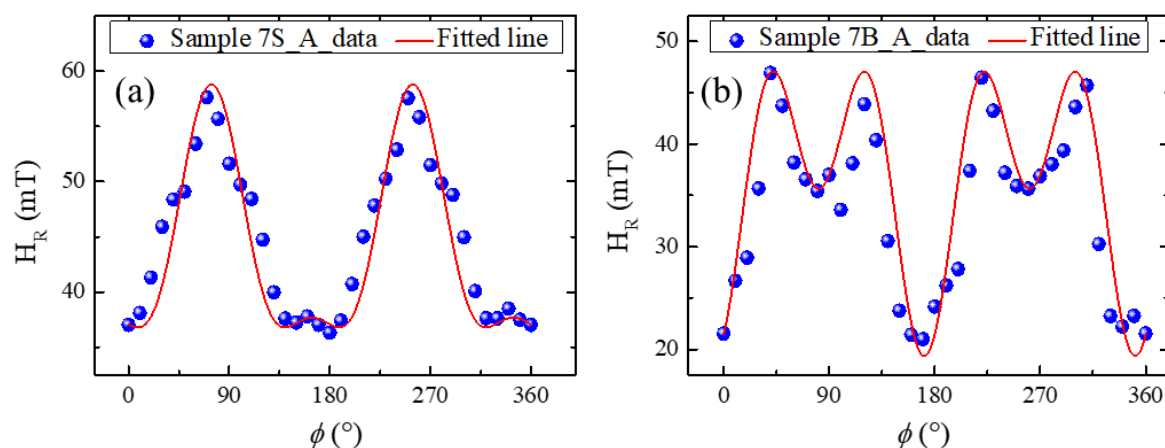


Figure 7.14: Angle dependent resonance field (H_R) plot and corresponding fits for the samples (a) 7S_A and (b) 7B_A measured using ferromagnetic resonance (FMR) technique at a fixed frequency of 8 GHz.

To observe the effect of the Co/C₆₀ spinterface on the anisotropy symmetry of the textured Co thin film, angle dependent FMR measurement has been performed at a fixed frequency of 8 GHz on both single (7S_A) and bilayer (7B_A) samples. To quantify each anisotropy component present in the samples, resonance field (H_R) has been plotted as function of ϕ . Figure 7.14 shows the angle dependent H_R data for both the samples. The data has been fitted

using the dispersion relation (equation 5.3) where both the cubic and uniaxial anisotropy contributions are considered. This relation has been used earlier in chapter 5 to extract similar information for epitaxial Fe thin film having both cubic and uniaxial anisotropies. By fitting the angle dependent H_R data for sample 7S_A (figure 7.14(a)) both cubic (K_4) and uniaxial (K_2) anisotropy constants are extracted to be 6.2×10^3 and 1.2×10^3 J/m³, respectively. Similar fitting performed for sample 7B_A (figure 7.14(b)) provides the K_4 and K_2 to be 2.2×10^3 and 1.2×10^3 J/m³, respectively. Therefore, it can be observed that the cubic contribution remains the same in both the samples as it solely arises from the lattice matching at the Co/MgO interface and the substrate pre-annealing condition. However, the Co/C₆₀ spinterface has significant effect on the uniaxial anisotropy of the samples. This decrease of the uniaxial anisotropy for the bilayer sample by ~3 times can be attributed to the increase in dispersion in the anisotropy arose from the Co and C₆₀ lattice mismatch at their interface. It should be noticed that for the samples having Fe/C₆₀ spinterface, the uniaxial anisotropy got increased with better growth of the Fe layer. However, this behavior is reversed in case of the samples having Co/C₆₀ spinterface. The reason behind such reverse behavior in case of the textured Co/C₆₀ bilayers may be due the inverted nature of the sample. However, it has been observed in the previous chapter that the uniaxial anisotropy increased for the bilayer sample with polycrystalline Co/C₆₀ spinterface.

In summary, the structural and magnetic properties of single layer Co thin films prepared with different pre-annealing and substrate rotation conditions have been studied thoroughly. Textured Co thin films are observed due to the effect of substrate annealing prior to deposition whereas absence of substrate pre-annealing led to the formation of polycrystalline Co thin films. The anisotropy symmetry varies significantly with respect to the growth conditions. Along the easy axes magnetization reversal is governed by 180° DW motion for all the samples. The presence of ripple domains along intermediate axis for all the samples

can be explained from the inverted nature of the Co film. The magnetic properties of bilayer textured Co/C₆₀ sample have been studied and compared with its parent single layer Co thin film. About 1.40 ± 0.01 nm of C₆₀ layer next to the Co layer exhibits $1.15 \pm 0.32 \mu_B/\text{cage}$ magnetic moment due to the $p - d$ orbital hybridization between C and Co atoms. As expected, the induced moment increases in comparison to that of the polycrystalline Co/C₆₀ sample due to the better growth of the Co layer. However, in case of the textured Co/C₆₀ bilayer the uniaxial anisotropy decreases by ~ 3 times in comparison to that of the single layer sample. Such a decrease in anisotropy can be attributed to the increase in dispersion in the anisotropy due to the inverted nature of the films. Future work is necessary to understand this anisotropy behavior.

Chapter 8: Summary and Outlook

The main aim of this thesis has been to study the spinterface induced magnetic properties in ferromagnetic (FM)/organic semiconductor (OSC) heterostructures. Fe and Co have been chosen to be the FM whereas C_{60} has been chosen to be the OSC. Before studying the magnetic properties of the heterostructures, substantial amount of work has been performed to study the structural as well as the magnetic properties of the single layer FM thin films. Formation of a spinterface has been observed for all the FM/OSC interfaces studied in this thesis. Spin transfer from the FM thin film to OSC layers has been observed in the studied samples. The effect of such phenomena on the magnetization reversal, domain structures and anisotropy symmetry of the parent FM thin films has been studied. It has been observed that the spinterface induced magnetic properties are significantly different from their parent thin films. Further, the effect of the crystalline quality and the thickness of the FM layer on the spinterface properties have been discussed. The induced moment in C_{60} and the thickness of the spinterface for all the samples discussed in this thesis are summarized in the annexure.

Fe and Co layers have been prepared on commercially available Si (100) or MgO (001) substrates using dc magnetron sputtering technique. For the bilayer/trilayer samples C_{60} has been deposited in-situ using thermal evaporation technique. The structural properties viz. crystalline quality, surface topography, layer specific thickness, roughness and interfacial properties have been studied using XRD, AFM, XRR and SIMS, respectively. The hysteresis loops and corresponding domain images for all the samples have been measured using MOKE microscopy. The layer specific magnetic moments and the spinterface magnetic properties have been studied using the PNR technique. However, the magnetic moments of the single layer Fe or Co thin films have been obtained from the SQUID measurements. The quantification of the anisotropy contributions and the effect of spinterface on the anisotropy symmetry have been studied using FMR techniques.

Initially single layers of 3 nm Fe and Co films have been prepared on MgO (001) substrate. It should be noted that both Fe and Co exhibit epitaxial growth on MgO (001) substrate when deposited with specific growth parameters. However, due to ~16% mismatch between Co and MgO lattice constants, textured or polycrystalline growth of Co is more probable on MgO (001) substrate. In the present case, the growth of both the Fe and Co films in ultrathin limit is not proper due to the high deposition rate and absence of substrate rotation during deposition. A detailed study of magnetization reversal mechanism in ultrathin Fe film using both PNR and MOKE microscopy suggest the presence of transverse component away from the easy axis. However, the anisotropy is not properly defined in the ultrathin Fe film. In case of ultrathin Co films, an additional uniaxial anisotropy has been observed along with the oblique angle deposition induced uniaxial anisotropy when the substrate is pre-annealed [21]. The magnetization reversal mechanism has been explained in terms of 180° DW motion.

As the growth of both Fe and Co has not been found in proper crystalline structure, thicker films have been chosen further to prepare bilayer or tri-layer films of Fe/C₆₀ and Co/C₆₀ to probe the spinterface. Heterostructures of C₆₀ with Fe or Co films have been prepared on both Si (100) and MgO (001) substrates. Formation of spinterface has been observed in all the bilayer and tri-layer samples of Fe/C₆₀ and Co/C₆₀ due to the *p* - *d* hybridization between C and Fe/Co atoms. Bilayers and tri-layers of Fe/C₆₀ have been prepared on Si (100) substrates by varying the thickness of the Fe layer to study the effect of the thickness of the Fe layer on the spinterface properties. Due to the lattice mismatch between Fe and SiO₂, the growth of Fe is polycrystalline in nature. As a consequence, the Fe layer grows with a strain in its ultrathin limit. Therefore, both the induced moment and the thickness of the spinterface increase with increase in the Fe layer thickness. However, this relation may not be followed if the thickness of the Fe layer is increased beyond certain limit. Future analysis is necessary to find out the global relationship between the thickness of FM layer and the induced moment in the

spinterface. The oblique angle induced uniaxial anisotropy decreases for the Fe/C₆₀ bilayer samples in comparison to their single layer reference Fe samples. This may happen due to the increase in dispersion in the anisotropy due to the poor growth of Fe. In case of tri-layer samples the properties related to the top spinterface are not distinct as the layers above the C₆₀ are mostly interdiffused due to large lattice mismatch. Therefore, bilayer samples are chosen for further studies. The magnetization reversal for all the polycrystalline Fe and Fe/C₆₀ samples are explained in terms of 180° DW motion. Either branch or stripe domains are observed due to the polycrystalline growth and the presence of dispersion in the anisotropy in the samples. The size of the domains decreases for the bilayer samples in comparison to their respective single layer samples may be due to the added dispersion from the C₆₀.

To avoid the growth-related limitations encountered for the ultrathin films, 15 nm thick Fe/C₆₀ bilayer sample has been prepared where the Fe layer grows epitaxially on the MgO (001) substrate. The induced moment in C₆₀ and the thickness of the spinterface for Fe/C₆₀ bilayer on MgO (001) substrate are more than the ones observed for similar spinterface grown on Si (100) substrate. Therefore, the crystallinity of the FM layer plays an important role in optimizing the spinterface properties. Better crystallinity of the FM layer induces higher moment and more thickness of the spinterface. The magnetization reversal for both the single layer Fe and bilayer Fe/C₆₀ films are explained in terms of 90° DW motions. Depending on ϕ , two 90° domains appear successively or separately during the magnetization reversal. The magnetic C₆₀ (spinterface) certainly has profound effects on the magnetization reversal and the domain microstructure when compared to the results obtained from its reference single layer Fe film [9,17]. Further, the uniaxial anisotropy gets enhanced by two orders for the bilayer sample due to the orbital overlap between Fe and C₆₀ molecules.

Therefore, tunability of the anisotropy symmetry is achieved by the formation of the spinterface depending on the crystalline quality of the FM layer.

Further investigations have been performed for the Co/C₆₀ spinterfaces. Similar to the Fe/C₆₀ bilayers, the polycrystalline Co/C₆₀ spinterface exhibits less induced moment (0.8 μ_B /cage) in comparison to the textured ones (1.15 μ_B /cage). We found that the induced moment in Co/C₆₀ spinterface is less when compared with similar Fe/C₆₀ spinterface. However, enhancement in the anisotropy contribution has been observed for polycrystalline Co/C₆₀ samples when Ta is used as the seed layer between the Co and Si (100) substrate. Similar to the polycrystalline Fe samples, either branch or stripe domains are observed in these samples. The domain size as well as the coercivity of the bilayer sample increases due to the increase in exchange coupling at the Co/C₆₀ spinterface. Textured Co thin films are formed on MgO (001) substrate due to the effect of substrate annealing prior to deposition [25]. However, the textured Co exhibits inverted nature. Spin transfer has been observed at the Co/C₆₀ interface due to the $p - d$ orbital hybridization between C and Co atoms. As expected, the induced moment increases in comparison to that of the polycrystalline Co/C₆₀ sample due to the better growth of the Co layer. However, in case of the textured Co/C₆₀ bilayer the uniaxial anisotropy decreases by ~ 3 times in comparison to that of the reference single layer sample. Such decrease in anisotropy can be attributed to the increase in dispersion in the anisotropy due to the inverted nature of the films. Therefore, the message of this thesis work can be expressed in a nutshell by the following points:

- (i) Formation of spinterface has been observed at the Fe/C₆₀ as well as Co/C₆₀ interfaces.
- (ii) The induced moment and the thickness of the spinterface have been quantified systematically for polycrystalline, textured and epitaxial FM/OSC

heterostructures. The spinterface properties strongly depend on the thickness as well as the crystallinity of the ferromagnetic layer.

- (iii) The spinterface has a profound effect on the magnetization reversal mechanism of the Fe/C₆₀ and Co/C₆₀ bilayer samples. The domain size of the bilayer samples gets modified with respect to the single layer reference samples depending on the quality of the spinterface.
- (iv) The tunability of the anisotropy symmetry has been achieved by controlling the crystalline quality of the spinterface.

In future, further studies are required to optimize the tri-layers of FM/OSC/FM systems so that the spin information can be easily transferred from one FM to another FM layer via the OSC layer through formation of spinterfaces. So far, the observation of magnetoresistance (MR) at RT in OSC based spin valves are limited for a handful of systems. It is necessary to understand the spin transfer mechanism at FM/OSC interfaces and optimize the MR at RT to prepare devices for technological applications in organic spintronics. In order to achieve high MR at RT ferroelectric (FE) materials have been recently introduced as an underlayer to the OSC layer. Therefore, detailed study of organic spin valve with a FE material may provide an extra degree of freedom by controlling the device property using electric field. Extensive research is necessary to understand the interfacial properties of the heterostructures having both FM/OSC as well as FE/OSC junctions.

Annexure:

Summary of the magnetic properties of the samples having spinterfaces

Sample name	Sample structure	Crystalline quality of the FM layer	Moment in FM layer in reference sample	Moment in FM layer	Induced moment in C ₆₀	Thickness of the spinterface	Nature of anisotropy	Anisotropy constant in samples with spinterface	Anisotropy constant in reference samples
Sample 4B_A	Si (100) / SiO ₂ (native oxide)/Fe (3.5 nm)/C ₆₀ (10 nm)/Ta (3 nm)	Polycrystalline	1.49 ± 0.08 μ_B /atom	1.06 ± 0.02 μ_B /atom	1.37 ± 0.18 μ_B /cage	1.10 ± 0.08 nm	Uniaxial	Could not be measured	Could not be measured
Sample 4B_B	Si (100) / SiO ₂ (native oxide)/Fe (7.5 nm)/C ₆₀ (15 nm)/Ta (3 nm)	Polycrystalline	1.77 ± 0.04 μ_B /atom	1.36 ± 0.08 μ_B /atom	1.52 ± 0.05 μ_B /cage	1.50 ± 0.07 nm	Uniaxial	Could not be measured	Could not be measured
Sample 4B_C	Si (100) / SiO ₂ (native oxide)/Fe (18 nm)/C ₆₀ (40 nm)/Ta (3 nm)	Polycrystalline	1.98 ± 0.05 μ_B /atom	1.56 ± 0.06 μ_B /atom	1.90 ± 0.04 μ_B /cage	1.80 ± 0.06 nm	Uniaxial	$K_2 = 1.05 \times 10^4$ J/m ³	$K_2 = 2.16 \times 10^4$ J/m ³
Sample 4B_D	Si (100) / SiO ₂ (native oxide)/Fe (18 nm)/C ₆₀ (7 nm)	Polycrystalline	1.98 ± 0.05 μ_B /atom	1.56 ± 0.06 μ_B /atom	1.90 ± 0.04 μ_B /cage	1.80 ± 0.06 nm	Uniaxial	$K_2 = 1.05 \times 10^4$ J/m ³ (data similar to sample 4B_C)	$K_2 = 2.16 \times 10^4$ J/m ³

Sample name	Sample structure	Crystalline quality of the FM layer	Moment in FM layer in reference sample	Moment in FM layer	Induced moment in C ₆₀	Thickness of the spinterface	Nature of anisotropy	Anisotropy constant in samples with spinterface	Anisotropy constant in reference samples
Sample 4T_A	Si (100) / SiO ₂ (native oxide)/Fe (3.5 nm)/C ₆₀ (15 nm)/Fe (3.5 nm)/Ta (3 nm)	Polycrystalline	1.49 ± 0.08 μ _B /atom	Top: could not be measured due to high interdiffusion	Top: 1.37 ± 0.20 μ _B /cage	1.1 ± 0.1 nm	Weak uniaxial	Could not be measured	Could not be measured
				Bottom: 1.01 ± 0.02 μ _B /atom	Bottom: 1.37 ± 0.18 μ _B /cage	1.2 ± 0.1 nm			
Sample 4T_B	Si (100) / SiO ₂ (native oxide)/Fe (7.5 nm)/C ₆₀ (20 nm)/Fe (7.5 nm)/Ta (3 nm)	Polycrystalline	1.77 ± 0.04 μ _B /atom	Top: 1.11 ± 0.07 μ _B /atom	Top: 1.52 ± 0.05 μ _B /cage	1.60 ± 0.07 nm	Weak uniaxial	Could not be measured	Could not be measured
				Bottom: 1.25 ± 0.08 μ _B /atom	Bottom: 1.52 ± 0.05 μ _B /cage	1.60 ± 0.07 nm			
Sample 5B_A	MgO (001)/Fe(15 nm) /C ₆₀ (40 nm) /Ta(3 nm)	Epitaxial	2.20 ± 0.01 μ _B /atom	1.59 ± 0.02 μ _B /atom	2.95 ± 0.27 μ _B /cage	1.9 ± 0.1 nm	Uniaxial + Cubic	K ₂ = -4.7 × 10 ³ J/m ³ K ₄ = -1.2 × 10 ⁴ J/m ³	K ₂ = -49 J/m ³ K ₄ = -1.4 × 10 ⁴ J/m ³

Sample name	Sample structure	Crystalline quality of the FM layer	Moment in FM layer in reference sample	Moment in FM layer	Induced moment in C ₆₀	Thickness of the spinterface	Nature of anisotropy	Anisotropy constant in samples with spinterface	Anisotropy constant in reference samples
Sample 6B_A	Si (100)/Ta(5 nm)/Co(10 nm)/C ₆₀ (12 nm)/Ta(3 nm)	Polycrystalline	1.70 ± 0.03 μ_B /atom	1.60 ± 0.01 μ_B /atom	0.8 ± 0.2 μ_B /cage	1.99 ± 0.18 nm	Uniaxial	$K_2 = 1.71 \times 10^4 \text{ J/m}^3$	$K_2 = 8.78 \times 10^3 \text{ J/m}^3$
Sample 7B_A	MgO(001)/Co(25 nm)/C ₆₀ (20 nm)	Textured	1.76 ± 0.04 μ_B /atom	1.33 ± 0.02 μ_B /atom	1.15 ± 0.32 μ_B /cage	1.40 ± 0.01 nm	Uniaxial + Cubic	$K_2 = 1.2 \times 10^3 \text{ J/m}^3$ $K_4 = 2.2 \times 10^3 \text{ J/m}^3$	$K_2 = 1.2 \times 10^3 \text{ J/m}^3$ $K_4 = 6.2 \times 10^3 \text{ J/m}^3$

References:

- [1] C. B. Harris, R. L. Schlupp, and H. Schuch, *Phys. Rev. Lett.* **30**, 1019 (1973).
- [2] X. M. Zhang, S. Mizukami, T. Kubota, Q. L. Ma, M. Oogane, H. Naganuma, Y. Ando, and T. Miyazaki, *Nature Communications* **4**, 1392 (2013).
- [3] W. J. M. Naber, S. Faez, and W. G. van der Wiel, *J. Phys. D: Appl. Phys.* **40**, R205 (2007).
- [4] V. A. Dediu, L. E. Hueso, I. Bergenti, and C. Taliani, *Nat Mater* **8**, 707 (2009).
- [5] S. Sanvito, *Nature Physics* **6**, 562 (2010).
- [6] T. Moorsom *et al.*, *Phys. Rev. B* **90**, 125311 (2014).
- [7] T. L. A. Tran, P. K. J. Wong, M. P. de Jong, W. G. van der Wiel, Y. Q. Zhan, and M. Fahlman, *Appl. Phys. Lett.* **98**, 222505 (2011).
- [8] T. L. A. Tran, D. Çakır, P. J. Wong, A. B. Preobrajenski, G. Brocks, W. G. van der Wiel, and M. P. de Jong, *ACS applied materials & interfaces* **5**, 837 (2013).
- [9] S. Mallik, S. Mattauch, M. K. Dalai, T. Brückel, and S. Bedanta, *Sci. Rep.* **8**, 5515 (2018).
- [10] D. O. Smith, M. S. Cohen, and G. P. Weiss, *J. Appl. Phys.* **31**, 1755 (1960).
- [11] N. Chowdhury, S. Mallick, S. Mallik, and S. Bedanta, *Thin Solid Films* **616**, 328 (2016).
- [12] A. Hubert and R. Schfer, *Magnetic Domains* (Springer-Verlag, 1998).
- [13] A. Moridi, H. H. Ruan, L. C. Zhang, and M. Liu, *International Journal of Solids and Structures* **50**, 3562 (2013).
- [14] S. Mallik, A. M. Syed, A. Koutsioubas, S. Mattauch, B. Satpati, T. Bruckel, and S. Bedanta, (Under review).
- [15] T. Urano and T. Kanaji, *Journal of the Physical Society of Japan* **57**, 3403 (1988).
- [16] S. Mallik, *et al.* (Manuscript under preparation).
- [17] S. Mallik, N. Chowdhury, and S. Bedanta, *AIP Adv.* **4**, 097118 (2014).
- [18] K. Bairagi *et al.*, *Phys. Rev. Lett.* **114**, 247203 (2015).
- [19] S. Mallik, *et al.* (Manuscript under preparation).
- [20] S. Mallik, B. Sahoo, P. Sharangi, S. Mattauch, T. Bruckel, and S. Bedanta, (Under review).
- [21] S. Mallik and S. Bedanta, *J. Magn. Magn. Mater.* **446**, 270 (2018).
- [22] Y. Nukaga, M. Ohtake, M. Futamoto, F. Kirino, N. Fujita, and N. Inaba, *IEEE Trans. Magn.* **45**, 2519 (2009).
- [23] M. Pires, A. Cotta, M. Martins, A. Silva, and W. Macedo, *J. Magn. Magn. Mater.* **323**, 789 (2011).
- [24] C.-K. Lo, Y. Liou, C. Chang, I. Klik, Y. Yao, and J. Huang, *Appl. Phys. Lett.* **68**, 2155 (1996).
- [25] S. Mallik, S. Mallick, and S. Bedanta, *J. Magn. Magn. Mater.* **428**, 50 (2017).
- [26] F. Djeghloul *et al.*, *Sci. Rep.* **3**, 1272 (2013).
- [27] S. Steil *et al.*, *Nature Physics* **9**, 242 (2013).
- [28] G. Szulczewski, S. Sanvito, and M. Coey, *Nat Mater* **8**, 693 (2009).
- [29] S. S. P. Parkin, C. Kaiser, A. Panchula, P. M. Rice, B. Hughes, M. Samant, and S. H. Yang, *Nature Materials* **3**, 862 (2004).
- [30] J. F. Gregg, I. Petej, E. Jouguelet, and C. Dennis, *J. Phys. D: Appl. Phys.* **35**, R121 (2002).
- [31] A. Fert, *Angewandte Chemie* **47**, 5956 (2008).
- [32] P. A. Grünberg, *Rev. Mod. Phys.* **80**, 1531 (2008).
- [33] Z. V. Vardeny, *Organic Spintronics* (CRC Press, 2010), 1st Edition edn.

References

- [34] S. A. Wolf, D. D. Awschalom, R. A. Buhrman, J. M. Daughton, S. von Molnar, M. L. Roukes, A. Y. Chtchelkanova, and D. M. Treger, *Science* **294**, 1488 (2001).
- [35] I. Žutić, *Rev. Mod. Phys.* **76**, 323 (2004).
- [36] A. J. Drew *et al.*, *Nat Mater* **8**, 109 (2009).
- [37] M. Cinchetti, V. A. Dediu, and L. E. Hueso, *Nat Mater* **16**, 507 (2017).
- [38] Z. H. Xiong, D. Wu, Z. V. Vardeny, and J. Shi, *Nature* **427**, 821 (2004).
- [39] G. Szulczewski, H. Tokuc, K. Oguz, and J. M. D. Coey, *Appl. Phys. Lett.* **95**, 202506 (2009).
- [40] V. Dediu *et al.*, *Phys. Rev. B* **78**, 115203 (2008).
- [41] Z. G. Yu, *Phys Rev Lett* **106**, 106602 (2011).
- [42] X. Zhang, Q. Ma, K. Suzuki, A. Sugihara, G. Qin, T. Miyazaki, and S. Mizukami, *ACS applied materials & interfaces* **7**, 4685 (2015).
- [43] X. Zhang *et al.*, *Carbon* **106**, 202 (2016).
- [44] K. Wang, J. G. M. Sanderink, T. Bolhuis, W. G. van der Wiel, and M. P. de Jong, *Phys. Rev. B* **89**, 174419 (2014).
- [45] K. Wang, E. Strambini, J. G. M. Sanderink, T. Bolhuis, W. G. van der Wiel, and M. P. de Jong, *ACS Appl Mater Interfaces* **8**, 28349 (2016).
- [46] D. Sun, E. Ehrenfreund, and Z. V. Vardeny, *Chem Commun (Camb)* **50**, 1781 (2014).
- [47] I. Bergenti, V. Dediu, M. Prezioso, and A. Riminucci, *Philosophical transactions. Series A, Mathematical, physical, and engineering sciences* **369**, 3054 (2011).
- [48] T. D. Nguyen, F. J. Wang, X. G. Li, E. Ehrenfreund, and Z. V. Vardeny, *Phys. Rev. B* **87**, 075205 (2013).
- [49] K. V. Raman *et al.*, *Nature* **493**, 509 (2013).
- [50] S. Ding, Y. Tian, Y. Li, W. Mi, H. Dong, X. Zhang, W. Hu, and D. Zhu, *ACS Appl Mater Interfaces* **9**, 15644 (2017).
- [51] C. Barraud *et al.*, *Phys Rev Lett* **114**, 206603 (2015).
- [52] C. Barraud, *Nat. Phys.* **6**, 615 (2010).
- [53] M. Gobbi, F. Golmar, R. Llopis, F. Casanova, and L. E. Hueso, *Adv. Mater.* **23**, 1609 (2011).
- [54] F. Djeghloul *et al.*, *J Phys Chem Lett* **7**, 2310 (2016).
- [55] R. Friedrich, V. Caciuc, N. S. Kiselev, N. Atodiresei, and S. Blugel, *Phys. Rev. B* **91**, 115432 (2015).
- [56] D. Z. Li, C. Barreteau, S. L. Kawahara, J. Lagoute, C. Chacon, Y. Girard, S. Rousset, V. Repain, and A. Smogunov, *Phys. Rev. B* **93**, 085425 (2016).
- [57] R. Pang, X. Q. Shi, and M. A. Van Hove, *Journal of the American Chemical Society* **138**, 4029 (2016).
- [58] Z.-H. Yang, R. Pang, and X.-Q. Shi, *The Journal of Physical Chemistry C* **119**, 10532 (2015).
- [59] M. Lüders, N. Manini, P. Gattari, and E. Tosatti, *The European Physical Journal B-Condensed Matter and Complex Systems* **35**, 57 (2003).
- [60] A. Picone *et al.*, *ACS applied materials & interfaces* **8**, 26418 (2016).
- [61] K. Bairagi *et al.*, *Phys. Rev. B* **98**, 085432 (2018).
- [62] F. Al Ma'Mari *et al.*, *Nature* **524**, 69 (2015).
- [63] F. Al Ma'Mari *et al.*, *Proceedings of the National Academy of Sciences*, 201620216 (2017).
- [64] Y. Shao, R. Pang, H. Pan, and X. Shi, *arXiv preprint arXiv:1610.08247* (2016).
- [65] S. Cho, Y. Yi, J. Seo, C. Kim, M. Noh, K.-H. Yoo, K. Jeong, and C.-N. Whang, *Synthetic metals* **157**, 160 (2007).
- [66] A. Tamai, A. P. Seitsonen, F. Baumberger, M. Hengsberger, Z. X. Shen, T. Greber, and J. Osterwalder, *Phys. Rev. B* **77**, 075134 (2008).

References

- [67] S. Ghosh, S. Tongay, A. Hebard, H. Sahin, and F. Peeters, *J. Magn. Mater.* **349**, 128 (2014).
- [68] T. C. Tseng *et al.*, *Nature Chemistry* **2**, 374 (2010).
- [69] S. Blundell, *Magnetism in Condensed Matter* (Oxford U.P., New York).
- [70] R. Geng, The University of Georgia.
- [71] C. Kittel, P. McEuen, and P. McEuen, *Introduction to solid state physics* (Wiley New York, 1996), Vol. 8.
- [72] J.-H. Park, E. Vescovo, H.-J. Kim, C. Kwon, R. Ramesh, and T. Venkatesan, *Nature* **392**, 794 (1998).
- [73] J. Stöhr and H. C. Siegmann, *Magnetism: from fundamentals to nanoscale dynamics* (Springer Science & Business Media, 2007), Vol. 152.
- [74] P. Boross, B. Dóra, A. Kiss, and F. Simon, *Sci. Rep.* **3**, 3233 (2013).
- [75] A. Khaetskii, D. Loss, and L. Glazman, *Phys. Rev. B* **67**, 195329 (2003).
- [76] M. Getzlaff, (2008).
- [77] S. Cherifi, R. Hertel, A. Locatelli, Y. Watanabe, G. Potdevin, A. Ballestrazzi, M. Balboni, and S. Heun, *Appl. Phys. Lett.* **91**, 092502 (2007).
- [78] J. L. Bubendorff, S. Zabrocki, G. Garreau, S. Hajjar, R. Jaafar, D. Berling, A. Mehdaoui, C. Pirri, and G. Gewinner, *E. Phys. Lett.* **75**, 119 (2006).
- [79] Y. Shim and J. G. Amar, *Phys Rev Lett* **98**, 046103 (2007).
- [80] Y.-P. Fang, W. He, H.-L. Liu, Q.-F. Zhan, H.-F. Du, Q. Wu, H.-T. Yang, X.-Q. Zhang, and Z.-H. Cheng, *Appl. Phys. Lett.* **97**, 022507 (2010).
- [81] M. T. Umlor, *Appl. Phys. Lett.* **87**, 082505 (2005).
- [82] N. Chowdhury and S. Bedanta, *AIP Adv.* **4**, 027104 (2014).
- [83] S. Bedanta, T. Eimuller, W. Kleemann, J. Rhensius, F. Stromberg, E. Amaladass, S. Cardoso, and P. P. Freitas, *Phys. Rev. Lett.* **98** (2007).
- [84] M. Takahashi and T. Kono, *Journal of the Physical Society of Japan* **15**, 936 (1960).
- [85] J. W. Freeland, I. Coulthard, W. J. Antel, and A. P. J. Stampfl, *Phys. Rev. B* **63**, 193301 (2001).
- [86] H. B. Zhao, D. Talbayev, G. Lupke, A. T. Hanbicki, C. H. Li, M. J. van't Erve, G. Kioseoglou, and B. T. Jonker, *Phys Rev Lett* **95**, 137202 (2005).
- [87] Y. Hoshi, E. Suzuki, and M. Naoe, *J. Appl. Phys.* **79**, 4945 (1996).
- [88] P. Weiss, *Journal de Physique Théorique et Appliquée* **6**, 661 (1907).
- [89] K. J. Sixtus and L. Tonks, *Phys. Rev.* **37**, 930 (1931).
- [90] L. Landau and E. Lifshitz, *Phys. Z. Sowjetunion* **8**, 101 (1935).
- [91] F. Bloch, in *Zur Theorie des Austauschproblems und der Remanenzerscheinung der Ferromagnetika* (Springer, 1932), pp. 295.
- [92] L. Néel, *Adv. Phys.* **4**, 191 (1955).
- [93] S. Mallick, S. Mallik, B. B. Singh, N. Chowdhury, R. Gieniusz, A. Maziewski, and S. Bedanta, *J. Phys. D: Appl. Phys.* **51**, 275003 (2018).
- [94] H. S. Cho, C. Hou, M. Sun, and H. Fujiwara, *J. Appl. Phys.* **85**, 5160 (1999).
- [95] S. Chikazumi, *Phys. Rev.* **85**, 918 (1952).
- [96] Y. Wang, C. Nelson, A. Melville, B. Winchester, S. Shang, Z.-K. Liu, D. G. Schlom, X. Pan, and L.-Q. Chen, *Phys. Rev. Lett.* **110**, 267601 (2013).
- [97] E. Della Torre, *Magnetic hysteresis* (Wiley, 2000).
- [98] Y. Liu, D. J. Sellmyer, and D. Shindo, *Advanced magnetic materials: nanostructural effects* (Springer Science+ Business Media, 2006).
- [99] A. Aharoni, *Phys. Rev.* **119**, 127 (1960).
- [100] S. Bedanta, PhD Thesis, Universität Duisburg-Essen, Fakultät für Physik, 2006.
- [101] L. Néel, *Journal de Physique et le Radium* **12**, 339 (1951).
- [102] F. Stacey, *Aus. J. Phys.* **13**, 599 (1960).

References

- [103] E. C. Stoner and E. P. Wohlfarth, *Philosophical Transactions of the Royal Society A: Mathematical, Physical and Engineering Sciences* **240**, 599 (1948).
- [104] T. Gilbert, *Phys. Rev.* **100**, 1243 (1955).
- [105] S. Methfessel, S. Middelhoek, and H. Thomas, *J. Appl. Phys.* **32**, 1959 (1961).
- [106] K. J. Harte, *J. Appl. Phys.* **39**, 1503 (1968).
- [107] H. Hoffmann, *J. Appl. Phys.* **35**, 1790 (1964).
- [108] J. McCord, R. Schafer, R. Mattheis, and K. U. Barholz, *J. Appl. Phys.* **93**, 5491 (2003).
- [109] J. Olmsted and G. M. Williams, *Chemistry: the molecular science* (Jones & Bartlett Learning, 1997).
- [110] <http://www.chemalink.net/books/reader/64/3714.html>.
- [111] F. A. Carey and R. J. Sundberg, *Advanced organic chemistry: part A: structure and mechanisms* (Springer Science & Business Media, 2007).
- [112] T. Rabenau, A. Simon, R. K. Kremer, and E. Sohmen, *Z Phys B Con Mat* **90**, 69 (1993).
- [113] K. C. Chiu, J. S. Wang, and C. Y. Lin, *J. Appl. Phys.* **79**, 1784 (1996).
- [114] N. Atodiresei, J. Brede, P. Lazic, V. Caciuc, G. Hoffmann, R. Wiesendanger, and S. Blugel, *Phys. Rev. Lett.* **105**, 066601 (2010).
- [115] M. R. C. Hunt, S. Modesti, P. Rudolf, and R. E. Palmer, *Phys. Rev. B* **51**, 10039 (1995).
- [116] D. M. Sanders and A. Anders, *Surf Coat Tech* **133**, 78 (2000).
- [117] J. Singh and D. Wolfe, *Journal of materials Science* **40**, 1 (2005).
- [118] W. Kern, *Thin film processes II* (Elsevier, 2012), Vol. 2.
- [119] I. W. Boyd, in *Laser and Ion Beam Modification of Materials* (Elsevier, 1994), pp. 319.
- [120] M. B. Shah, D. S. Elliott, and H. B. Gilbody, *J Phys B-at Mol Opt* **20**, 3501 (1987).
- [121] P. Sigmund, *Phys. Rev.* **184**, 383 (1969).
- [122] R. Behrisch, (1981).
- [123] P. J. Kelly and R. D. Arnell, *Vacuum* **56**, 159 (2000).
- [124] S. Swann, *Physics in technology* **19**, 67 (1988).
- [125] D. Depla, S. Mahieu, and J. Greene, in *Handbook of Deposition Technologies for Films and Coatings (Third Edition)* (Elsevier, 2010), pp. 253.
- [126] R. C. Jaeger, *Introduction to Microelectronic Fabrication: Volume 5 of Modular Series on Solid State Devices* (Prentice Hall Upper Saddle River, 2001), Vol. 2.
- [127] Mantis Deposition System, <https://www.mantisdeposition.com/systems/view/info/qprep-series.html>.
- [128] <http://www.mantisdeposition.com/?url=nanoparticlesources>.
- [129] C. Clavero, J. L. Slack, and A. Anders, *J. Phys. D: Appl. Phys.* **46**, 362001 (2013).
- [130] F. J. Humphreys and M. Hatherly, *Recrystallization and related annealing phenomena* (Elsevier, 2012).
- [131] G. Binnig, C. F. Quate, and C. Gerber, *Phys Rev Lett* **56**, 930 (1986).
- [132] F. Moreno-Herrero, J. Colchero, J. Gomez-Herrero, and A. M. Baro, *Physical review. E, Statistical, nonlinear, and soft matter physics* **69**, 031915 (2004).
- [133] N. Jalili and K. Laxminarayana, *Mechatronics* **14**, 907 (2004).
- [134] AFM CSI, <https://www.csinstruments.eu/nano-observer-afm-microscope/>.
- [135] T. Russell, *Materials science reports* **5**, 171 (1990).
- [136] M. A. Omar, *Elementary solid state physics: principles and applications* (Pearson Education India, 1975).
- [137] W. H. Bragg and W. L. Bragg, *Proc. R. Soc. Lond. A* **88**, 428 (1913).
- [138] N. W. Ashcroft and N. D. Mermin, *Google Scholar* **403** (2005).

References

- [139] Rigaku XRD, W. H. Bragg, and W. L. Bragg, Proc. Royal. Soc. A 88, 428 (1913).
- [140] <https://www.bruker.com/products/x-ray-diffraction-and-elemental-analysis/x-ray-diffraction/d8-advance/overview.html>.
- [141] I. Hamley and J. S. Pedersen, Journal of applied crystallography **27**, 29 (1994).
- [142] L. G. Parratt, Phys. Rev. **95**, 359 (1954).
- [143] GenX, <http://genx.sourceforge.net/index.html>.
- [144] P. Williams, Annual Review of Materials Science **15**, 517 (1985).
- [145] H. Liebl, Analytical Chemistry **46**, A22 (1974).
- [146] H. W. Werner, Vacuum **22**, 613 (1972).
- [147] J. P. Hofmann, M. Rohnke, and B. M. Weckhuysen, Physical chemistry chemical physics : PCCP **16**, 5465 (2014).
- [148] NPL SIMS, <http://www.nplindia.in/electron-ion-microscopy>
- [149] B. D. Josephson, Phys. Lett. **1**, 251 (1962).
- [150] P. W. Anderson and J. M. Rowell, Phys. Rev. Lett. **10**, 230 (1963).
- [151] R. C. Jaklevic, J. Lambe, A. H. Silver, and J. E. Mercereau, Phys. Rev. Lett. **12**, 159 (1964).
- [152] SQUID Quantum Design, <https://www.qdusa.com/company/index.html>.
- [153] M. Faraday, Philosophical Transactions of the Royal Society of London **136**, 1 (1846).
- [154] J. Kerr, The London, Edinburgh, and Dublin Philosophical Magazine and Journal of Science **3**, 321 (1877).
- [155] R. Schäfer, Handbook of magnetism and advanced magnetic materials (2007).
- [156] L. Landau, (Pergamon Press Reading, MA, 1960).
- [157] S. Polisetty, J. Scheffler, S. Sahoo, Y. Wang, T. Mukherjee, X. He, and C. Binek, Review of Scientific Instruments **79**, 055107 (2008).
- [158] A. Arora, S. Ghosh, and V. Sugunakar, Rev. Sci. Inst. **82**, 123903 (2011).
- [159] Z. Q. Qiu and S. D. Bader, Review of Scientific Instruments **71**, 1243 (2000).
- [160] Kerr Microscope Evico Magnetics, <http://www.evico-magnetics.de/>.
- [161] T. Beetz and C. Jacobsen, Journal of synchrotron radiation **10**, 280 (2003).
- [162] A. Miniewicz, A. Sobolewska, A. Kochalska, E. Schab-Balcerzak, A. C. Mitus, G. Pawlik, B. Sahraoui, and F. Kajzar, NONLINEAR OPTICS QUANTUM OPTICS **36**, 169 (2007).
- [163] A. Schreyer, J. F. Ankner, T. Zeidler, H. Zabel, M. Schafer, J. A. Wolf, P. Grünberg, and C. F. Majkrzak, Physical review. B, Condensed matter **52**, 16066 (1995).
- [164] A. Schreyer, C. F. Majkrzak, T. Zeidler, T. Schmitte, P. Bodeker, K. TheisBrohl, A. Abromeit, J. A. Dura, and T. Watanabe, Phys. Rev. Lett. **79**, 4914 (1997).
- [165] A. Schreyer, K. Brohl, J. F. Ankner, C. F. Majkrzak, T. Zeidler, P. Bodeker, N. Metoki, and H. Zabel, Physical review. B, Condensed matter **47**, 15334 (1993).
- [166] F. Klose, C. Rehm, D. Nagengast, H. Maletta, and A. Weidinger, Phys. Rev. Lett. **78**, 1150 (1997).
- [167] A. Schreyer, J. Ankner, M. Schäfer, T. Zeidler, H. Zabel, C. Majkrzak, and P. Grünberg, J. Magn. Magn. Mater. **148**, 189 (1995).
- [168] G. P. Felcher, W. Lohstroh, H. Fritzsche, M. Munzenberg, H. Maletta, and W. Felsch, Appl. Phys. Lett. **72**, 2894 (1998).
- [169] J. A. C. Bland, D. Pescia, and R. F. Willis, Phys. Rev. Lett. **58**, 1244 (1987).
- [170] T. Nawrath, H. Fritzsche, F. Klose, J. Nowikow, and H. Maletta, Phys. Rev. B **60**, 9525 (1999).
- [171] H. Fritzsche, Y. T. Liu, J. Hauschild, and H. Maletta, Phys. Rev. B **70**, 214406 (2004).
- [172] G. P. Felcher, Phys. Rev. B **24**, 1595 (1981).

References

- [173] A. Paul and S. Mattauch, *J. Phys. D: Appl. Phys.* **43**, 185002 (2010).
- [174] J. F. Ankner and G. P. Felcher, *J. Magn. Magn. Mater.* **200**, 741 (1999).
- [175] H. Zabel, *Appl Phys a-Mater* **58**, 159 (1994).
- [176] S. Mattauch *et al.*, *Journal of Applied Crystallography* **51**, 646 (2018).
- [177] Y. Khaydukov, O. Soltwedel, and T. Keller, *Journal of large-scale research facilities JLSRF* **1**, 38 (2015).
- [178] C. Kittel, *Phys. Rev.* **71**, 270 (1947).
- [179] C. Kittel, *Phys. Rev.* **73**, 155 (1948).
- [180] FMR Spectrometer NanoOsc, <https://www.qdusa.com/products/nanosc-fmr-spectrometers.html>.
- [181] K. Cai *et al.*, *Nat Mater* **16**, 712 (2017).
- [182] M. Yang *et al.*, *Sci Rep* **6**, 20778 (2016).
- [183] V. K. Joshi, *Engineering science and technology, an international journal* **19**, 1503 (2016).
- [184] E. Liu *et al.*, *Appl. Phys. Lett.* **107**, 172403 (2015).
- [185] C. Gould, C. Ruster, T. Jungwirth, E. Girgis, G. M. Schott, R. Giraud, K. Brunner, G. Schmidt, and L. W. Molenkamp, *Phys. Rev. Lett.* **93**, 117203 (2004).
- [186] Y. Shim, V. Borovikov, and J. G. Amar, *Phys. Rev. B* **77**, 235423 (2008).
- [187] Q. F. Zhan, S. Vandezande, C. Van Haesendonck, and K. Temst, *Appl. Phys. Lett.* **91**, 122510 (2007).
- [188] Y. F. Zheng and J. G. Zhu, *J. Appl. Phys.* **85**, 4776 (1999).
- [189] O. Idigoras, A. K. Suszka, P. Vavassori, P. Landeros, J. M. Porro, and A. Berger, *Phys. Rev. B* **84** (2011).
- [190] O. Idigoras, A. K. Suszka, P. Vavassori, B. Obry, B. Hillebrands, P. Landeros, and A. Berger, *J. Appl. Phys.* **115**, 083912 (2014).
- [191] O. Idigoras, P. Vavassori, J. M. Porro, and A. Berger, *J. Magn. Magn. Mater.* **322**, L57 (2010).
- [192] B. M. Lairson, A. P. Payne, S. Brennan, N. M. Rensing, B. J. Daniels, and B. M. Clemens, *J. Appl. Phys.* **78**, 4449 (1995).
- [193] K. Postava, H. Jaffres, A. Schuhl, F. N. VanDau, M. Goiran, and A. R. Fert, *J. Magn. Magn. Mater.* **172**, 199 (1997).
- [194] M. Buchmeier, R. Schreiber, D. E. Burgler, and C. M. Schneider, *Phys. Rev. B* **79**, 064402 (2009).
- [195] M. L. Zhang, J. Ye, R. Liu, S. Mi, Y. Xie, H. L. Liu, C. Van Haesendonck, and Z. Y. Chen, *Chinese Physics B* **25**, 047503 (2016).
- [196] J. H. Liang, J. Z. Cao, J. X. Li, and Y. Z. Wu, *J. Appl. Phys.* **117**, 17E129 (2015).
- [197] R. M. Osgood, B. M. Clemens, and R. L. White, *Phys. Rev. B* **55**, 8990 (1997).
- [198] Paritosh and D. J. Srolovitz, *J. Appl. Phys.* **91**, 1963 (2002).
- [199] S. Mallick, S. Mallik, and S. Bedanta, *J. Appl. Phys.* **118**, 083904 (2015).
- [200] R. Gieniusz, L. T. Baczewski, Z. Kurant, A. Maziewski, and A. Wawro, *J. Magn. Magn. Mater.* **310**, 2198 (2007).
- [201] J. Sinha *et al.*, *Appl. Phys. Lett.* **102**, 242405 (2013).
- [202] P. F. Carcia, *J. Appl. Phys.* **63**, 5066 (1988).
- [203] R. Naik, C. Kota, J. S. Payson, and G. L. Dunifer, *Phys. Rev. B* **48**, 1008 (1993).
- [204] M. Gruber *et al.*, *Nat Mater* **14**, 981 (2015).
- [205] B. Chakraborty, A. Shard, M. Dalai, and G. Sehgal, *Surface and Interface Analysis* **46**, 36 (2014).
- [206] B. R. Chakraborty, S. K. Halder, K. K. Maurya, A. K. Srivastava, V. K. Toutam, M. K. Dalai, G. Sehgal, and S. Singh, *Thin Solid Films* **520**, 6409 (2012).

References

- [207] R. Moroni, D. Sekiba, F. B. de Mongeot, G. Gonella, C. Boragno, L. Mattera, and U. Valbusa, *Phys. Rev. Lett.* **91**, 167207 (2003).
- [208] D. Sekiba, R. Moroni, G. Gonella, F. B. de Mongeot, C. Boragno, L. Mattera, and U. Valbusa, *Appl. Phys. Lett.* **84**, 762 (2004).
- [209] K. Chen, R. Frömter, S. Rössler, N. Mikuszeit, and H. P. Oepen, *Phys. Rev. B* **86**, 064432 (2012).
- [210] Y. V. Goryunov, M. G. Khusainov, I. A. Garifullin, F. Schreiber, J. Pelzl, T. Zeidler, K. Brohl, N. Metoki, and H. Zabel, *J. Magn. Magn. Mater.* **138**, 216 (1994).
- [211] N. Chowdhury, S. Bedanta, and G. S. Babu, *J. Magn. Magn. Mater.* **336**, 20 (2013).
- [212] H. W. Xi, K. Z. Gao, O. Y. Jun, Y. M. Shi, and Y. Z. Yang, *J. Phys.: Cond. Matt.* **20**, 295220 (2008).
- [213] <http://gwyddion.net/>.
- [214] Z. Qing-feng, V. Stijn, T. Kristiaan, and H. Chris Van, *N. J. Phys.* **11**, 063003 (2009).
- [215] G. Sharma, U. P. Deshpande, D. Kumar, and A. Gupta, *J. Appl. Phys.* **112**, 023910 (2012).
- [216] K. S. Ryu, S. H. Yang, L. Thomas, and S. S. Parkin, *Nat Commun* **5**, 3910 (2014).
- [217] Y. Tserkovnyak, A. Brataas, and G. E. Bauer, *Phys Rev Lett* **88**, 117601 (2002).
- [218] B. B. Singh, S. K. Jena, and S. Bedanta, *J. Phys. D: Appl. Phys.* **50**, 345001 (2017).
- [219] A. Conca, S. Keller, L. Mihalceanu, T. Kehagias, G. P. Dimitrakopoulos, B. Hillebrands, and E. T. Papaioannou, *Phys. Rev. B* **93**, 134405 (2016).
- [220] S. Mallik, S. Mattauch, M. K. Dalai, T. Bruckel, and S. Bedanta, *Sci Rep* **8**, 5515 (2018).
- [221] M. Sougata, M. Srijani, S. Braj Bhusan, C. Niru, G. Ryszard, M. Andrzej, and B. Subhankar, *J. Phys. D: Appl. Phys.* (2018).
- [222] S. Mallick and S. Bedanta, *J. Magn. Magn. Mater.* **382**, 158 (2015).
- [223] E. Fatuzzo, *Phys. Rev.* **127**, 1999 (1962).
- [224] M. Labrune, S. Andrieu, F. Rio, and P. Bernstein, *J. Magn. Magn. Mater.* **80**, 211 (1989).